A new role for Sonic Hedgehog signalling in morphogenesis of the spinal cord

Thesis for Doctoral Degree

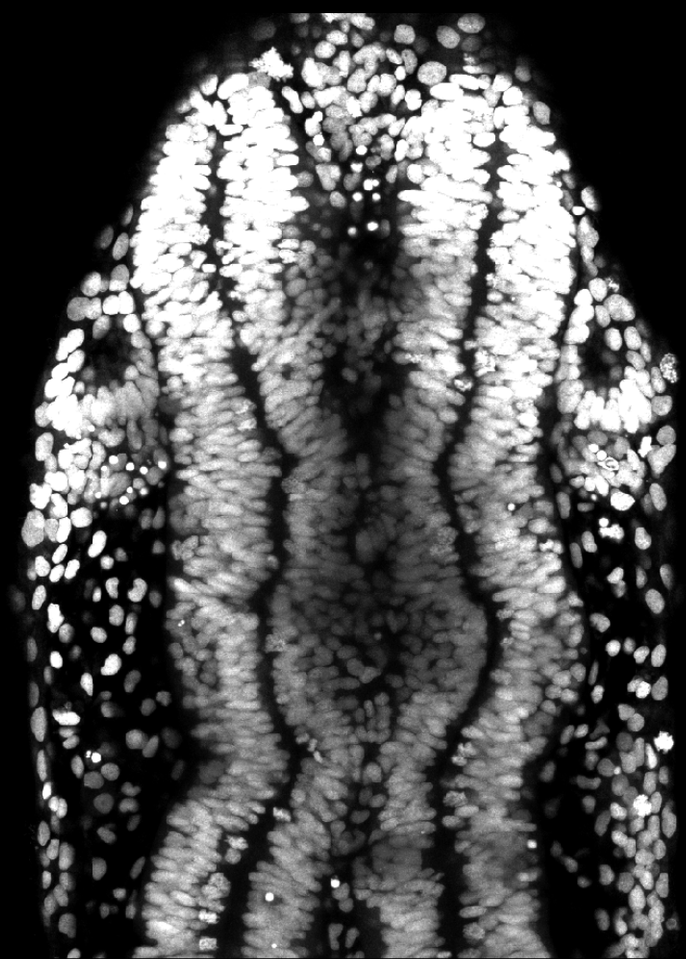

Irene Gutiérrez Vallejo

Universitat de Barcelona
October 2015

Programa de Doctorado del Departamento de Genética

Facultad de Biología

Universitat de Barcelona

TESIS DOCTORAL

A new role for Sonic Hedgehog signalling in morphogenesis of the spinal cord

Nuevas funciones de la vía de señalización Sonic Hedgehog en la morfogénesis de la médula espinal

Memoria presentada por

Irene Gutiérrez Vallejo

Para optar al grado de

Doctora por la Universitat de Barcelona

Esta Tesis Doctoral ha sido realizada en el Departamento de Biología del Desarrollo del Instituto de Biología Molecular de Barcelona (IBMB), perteneciente al Consejo Superior de Investigaciones Científicas (CSIC), bajo la dirección de la Dra. Elisa Martí Gorostiza y y la Dra. Murielle Saade

Directora	Co-directora	Alumna	Tutor
Dra. Elisa Martí	Dra. Murielle Saade	Irene Gutiérrez	Dr. Florenci Serras

Barcelona, Octubre 2015

Acknowledgements

Lo mejor que he encontrado durante este doctorado han sido las personas con las que he compartido tiempo dentro y fuera del trabajo. Y me siento inmensamente agradecida por ello.

To Bart, for the co-working and mentoring during the first two years of my PhD. Thanks for sharing the knowledge in science and behind science. Too many times I remembered many of your wise words. I truly appreciate now looking backwards all that knowledge that you helped me to acquire and all what I learnt from your methodic hard work.

A la gente del laboratorio de Enrique Martín, por los inicios compartidos y las lluvias de ideas, y en especial a Amayra, María, Sri, Fede y Sofía, también por los muy buenos ratos fuera del laboratorio. Aquellos seminarios compartidos siempre fueron un motor de autosuperación para mí.

A Mariona Arbónes y a todo su laboratorio, Sonia, Mª José, Juan e Isa, por la continua aportación de ideas y siempre en un ambiente tan amigable. A Marian Martínez y a toda su gente, Ale, Raquel y Mari, por su grata compañía. Con mención especial a Conchi, nuestra científica internacional con la que nos quedamos con ganas de compartir mucho más.

To Jon Clarke and his people. Not only for the time invested on me learning at his laboratory, but for the great mentoring during that time. The time I spent there was one of the most motivating periods so far, even with the fish not laying and the experiments not working. I am deeply grateful to you and to your group for letting me the opportunity of working in such a stimulating environment.

A Seb, Julien por compartir con nosotros su experiencia e ayudar a impulsar el proyecto. A Javier Buceta, por empezar a ayudarnos a adoptar nuevas perspectivas de una forma siempre amena y entretenida, y por transmitir tan bien todo lo que sabes. A Elena Rebollo, porque si me encanta la microscopía en parte es gracias a ti, porque no he parado de aprender cuando me has ayudado durante la tortura de los time-lapse. A Xavi, por cuidar tan bien de "sus hijos" los peces que me ponían maravillosamente huevos después de sus canciones mañaneras, y por tener siempre una gran sonrisa para empezar el día. Ya sabes cuánto te he echado de menos! A Marieta, porque he disfrutado muchísimo lo poquito que he podido trabajar contigo. He aprendido mucho de la mejor profe que podía tener, y siempre con una sonrisa y pasándolo bien. El mundo debería tener mucha más gente como tú.

A los viejos pollos; A David y Andreas por los buenos ratos compartidos en el laboratorio. A Estel, por su dulzura en todo momento; A Tiago, mi "primer amigo", porque por algún motivo que no logro entender te he echado de menos a mi derecha desde el día que te fuiste. Me he reído muchísimo contigo, cada día me obligabas a hacerme preguntas nuevas y aprendía alguna curiosidad. Espero que sigamos compartiendo visiones parecidas sobre el mundo y la vida. A los nuevos pollos, René, nuestro mejicano favorito, y Luci, la mejor pastelera-científica de todos los tiempos. Habéis sido un soplo de aire fresco cuando lo necesitábamos, y espero que no dejemos de compartir muy buenos ratos. Aquí y en las Américas!

A Eleni, mi estudiantita favorita desde ahora hasta la eternidad. No sólo por lo muchísimo que me has ayudado y que has aportado a este trabajo, también por tu entusiasmo y lo divertido

que es compartir tiempo contigo. Sabes que opino que eres muy inteligente y trabajas genial, tu jefecita confía un montón en tí... Best estudiantita ever! A Sus, por tener siempre su gran sonrisa, y además de ser la mejor técnico y sacar los RNAs más concentrados del mundo (ahora no es peloteo!) por cuidarme a mí y a todos en todo momento, via mail, whatsapp y cafés de urgencia... mil gracias, eres una pieza clave de nuestro labo. Y a Juanito, además de por ser un técnico genial, por la alegría que nos traes al laboratorio... tenemos un equipo estrella de técnicos! A Ángeles, por engañarme tan bien para quedarme, porque empecé con muchísima motivación en gran parte gracias a ti. Gracias por ser una gran compañera de laboratorio, de aventuras, viajes, cotilleos y confidencias. Estoy segura de que quedan más por venir. A Gwen, ya sabes que si me tratas bien te dejo ser mi jefe algún día, y si no siempre nos quedará el chiringuito. Por ser un gran guía y un gran amigo, porque he disfrutado tanto de las conversaciones sobre ciencia, como de cotilleos o crisis existenciales, y incluso de las que no tenían sentido en las fiestas varias. Te admiro muchísimo y no he parado de aprender de ti durante todo este tiempo, sabes que creo que eres el mejor. To Mumu. You don't need me to write here what you meant all this time, but it just kept increasing. You even became my co-director ;) I know I will keep sharing good times with you and mini-you, but in any case huge thanks for all what we shared, all what you taught me, all the conversations about everything on earth, all the laughs and even all few tears. Huge thanks, it makes me happy to think that we will keep climbing trees upside down and talking about life together.

Mis compañeros de laboratorio han sido mi pequeña familia, y de todos y cada uno de ellos creo que son grandes profesionales y lo que yo creo que es más importante, grandes personas. No puedo sentirme más agradecida por haberme rodeado de gente así, sólo por la gente que he encontrado estos años ya han valido la pena.

A 'la jefa', Elisa. Por supuesto sin ella esto no hubiese sido posible, pero no sólo por su labor como directora. Todos nosotros sabemos que han sido unos años con momentos críticos y sólo gracias a ella nos hemos mantenido a flote. Y personalmente sin sus empujoncitos, tanto los morales como los profesionales, no sé ver cómo hubiese acabado esta tesis. Gracias por todo, por la guía y el apoyo científico y moral, por haber confiado en mí (o almenos algunas veces☺) y por haberme empujado en esos momentos, sobretodo los morales. Tengo mucho que aprender de tu espíritu luchador.

Al circo de bataleros y acróbatas que me rodea en la vida fuera del laboratorio, porque me han dado color y insuflado energía todo este tiempo, y en especial a Meri, Jelen y Caro, en las que he descubierto un súper-equipo con el que espero compartir mucho más.

A la Cèlia i Bea, la meva tríada inquebrantable des de la universitat. Ja sabeu com d'importants per mí, i només espero que continuem compartint les vides paral·leles a la ciència (o no), i sobretot les alegríes i moltíssims riures i visites a països diversos per molts anys més. A l'Arnau i la Cris, que completen el equip de biòlegs amb innombrables sopars, xafarderies personals i científiques.

To Justin. For unconditionally being there in the last 5 years, sharing what is good and not so good. For always trying your best to boost my confidence, to support me and to draw a smile, however and whenever. You also made this possible.

Y siempre lo más importante va al final. El agradecimiento más grande de todos se lo debo a mi familia por el apoyo y el calor que siempre me han hecho sentir: mi abuela, mi tía, mi hermana,

y sobretodo a mis padres. Por todas sus velitas. Por el soporte constante, por su esfuerzo por brindarnos siempre lo mejor de lo mejor, porque cuando he flaqueado han sido mi pilar y porque han tomado cada una de mis alegrías como suyas propias. Todo lo que haga en esta vida sin duda os lo debo a vosotros, esto es tan sólo una cosa más que puede que os enorgullezca, pero no tanto como me enorgullece a mí tener una familia así. Os quiero infinitamente y esto os lo dedico a vosotros.

SUMMARY

Development of the posterior spinal cord involves secondary neurulation, a process poorly understood in which neural tube is formed by cavitation of the tail bud. Comprehension of secondary neurulation is required to understand the morphogenetic origin of high prevalence neural tube defects such as spina bifida.

In zebrafish embryos neurulation goes through a stage of neural rod; a neural primordium that hollows a lumen in the middle. To form a single continuous lumen, cells converge to the tissue centre, divide in stereotyped orientations perpendicular to it (the so-called C-Divisions), and form a tissue midline composed by apical polarity components that will later originate the central lumen. Polarizing events start with the centrosomes positioning in the midline under the control of unknown cues. Sonic Hedgehog has been widely described as a midline signaling protein in other systems, and its components are located in the apical cilium and the underlying basal body, formed by a centrosome.

Shh expression onset occurs during gastrulation in embryonic midline structures –notochord and floor plate- and maintained along neurulation, suggesting a role of Shh in neural tube morphogenesis. Treatment with the Shh inhibitor cyclopamine disrupts the luminal surface, while Shh pathway activation (Shh-GOF) produces partial to total lumen duplication. Shh-LOF/Shh-GOF display defects in neural lumen positioning and/or formation, confirming a role of Shh in lumen formation. Shh-LOF and Shh-GOF preserve their apicobasal polarity and tissue architecture. Analysis of the dynamics of tissue convergence in ShhGOF embryos shows that compared to the same WT stages the neural plate is wider and the neural plate borders stop converging later in development, suggesting delayed cell convergence movements. However comparison between Shh-GOF and WT cell trajectories to the midline reveals no differences in motion. We found that trajectories of cells committing C-Divisions had indistinguishable motion properties compared to their neighbouring cells, and that Shh-GOF cellular motion properties –velocity and persistency- are resistant to Shh activity. We next analysed the behaviour of dividing cells and observed that mitosis progressively lengthened along neurulation. Detailed analysis of the mitotic phases shows that Shh-GOF cells show shortened mitoses from condensation to anaphase,

but spend the same time –or slightly longer- in metaphase. C-Divisions need orient their metaphase plate so they divide perpendicularly to the midline, giving rise to daughter cells that lie at the sides of the prospective lumen. In C-Divisions, metaphase plate rotations are decreased and slower. We next assessed if division orientation was compromised along neural tube formation. Analysis of division orientation shows higher variability in ShhGOF embryos especially at early stages, a fact that would have morphogenetic consequences in the C-Divisions and lumen formation. With similar cell motion properties and similar metaphase duration between WT and ShhGOF mitotic cells, the latter have quicker mitoses, less metaphase rotations and the stereotyped orientation of polarizing C-Divisions is altered, thereby affecting lumen formation.

RESUMEN

Los vertebrados amniotas forman el tubo neural posterior por neurulación secundaria, un proceso apenas estudiado en el que el tubo abre un lumen en el centro. Proponemos el pez cebra (*Danio rerio*)como modelo para entender el origen embrionario de defectos derivados de fallos en la neurulación secundaria, como es la espina bífida.

Durante la neurulación del pez cebra los progenitores neurales compaginan proliferación y convergencia hacia el centro del tejido. Tras la formación de un primordio neural condensado,las células orientan su eje de división perpendicular al eje central (C-Divisions), originando una linea media de polaridad apical que formará el lumen. La polarización empieza con la localización medial del centrosoma, que en interfase constituye la base del cilio. Los componentes de la vía Sonic Hedgehog (Shh) se hallan en el cilio, empezando *shh* a expresarse en estructuras mediales de la gástrula y néurula -futuras notocorda y placa del suelo-. La inhibición de Shh perturba la continuidad del lumen, y la activación de Shh (Shh-GOF)produce fenotipos de duplicación luminal, sugiriendo que Shh regula la localización/formación del lumen. La polaridad apicobasal de las células permanece intacta, pero el primordio neural es más ancho durante la neurulación. Sin embargo la motilidad de los núcleos y los cilios hacia la línea media es resistente a la actividad de Shh. La duración de las mitosis incrementa a lo largo de la neurulación, y las células Shh-GOF presentan mitosis más rápidas, sin acortamiento de la metafase. Lo mismo sucede en las C-Divisions, en las que la metafase presenta menor rotación y mayor variabilidad en el plano final de división, originando líneas medias ectópicas y duplicación del lumen. Los cambios en los niveles de activación de Shh conllevan consecuencias en la morfogénesis del lumen a través de la regulación de las divisiones durante la formación del tubo neural.

INDEX

1. INTRODUCTION

1.1. NEURAL TUBE DEFECTS (NTDs)

Neural tube defects (NTDs) rank among the most common categories of birth defects (Creasy and Alberman, 1976), affecting an average of one every 1000 established pregnancies worldwide (Mitchell, 2005). Around 20% of individuals with birth defects die *in utero* (Dolk et al., 2010) while 9-10% will die during the first year of life (Malcoe *et al.*, 1999). Unfortunately, those who live beyond one year of age are often destined for a life of ill health with repeated medical and surgical interventions. The high prevalence and the fatal consequences of NTDs has put on the spotlight for several decades the study of the neural tube formation and triggered the effort to search the genetic basis of this range of malformations.

1.1.1 Main types of NTDs

NTDs cover a wide spectrum of clinical severity (reviewed in Copp and Greene, 2013a; Greene and Copp, 2014) that we can classify in the following categories depending on the affected region and on the degree of exposure to the amniotic fluid during embryonic development:

1.1.1.1 Open NTDs

They result from a failure of primary neurulation. The neural tube remains opened *in utero*, leading to its degeneration and loss of neurological function below the lesion level. Cases of open NTDs are anencephaly, craniorachischisis -both affecting the brain and invariably lethal before or at birth- and open spina bifida.

- **Exencephaly and anencephaly:**

Exencephaly takes place when, despite of the brain neural folds remaining exposed to the environment, the neuroepithelium proceeds with growth and differentiation therefore protruding from the developing brain. Later in development, the skull vault wont form over the open region, producing the degeneration of the exposed neural tissue and giving rise to anencephaly.

- **Craniorachischisis:**

Around 10% of NTDs are identified as craniorachischisis, a malformation that comprises an extensive lesion in which the entire neural tube remains open from midbrain to low spine. Such individuals show a characteristically short rostro-caudal body axis, a phenomenon that results from a disruption of the embryonic process of convergent extension and that is specifically defective in craniorachischisis. Convergent-extension is a morphogenetic event that depends the planar cell polarity (PCP) pathway.

- **Open spina bifida –myelocele or myelomeningocele-:**

Spina bifida occurs when the progression of spinal neurulation along the body axis is severely delayed. The neural tissue is exposed to the amniotic fluid - named myelocele when is directly exposed, myelomeningocele when it has a meninges-covered sac -. At the time when the sclerotomal component of the axial mesoderm should migrate dorsally to surround the neural tube to form the vertebral arches, the sclerotome is unable to cover the open neuroepithelium, giving rise to a bifid vertebral column. Open spina bifida is generally compatible with postnatal survival, resulting in neurological impairment below the level of the lesion that can lead to lack of sensation, inability to walk and incontinence. Associated conditions include hydrocephalus, which often requires cerebrospinal fluid shunting, vertebral deformities, and genitourinary and gastrointestinal disorders.

1.1.1.2 Herniation NTDs

Herniation defects are those in which meninges - the membranes that cover the brain and the spinal cord-, with or without brain or spinal cord tissue, become exteriorised through a pathological opening in the skull or vertebral column. Two cases of herniation NTDs are encephalocoele and meningocele. Encephalocoele can be lethal depending on the extent of brain damage during herniation.

- **Encephalocoele:**

Encephalocoele has its origin in a defective cranial mesoderm development. A persistent opening in the skull allows the meninges -and in severe cases the brain- to herniate creating an extra-cranial mass. The origin of encephalocoele is not a defective neurulation: there is no evidence of a failed neural tube closure in this situation. A particular case of encephalocoele is the Meckel-Gruber syndrome, which has been found to be a ciliopathy -that is, several of the causative genes have key functions in determining the structure and function of primary cilia-. Many other inherited human disorders have been attributed to genes underlying ciliary function, however open NTDs have not generally been reported as such. Hence, exencephaly appear to be developmentally and genetically distinct from encephalocoele.

- **Meningocele**

Spinal meningocele resembles encephalocoele in comprising herniation of meningeal tissue through a skeletal opening in the vertebral column. However, much less is known about the etiology or pathogenesis of meningocele: animal models are required to advance understanding of this defect.

1.1.1.3 Closed NTDs

There is very little experimental evidence from animal models to identify the developmental origin of closed spinal lesions. However, neurosurgical literature comes up with the likely speculation that closed neural tube defects are due to disruption of secondary neurulation. This hypothesis would make sense for the following reasons:

A-Most defects are at the sacro-coccygeal level (precisely at the level where secondary neurulation happens).

B-They do not open to the external environment; the spinal cord is characteristically ‘tethered’ of adjacent tissues -as expected of faulty tissue separation during secondary neurulation-.

C-Cell types of multiple germ layers are often present, representing the multi-potential nature of the tail bud.

In contrast with open NTDs the spinal cord structure is covered by skin. Examples of

closed NTDs range from asymptomatic spina bifida occulta to severe spinal cord tethering, being less severe than open NTDs. Lumbosacral spinal cord tethering can be associated with lower limb motor and sensory deficits and a neuropathic bladder. The severity of symptoms increases with age and surgical untethering of the cord may provide some relief from disability. Closed NTDs show defects of skeletal development, such as absent neural arches or a midline body spur, and are associated with spinal cord abnormalities such as hydromyelia - consisting in overdistension of the central canal- and diplomyelia or diastematomyelia -a longitudinal duplication or splitting and tethering of the cord's lower end-. Additionally, these disorders are often associated with lipoma and anorectal abnormalities, such as anal stenosis or artresia. The lack of knowledge about the developmental process itself makes closed NTDs the least well-defined group of neural tube lesions.

1.1.1.4 Other defects affecting neural tube development

We can consider a last category of abnormalities that fit the description of NTDs but in which the neural tube formation is affected through the disturbance of later developmental events different than neurulation itself.

- **Iniencephaly:**

Iniencephaly is a severe defect of the cervical spine, including bifid neural arches, with backward flexion of the skull and an extremely short neck. It often co-exists with occipital encephalocele and there is a strong female preponderance, as in anencephaly. It is not yet determined whether this defects arises during neurulation or later during cervical skeletogenesis.

- **Hydrocephalus:**

Hydrocephalus is not classified as an NTD *per se*, however it is very commonly associated with open spina bifida. This defect occurs from the presence of the Chiari type II malformation, in which the brain stem descends into the foramen magnum, therefore blocking circulation of cerebro-spinal fluid and leading to hydrocephalus. The origin of Chiari II malformation and its association with open spina bifida is still

controversial.

1.1.2 The genetic basis of NTDs

NTDs have multifactorial etiology with both genetic and environmental factors, with genetic factors accounting for up to 70% of the variance in NTD prevalence (Leck, 1974). The few non-genetic or environmental factors that have been associated with NTDs are well characterized and taken into account during pregnancy monitoring. One of the best-known causes is vitamin B12 deficiency, which -as any condition that diminishes folate metabolism or availability- acts as a teratogen producing NTDs (Burren *et al.*, 2008). The same applies after taking the anticonvulsant carbamazepine or the antibiotic trimethoprim. In all these cases the risk of malformation is prevented by exogenous folic acid supply (Burren *et al.*, 2008), a measure that has been clinically implemented for primary prevention of NTDs. However not all NTDs respond to folic acid supply. Valproic acid (VPA), a widely used anticonvulsant agent, also increases the risk of NTDs by approximately 10-fold, when taken during early pregnancy (Lammer *et al.*, 1987). Other factors such as diabetes mellitus, maternal obesity -via glycaemic dysregulation- and hyperthermia -such as high maternal fever or extreme sauna usage- also predispose to neural tube malformations (Copp and Greene, 2013a).

A better understanding of genetic factors causing NTDs is beginning to emerge. One of the evidences for the stronger component of genetic causation is the high recurrence risk for siblings of index cases (2-5%), although the nature of this genetic contribution remains unclear (Leck, 1974). NTDs occur at high frequency across the world, but with a sporadic pattern that rarely involves multi-generational families: this evidence is consistent with a multifactorial polygenic or oligogenic pattern of inheritance, rather than a model based on single dominant or recessive genes with partial penetrance.

A high number of mutant genes cause open NTDs in mice, however much less is known about the genetic causation of human NTDs. The embryonic development of NTDs is complex, with diverse cellular and molecular mechanisms operating at different levels of the body axis. In order to search for the genes causing human NTDs, analyses has

focused on two groups of genes:

A - Human genes participating in metabolic processes that have been closely linked to NTDs risk in the pregnancy (folate one-carbon metabolism and glucose metabolism). In view of the preventive action of folic acid intake during pregnancy, the genes participating in folate one-carbon metabolism have been centre of attention in research. The most robust finding to emerge from this analysis has been the C677T and A1298C polymorphisms of methylene tetrahydrofolate reductase (*MTHFR*), which encodes a key enzyme of folate metabolism responsible for homocysteine remethylation. These polymorphisms are associated with approximately 1.8-fold increased risk of NTDs (Amorim *et al.*, 2007). Despite of the predisposition of diabetic pregnancy to NTD, no positive associations have been found for genes regulating glucose metabolism.

B - Orthologues of the mouse genes that have been described as models for NTDs.

More than 200 genetic models of NTD have been described in mice, which include examples all the main open NTD phenotypes: anencephaly, open spina bifida and craniorachischisis (Harris and Juriloff, 2010). These mouse models have provided information on the role of molecular signalling pathways and cell biological processes in neurulation, especially on the primary one. The human orthologues of some of the mouse genes have been examined as candidates for human NTD causation, using either case-control association studies or direct sequencing in mutation screens. However, a part from some studies that have identified putative human mutations in the planar cell polarity pathway, there have been few other positive findings (Greene *et al.*, 2009).

Among the critical cellular processes for the mouse neural tube closure we can find(Copp and Greene, 2010):

- Cytoskeletal proteins, which are essential for cranial closure.
- Cell cycle and neurogenesis-related proteins, which ensure a sufficient number of proliferating cells while avoiding premature neuronal formation that prevents neural tube closure.
- Cell viability-related proteins, without which apoptosis is excessive.

- Cell surface–extracellular matrix interactions, which operate via unknown mechanisms.

It is therefore predictable that changes in master regulatory pathways of embryonic development will affect directly or indirectly the above mentioned cellular processes. Through the identification of mouse mutants displaying NTDs, the main signalling pathways essential for neural tube closure have been identified, including Planar Cell Polarity (PCP), Sonic hedgehog (Shh) and Bone Morphogenetic Protein (BMP) signalling pathways. Other signalling pathways have been described to be important for neural tube closure, such as Notch pathway -via regulation of neurogenesis-, Inositol metabolism -with protein phosphorylation via protein kinase C- and Retinoid signalling -via unknown mechanisms-.

1.1.2.1Planar Cell Polarity (PCP)

At the onset of neurulation the neural plate lengthens and narrows through a process named convergent extension that is required to ensure that the neural folds are close enough to initiate the neural tube closure (Ybot-Gonzalez *et al.*, 2007b). Cells first move towards the tissue midline, where they intercalate leading to medio-lateral narrowing (convergence) and rostro-caudal lengthening (extension) of the body axis (Keller *et al.*, 2008). There is a specific relationship between PCP signalling pathway, convergent extension and initiation of neural tube closure, hence several mouse mutants of PCP pathway components suppress convergence and extension movements leading to a broadened neural plate that results in closure failure and consequent craniorachischisis (Greene *et al.*, 1998). Homozygous mice for each PCP pathway mutant and compound heterozygotes for some pairs of the genes produce craniorachischisis as well, such as Vangl2 +/; Celsr1 +/− and Vangl2 +/−; Scrb1+/−. However, combination of Vangl2 mutants in double heterozygosity with Ptk7 (PCP pathway) or Grhl3 (non-PCP pathway) give rise to open spina bifida, demonstrating that the precise combination of apparently closely-related gene defects can produce the whole range of NTDs (reviewed in Copp and Greene, 2010).

1.1.2.2 Sonic Hedgehog (Shh)

To achieve dorsal closure, the neuroepithelium bends to bring the tips of the neural folds into apposition. In mice embryos bending occurs in a stereotypical manner at hinge points: a ventral median hinge point (MHP) and paired dorso-lateral hinge points (DLHPs) (Shum and Copp, 1996). The MHP is induced by Shh signalling emanating from the notochord located ventral to the neuroepithelium midline; despite of its importance for floor plate development (Chiang *et al.*, 1996; reviewed in Placzek and Briscoe, 2005), the latter it is not required for neural tube closure (Ang and Rossant, 1994; Chiang *et al.*, 1996). However, DLHPs are essential for the neural tube closure in the low spinal region, as shown in Zic2 mutant embryos that lack DLHPs and develop severe spina bifida (Ybot-Gonzalez *et al*. 2007a). The formation of DLHPs is regulated through the interplay of inhibitory and inductive signals that determine their appearance at different axial levels. Shh signalling from the notochord and BMP signalling from the surface ectoderm at the neural folds act as repressors of DLHP formation, while the BMP antagonist noggin expressed at the dorsal region is sufficient to induce DLHPs (Ybot-Gonzalez *et al.*, 2002; Ybot-Gonzalez *et al.*, 2007a; Greene and Copp, 2014).

There is a wealth of mouse mutants affecting Shh signalling, either directly or via effects on cilia function; in some of these mutants neural tube closure is disturbed in the brain, spine, or both, leading to NTDs. Mutants having direct effects on the Shh pathway fall into two groups: those that diminish signalling cause holoprosencephaly and cyclopia but not NTDs, whereas those that activate signalling produce NTDs in almost all cases. A third group of mutants, principally those that affect Shh signalling indirectly via effects on cilia function, have rather variable consequences for neural tube closure (reviewed in Murdoch and Copp, 2010). Thus, generally NTDs result from mutations that enhance Shh signalling, such as mutations on Shh pathway repressors, like the receptor Patched1 or the protein Kinase A, or cilia-related genes such as Gli3, Rab23, Fkbp8, Tulp3, and Ift40 (reviewed in Copp and Greene, 2010; Murdoch and Copp, 2010; Miller *et al.*, 2013). Mutants with increased Shh signalling display NTDs at cranial and/or low spinal levels, such as spina bifida (Murdoch and Copp, 2010). In

contrast, loss of function of Shh pathway activators, including the activating receptor Smoothened and the ligand Shh itself, apparently does not produce NTDs (Zhang *et al.*, 2001; Ybot-Gonzalez *et al.*, 2002), whereas over-expression of such proteins can compromise neural tube closure. These findings argue for a negative influence of Shh signalling on neural tube closure.

It remains to be determined whether this effect of Shh signalling is mediated via DV gene expression patterning or through earlier effects on cell–cell and cell–matrix adhesion that may underlie neural plate bending. It will be interesting to determine in the future whether misregulation of the Shh pathway can be implicated as a risk factor in human cases of anencephaly or spina bifida.

1.1.3 Neurulation failure leads to NTDs

Albeit the increasing knowledge about the genetic risk factors that cause NTDs, understanding of the cellular and molecular mechanisms by which human NTDs arise is yet poor. NTDs comprise a set of birth defects that are thought to arise during the third and fourth weeks after fertilisation, however many questions remain about the precise timing and developmental origin of these disorders. During this time, formation of the neural tube -neurulation- takes place by two different mechanisms; primary neurulation, at more rostral levels, and secondary neurulation at the posterior sacro-coccygeal levels. Most described NTDs come from defective primary neurulation, while secondary neurulation remains poorly understood.

1.1.3.1 Primary neurulation defects

Anomalous primary neurulation can lead to severe open neural tube defects. In mammals (including humans) and birds, the primary neural tube closure is a discontinuous process that starts at several points along the rostro-caudal axis, named closure points. The regions that remain open between closure points are called "neuropores", which will close by 'zippering' the neural tissue from the closures (Figure 1.1) (reviewed in Copp and Greene, 2013b). In mouse there are three closure points (Figure 1.1A), while in human there are apparently only two (Figure 1.1B) (further explained in section 2.1.4).

Failure of closure or 'zippering' events will lead to incomplete closure of the cranial neural tube (Copp, 2005). In *loop-tail* mutant (Vangl2, the homologue of Drosophila strabismus/Van gogh) the failure of closure 1 leads to the most severe NTD, craniorachischisis, highlighting it as a fundamental neurulation event (Copp *et al.*, 1994). The wave of zippering down the neural tube can be arrested at any stage, yielding an open spina bifida of varying length depending on the time of closure cessation, as it happens in *Kumba* -long spina bifida-or *curly tail*-small sacral spina bifida- mutants (van Straaten and Copp, 2001; Ybot-Gonzalez *et al.*, 2007a).

1.1.3.2 Secondary neurulation defects

The effects derived from defective primary neurulation are better understood than the defects coming from secondary neurulation, given that knowledge about this process is still poor. Closed NTDs and some forms of spina bifida are thought to be traceable to secondary neurulation defects, since morphogenesis at sacral and coccygeal regions relies on this process (Lemire, 1969; Schoenwolf, 1984).

1.1.3.3. The need of experimental models to understand neurulation

An accurate understanding of the normal process of neural tube formation is critical to further comprehension of the origin and prevention of NTDs. Mice studies have longbeen useful in order to screen and identify the underlying genetic causes of human NTDs, mainly due to the highly comparable development between mice and human. However, several technical limitations arise to study detailed cellular processes.

A wide variety of state-of-the-art techniques have been developed to deepen the knowledge of early morphogenetic processes in other animal experimental models, such as chick, frog or zebrafish embryos. This has provided new systems and powerful analysis tools to shed light into the developmental processes that lead to a functional neural tube. In these models fundamental cellular and morphological processes underlying normal morphogenesis can be described in higher detail thanks to

techniques such as transgenesis and live imaging.

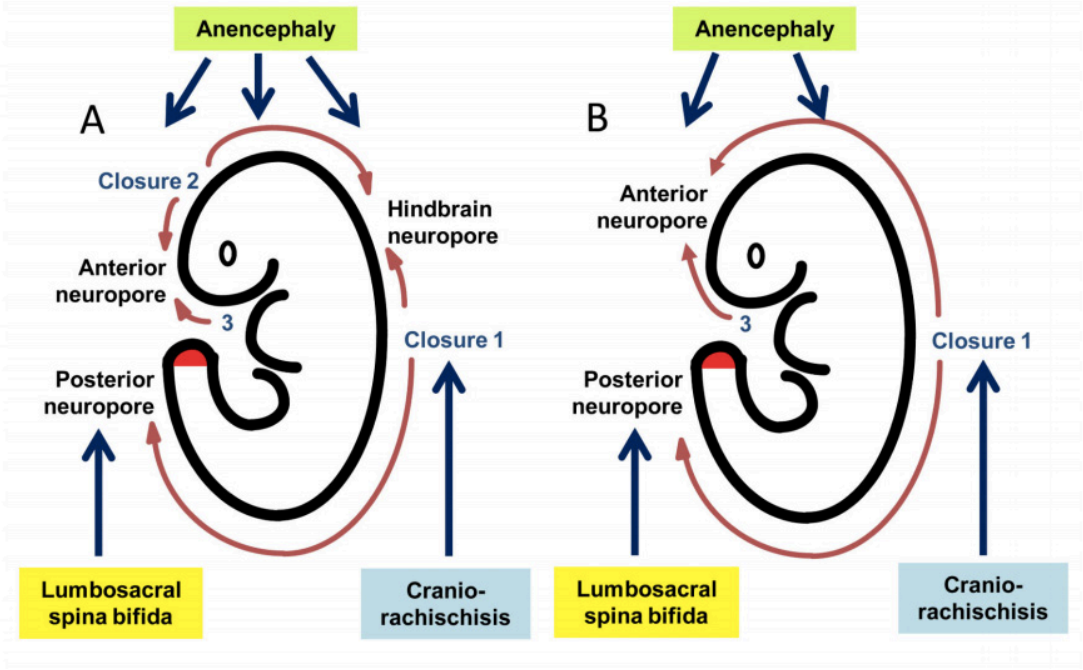

Figure 1.1: Representation of the main events of neural tube closure and their derived neural tube defects in mouse (A) and human (B) embryos.
The main types of NTD resulting from failure of closure at different levels of the body axis are indicated. The red shading on the tail bud indicates the site of secondary neurulation in both species. The initial closure event (Closure 1) occurs at the hindbrain/cervical boundary and closure spreads bidirectionally from this site. In the mouse, a second *de novo* closure site (Closure 2) occurs at the forebrain/midbrain boundary with closure also spreading rostrally and caudally. Closure 2 does not appear to occur in human embryos (B). A third event (Closure 3) occurs in both species at the rostral extremity of the neural plate, with closure spreading caudally from here. Hence, in mice, closure is completed sequentially at the anterior neuropore, hindbrain neuropore and posterior neuropore. In humans, owing to the lack of Closure 2, there are likely to be only two neuropores: anterior and posterior. (C)

Source: *Neural tube defects – disorders of neurulation and related embryonic processes* (Copp and Greene, 2013a)

1.2.-NEURULATION MECHANISMS IN VERTEBRATES

The simplicity of spinal cord eases the study of developmental processes such as morphogenesis, growth and patterning. A wide variety of animal models have been used aiming to understand the morphogenetic processes that lead to the formation of the spinal cord. Chordates are animals characterized, among other anatomical features, by possessing a notochord and a hollow dorsal nerve cord. Vertebrates are included in this phylum, and depending on their embryonic development we can further classify into amniotes and anamniotes. Amniotes are a clade of tetrapod vertebrates comprising sauropsids (reptiles and birds) and mammals that lay their eggs on the land or retain the fertilized egg within the mother and develop into a terrestrial form with limbs, while anamniotes typically lay their eggs in water, including fish and amphibians.

Neurulation is the term that defines the set of morphogenetic movements that shape an initial group of cells into hollow neural tube, the future brain and spinal cord. Although the mode of neurulation varies considerably at the morphological level, the outcome of the whole process is the same in all species and at all axial levels: the formation of a tubular structure. The neural tube is formed by a pseudo-stratified epithelium single layer, i.e. elongated cells seem overlapping although each cell extends from the basal lamina to the lumen of the neural tube. Neuroepithelial cells undergo the process of interkinetic nuclear migration, which consists in an oscillatory nuclear movement synchronized with the progression of the cell cycle, with mitosis taking place at the apical surface (reviewed in Taverna and Huttner, 2010).

Chordates are able to neurulate using a wide variety of mechanisms; a close look to the intense research done in the last decades reveals differences on the process of neurulation depending on the animal model and, in most species, depending on the antero-posterior axis level. Taking these differences into consideration, neurulation can be classified in two categories based on the sequence of morphogenetic events,

namely primary and secondary neurulation. Despite of the striking differences between both neurulation mechanisms, they lead to the same end product: a hollow neural tube.

1.2.1 Primary neurulation in amniotes

The term "primary" refers to the tissues involved in this process as derived from the three germ layers of the "primary body development". Primary neurulation occurs in the amniote vertebrates anterior cervico-thoracic region, where the brain and the future trunk will arise. This process has been carefully described in several vertebrate species. The main characteristic of primary neurulation is that it occurs from a pre-existing epithelium: an organized and contiguous sheet of cells held together by junctional complexes, with a characteristic apicobasal polarity. Briefly, the process consists on the following steps(Figure 1.3A):

-Neural plate formation and shaping

-Neural plate bending, forming the neural groove

-Neural groove closure

Despite of slight differences between species the basic specific steps specific to primary neurulation are well conserved.

1.2.1.1 Neural plate formation

The primitive streak is a structure that forms in the blastula during the early stages of amniotes embryonic development. The origin of the primitive streak relies on mesenchymal cells that arrange along the midline, establishing bilateral symmetry, the rostral to caudal axis and the place where cells will ingress and migrate during gastrulation and germ layer formation (Mikawa *et al.*, 2004; Downs, 2009). The movements of the primitive streak are coordinated with the different stages of neurulation: it progresses towards the caudal region during the formation of the neural plate, and afterwards its rostral end -the Spemann's organizer or, in avian embryos, the Hensen's node - regresses during shaping, bending and closing the neural groove (reviewed in Colas and Schoenwolf, 2001). The organizer is the responsible for

neural plate induction, which consists in supressing the epidermal fate and keep the default neural state of the naïve ectoderm (reviewed in Jessell and Sanes, 2000). The resulting neural plate is formed by an epithelial sheet of cells.

1.2.1.2 Shaping of the neural plate

Formation of the neural plate initially involves apico-basal thickening, and epithelial cells become columnar and polarized. Then, the neural plate undergoes convergent extension movement; that is, it narrows medio-laterally and elongates rostro-caudally (reviewed in Colas and Schoenwolf, 2001). Experiments of isolation of the neural plate conclude that neuroepithelial cells drive neural plate shaping, but full rostro-caudal extension requires gastrulation movements, especially regression of the primitive streak.

1.2.1.3 Bending of the neural plate

Once neural plate shaping has started its bending begins. The main strategy to bend the neural plate consists in defining the "hinge points"; so-called because in these regions cells become wedge shaped and the epithelium can bend. The number and location of hinge points can vary among species and along the antero-posterior axis within one individual embryo, mainly affecting elevation and convergence of the neural folds, and therefore the resulting diameter of the neural tube and the shape of its lumen (Colas and Schoenwolf, 2001)(reviewed in Lowery and Sive, 2004).

In the chick embryo bending involves two simultaneous steps: furrowing and folding. Furrowing gives rise to the central groove that corresponds to the future lumen of the neural tube, and occurs in 3 localized hinge points: one overlying the notochord, named the median hinge point (MHP), and a lateral pair within the neural folds. Folding of the neural plate takes place through movement around the hinge points, elevation towards the medial hinge of the lateral neural folds and their convergence to the midline around the dorso-lateral points.

Furrowing is driven by changes in the cells forming the MHP, which have a different shape from lateral neuroepithelial cells. MHP cells are induced by the secreted protein Sonic Hedgehog (Shh) from the underlying notochord (Smith and Schoenwolf, 1989).

Chick embryos without notochord do not develop MHP cells, and although neural plate bending can occur, the resulting neural tube has an abnormal morphology. Shh signal is essential for the later formation of the floor plate of the neural tube, an important signalling centre (reviewed in Jessell and Sanes, 2000).

Folding, however, requires not only the neural fold but also the apposing neural ectoderm, which is bound together through extracellular matrix. This binding seems suited for transducing the forces needed to fold the flat neural plate and to converge towards the dorsal midline. In fact, only the neural folds and the immediately adjacent ectoderm are required for the folding movement: when all the resting neural plate is extirpated, the most dorsal neuroepithelium and other lateral tissues still can extend towards the midline and fuse (Smith and Schoenwolf, 1991).

In mice embryos, neurulation does not require a functional MHP, as occurs in Shh null mice which lacks normal MHP and floor plate and still has a closed neural tube (Chiang *et al.*, 1996). Here, the bending process increases complexity by combining three different modes of neural plate bending along the mouse primary spinal cord, and they take place consecutively as neurulation progresses (Shum and Copp, 1996).

- Mode 1: There is a single MHP overlying the notochord. After the neural fold fusion the tube has a slit shape.
- Mode 2: In addition to the MHP there are two dorsolateral hinge points, giving rise to a diamond shaped lumen.
- Mode 3: The entire neuroepithelium exhibits bending and the resulting neural tube has a circular lumen.

These modes need to be well coordinated along time to form a properly shaped final tube. *Curly tail* embryos -a mutant predisposed to neural tube defects- exhibit a delay in transition from Mode 2 to Mode 3 preceding faulty closure of the posterior neuropore. This heterogeneity of neurulation morphogenesis in the mouse embryo indicates that the underlying mechanisms may vary along the body axis. It has been suggested that Mode 1 neurulation is largely driven by extrinsic forces generated in adjacent tissues to the neuroepithelium, whereas Mode 3 neurulation is dependent primarily on intrinsic forces generated in the neuroepithelium. Indeed, the transition

from primary neurulation (Mode 3) to secondary neurulation would be a smooth continuation of this trend, with loss of contact between the secondary neuroepithelium and the outside of the embryo (Shum and Copp, 1996).

1.2.1.4 Closure of the neural groove

To conclude neural tube closure the apposing neural folds need to contact in the dorsal midline, where they adhere to one another and fuse. Fusion establishes the roof of the neural tube and separates it from the overlying epidermal ectoderm. Epithelial fusion comprises initial adherence via cellular protrusions regulated by Rho-GTPases and Eph-ephrin interactions (reviewed in Pai *et al.*, 2012).

In the mouse embryo we can account for three different anterior closure points (Figure 1.1):

1. Closure 1: at embryonic day (E) 8.5 in the hindbrain
2. Closure 2: 12h after closure1 in the forebrain-midbrain boundary
3. Closure 3: At the rostral end of prospective forebrain.

In between the closure points there will remain open regions, also called neuropores. Neuropores will close by 'zipping up' the neural tissue from the closures. The caudal neuropore closure represents the limit between the end of primary neurulation and the beginning of secondary neurulation. Slight variations occur between species referring to the timing and location this limit. For example, in human -and mice- embryos the caudal neuropore closure occurs at the level of somite 32-34 (future sacral vertebra 2) (Nievelstein *et al.*, 1994; O'Rahilly and Muller, 1994). In chick and quail embryos it occurs at the level of the somite 27 (Catala *et al.*, 1996), which corresponds to the transition from the truncal (thoracic vertebrae) to lumbar (lumbo-sacral vertebrae) spinal cord.

1.2.2 Secondary neurulation in amniotes

Although development of the nervous system is a major area of research, so far studies have been mainly focused on the primary neural tube. In contrast, the molecular control and subsequent development of the secondary neural tube remains largely unknown. The term secondary neurulation refers to the "secondary body

development", taking place after more anterior regions have developed. It is a characteristic process for the formation of the posterior neural tube of birds and mammals and occurs at the posterior future lumbar and tail region.

The essential difference towards primary neurulation is that the secondary posterior neural tube derives from tissue of the undifferentiated tailbud, a blastema situated along the midline under the overlying ectoderm, which is completely sealed (Figure 1.3B). The tailbud is constituted by a mesenchymal cell population similar to the neighbouring mesoderm, unlike the epithelial neural plate intermediary in primary neurulation, which shares many cellular traits with the adjacent ectoderm (reviewed in Duband, 2010).

A broad definition for mesenchymal tissue would be a "loosely associated group of cells". Tailbud mesenchymal cells show no obvious cell polarity, nor basement membrane or tight junctions, but they express the adherens junction marker N-cadherin instead of E-cadherin (Duband, 2010). Detailed analysis of cell movements during secondary neurulation is still missing.

These mesenchymal cells then condense to form a medullary cord or rod, that undergoes mesenchymal to epithelial transformation and cavitate through multiple lumens that eventually coalesce and form a single epithelial tube (Figure 1.3B) (Criley, 1969; Griffith *et al.*, 1992; Catala *et al.*, 1995; Colas and Schoenwolf, 2001; Shimokita and Takahashi, 2011). Whether this process requires to be induced by signalling from adjacent tissues -as the primary neural plate is induced by the notochord- still remains unexplored.

1.2.2.1 Human

Alike other amniotes, human embryos show the two types of neurulation. At 4 weeks, human embryos show in parallel primary neurulation from the cranial area to the caudal neuropore, and secondary neurulation in more caudal tail regions. The gradual closure of the neural tube along the rostrocaudal body axis isparalleled by the differentiation of the median hinge point cells at the ventral midline of the tube and by its temporary close association with the notochord (Saraga-Babic *et al.*, 1993). At 5 weeks both parts of the neural tubes fuse and from a single continuous lumen. The

junctional region between primary and secondary neurulation shows condensed mesenchyme between the neural plate and the notochord, unlike more anterior regions in where notochord is directly attached to the neural plate (Saitsu and Shiota, 2008). During the 5th-8th developmental weeks, the neuroepithelium differentiating into three distinct layers is accompanied by an underlying notochord, while posterior regions show multiple isolated cavities. The fact that caudal-most regions of the developing spinal cord have separate lumina while keeping apparently normal notochords and no major axial disturbances, (Saraga-Babic *et al.*, 1993; Saraga-Babic *et al*., 1995) suggesting that posterior secondary neurulation involves different mechanisms than anterior primary neurulation. Altogether, these observations suggest that the relationship between the neural plate and the notochord may play a role in neural tube morphogenesis and the mode of cavitation during secondary neurulation (Saitsu and Shiota, 2008). This idea was strengthened through the analysis of an abnormal human embryo with duplicated spinal cords that showed bilateral asymmetry and irregular floor and roof plates. This was accompanied by an abnormally enhanced pattern of neuroepithelial differentiation at the dorsal regions and scattered supernumerary groups of notochord cells, suggesting that the split notochord could induce the spinal cord duplication(Saraga-Babic *et al.*, 1993).

1.2.2.2 Mouse

The mouse secondary neural tube arises after the medullary cord formation from two different structures depending on the embryo stage (Figure 1.2).

- Day 9.5–10 embryos:

The entire mesenchymal region undergoing neurulation becomes epithelial forming the "medullary rosette" (Figure 1.2a), which consists of elongated tail bud cells radially arranged around a central lumen formed by cavitation. At this time, the secondary neural tube is formed by progressive enlargement of the central lumen and addition of tail bud cells to the rosette.

- Day 11-12 embryos:

The dorsal part of the medullary cord becomes an epithelium while the ventral part remains mesenchymal, forming the "medullary plate" (Figure 1.2b). The medullary

plate consists of elongated tail bud cells, but they do not surround a central cavity. Instead, mesenchymal cells are progressively recruited to the epithelium to eventually form a tube (Schoenwolf, 1984; reviewed in Lowery and Sive, 2004). Free cells and cellular debris are frequently encountered in the forming lumen, however apoptotic cells are absent. As the medullary rosette/plate forms and cavitates, mesenchymal cells progressively become epithelial through formation of intercellular junctions at the luminal ends.

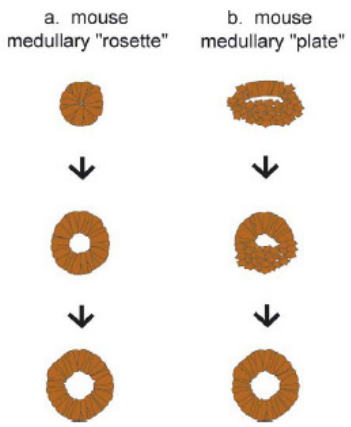

Figure 1.2: Mouse secondary neurulation.
The neural tube is shown subsequent to mesenchyme condensation into the medullary cord.
(a) The medullary rosette, a solid mass of epithelium, expands to form a lumen.
(b) The medullary plate comprises a dorsal epithelium and ventral mesenchyme. The epithelium expands to replace the mesenchyme with concomitant lumen expansion.

Source: *Strategies of vertebrate neurulation and a re-evaluation of teleost neural tube formation* (Lowery and Sive, 2004)

In both processes, cavitation results from the apicobasal polarization tailbud cells and their incorporation into a primitive neuroepithelium, forming the walls of the secondary neural tube (Schoenwolf, 1984).

Once the secondary neural tube is formed, it expresses several patterning genes in restricted domains similar to those in the primary neural tube, but fails to develop a functional floor plate and lacks any neuronal differentiation despite of the appropriate expression of Bone Morphogenetic Protein 4 and Sonic Hedgehog (Shum *et al.*, 2010). The secondary notochord is competent to induce motor neurons in naive neural plate explants *in vitro*. Nevertheless, isolated secondary neural tube in culture in the presence of exogenous Shh is insufficient to induce motor neuron differentiation, supporting the notion that the lack of motor neuron differentiation is an intrinsic property of the mouse secondary neural tube; therefore it does not follow the same developmental pathway as the primary neural tube (Shum *et al.*, 2010).

1.2.2.3 Chick

Most knowledge about amniotes secondary neurulation comes from studies on avian embryos, although it has not been yet as deeply characterized as primary neurulation. The chick embryo has been extensively used as a paradigm for vertebrate neurulation, and classic quail transplant experiments have shed light on morphogenetic movements involved in early neurulation.

The same four basic morphogenetic processes have been described in chick embryo secondary neurulation: (1) Segregation of the medullary cord cells, (2) formation of the medullary cord, (3) cavitation of multiple lumens and (4) lumen coalescence (Figure 1.3B).

Cells first aggregate on the midline forming the medullary cord: a cylinder of densely packed mesenchymal cells (Schoenwolf and Delongo, 1980; Catala *et al.*, 1995; Catala *et al.*, 1996; Yang *et al.*, 2003). This cell segregation from adjacent regions is associated with a process of mesenchymal to epithelial transition, that involves the formation of a layer of extracellular material between adjacent organ rudiments, intercellular junctions and apicobasal cell polarization (Schoenwolf and Delongo, 1980; Yang *et al.*, 2003; Shimokita and Takahashi, 2011).

The mesenchymal to epithelial transition process propagates from anterior to posterior and from the dorsal peripheral cells to the ventral region (Shimokita and Takahashi, 2011). Small intercellular junctions are first formed at the basal outer ends of the elongating peripheral cells and then at their apical inner ends (Schoenwolf and Delongo, 1980). The progressive epithelial character is defined by the appearance of apicobasal polarity markers, such as N-Cadherin (apical) and Laminin (basal) accumulated at the prospective basal and luminal surfaces of the secondary tube. Concomitant with the epithelial character, cells start expressing Sox2, a pan-marker for neural progenitors (Shimokita and Takahashi, 2011). The resulting medullary cord forms a continuous structure with the primary neural tube.

Next, lumen formation starts with the formation of multiple small cavities that later on coalesce into one single lumen (Schoenwolf and Smith, 1990; Catala *et al.*, 1995; Yang *et al.*, 2003). Cavitation always occurs first at the junction between the peripheral and

central cellular populations. The central cells of the medullary cord don't show apicobasal polarization as the peripheral cells, however they also eventually elongate and are cleared up from the lumen (Schoenwolf and Delongo, 1980; Shimokita and Takahashi, 2011). How this happens is not well known, it has been hypothesised that central cells intercalate into the lateral walls of the developing neural tube as lumina coalesce. Coalescence is completed by stage 35, and the whole neural tube is transformed into one tube with a single continuous lumen (Yang *et al.*, 2003). Further studies are needed to achieve a deeper understanding on lumen formation and coalescence processes.

Primary and secondary neurulation events overlap in time at the level of the posterior neuropore. Actually, there is a physical overlap region in where primary neurulation occurs dorsally and secondary neurulation more ventrally within the same neural tube, and the two neural tubes eventually coalesce into a single one (Schoenwolf and Delongo, 1980; Yang *et al.*, 2003).The transition between the two modes of spinal cord formation occurs in such a way that the secondary neural tube is undistinguishable from its anterior counterpart (Catala *et al.*, 1995; Le Douarin *et al.*, 1998). The floor plate and the notochord in the secondary and primary neurulation regions share a common origin -the Hensen's node- thereby demonstrating some continuity between the two mechanisms of neurulation (Catala *et al.*, 1996). The Hensen's node at 6-somite stage already contains all the material necessary to form the notochord and floorplate from the upper thoracic level down to the extremity of the tail. However the presumptive secondary tube cells have a different origin: in stage 8 embryos it is found distinctly mapped from the tail forming mesoderm, in an area of the epiblast posteriorly located to the Hensen's node. When these cells are traced, only the cells forming the tube are labelled at later stages, while the cells forming the notochord or the surrounding tissues are not (Shimokita and Takahashi, 2011). This region is devoided of basal laminin accumulation, unlike the surrounding epiblast cells (Shimokita and Takahashi, 2011), a feature that raises the possibility that these cells ingress to start the secondary neurulation.

One striking difference between the two neurulation mechanisms is that in primary neurulation the contribution of the neural plate to the neural tube is strictly unilateral,

whereas it involves extensive bilateral cell mixing in the dorsal side during secondary neurulation (Catala *et al.*, 1996), as occurs in teleost neural tube formation.

1.2.3 Neurulation in anamniotes

Two anamniote animal models have been extensively studied in order to understand the morphogenetic processes underlying neurulation: *Xenopus laevis* (African clawed frog) (Figure 1.3C) as a representative amphibian embryo model, and *Danio rerio* (Zebrafish) (Figure 1.3D) as a teleost -an infraclass of bony fishes- example development.

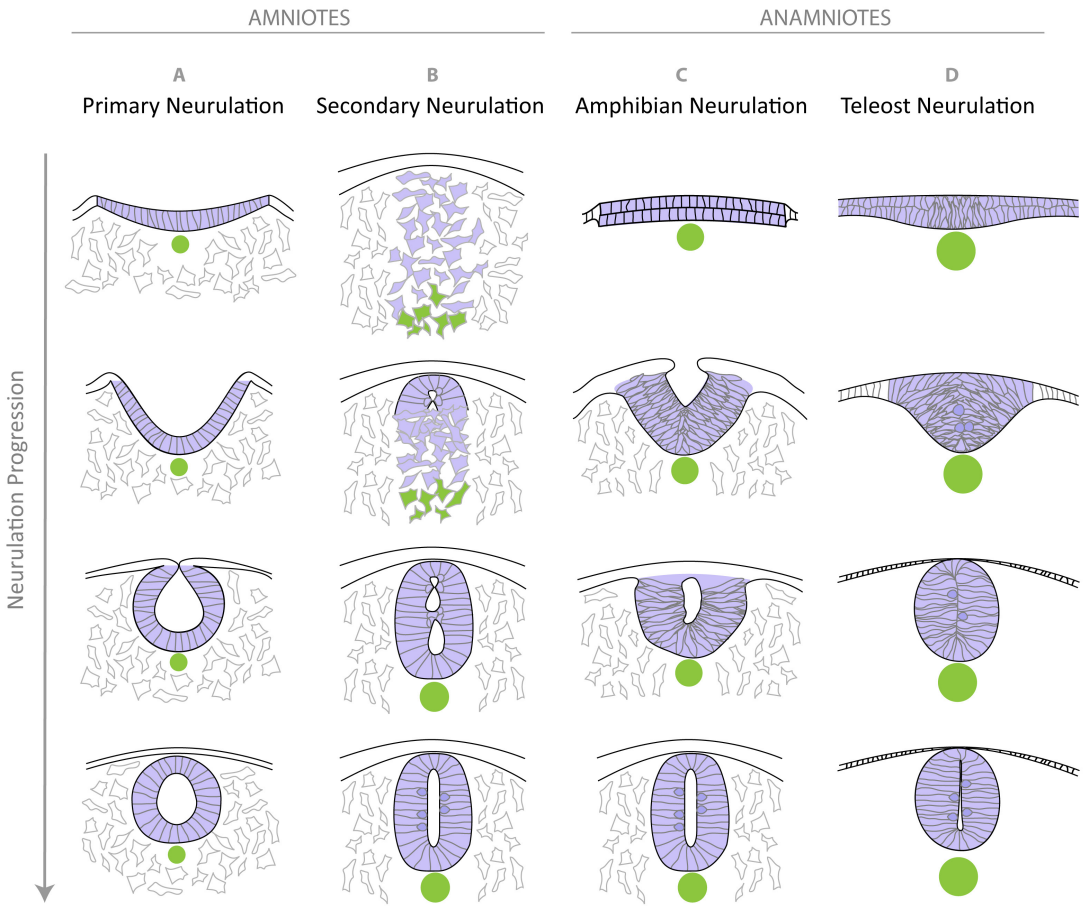

Figure 1.3: Strategies of vertebrate neurulation
(A) Amniotes primary neurulation -chick- occurs from a pre-existing epithelium and involves neural plate formation, bending and closure. Notochord is formed before neurulation. (B) Amniote -chick- secondary neurulation -chick- starts by condensation of mesenchymal cells into the medullary cord, that trough unknown mechanisms become progressively epithelial towards the ventral region. Multiple lumens form by cavitation in the midline, and after coalesce into a single lumen. Notochord forms during neurulation. (C) Amphibian neurulation -Xenopus- starts from a bilaminar neural plate that invaginates. After neural folds fusion, neural plate cells undergo radial intercalation and form a monolayered epithelium that surrounds the lumen. (D) Teleost neurulation -zebrafish- forms by convergence movements in a multilayered neural plate and cell interdigitation, resulting in the formation first of a keel, then a rod. Cavitation occurs in the midline after stereotyped cell divisions. Notochord is formed before neurulation.
Neural tube cells are represented in purple, notochord in green.

1.2.3.1 *Xenopus*

Xenopus neurulation occurs by smooth rolling of a flat neural sheet, a feature shared with primary neurulation regions in amniote embryos. However, while amniote embryos thicken the neural plate monolayer through apicobasal elongation -also called "palisading"-,the *Xenopus* embryo neural plate is bilaminar and only deep cells undergo elongation (Colas and Schoenwolf, 2001) (Figure 1.3C). This bilaminar structure undergoes a complex set of cell movements, starting only after the dorsal fusion of the neural folds. Next, takes place the medially directed migration and radial intercalation of the neural crest cells and deep neural cells through medio-laterally polarized cellular protrusions. Protrusions in neural crest cells are monopolar, while in deep neural cells are bipolar (Davidson and Keller, 1999). Directed medial cell migration and intercalation simultaneously contributes to the narrowing of the wide anlagen by helping convergent extension movements. Once cells have intercalated, the cells undergo a mesenchymal to epithelial transition and form a single-layered array of cells surrounding a lumen. Radial intercalation begins among the ventral cells and progresses to more dorsal cells after dorsal fold fusion, coinciding with the ventral-to-dorsal reconstruction of the neural lumen (Davidson and Keller, 1999). The lumen of the spinal cord is initially occluded and somehow similar to the solid rod "keel" stage in teleosts. Indeed, zebrafish embryos open the initially occluded lumen (Davidson and Keller, 1999; Duband, 2010), and cell intercalation occurs during neurulation as in zebrafish (Papan and Campos-Ortega, 1994).

The amphibian model then combines features of both primary and secondary neurulation: neural folds elevate and fuse as it occurs in avian and mammal primary neurulation, and hinge points are important to do so (Haigo *et al.*, 2003). However the radial intercalation between the two different layers reminds to the mesenchymal to epithelial transition characteristic of secondary neurulation.

1.2.3.2 Zebrafish

In teleosts the neural tube is apparently formed uniformly along the antero-posterior axis, although thickness of the neural plate decreases towards spinal cord regions

(Tawk *et al.*, 2007; Harrington *et al.*, 2010). Briefly, the neural tube is formed from a solid rod primordium that undergoes cellular rearrangements and hollows to form a central lumen (Papan and Campos-Ortega, 1994; Lowery and Sive, 2004; reviewed in Clarke, 2009). Cells of the neural plate need to converge to the tissue midline and invaginate ventrally in order to form a transient tissue known as the neural keel (Figure 1.3D). At this stage cells interdigitate and polarize apically, forming a second transient structure: the neural rod. During this time the control of division orientation plays a major morphogenetic role. After epithelial apico-basal polarity is established the lumen opens forming the neural tube (Lowery and Sive, 2004; Hong *et al.*, 2010)(reviewed in Clarke, 2009). Alike primary neurulation, there is correspondence between initial medio-lateral positions in the neural plate with final ventro-dorsal positions in the neural tube (Papan and Campos-Ortega, 1994; Lowery and Sive, 2004).

1.2.4 Is the Zebrafish embryo a good model to understand Secondary Neurulation and Neural Tube Defects?

Through the *in vivo* analysis of the zebrafish embryo we are achieving a deeper understanding about the cellular events and tissue dynamics during cell convergence, polarization, intercalation and sorting during the formation of the neural tube. These mechanisms are likely to be relevant to amniote secondary neurulation, but technical difficulties have hindered the progression in this field so far.

When comparing zebrafish neurulation with the scattered current knowledge about amniote secondary neurulation several parallelisms arise:

- Both neurulation mechanisms characterized by the complete absence of both neural folds and a neural groove (Lowery and Sive, 2004; Hong and Brewster, 2006).
- Neurulation initiates through cell convergence to the tissue midline and accumulation into a solid neural rod (Papan and Campos-Ortega, 1994)(reviewed in Clarke, 2009), reminiscent to the secondary medullary cord in amniotes.
- Neuroepithelial cells polarize progressively, elongate and organize into a tube (reviewed in Colas and Schoenwolf, 2001). The zebrafish neural plate cells do not exhibit organized junctional complexes, instead the neural tube formation involves the progressive polarization of a inmature epithelial tissue (Duband, 2010). This reminds

to the mesenchymal to epithelial transition driving medullary cord formation in amniotes.

- In chick secondary neurulation bilateral cell mixing is observed (Catala *et al.*, 1996). In zebrafish, cell precursors located on one side of the embryo contribute to descendant daughter cells lying on the two sides of the neural tube (Kimmel *et al.*, 1994; Tawk *et al.*, 2007). This process has been deeply characterized and involves stereotyped cell divisions named C-Divisions (reviewed in Clarke, 2009)

- Neural lumen is formed secondarily by cavitation of the rod (Papan and Campos-Ortega, 1994)(reviewed in Clarke, 2009)

- The zebrafish neural plate also progresses from poor cell organization to a stable, pseudo-stratified epithelium with apicobasal polarity (Hong and Brewster, 2006), although comparison of cell behaviours with secondary neurulation is not possible since the latter has not been elucidated yet.

In contrast with the multiple lumen coalescence characteristic of secondary neurulation, zebrafish cavitation occurs through continous ventral to dorsal polarization opening. However common mechanisms important for lumen opening and coalescence may arise from the study of the zebrafish neurulation process, giving clues into the mechanisms involved in amniote primary and secondary lumen fusion and secondary lumen formation.

Based on the similarities between teleost neurulation and amniote secondary neurulation, we propose the zebrafish embryo as a good experimental model to study neural tube defects deriving from secondary neurulation processes, offering great advantages, such as accessibility of early embryos and the ability to use powerful genetic tools and molecular techniques to analyse the zebrafish nervous system.

1.3. TELEOST NEURAL TUBE MORPHOGENESIS

Embryogenesis can be coarsely divided into three main aspects:

1- Determination of the embryonic axes: antero-posterior (AP), dorso-ventral (DV) and mediolateral (ML).

2- Specification of the three germ layers -endoderm, mesoderm and ectoderm- happening during gastrulation.

3- Organ patterning and diversification of cell fates along the embryonic body.

The word morphogenesis literally means "creation of the shape", and major morphogenetic processes that will determine the embryo shape occur during gastrulation. The zebrafish embryo has a simple architecture when initiates gastrulation movements: the blastoderm, which will give rise to all embryonic tissues, rises on top (also named animal pole) of the syncytial yolk cell (the ventral side of which is also named vegetal pole). Next, a sequence of complex cell movements precedes neural plate formation, such as epiboly, in which the blastoderm becomes thinner through radial intercalation and expands from the animal to the vegetal pole spreading along the yolk cell, and emboly, whereby mesendodermal precursors (hypoblast) internalize and migrate beneath the prospective ectoderm (epiblast) towards the animal pole (Warga and Kimmel, 1990; Solnica-Krezel and Sepich, 2012). Finally, mediolateral cell intercalations in both the epiblast and hypoblast mediate convergence and extension movements towards the dorsal side of the gastrula, therefore cells that were initially neighbouring one to another become dispersed along the anterior-posterior axis of the embryo (Warga and Kimmel, 1990).

1.3.1 Convergent extension (CE)

Convergence and extension (C&E) are highly conserved morphogenetic movements that shape all germ layers during vertebrate gastrulation. In zebrafish, alike other vertebrates, C&E movements are driven by the combination of highly polarized cell behaviours, including directed migration, radial and planar intercalations, and oriented cell divisions (Tada and Heisenberg, 2012). A type of C&E is Convergent Extension (CE),

a mechanism triggering body axis elongation without growth, relying solely on cell movement. At the onset of gastrulation cells move over the yolk forming a cohesive sheet. During epiboly the movement trend is towards the vegetal pole, and throughout the rest of gastrulation cells tend to converge towards the dorsal midline, elongate along the ML axis and orient their divisions along the animal-vegetal axis (Concha and Adams, 1998; Gong *et al.*, 2004; Quesada-Hernandez *et al.*, 2010). The trajectories of cells closer to the animal pole are biased anteriorly, and those closer to the vegetal pole are biased posteriorly, therefore the tissue elongates in the AP axis (i.e extends) while narrows the ML axis (i.e converges)(Sepich *et al.*, 2005; reviewed in Solnica-Krezel and Sepich, 2012; Tada and Heisenberg, 2012). CE mainly involves two types of cell movement: medio-lateral cell intercalation, which means oriented exchanges of neighbouring cells, and collective cell migration, in which cells move in cohesive cluster with no neighbour exchange (reviewed in Tada and Heisenberg, 2012). There is a common set of core cellular processes, by which CE is achieved in the various contexts across vertebrate species, such as cell polarization, actomyosin contraction and cell adhesion dynamics. Nevertheless, many questions remain unclear such as the instructive signals and cues that polarize cells undergoing intercalation and collective migration during CE.

1.3.1.1 The Wnt/PCP pathway is a main regulator of CE

Several studies across vertebrate species have highlighted the Wnt/PCP signalling pathway as one of the main regulators of cell movements underlying CE, suggesting a general mechanism linking cell polarization to body axis elongation (reviewed by Gray *et al.*, 2011). Zebrafish embryos carrying mutations in several of the Wnt/PCP pathway core components and in Wnt11/ Wnt5 ligands exhibit a characteristic morphogenetic phenotype of impaired CE, with shorter AP and broader ML body axes (Heisenberg *et al.*, 2000; Kilian *et al.*, 2003). In the zebrafish gastrula, internalized mesodermal cells first move anteriorly, towards the animal pole, but at mid-gastrulation they change their movement towards dorsal, marking the start of CE (Sepich *et al.*, 2005). At these early CE stages, mesodermal cells undergo dorsal migration as individuals along irregular paths; however, as gastrulation progresses these cells become mediolaterally

elongated and migrate dorsally as a group, faster and along straighter trajectories. This change fails to occur in Wnt/PCP signalling mutants, including mutants for *vangl2* (also known as trilobite) (Jessen *et al.*, 2002), where polarized radial and planar ML intercalations are also impaired (Yin *et al.*, 2008). Analysis of elongation, orientation and migration cell behaviours in zebrafish *vangl2* mutant embryos has shown the requirement of Vangl2 for the medio-lateral cell polarization. Vangl2 accumulates at the plasma membrane of converging cells, particularly enriched at the anterior cell edges of highly medio-laterally elongated cells, and this accumulation is stage-dependent and relying on an extracellular signal that has not been elucidated yet, distinct from PCP signalling or other gastrulation regulators including BMP and Nodal (Roszko *et al.*, 2015). Additionally, Vangl2-depleted cells fail to migrate along a straight path towards the dorsal midline. Instead, vangl2 mutant cells exhibit an biased alignment and movement towards the anterior pole, suggesting that PCP signalling promotes effective medio-lateral movement in part by suppressing anteriorward cell polarity and movement (Roszko *et al.*, 2015), although the molecular mechanism underlying medio-lateral polarization remains unknown.

Wnt-PCP signalling is required to (1) orient cell divisions and cell migration in the AP axis (Concha and Adams, 1998; Gong *et al.*, 2004), (2) perform radial intercalations that elongate the body though separation of anterior and posterior neighbours (Yin *et al.*, 2008) and (3) to asymmetrically localize cellular organelles and PCP pathway components along the AP axis (Ciruna *et al.*, 2006; Yin *et al.*, 2009). Despite the requirement of Wnt/PCP signalling for cell polarization during CE in gastrulation, there is no direct evidence that Wnt/PCP signaling directly polarizes cells in this process (reviewed in Tada and Heisenberg, 2012). Prechordal plate-notochord border cells are yet uncharacterized (Kai et al., 2008) and it remains unknown whether these different cell populations play a role in establishing cell polarization during CE.

1.3.1.1.1 Evidences for PCP-dependent mechanical cues

There are emerging evidences in other model systems linking the PCP pathway with mechanical cues and cell shape changes. A PCP-dependent signalling cascade leading

to midline cell convergence has been carefully described in the chick neural plate, demonstrating that PCP signals confer contractility on the actomyosin associated to adherens junctions, producing cellular forces that promote apical constriction, neural plate bending and midline convergence of neuroepithelial cells (Nishimura *et al.*, 2012). The effects of PCP on apical constriction are conserved in Xenopus embryos, in which PCP-dependent regulation of morphogenesis takes place through cadherin mediated cell-cell adhesion, leading to actin reorganization and myosin contractility that produce tissue tension and directs the correct assembly of ECM (Dzamba *et al.*, 2009). This study supports a model in which cell-cell adhesions transfer the tension required to direct ECM assembly. Additional evidences link PCP pathway to force transduction in Xenopus blastopore bottle cells, in which the PCP pathway triggers Shroom3-mediated apical actin constriction and Vangl2 is required for the apical accumulation of Rab11, a recycling endosome marker associated to Myosin V (Ossipova *et al.*, 2015). Pointing in the same direction, a study of biomechanical forces in *Xenopus* has demonstrated that CE force production is regulated by myosin II contractility, and that while notochord does not contribute to force generation, the paraxial mesoderm and the neural plate are the major contributors to this process (Zhou *et al.*, 2015). Further analysis dissecting the effects of PCP pathway on tissue mechanics and cell contractility during zebrafish CE needs to be done.

1.3.1.1.2 Links between PCP pathway, cilia/MTOC and polarity

Remarkably, the core PCP components Vangl2, Dvl and Inversin, are found within the cilium or the underlying basal body (Ross *et al.*, 2005; Simons *et al.*, 2005; Park *et al.*, 2008) and functional interference with intraflagellar transport proteins or proteins located in the cilium basal body enhances defective CE movements in mice and zebrafish harbouring mutations in core PCP genes (Ross *et al.*, 2005; Cao *et al.*, 2010). These observations suggest that cilia are intrinsically involved in PCP processes, probably through the reception of extracellular cues (Gray *et al.*, 2011). However, zebrafish mutants lacking both maternal and zygotic *ift88* function, and consequently all ciliary axonemes, display no CE defects (Huang and Schier, 2009; Borovina and Ciruna, 2013). Definitive evidence for the cilium regulating PCP signalling is still

missing, however multiple observations support the notion that PCP signalling influences cilium. Microtubule Organizing Centres (MTOCs), the main functions of which are the organization cilia and the organization of the mitotic spindle, are randomly distributed inside the cells during early gastrulation. When cells become medio-laterally elongated at CE, PCP pathway components drive the posterior localization of MTOCs (Sepich *et al.*, 2011). Likewise, maternal-zygotic (MZ) *tri/vangl2* zebrafish mutants fail to position posteriorly the basal bodies in the floor plate (Borovina *et al.*, 2010).

Insight on other mechanisms suggest other ways by which Wnt/PCP signalling could contribute to CE movements during zebrafish gastrulation, such as the requirement of Vangl2 for proper cell intercalation (Yin *et al.*, 2008) or the Vangl2 and Pricke1a mediated regulation of ECM (Dohn *et al.*, 2013). An intricate view of the control of CE cellular behaviours mainly controlled by the Wnt/PCP pathway is beginning to emerge. Deeper studies are required in order to understand the contribution of cilia-dependent regulation, tissue tensions and interactions with other pathways to completely decipher the molecular mechanisms controling CE in the zebrafish embryo.

1.3.2 Neurulation

Teleost neurulation involves different mechanisms than amniote primary neurulation, whereby the neural tube is formed from a solid rod primordium that undergoes cellular rearrangements and hollows to form a neural tube (Papan and Campos-Ortega, 1994)(reviewed in Lowery and Sive, 2004; Clarke, 2009). First, cells of the neural plate simultaneously converge medially and invaginate ventrally (Figure 1.3A,B), forming a transient tissue known as the neural keel (Figure 1.3C,D). At the neural keel cells interdigitate and progressively polarize (Figure 1.3C,D), forming the second transient structure: the neural rod (Figure 1.3E). At the midline of this structure, once apicobasal polarity is established, the lumen opens forming the neural tube (Figure 1.3F) (Lowery and Sive, 2004; Clarke, 2009; Hong *et al.*, 2010). Despite of the differences in neural plate thickness along the antero-posterior axis, from a multilayered structure in future brain areas to a single cell thickness in the future spinal cord (Tawk *et al.*, 2007), the neurulation mechanism appears to be uniform

(Harrington et al., 2010). Alike primary neurulation, there is correspondence between initial medio-lateral positions in the neural plate with final ventro-dorsal positions in the neural tube (Papan and Campos-Ortega, 1994; Lowery and Sive, 2004)

1.3.2.1 Cellular Organisation and Polarity of the Neural Primordium

Prior to neurulation, the amniote monolayered primary neural plate shows well-defined apico-basal polarity, which is inherited from the epiblast early in development (reviewed in Ueno and Greene, 2003; Clarke, 2009). However, the nature of the zebrafish neural plate has long been discussed and the mechanisms underlying polarization along neurulation are not yet clear. The neural keel was initially thought to be a mesenchymal tissue (Reichenbach *et al.*, 1990), but later studies challenged this view, considering neural plate cells to be epithelial (Kimmel *et al.*, 1995; Geldmacher-Voss *et al.*, 2003). Therefore these cells would not be considered mesenchymal nor conventionally epithelial, but they undergo a transition towards an epithelial character, starting up with basal polarity and progressively forming apical complexes.

The three germ layers gradually acquire apicobasal polarity during zebrafish gastrulation. Epithelia typically form a cellular sheet bounded basally by extracellular matrix (ECM), with basally positioned nuclei and apically located centrosomes, cilia, adhesion and polarity complexes. At the onset of zebrafish gastrulation, ectodermal cells pack into a sheet (Concha and Adams, 1998). A secreted extracellular coat of fibronectin and laminin accumulates at the prospective basal sides of the ectoderm and mesoderm, first as discontinuous patches during gastrulation and becoming later continuous by the end of gastrulation (Latimer and Jessen, 2010). By mid-gastrulation the superficial ectodermal sheet and deeper mesoderm layers are well separated (Warga and Kimmel, 1990; Concha and Adams, 1998) and MTOCs are polarized along the superficial-deep axis, being enriched near the surface of the embryo, possibly reflecting the earliest step towards the nascent ectodermal apico-basal polarity (Sepich *et al.*, 2011). Later during CE, strikingly, the MTOC is positioned in posterior-medial regions of these cells, and not along the axis of cell migration as described for other cell types undergoing directed migration (Sepich *et al.*, 2011). Finally, during

segmentation stages, apical polarity becomes evident by asymmetric distribution of classical markers: Pard3 (Tawk *et al.*, 2007; Hong *et al.*, 2010) accompanied by the tight junction marker ZO-1 (Hong and Brewster, 2006; Yang *et al.*, 2009) and the polarity component aPKC (Hong and Brewster, 2006). Cells converging towards the midline intercalate through stable cell protrusions, and this stabilisation appears to dependent on N-Cadherin (cdh2). Subsequently, when N-Cadherin is lost, intercalation does not occur (Hong and Brewster, 2006). N-cadherin and ZO-1 have been proposed to be required to initiate apico-basal polarity of neural progenitor cells around the 10-somite stage (Yang *et al.*, 2009). The gradual changes in the microtubular organisation, from radial to linear, coincide with the progressive decrease of membrane protrusions and centrosomal movements towards the cell medial tip (Hong *et al.*, 2010), which may be an additional feature of maturing apico-basal polarity in the neural epithelium. Therefore, complete apico-basal polarity is missing until late neural keel stages, when a midline is established (Clarke, 2009; Geldmacher-Voss et al., 2003; Hong and Brewster, 2006; Yang et al., 2009).

In the neural rod, prior to lumen opening, centrosomes gradually localise to the part of the cell closest to the tissue midline, despite the nucleus initially remaining lateral (Figure 1.3C) (Buckley *et al.*, 2013). However, the cues directing this movement are yet unknown. Par3 has been implicated in centrosomal localisation and may function upstream of microtubules to localise the centrosome to the apical cortex (Hong *et al.*, 2010). Despite of the studies describing the different steps of the progressive formation of apico-basal polarity, the precise order of events and the initiators of the process remain remarkably unclear.

1.3.2.2 Oriented cell divisions

Oriented cell divisions have high morphogenetic relevance in the zebrafish both in gastrula and neurula stages. In the zebrafish neural rod, a number of divisions must align their mitotic spindle perpendicularly to the prospective luminal surface in order to form a single straight lumen.

1.3.2.2.1 General mechanisms of mitotic spindle orientation

Oriented division is achieved through the controlled positioning of the mitotic spindle, which is composed of polar microtubules, microtubule organising centres (most often centrosomes) at the poles and astral microtubules, which anchor the spindle poles to the cell membrane. Spindle orientation can be controlled by extrinsic or cell intrinsic mechanisms and by physical constraints, such as cell geometry. In a context dependent manner, spindle orientation can remain constant through several rounds of cell division, or contrarily undergo stereotypical rotations prior to division (Geldmacher-Voss *et al.*, 2003; Kieserman and Wallingford, 2009).

The Wnt/PCP pathway has been described as an extrinsic mechanism governing spindle orientation through cytoskeletal rearrangements that in turn generate cell shape changes (Gong *et al.*, 2004; Quesada-Hernandez *et al.*, 2010). During zebrafish gastrulation and neurulation, abrogation of members of the pathway results in changes in cell shape and randomisation of division orientation (Gong *et al.*, 2004; Quesada-Hernandez *et al.*, 2010; Zigman *et al.*, 2011)

One of the intrinsic cues in the control of spindle orientation in vertebrates is the LGN/NuMA/Gαi complex, which is involved in defining the axis of epithelial divisions through the interaction with cortical dynein to generate pulling forces on astral microtubules (Morin *et al.*, 2007; reviewed in Zheng, 2010; Peyre *et al.*, 2011). In mammalian cells, the LGN/NuMA/Gαi complex co-localises with the apical Par polarity protein complex via the adaptor protein Inscuteable (Lechler and Fuchs, 2005) therefore linking apico-basal polarity with mechanisms of spindle positioning.

The mechanisms intrinsically orienting the spindle highlight the importance of forces in this process. The role of mechanical forces in defining spindle orientation has been described during *Xenopus* epiboly, in where mitotic spindles have a dynamic behaviour, but are firmly kept within this plane through balance of counteracting forces. Apical forces act through active cortical flows of F-Actin/myosin-2, and basal forces through microtubules and myosin-10, keeping the dynamic stability of spindle orientation (Woolner and Papalopulu, 2012). During zebrafish epiboly, the control of division orientation in the enveloping cell layer also relies on tension, cell elongation and myosin II activity, while absence or excess of tissue tension leads to ectopic cell fusions (Campinho *et al.*, 2013). It has been shown that cells orient their mitotic

spindle according to cell shape. In this context, cells may sense their shape by measuring the length of microtubules from the centrosome to the cell surface (Minc *et al.*, 2011). As the microtubule network is remodelled to generate the mitotic spindle, animal cells entering mitosis replace their interphase actin cytoskeleton with a contractile mitotic actomyosin cortex that is tightly coupled to the plasma membrane and drives mitotic cell rounding (Lancaster and Baum, 2014), altogether remarking that purely mechanical cues coming from cytoskeletal arrangements and cell geometry can exert strong effects on morphogenesis through control on cell division.

In zebrafish neural rod, one of the components governing spindle orientation is the polarity protein Scribble through assembly of cadherin adhesion complexes and independently of canonical apico-basal and planar polarity pathways (Zigman et al., 2011). Interestingly, (*ift88*) zebrafish mutant embryos, a protein required for cilia formation, plays a role in orienting cell divisions during gastrulation and neurulation independently from PCP signalling (Borovina and Ciruna, 2013), thereby making a possible link between cilia functionality and spindle orientation.

1.3.2.2.2 Polarised Divisions

During the neural keel and rod stages, concomitant with changes in the neural tissue morphology, there is a switch of the preferential division plane from AP to ML (Concha and Adams, 1998; Geldmacher-Voss *et al.*, 2003), always occurring between 15th and 16th embryonic divisions (Kimmel *et al.*, 1994). As such, division 14 occurs in the gastrula elongating the tissue, while division 16 occurs in the neurula and splits the clones bilaterally (Papan and Campos-Ortega, 1994; Concha and Adams, 1998; Geldmacher-Voss *et al.*, 2003). Therefore mitoses change in orientation during the neural plate stage, from AP (early) to ML (late, and starting in ventral regions) (Geldmacher-Voss *et al.*, 2003) have pivotal consequences in the spinal cord morphogenesis.

In the neural plate and tube stage mitosis are mostly planar -parallel to the neuroepithelial plane- (Concha and Adams, 1998; Geldmacher-Voss *et al.*, 2003), but in

the intermediate phases of neural keel and rod they transiently undergo orthogonal divisions, ensuing bilateral progeny (Figure 1.4C-E) (Kimmel *et al.*, 1994; Papan and Campos-Ortega, 1994; Concha and Adams, 1998). The orthogonal orientation of neural keel and rod mitoses is achieved through a 90º rotation of the spindle pole, initially assembled parallel to the neuroepithelium (Geldmacher-Voss *et al.*, 2003)

These mediolaterally orientated orthogonal cell divisions have been after well characterised and termed C-Divisions (Crossing Divisions), as one daughter cell crosses the midline (Figure 1.4C-E) (Tawk *et al.*, 2007). Concomitant with C-Divisions the tissue progressively acquires apical polarity. The localization of Par3 in the cleavage furrow has been shown to be important for midline crossing (Tawk *et al.*, 2007), however the molecular control underlying this transient stereotyped spindle rotation remains unknown. Cell polarisation, however, does not rely on C-Divisions. Indeed, cells assemble an apical domain in the part of the cell that is positioned at the midline of the neural rod, prior to division (Buckley *et al.*, 2013)(reviewed in Compagnon and Heisenberg, 2013). This polarization takes place even when division is experimentally blocked at the time where C-Divisions occur, subsequently forming a central midline with apical polarity components (Figure 1.4D,E) (Ciruna *et al.*, 2006; Tawk *et al.*, 2007; Buckley *et al.*, 2013). Is not yet known what cues determine apical protein localisation, but they apparently work independently from division. Altogether, the ability of cells to polarize in the intersection with the tissue midline and the following oriented C-Divisions across the tissue trigger formation of neural rod midline and lumen (Figure 1.4E,F), but the signals instructing the apical polarity establishment, the midline placement of C-Divisions and their stereotyped mitotic orientation still remain elusive.

Coordination between C-Divisions and neural plate convergence is necessary to form a single midline and therefore a single lumen. PCP-pathway *trilobite* mutants (Sepich *et al.*, 2000) show defective convergence, and therefore ectopic C-Divisions leading to formation of duplicated neural tubes with proper apico-basal polarity and defined lumens (Ciruna *et al.*, 2006). However, PCP pathway does not seem to regulate the midline crossing of these divisions (Tawk *et al.*, 2007), and even when divisions are

blocked the cells are able to cross the midline (Ciruna *et al.*, 2006; Tawk *et al.*, 2007), showing that lumen duplication -and in general lumen formation- largely relies on C-Divisions. Remarkably, if C-Divisions loose their orientation towards the midline the neural tube morphology gets disorganised and a single continuous lumen cannot be formed (Quesada-Hernandez *et al.*, 2010), demonstrating the strong morphogenetic influence of C-Divisions. Underlying mesoderm cells move coordinately with neuroectodermal cells during convergence of the neural plate and keel formation (Araya *et al.*, 2014). In absence of mesoderm this coordination is lost and movements are severely disrupted, but despite of the severely affected architecture of the neural tube apical polarity is still formed.

1.3.2.3 Lumen formation

Neurulation concludes with the formation of a tubular structure or lumen that in this particular tissue is also named the neurocoel (Figure 1.4F). However, Morphogenetic mechanisms underlying the formation of a tube can greatly vary between different tissues.

1.3.2.3.1 Mechanisms of lumen formation

Depending on the characteristics of the tissue that originates the tube and the morphogenetic processes we can classify them as wrapping, budding, cavitation and hollowing:

1- If the tube is formed from a pre-existing polarised epithelial sheet, and cell shape changes such as apical constriction take part in this process:

- **Wrapping**: An epithelial sheet, already polarised, invaginates and rolls creating a long tube. This process takes place, for example, in amniote primary neurulation (Lubarsky and Krasnow, 2003; Sawyer *et al.*, 2010; Iruela-Arispe and Beitel, 2013).
- **Budding**: Epithelial cells from a sheet or tube invaginate to create a new short tube of bud, as it occurs in the formation of the *Drosophila* salivary gland (Andrew and Ewald, 2010). In this case the tube remains connected to the original structure, different to wrapping in which the tube is independent from the original tissue.

2- If the tube is formed from an unpolarised group of precursors undergo

mesenchymal to epithelial transition and a lumen is formed *de novo*(reviewed in Lubarsky and Krasnow, 2003; Iruela-Arispe and Beitel, 2013)

- Cavitation: Refers to the elimination of central cells in order to create a lumen, involving cell death to a certain degree. Apoptosis is necessary to eliminate unpolarized cells, contributing to the efficiency of other mechanisms such as hollowing (Mailleux *et al.*, 2008; Martin-Belmonte *et al.*, 2008). Cellular rearrangement often occurs, such as described in the zebrafish gut formation, which starts as a rod and requires a combination of cavitation and hollowing to open a lumen(Bagnat *et al.*, 2007; Horne-Badovinac and Munro, 2011).

- Hollowing: This process can happen as cell hollowing or cord hollowing. Cell hollowing applies to very small lumen, as it happens in capillaries, in which coalescence of small vesicles form a larger vesicle or vacuole, which in turn fuses to the plasma membrane. Fusion of vacuoles from neighbouring cells ends up forming a lumen (Kamei *et al.*, 2006). During cord hollowing a similar exocytic process takes place, but vesicles deliver apical membrane components and fluid to the intercellular space, therefore polarizing the tissue at the same time that the lumen is formed (reviewed in Lubarsky and Krasnow, 2003; Andrew and Ewald, 2010). The developing zebrafish gut would mainly undergo this process (Bagnat *et al.*, 2007), and neural tube formation seems to mostly fit in this category, although apical polarity is localised prior to lumen formation (Buckley *et al.*, 2013) and divisions take part this process (Tawk *et al.*, 2007).

1.3.2.3.2 Molecular mechanisms of lumen formation

Most knowledge about the fundamental molecular mechanisms for lumen formation have been provided by *in vitro* experimental work on MDCK cells, which when grown in 3D environment they form multicellular cysts with a central lumen, allowing to identify the molecular mediators of lumen formation. PTEN signalling has role on lumen formation by a cascade of protein recruitments, including Cdc42, and ending up with aPKC apical localization, and loss of function of any of the cascade elements prevents apical surface development and leads to the formation of multiple lumens

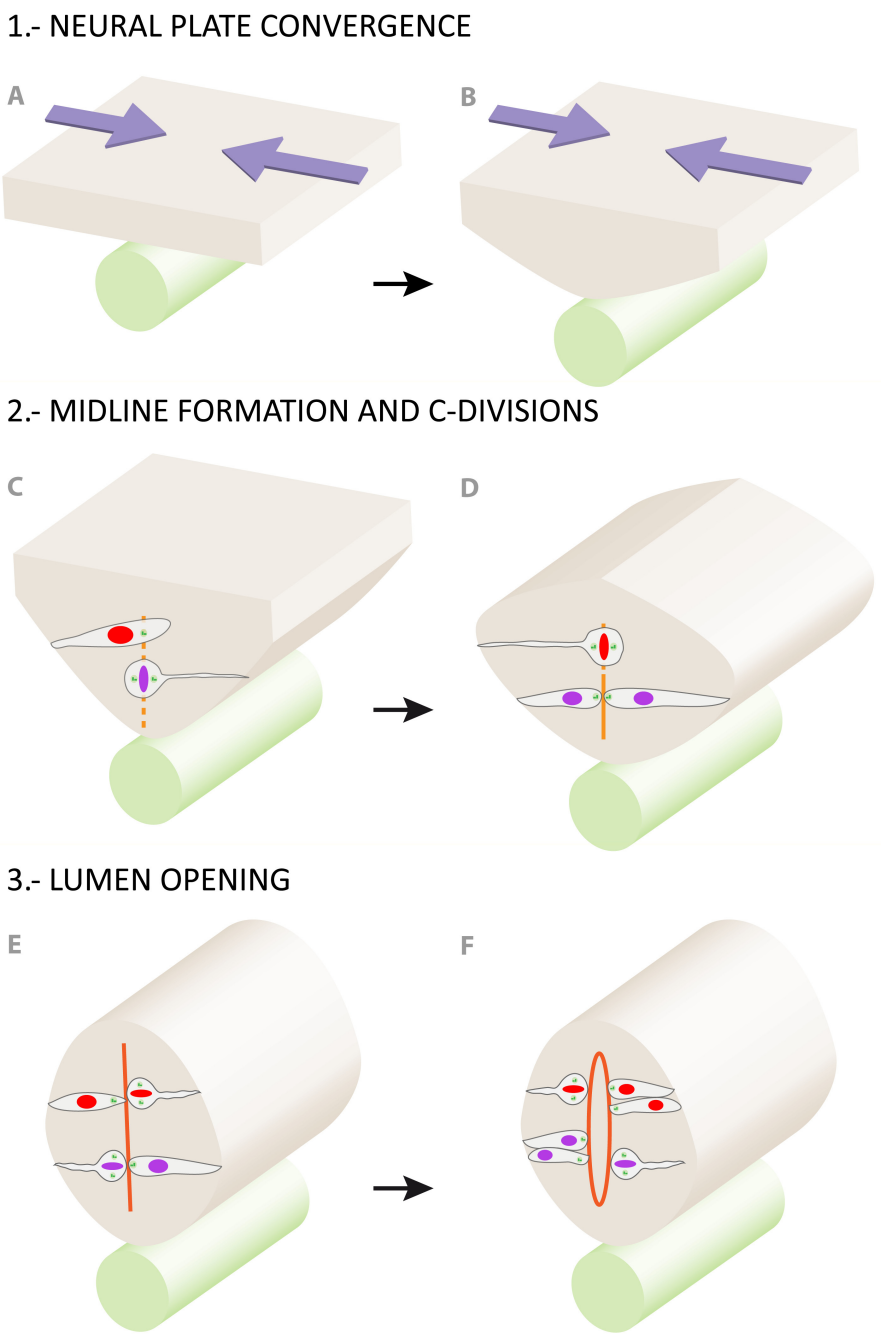

Fig. 1.4: Teleost neurulation:
(A,B) The neural plate (A) undergoes convergence movements -purple arrows-, forming a transient tissue known as the neural keel (B-D). (C) Prior to division the cells polarize (red cell), starting with the localization of the centrosome (green dot) at the prospective tissue midline (orange dotted line), and followed by an orthogonal mitotic orientation (purple cell). These transient divisions are named C-Divisions as one daughter cell crosses the midline. (D) C-Divisions give rise to a bilateral progeny (purple cells) at either side of the midline. (E) Neuroepithelial cells perform planar divisions at the apical margin. (F)The lumen opens at the midline forming the neural tube.
Notochord is represented in green

cleavage furrows with their corresponding apical proteins lead to ectopic lumens (Jaffe *et al.*, 2008), supporting the role of divisions in defining lumen location. ECM matrix has also been involved in polarity formation: MDCK cells in 3D culture initially form cysts with apical proteins in the periphery and baso-lateral markers in the inner surface, but after embedding in ECM matrix the inversely reorient their polarity, apical in-basolateral out (Liu *et al.*, 2007). Strikingly, physical confinement seems sufficient to promote lumen formation in MCDK cells independently of the substrate, suggesting that mechanical properties such as tension might be at the top of the regulatory network for lumen formation (Rodriguez-Fraticelli *et al.*, 2012).

1.3.2.3.3 Formation of a lumen in the Zebrafish spinal cord

In the zebrafish embryo, the generation of the apical specializations of the lumen must occur in the center of the neural rod after the neural cells have undergone convergence, invagination and interdigitation across the midline.

An approach similar to *in vitro* cyst cultures was developed by ectopic transplantation experiments of neural cells into the zebrafish yolk in order to understand the intrinsic cell ability to form a lumen along development (Girdler *et al.*, 2013). In this context, neural cells are able to self-organize into epithelial cysts, and heterochronic transplants demonstrate that prior to gastrulation the cells are already "scheduled" to polarize, depending on developmental time rather than environmental signals or morphogenetic movements (Girdler *et al.*, 2013). At the tissue level, some insights on the mechanisms underlying teleost neural tube lumen formation are arising, and are mostly based on the proper fulfilment of the morphogenetic processes described above: convergence, polarization and oriented mitosis (Tawk *et al.*, 2007; Quesada-Hernandez *et al.*, 2010; Zigman *et al.*, 2011; Buckley *et al.*, 2013; Araya *et al.*, 2014).

Further studies need to be done in order to uncover the role of vesicle trafficking in the localisation of apical polarity in the neural rod midline, such as Rab11-mediated trafficking, that has been involved in gut lumen formation (Alvers *et al.*, 2014). Most current knowledge about the actual molecular networks underlying lumen formation

comes from studies performed in *in vitro* systems. Extrapolation of the data obtained *in vitro* to the *in vivo* zebrafish neurocoel formation will definitely clarify the fundamental molecular mechanisms for this process.

1.4. THE SONIC HEDGEHOG SIGNALLING PATHWAY

1.4.1 Shh general functions in neural development

Sonic hedgehog (Shh), is a secreted signalling molecule, member of the hedgehog family, and controls a multitude of processes during vertebrate embryogenesis such as proliferation and embryonic patterning. Shh was initially described as a midline signalling protein secreted from the notochord and the floor plate (Echelard *et al.*, 1993; Marti *et al.*, 1995a) and subsequently identified as a morphogen responsible for patterning the vertebrate central nervous system (Marti *et al.*, 1995b)

As a morphogen, Shh drives the specification of different populations of neural progenitors in a concentration-dependent manner (reviewed in Jessell, 2000; Ingham and McMahon, 2001). The correct spatial and temporal expression of Shh signal is crucial for patterning (Echelard *et al.*, 1993; Krauss *et al.*, 1993; Johnson *et al.*, 1994; Barth and Wilson, 1995). It has been shown that, during zebrafish neural tube formation, the progenitors of different fates are spatially mixed following heterogeneous Shh signalling responses, and later cell sorting rearranges them into bordered domains (Xiong *et al.*, 2013).

The absolute levels of secreted protein determine the induction of different cell types. At high concentrations, Shh induces floor plate while at lower concentrations motor neurons and interneurons can be induced (Marti *et al.*, 1995a; Roelink *et al.*, 1995; Ericson *et al.*, 1997)(reviewed in Jessell, 2000; Ingham and McMahon, 2001). Misexpression experiments demonstrate that the correct spatial and temporal pattern of *shh* expression is critical for the normal development of the embryo (Krauss *et al.*, 1993; Roelink *et al.*, 1994; Strahle *et al.*, 1997).

Shh also promotes the proliferation and survival of neural progenitor cells through regulation of cell cycle (Cayuso *et al.*, 2006). Misregulation of the *Shh* signalling pathway can cause a variety of tumours in humans including basal cell carcinoma and medulloblastoma (reviewed in Ingham, 1998; Bale and Yu, 2001; Marino, 2005).

In vertebrates, expression of *shh* is highly restricted to regions with organiser activity (Krauss *et al.*, 1993; Strahle *et al.*, 1996; Scholpp *et al.*, 2006). In line with this, the mouse mutant for Shh reveals profound axial morphogenetic defects, including holoprosencephaly, cyclopia, and absence of the spinal column and most of the ribs (Chiang *et al.*, 1996), pointing to Shh as an important signal in morphogenesis of the central nervous system.

In the zebrafish embryo, *shh* expression begins during epiboly, before there is a notochord or neural tube (Krauss *et al.*, 1993). Later, *shh* is expressed in the midline mesoderm comprising the notochord, prechordal plate and the overlying neuroectoderm precursors that give rise to the floor plate. Other regions of expression are the posterior limb bud and the endoderm (Echelard *et al.*, 1993; Krauss *et al.*, 1993; Riddle *et al.*, 1993; Strahle *et al.*, 1996).

Unlike the fly, which has a single Hedgehog gene, there are several homologue genes in vertebrate species. Three Hedgehog genes were identified in the mouse: Desert hedgehog (Dhh), Indian hedgehog (Ihh), and Sonic hedgehog (Shh) (Ingham and McMahon, 2001). Further duplication events appear to have occurred in teleosts, therefore the zebrafish possesses at least five hedgehog genes: *sonic hedgehog (shh or shha)* (Krauss *et al.*, 1993), *tiggywinkle hedgehog (twhh* or *shhb) (*Ekker et al., 1995*); echidna hedgehog (ehh* or *ihhb)* (Currie and Ingham, 1996), *indian hedgehog* (*ihh or ihha) and* desert hedgehog *(dhh)* (Avaron *et al.*, 2006). In comparison to the phenotype of shh −/− mice (Chiang *et al.*, 1996), lack of *shh* (named sonic-you in zebrafish) causes milder defects in the zebrafish neural tube. In particular, the floor plate forms in mutants homozygous for loss-of function alleles (Schauerte *et al.*, 1998). Loss of *shh* function may be compensated for the closely related member of the hh family that are expressed in overlapping domains of the zebrafish body axis (Ekker *et al.*, 1995; Currie and Ingham, 1996)

1.4.2 Primary cilia harbour Shh pathway components

The primary cilium is an antenna-like projection of the cell that consists of nine microtubule doublets surrounded by ciliary membrane. The primary cilium is nucleated at its base by the basal body, consisting of the eldest centriole in the cell -also named

the mother centriole- with associated appendage proteins that dock it to the plasma membrane (reviewed in Seeley and Nachury, 2010; Garcia-Gonzalo and Reiter, 2012; Kim and Dynlacht, 2013). The centrioles and their surrounding pericentriolar matrix constitute centrosome, the main microtubule- organizing centre, which is a key organelle for cell polarity (Bornens, 2012). In division, the centrosomes organize the mitotic spindle. Primary cilia are therefore disassembled prior to mitosis so that the centrioles can function at the poles of the mitotic spindle (reviewed in Seeley and Nachury, 2010; Garcia-Gonzalo and Reiter, 2012; Kim and Dynlacht, 2013). At the end of cell division, the daughter centriole of the previous cell cycle matures into a new mother centriole and will, as the old mother centriole, nucleate a new cilium in early G1 (Nigg and Stearns, 2011). Although the ciliary membrane is continuous with the plasma membrane, entry of membrane proteins into the cilium is restricted (Nachury *et al.*, 2010; Reiter *et al.*, 2012). Thus, the primary cilium forms a separate cell compartment, providing a platform for several extracellular signals, among them Sonic Hedgehog (Shh).

The normal structure of the ciliary axoneme is required to translate different levels of Shh ligand into differential regulator of the Gli transcription factors that implement Shh signals (Caspary *et al.*, 2007). Almost all components of the Sonic hedgehog (Shh) signalling pathway are localized to the cilium, and their localization changes in response to the Shh ligand (Figure 1.5) (Corbit *et al.*, 2005; Haycraft *et al.*, 2005; Rohatgi *et al.*, 2007; Chen *et al.*, 2009; Wen *et al.*, 2010). In the absence of ligand, the Gli zinc finger transcription factors Gli2 and Gli3 are localized to the tips of cilia and are processed to form transcriptional repressors (Huangfu *et al.*, 2003; Haycraft *et al.*, 2005; Liu *et al.*, 2005). This processing involves the phosphorylation and cleavage of the full-length Glis, with the N-terminal domain acting as the repressor and the C-terminal domain being degraded (Wang *et al.*, 2000). Protein kinase A (PKA) is a conserved negative regulator of the Shh pathway (Epstein *et al.*, 1996; Hammerschmidt *et al.*, 1996) that integrates the transduction of the Shh pathway at the cilium base (Barzi *et al.*, 2010) and triggers a cascade of Gli3 phosphorylation events that lead to cleavage into their repressor form (Tempe *et al.*, 2006). The receptor for the Shh ligand, Patched (Ptch1), is also found in the ciliary membrane, and

represses pathway activation in the absence of ligand by inhibiting the downstream activator, Smoothened (Rohatgi *et al.*, 2007). When Shh ligand is present, Shh binds Ptch1, causing it to move out of the cilium, and this allows Smo to enter (Corbit *et al.*, 2005; Rohatgi *et al.*, 2007). Smo localization to the cilium inhibits Gli repressor (GliR) formation and the full-length Glis become Gli activators (GliA) (McMahon *et al.*, 2003). Suppressor of Fused (Sufu), an inhibitor of Gli activity, is also localized to the tips of cilia, although Sufu was found to inhibit Shh signalling independently of the cilium by binding and sequestering the Glis in the cytoplasm (Chen *et al.*, 2009; Jia *et al.*, 2009; Humke *et al.*, 2010; Tukachinsky *et al.*, 2010)

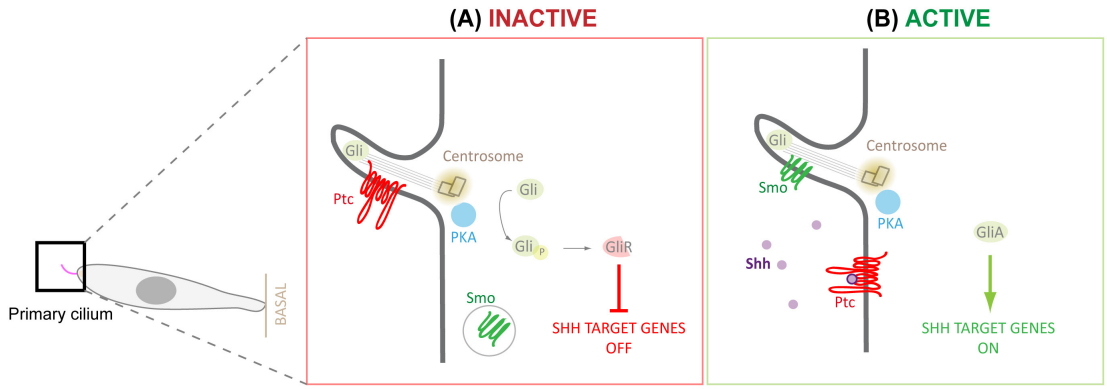

Figure 1.5 - Shh pathway components are located at the primary cilium
Most components of the Shh signalling pathway are at the apical cilium and their localization changes in response to Shh ligand. (A) The pathway is inactive in absence of Shh ligand. Gli full-length transcription factors localized to the tips of cilia are phosphorylated and cleaved to from Gli Repressor (GliR) factors that negatively regulate target genes. Protein kinase A (PKA) is at the cilium base and negatively regulates the pathway through Gli phosphorylation events that lead to cleavage into their repressor form. Patched (Ptc) is the receptor for Shh ligand, located at the ciliary membrane, and represses the pathway in the absence of Shh by inhibiting the downstream activator, Smoothened (Smo). (B) The pathway is active in presence of Shh ligand. Shh binds to Ptc causing it to move out of the cilium. The previously repressed receptor Smo is now allowed into the cilium, leading to the activation of the pathway and the formation of full-length Gli activators (GliA). Bidirectional intraflagellar transport is required for these processes, but the precise targeting and movements are not clear.

The precise targeting of Shh signalling proteins and their movement in and out of the cilium is not clear, but intraflagellar transport is required (Huangfu *et al.*, 2003; Haycraft *et al.*, 2005; Liu *et al.*, 2005). Intraflagellar transport is the bidirectional movement of ciliary protein complexes and is required to build and maintain the cilium (reviewed in Rosenbaum and Witman, 2002; Pedersen *et al.*, 2008). Anterograde IFT carries cargo toward the tip of the cilium, while retrograde transport carries turnover products out of the cilium. Deletion of anterograde or retrograde IFT proteins results

in distinct ciliary phenotypes, but in either case, both GliA and GliR are affected, resulting in disrupted Shh activity (Huangfu *et al.*, 2003; Huangfu and Anderson, 2005; Liu *et al.*, 2005; May *et al.*, 2005; Houde *et al.*, 2006; Ocbina and Anderson, 2008; Tran *et al.*, 2008; Cortellino *et al.*, 2009). Surprisingly, disruption of ciliary structure does not always affect Shh signalling, as shown by *Rfx3* mouse mutants, which have short cilia and normal Shh activity (Bonnafe *et al.*, 2004). As in mouse, zebrafish cilia are required to mediate the activities of Hh, Ptc, Smo and PKA, however *ift88* mutants lacking cilia display decreased and expanded Hh activity (Huang and Schier, 2009). This remarks the limited knowledge about how a list of ciliary and basal body protein mutants affects Shh signalling.

Aberrant ciliary function has also been linked to human genetic diseases such as Bardet-Biedl syndrome (BBS). There is a core complex of seven core proteins that constitute the BBSome, which includes several Rab proteins. Rab proteins are GTPases that regulate multiple aspects of vesicle transport, membrane trafficking processes and participate in the ciliary membrane assembly (Westlake *et al.*, 2011).

Cilia are gradually being revealed to have important roles in other signalling systems, not just the Hedgehog pathway (Berbari *et al.*, 2009). Therefore, the possibility arises that the ciliary mutants may have NTDs as the result of misregulation of other signalling events. There is evidence to support a role for cilia in function of the mammalian PCP pathway (Ross *et al.*, 2005; Jones *et al.*, 2008). So far, disruption of core components of the PCP pathway has led to different NTDs from those seen in Hh pathway mutants. Specifically, loss of function of the core PCP genes such as *Vangl2*, *Celsr1* and *Dishevelled*, results in the severe NTD craniorachischisis in which the neural tube is open along most of the body axis, owing to failure of initiation of neural tube formation, at Closure 1 (Murdoch *et al.*, 2001; Curtin *et al.*, 2003; Wang *et al.*, 2006). This phenotype is distinct from the exencephaly and spina bifida seen in the cilia mutants with abnormal Shh pathway activity, arguing against a commonality. However, partial disruption of PCP pathway activity can result in spina bifida, as seen in some *Vangl2* heterozygous mutants (Copp *et al.*, 1994), or in compound heterozygous mutants between *Ptk7* and *Vangl2* (Lu *et al.*, 2004), while exencephaly is

observed in a proportion of compound mutants between *Vangl2* and Cordon bleu (*Cobl*) (Carroll *et al.*, 2003) or between *Vangl2* and *Bbs4 (Ross et al., 2005)*. Thus it is not possible on phenotype alone to fully exclude an involvement in the PCP pathway.

2. OBJECTIVES

2. OBJECTIVES

The aim of this thesis is to increase the knowledge of neural tube formation in teleosts, expecting to contribute to understanding biology of secondary neurulation and neural tube defects. By taking advantage of the imaging techniques offered by transparent zebrafish embryos I aim to examine the effects of Sonic Hedgehog (Shh) on the mechanisms driving lumen formation *in vivo.*

My main objectives are:

- To investigate the role of Shh signalling in spinal cord midline positioning and lumen formation.

- To characterise the effects of Shh activity in cell polarization and cell motility during neural tube formation.

- To examine the influence of Shh on mitosis dynamics and orientation of divisions as a potential cause of neural tube defects.

3. MATERIALS AND METHODS

3. MATERIALS AND METHODS

3.1 Animals

Wild-type, transgenic and mutant zebrafish were maintained under standard conditions (Westerfield, 2000) on a 14-hour photoperiod in the PCB Animal Facility. Embryos were obtained from timed matings and raised at 28.5°C in fish water with methylene blue (Sigma Aldrich) or embryo medium (E2) (Westerfield, 2000). Reducing incubation temperature to 23°C from five hours post-fertilisation caused development to proceed at a slower rate, enabling early embryonic stages to be visualised at an appropriate time. Embryos were staged according to published criteria (Kimmel et al., 1995) and stages are given in terms of hours post fertilisation (hpf).

3.1.1 Wild-type strains

PCB Wild-type AB Tubingen and Tupfel Long fin.

3.1.2Transgenic lines

- *Tg(-2.2shh:gfp:ABC)*(Shh-GFP) (Shkumatava *et al.,* 2004). Obtained from King's College Fish Facility.
- *Tg(olig2:EGFP)vu12*(Olig2-GFP) (Shin *et al*., 2003). Obtained from King's College Fish Facility.
- *Tg(isl1:GFP)rw0* (Islet1-GFP) (Higashijima *et al.,* 2000). Obtained from King's College Fish Facility.
- *Tg(actb2:Arl13b-GFP)hsc5* (Arl13B-GFP) (Borovina *et al.*, 2010) (Arl13B-GFP). Kindly donated by Brian Ciruna

3.2 Cyclopamine treatment

Cyclopamine (TRC, Cat.number C988400) was solved in 100% Ethanol to a concentration of 10mM, aliquoted in 10µL and stored at -20ºC. Prior to use, cyclopamine was briefly warmed (30sec).

Chorions of 5-6hpf embryos were perforated with a sharp forceps to help drug

diffusion. Embryos were plated in E3 medium 48-multiwell plates (5 embryos/well). E3 was replaced by 200 µL 300µM-Cyclopamine solution or control EtOH solution and incubated at 28.5ºC until 24hpf.

3.3DNA constructs

The following DNAs were inserted into pCS2+ expression vector for RNA transcription under the SP6 promoter.

- A constitutive activated form of the receptor Smoothened (SmoM2) (Xie *et al.*, 1998)
- A dominant-negative form of the cAMP-dependent kinase A (dnPKA) (Epstein *et al.*, 1996).

The following constructs were used as injection control markers and for *in vivo* time lapse experiments cell labelling:

- pCS2 membrane-GFP
- pCS2 Histone2B-RFP (H2B-RFP)

3.4 mRNA Synthesis

PCS2+ expression vectors were linearised with various restriction enzymes (Promega) for 2 hours at 37ºC and precipitated at -20ºC overnight in 70% ethanol and 0.05M sodium acetate. DNA was then washed in 70% ethanol and resuspended in nuclease-free dH20 (Ambion). Sense strand capped mRNA was transcribed using the mMESSAGE SP6 Kit (Ambion) and purified through a column (Roche). Resulting RNA concentration was measured using a spectrophotometer or nanodrop (Thermoscientific).

3.5 Microinjection

All injections were carried out under a dissecting microscope using agarose plate with dents to hold the embryos. Injections were delivered using a glass micropipette with filament (Harvard Apparatus) mounted on a micromanipulator and attached to a Narishige™ Digital Microinjector. mRNAs were injected at the one-cell stage for ubiquitous expression at 100-400pg per embryo and never exceeding the volume of 1nL.

3.6 Immunohistochemistry

3.6.1 Whole mount immunohistochemistry

In toto embryo immunostaining procedure was carried out as follows:

- Embryos were fixed in 4% paraformaldehyde (PFA) (Sigma) in PBS (Sigma) for 2 hours at room temperature (RT) or overnight at 4°C.
- Embryos were washed 3 x 5mins in PBT (PBS + 0.1% Triton-X-100).
- Embryos were incubated in blocking solution (10% goat serum in PBT) for at least 30min at RT.
- Embryos were incubated in antibody solution (1% goat serum in PBT) with primary antibody overnight at 4ºC with gentle shaking.
- Following incubation, embryos were washed 4 x 30 mins in PBT.
- Embryos were then incubated in secondary antibodies in blocking solution for 2 hours at room temperature.
- Finally, embryos were initially washed 3 x 5 min in PBT, followed by longer 30 min washes and transferred to PBS for imaging. A primary antibody for ZO-1 was used (Table 2.1) in combination with Alexa® Fluor 488conjugated secondary antibody (1:500, Invitrogen).

3.6.2 Flee-floating sections immunohistochemistry

Immunostaining of transversal sections of the embryos was carried out as follows:

- Embryos were fixed in 4% paraformaldehyde (PFA) (Sigma) in PBS (Sigma) for 2 hours at room temperature (RT) or overnight at 4°C.
- Embryos were embedded in plastic moulds with a warm 5% agarose - 10% sucrose matrix and cooled down to solidify
- Agarose embryo-blocks were sectioned at 40µm thickness in a Leica Vibratome (VT1000S), obtaining free-floating transversal sections.
- Sections were washed 3 x 5mins in PBT (PBS + 0.1% Triton-X-100).
- Sections were incubated in blocking solution (10% goat serum in PBT) for at least 30min at RT.

- Sections were incubated in antibody solution (1% goat serum in PBT) with primary antibody overnight at 4ºC with gentle shaking.
- Following incubation, sections were washed 3 x 10mins in PBT.
- Sections were then incubated in secondary antibodies in antibody solution for 2 hours at room temperature.
- Finally, embryos were initially washed 3 x 10 min in PBT washes and transferred to water for glass-slide mounting, and covered by Mowiol© and a glass-coverslip.
- Various primary antibodies were used (Table 2.1) in combination with Alexa® Fluor (488, 555, 633) conjugated secondary antibodies (1:1000, Invitrogen).

Table 3.1. Primary Antibodies Used

Antibody	Source	Catalogue Number	Host Species	Dilution
ZO-1	Invitrogen	339111	Mouse monoclonal IgG	1/500
Phospho-Histone3	Sigma	H9908	Rat monoclonal IgG	1/1000
Laminin-111	Sigma	L9393	Rabbit polyclonal	1/1000
Acetylated Tubulin	Sigma	T6793	Mouse monoclonal IgG	1/1000

3.7 Counter-stains

Counter-stains were added during incubation with secondary antibody or for and additional 30min hour at RT following immunohistochemistry. DAPI (1:5000) (Sigma) was used to visualise nuclei. Alexa Fluor®-555 Phalloidin was used to visualize F-actin/tissue structure.

3.8 Microscopy

3.8.1 Selective Plane Illumination Microscopy (SPIM) Live Imaging

3.8.1.1 Sample mounting

Embryos at 10hpf were dechorionated and embedded in 0,8% low-melting point agarose (A9414, Sigma) in E3 embryo medium and 200 mg/l Tricaine (MSS-222,

E102521, Sigma). A glass capillary (Brand, 1,5mm inner diameter) with a tight-fitting plunger was used to pump the liquid agarose with the embryo into it. The embryo was placed with its main axis perpendicular to the capillary and the agarose was let to solidify inside the capillary before pushing it out for imaging. The rotation of the capillary inside the microscope acquisition chamber enabled mutiview imaging of dorsal and transversal views.

3.8.1.2 Image acquisition

A Lightsheet Z.1 microscope (Carl Zeiss, Germany) was used for long-term time-lapse imaging of zebrafish developing embryos. Images were acquired with a 20x/1.0 water immersion objective, 488 and 561nm lasers and two Sony ICX 285 CCD cameras (AxioCam, Carl Zeiss). Dorsal and transversal views of each embryo were acquired every 2 minutes for 10 hours. A 75 to 250µm Z-stack was acquired with a step size of 1.5 to 3 µm. The sample was sequentially illuminated from both sides and a post-processing fusion step of the two views was subsequently applied (with Lightsheet Z.1 Multiview Processing software), followed by a deconvolution processing step.

3.8.1.3 Image processing

The dual side lightsheet illumination fusion process was performed through Mean Fusion algorithm (ZEN software) and the deconvolution step was applied afterwards with the Fast Iterative algorithm available in ZEN software too.

3.8.2 Confocal Microscopy Imaging

3.8.2.1 Sample mounting for Live Imaging

Embryos were mounted in 1.5% low-melting point agarose and supported in aMatTek glass-bottom petri dish covered with E3 medium. From 16hpf, embryos were anaesthetised in 200mg/l Tricaine. A heated environmental chamber at 28.5ºC was used, and embryos were imaged from a dorsal view unless otherwise indicated.

3.8.2.2 Sample mounting for fixed preparations

in toto fixed preparations were mounted on a cover-slip glued with silicone to a FrameSlide (11505151, Leica) in 1.5% low-melting point agarose. A chamber was made by surrounding the samples with a silicone ring, filling up with water and covering with an extra cover-slip.

Free-floating transversal sections were mounted on a glass-slide and covered by Mowiol© and a glass-coverslip for imaging.

3.8.2.3 Image acquisition

Embryos were imaged on an inverted microscope (inverted Zeiss Axio Observer Z1) Microscope, equipped with an Argon multiline gas laser at 488 nm and a DPSS laser at 561 nm. The objectives used were a 25X (NA 0.75) or a 40X (NA 1.2), both water immersion. Images were acquired from 25–50 optical sections spaced 2 µM apart at 1-2min intervals for up to 12 hr using ZEN software (Zeiss).

3.8.3 Widefield Macroscopy

Embryos were fixed in PFA4% during 3h at RT, washed in PBS and embedded in a soft 3% Methycellulose matrix on a glass slide. Widefield fluorescence and brightfield images were acquired in a Macroscope MVX10 attached to a Olympus DP72 camera. Merged pictures were produced in ImageJ.

3.9 Image analysis

3.9.1 General Image Analysis

Raw confocal data was exported to ImageJ (http://rsbweb.nih.gov/ij/). Projections of z-stacks are maximum projections unless otherwise indicated. Figures and schematics were constructed using Adobe Illustrator CS4. All time-lapse movies were normalized taking the start of otic vesicle opening as 17hpf.

3.9.2 Cilia 2D Manual Tracking

For cilia trackings calibrated 3µM projections of confocal time-lapse movies were used. Gaussian blur and Laplacian filters were applied for sensitive cilia detection and

Particle Tracker plugin was used (http://fiji.sc/Particle_Tracker). Parameters applied: radius 5, cutoff 10, percentile 1%, displacement 3, linkage 2. Filtered trajectories longer than 30 frames were selected, verified and corresponding coordinates were exported for analysis. A representative trajectory selection was overlaid in snapshots with illustrative purpose using the Manual Tracking plugin.

3.9.3 Nucleus 3D Semi-automatic Tracking

C-Division trackings:

For 3D nucleus trackings calibrated, fused and deconvolved subsets of SPIM time-lapse movies were used. Images were exported to ImageJ and converted to 8bit and reverted backwards for Trackmate plugin nucleus trajectory detection. Parameters applied were the following: DoG detector, 5µm, no subpixel precision, nearest neighbour search, maximum distance between points 5µm, no filters.

The generated table "*tracks in spots statistics"* was saved (.xls) to be opened in the Trackmate Process Manual macro developed by Sébastien Tosi (IRB imaging facility), which allows the semi-automatic tracking of spots detected by Trackmate and trajectory manual verification and correction. In the backwards movie, cells performing a C-Division and detected by Trackmate (blue square) would be selected and their trajectory followed at every timepoint and corrected when necessary. Trajectories were saved as a multiple ROI file.

Adjacent cells trackings:

For analysis of the cells initially adjacent to a C-Division, the same 8 bit movie subset that was analyzed backwards for C-Divisions was used, but forward in time and with the initial point of each C-Division labelled by a circle. Same parameters were applied for Trackmate plugin nucleus trajectory detection.

The generated table "*tracks in spots statistics"* was saved (.xls) to be opened in the Trackmate Process Manual macro. In the forward movie, 2 to 4 cells adjacent to the initial trajectory point of the analyzed C-Divisions and detected by Trackmate (blue square) would be selected and their trajectory followed at every timepoint and corrected when necessary. Trajectories were saved as a multiple ROI file.

Trajectory visualization of C-Divisions and their initially adjacent cells

Tracks Visualization Macro 1.3 developed by Sébastien Tosi (IRB imaging facility), was used to simultaneously visualize the backward C-Division tracks and the forward Adjacent cells tracks in two different colours to allow the comparison between trajectories in ImageJ 3D viewer. A time-lapse representative snapshot was selected to represent overlaid trajectories.

3.9.4 Mitosis length analysis

Mitosis spotted in SPIM generated movies at different developmental timepoints were analyzed in both dorsal (n=60) and transversal (n=60) embryonic views. Mitotic phases were identified by the nuclear H2B-RFP and membrane-GFP markers. ANOVA and t-student tests were applied for statistical analysis.

3.9.5 Metaphase plate rotation analysis

Mitosis spotted in SPIM generated movies at different developmental timepoints were analysed in the transversal embryonic view (n=60). A line was drawn representing the centre of the tissue (dorso-ventral axis in transversal view, antero-posterior axis in the dorsal view). Using the ImageJ Angle Measurement command, the angle between the mitotic metaphase plate and the centre of the tissue was measured at each recorded timepoint (degrees). Differences between angle measurements in consecutive timepoints were taken as metaphase rotations. The sum of metaphase rotation angles in a single mitosis metaphase was calculated and expressed as Metaphase Total Rotation (degrees). Speed was calculated by calculating the ratio between the metaphase total rotation and the metaphase time, and expressed as Metaphase Rotation Speed (degrees/min). Mann-Whitney test was applied for statistical analysis.

3.9.6 Mitotic spindle orientation analysis

All mitosis taking place in one single z-plane in SPIM time-lapse movies were analysed in the transversal embryonic view. A line was drawn representing the centre of the tissue, and a line representing the mitotic spindle was drawn between the two sister cell nuclei at anaphase or telophase mitotic cells. The angle between the centre of the

tissue and the mitotic spindle axis as measured with the Angle Measurement ImageJ command and represented in excel polar graphs (degrees).

3.10 Statistical Analysis

Microsoft Excel and Graphpad Prism 4 were used for numerical and accompanying statistical analysis and graphic representations. Two-tailed t-Student test was applied for statistical analysis unless otherwise indicated. Mann-Whitney test was applied for metaphase plate rotation analysis (Section 4.7, figure 4.11 F,G)

4. RESULTS

4 - RESULTS

4.1.-Sonic hedgehog is expressed in early developing ZF embryos

Zebrafish (ZF) contains two sonic hedgehog (*shh*) genes; *shha* (former sonic-you, *syu*) and *shhb* (former tiggy winkle hedgehog: *twh, twhh*) both expressed in midline structures, albeit expression of *shhb precedes that of shha. shhb expression* is first detected at about 50 % epiboly and, by the end of gastrulation, it is expressed throughout the entire axis including the tailbud (Ekker *et al.*, 1995). *shha* expression appears later in both presumptive neural and notochordal cells (Krauss *et al.*, 1993; Ekker *et al.*, 1995). *shha* expression is reliably detected using the reporter transgenic line Tg-Shh:GFP (Shkumatava *et al.*, 2004, Figure 4.1A,B). Moreover, Shh responding cells can be readily detected within the neural plate, as early as 10hpf (Xiong *et al.*, 2013). This early expression suggested a possible role for Shh in neural tube morphogenesis.

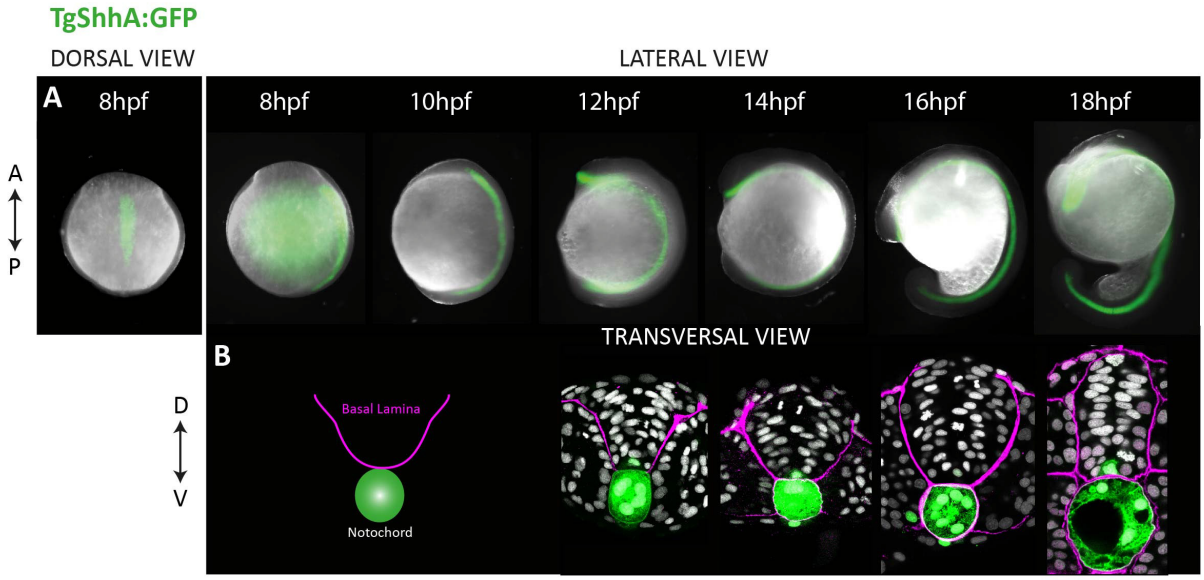

Figure 4.1 - *sonic hedgehog a* is expressed in early developing Zebrafish embryos
Transgenic ShhA:GFP (Tg-ShhA:GFP) zebrafish embryos, 8-18 hour post fertilization (hpf) show *shha* expression in the embryo midline structures along early development. (A) *in toto* zebrafish embryos show *shha* expression (green) in the emerging anterior notochord (8hpf). *shha* expression is later established in the notochord and floor plate along the entire anterior to posterior axis (10-18hpf). Notice that *shha* expression starts when convergence and extension morphogenetic processes occur, prior to neurulation. (B) Show representative transversal sections of Tg-ShhA:GFP embryos, at the corresponding developmental stages (12-18 hpf). *shha* (green) is expressed in the notochord and floor plate along progressive stages of the developing neural tube (neural keel, neural rod, neural tube). Neural tissue is delimited by Laminin1 staining (magenta), a component of the basal lamina. White show nuclei stained with DAPI. (A-P and D-V indicate embryo axis).

4.2.-Sonic hedgehog signalling controls lumen formation in ZF neurulation

To begin to test a role for Shh signalling in neural tube formation, we treated embryos with the Shh inhibitor cyclopamine (Figure 4.2A). The efficiency of cyclopamine treatment was assessed by the inhibition of Olig2-expression using the reporter transgenic line (Tg-Olig2:GFP), which showed a dose-response reduction in Olig2 expression in motor neuron progenitors, with full abolishment of Olig2 expression at 300µM cyclopamine treatment (Figure 4.2B-G). In order to minimize antero-posterior variation, we analysed the phenotype at the hindbrain and anterior spinal cord levels, taking the otic vesicle as a landmark (Figure 4.2H,I). By 24 hours post fertilization (hpf) at the caudal hindbrain-anterior spinal cord levels, the neural tube shows a well organized midline lumen lined by apical proteins, such as the tight junction marker Zonula Occludens 1 (ZO-1) (Figure 4.2H). In contrast, embryos raised in 300µM cyclopamine from 5hpf, showed a discontinuous ventricular surface at 24hpf (Figure 4.2I). This phenotype is likely to result from the blockade of Shhb early activity, since the mutant *syu* embryo display normal neural tube morphology (Araya *et al.*, 2014).
Transverse spinal cord sections confirm the existence of discontinuous lumens in the cyclopamine treated embryos, through the anterior and posterior spinal cord (Figure 4.3A-F). However, the architecture of the neural tissue is well conserved, since Laminin is still lining the basal perimeter of the neural tube (Figure 4.3A-F), while mitosis are organized close to the discontinuous lumens (Figure 4.3A-F). Moreover, the apico-basal polarity of neuroepithelial (NE) cells is conserved as shown by (i) the expression of ZO-1 lining the multiple lumens (Figure 4.3A,B), (ii) the basal positioning of early differentiated neurons identified by the expression of Acetylated Tubulin (Figure 4.3C,D), as well as (iii) the actin accumulation at the apical adherens junctions (Figure 4.3E,F). These results suggest that Shh signalling might be required for lumen positioning and/or lumen formation during neurulation in zebrafish embryos.

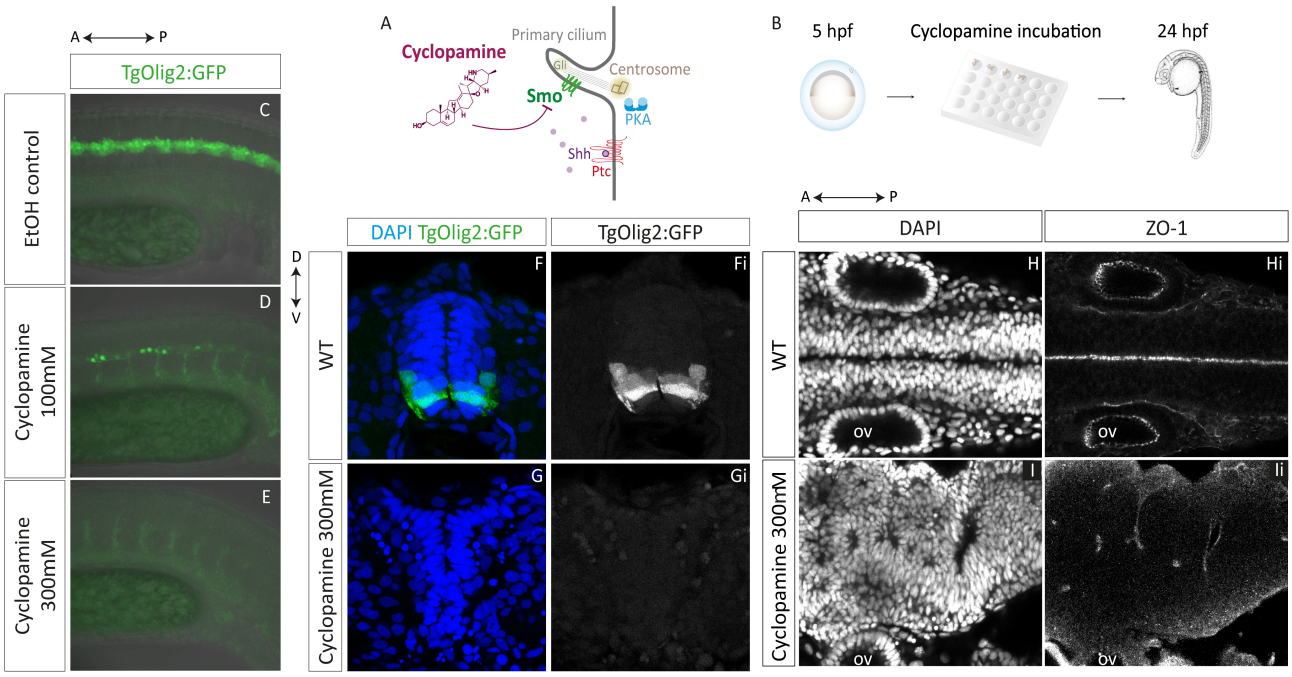

Figure 4.2 - Cyclopamine treatment inhibits Shh signalling and disrupts neural tube lumen formation

(A) Schematic representation of the Shh signalling pathway associated to the primary cilia. Cyclopamine is a Shh antagonist that blocks the pathway at the level of the activating membrane receptor Smoothened (Smo). (B) Schematic representation of the experimental design for in vivo blocking Shh-signalling. Embryos were harvested at 5hpf, around the onset of Shh expression, and incubated in E3 medium with the corresponding ethanol or cyclopamine concentrations at 28.5ºC until reaching 24hours post fertilization (hpf). (C) Efficiency of the cyclopamine treatment was tested using the reporter line Tg-Olig2:GFP as a readout of Shh activity. Selected images show lateral views of TgOlig2:GFP embryos, 24hpf after the indicated treatment. Control embryos show well-organized columns of Olig2+ cells (green). (D) 100µM cyclopamine treatment diminished the population of Olig2+ progenitors (E) 300µM treatment completely abolished Olig2 expression. (F, Fi) Representative transversal sections of Tg-Olig2:GFP 24hpf embryos show Olig2 expression (green) in the motor neuron progenitors of WT embryos, 24hours after control treatment. (G, Gi) Show the absence of Olig2 expression after cyclopamine treatment. Blue show nuclei stained with DAPI. (H,Hi) Representative *in toto* dorsal view at the otic vesicle level shows a well-defined midline lumen, lined by the expression the apical component ZO-1, in embryos 24hours after control treatment. (I, Ii) Lumen formation is disrupted in cyclopamine treated embryos.
White show nuclei stained with DAPI. (A-P and D-V indicate embryo axis).

We next studied whether Shh activity was sufficient to alter lumen formation in the developing ZF spinal cord. To that end, embryos were injected at one cell stage with two activators of the Shh pathway: SmoothenedM2 (SmoM2; Xie *et al.*, 1998) or dominant negative PKA (dnPKA; Epstein *et al.*, 1996),) (Figure 4.4A,B). The efficiency of Shh-Gain of Function (Shh-GOF) experiments was assessed by the over-expression of Olig2, a direct target of the Shh pathway, using the reporter transgenic line (Tg-Olig2:GFP), which showed an expansion of the Olig2 domain (Figure 4.4C,D). Moreover, Shh-GOF mutant embryos showed ectopic motor neuron differentiation, as assessed by the expression of Islet1 in the transgenic ZF line (Tg-Islet1:GFP) (Figure 4.4E,F). By 24hpf, Shh-GOF mutant embryos display severe neurulation defects ranging

from partial to total lumen duplication. Moreover, duplicated neural tube show duplicated motor neuron columns, as seen in the Tg-Islet1:GFP line (Figure 4.4G,H).

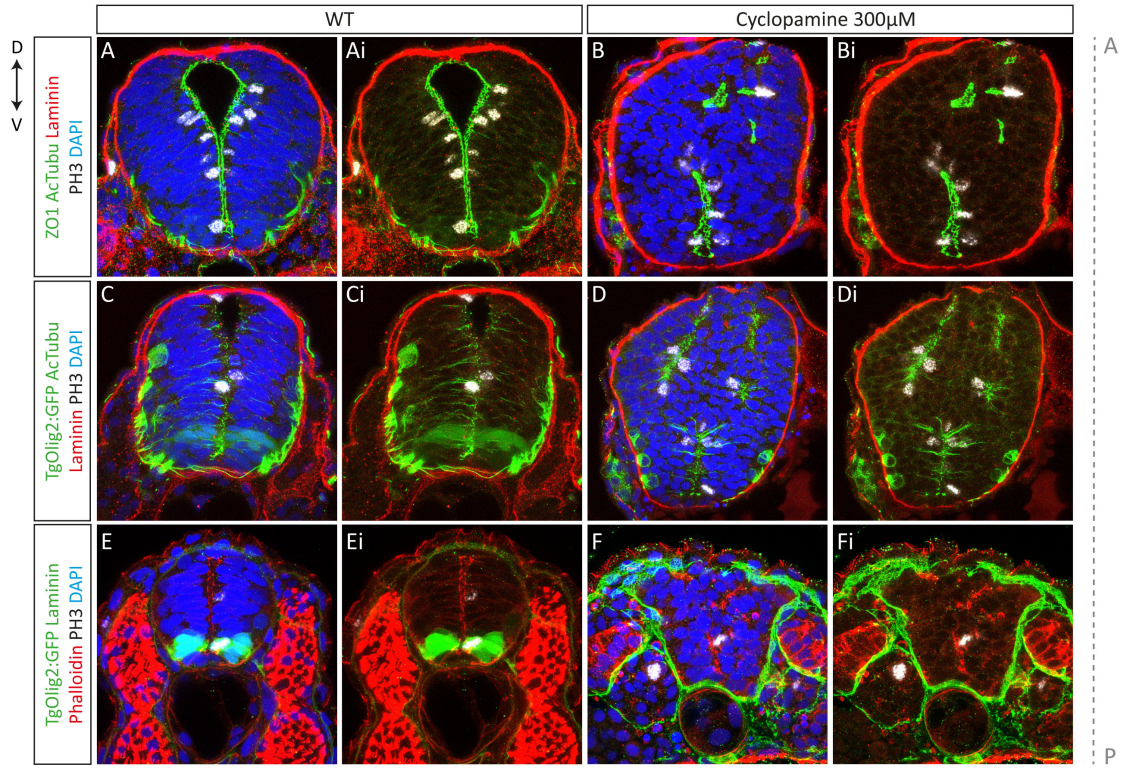

Figure 4.3 - Neural tube lumen formation is disrupted in cyclopamine-treated embryos
Selected transverse sections through the spinal cord of embryos 24 hours after cyclopamine incubation show neural tube defects, although the histology of the neuroepithelium is well conserved. (A, Ai) Representative sections through the anterior spinal cord level show ZO-1 (green) lining the neural tube lumen, Acetylated Tubulin (green) expressing neurons at the basal side of the neuroepithelium, Laminin (red) lining the basal side of the NT, and PH3 (white) staining mitotically active cells facing the NT lumen. (B, Bi) Section through a similar anterior spinal cord of cyclopamine treated embryos shows multiple discontinuous lumens. Immunostainings show that the neural tissue architecture and cell polarity are well preserved; ZO-1 immunostaining lines the multiple lumens, where PH3+ mitosis localize. Laminin staining lines the basal lamina. (C, Ci) Sections through the intermediate spinal cord level of Tg-Olig1:GFP (green) embryos show AcTubulin (green) immunostained primary cilia lining the neural tube lumen, as well as labelling early differentiated neurons. (D, Di) Cyclopamine treated embryos show multiple discontinuous lumens and absence of Olig2 expression. Neurons remain basally located, while cilia appear in the misplaced luminal surfaces. (E, Ei) Sections through the caudal spinal cord level of Tg-Olig1:GFP (green) embryos show Laminin staining (green) and actin labelling (Phalloidin, red) staining. (F,Fi) Cyclopamine treated embryos show multiple discontinuous lumens and absence of Olig2 expression. Basal lamina lines the entire NT, actin labelling (phalloidin) marks apical adherent junctions.
Blue show nuclei stained with DAPI. (A-P and D-V indicate embryo axis).

Transverse spinal cord sections confirmed the existence of continuous lumens in the Shh-GOF mutant embryos, through the anterior and posterior spinal (Figure 4.5A-H). However, the architecture of the neural tissue is well conserved, since a Laminin1 expressing basal lamina is still lining the basal perimeter of the neural tube (Figure

4.5A-H), while mitosis organized close to the duplicated lumens (Figure 4.5C-F). Moreover, the apico-basal polarity of NE cells is well conserved as shown by the expression of ZO-1 lining the duplicated lumens (Figure 4.5A,F), as well as the actin accumulation at the apical adherent junctions (Figure 4.5G,H). Together these results indicate a role for Shh-signalling in lumen positioning and/or lumen formation during neurulation, and prompted us to search for the possible mechanisms generating these neural tube defects.

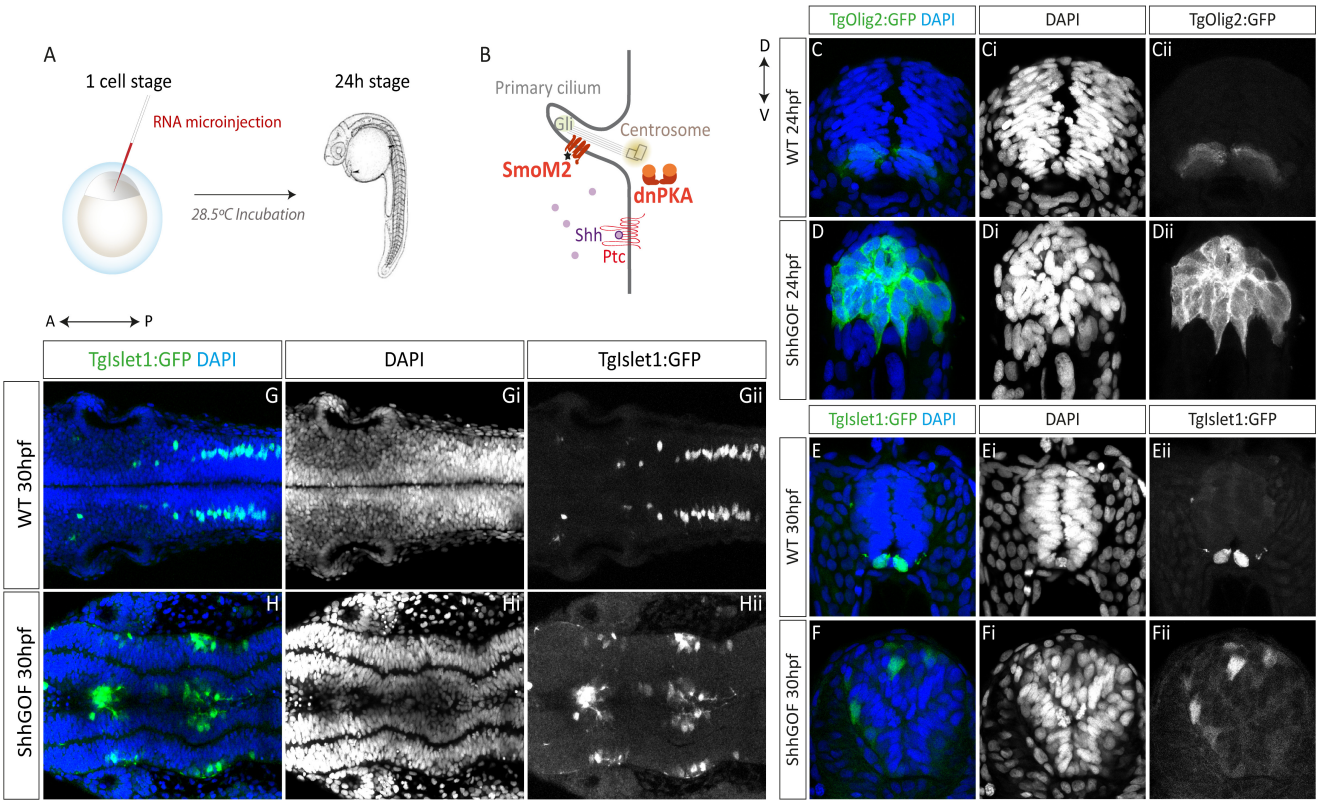

Figure 4.4 - Constitutive activation of the Shh pathway cause lumen duplications
(A) Schematic representation of the experimental design for in vivo activating Shh-signalling. Embryos were injected at 1 cell stage and incubated at 28.5ºC until reaching 24hours post fertilization (hpf). (B) Schematic representation of the Shh signalling pathway associated to the primary cilia. Activators of the Shh pathway were; a mutant version of the receptor Smo (SmoM2), and a dominant negative version of PKA (dnPKA). (C, D) Efficiency of the activation of Shh-signalling was tested using the reporter line Tg-Olig2:GFP as a readout of Shh activity. Selected images show transverse sections of Tg-Olig2:GFP embryos, 24hpf after Shh activation. Control embryos show well organized bilateral columns of motor neuron progenitors expressing Olig2+ (green). (D) Shh-gain of function (Shh-GOF) mutant embryos show increased population of Olig2+ progenitors (E, F) Efficiency of the activation of Shh-signalling was tested using the reporter line Tg-Islet1:GFP as a readout of Shh activity. Selected images show transverse sections of Tg-Islet1:GFP embryos, 24hpf after Shh activation. Control embryos show well organized bilateral pairs of Islet+ motor neurons (green). (D) Shh-gain of function (Shh-GOF) mutant embryos show ectopic Islet1+ neurons. (G, H). Representative *in toto* dorsal view, at the otic vesicle (OV) level, shows a well defined midline lumen in control embryos, 24hours after control injection. Bilateral columns of Islet1+ motor neurons (green) are visible. (I) Lumen is duplicated in Shh-GOF mutant embryos. Islet1+ columns of motor neurons are also duplicated along the duplicated lumens. DAPI (blue) stains nuclei. (A-P and D-V indicate embryo axis).

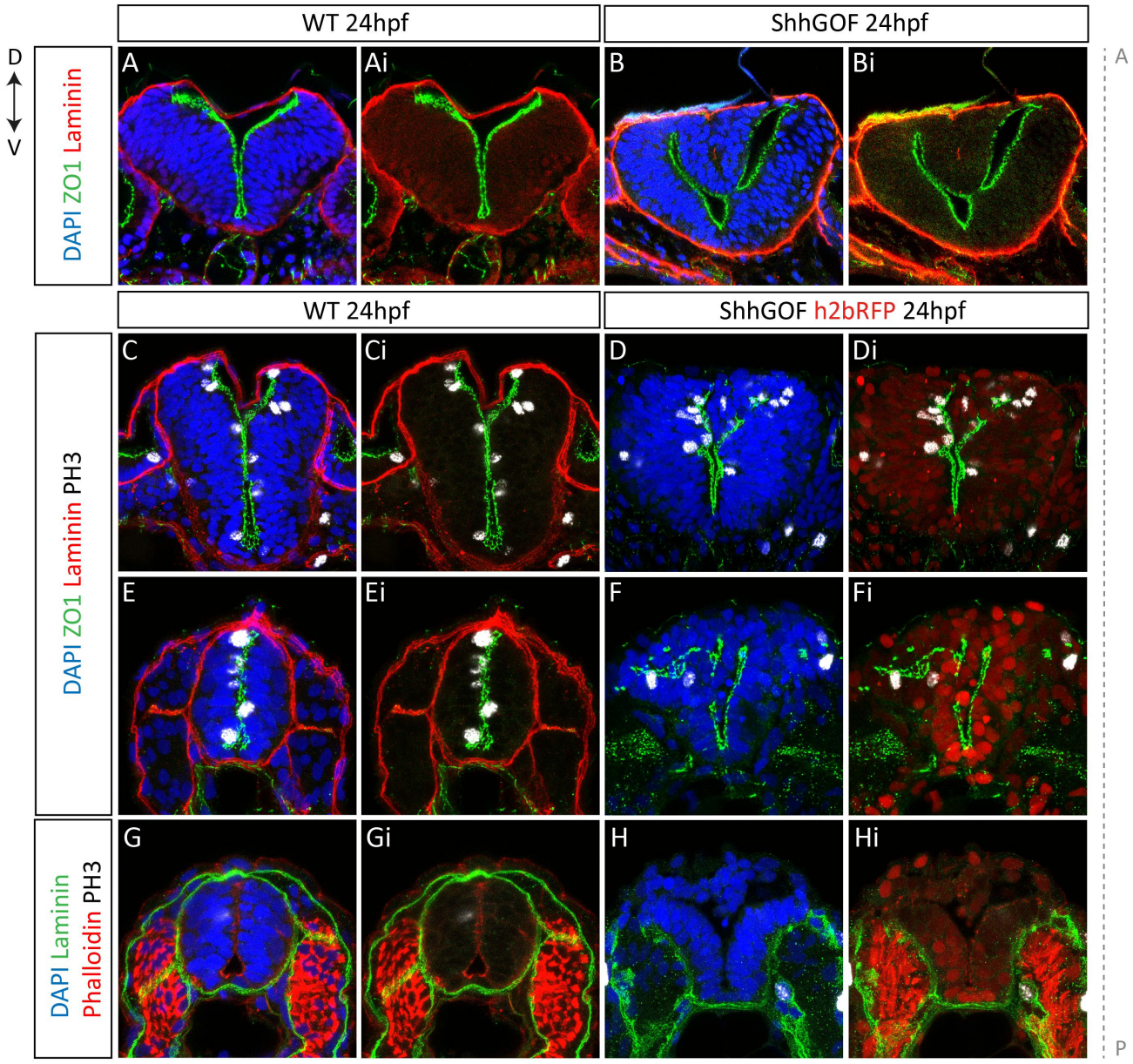

Figure 4.5- Constitutive activation of the Shh pathway cause lumen duplications
Transverse sections through the spinal cord of embryos 24 hours after activation of Shh signalling show neural tube lumen duplications without major changes in cell polarity. (A, Ai) Representative section through the hindbrain level show ZO-1 (green) lining the neural tube lumen and Laminin (red) lining the basal side of the NT. (B, Bi) Section through a similar hindbrain level of Shh gain-of-function (Shh-GOF) embryos show a total lumen duplication. Immunostaining show that the neural tissue architecture and cell polarity are well preserved; ZO-1 immunostaining lines the multiple lumens, Laminin staining basal lamina lines the duplicated NT. (C, Ci, E, Ei) Representative sections through the hindbrain level (C, Ci) and spinal cord level (E, Ei) show ZO-1 (green), lining the neural tube lumen, Laminin (red) lining the basal side of the NT, and PH3 (white) staining mitotic cells facing the NT lumen. (D, Di, F, Fi) Representative sections through similar levels of Shh gain of function (Shh-GOF) embryos at the hindbrain level (D,Di) and spinal cord level (F, Fi) show ZO-1 (green), lining the neural tube lumen, Laminin (red) lining the basal side of the NT and PH3 (white) staining mitotic cells facing the NT lumen. Lumens are totally or partially duplicated in Shh-GOF embryos with preserved apicobasal cell polarity and NT histology. (G, Gi) Section through the posterior spinal cord show Laminin (green) lining the basal side of the NT, actin labelling (Phalloidin, red), and PH3 (white) staining mitotic cells. (H, Hi) Lumen appears dorsally duplicated in Shh-GOF embryos.
Blue show nuclei stained with DAPI. (A-P and D-V indicate embryo axis).

4.3.- Convergence is delayed in Shh-GOF mutant embryos

At the onset of neurulation, the ZF neural plate is composed of two cell layers. Radial intercalation transforms the cellular organization of the NE into a single cell layer, beginning at the neural plate/early keel stage and extending into the late neural rod stage. Convergence movements towards the midline progressively rounds up the neural plate to form a nerve rod (Figure 4.6A).

Because delayed neural keel convergence has been thought to be a major contributor to neural tube defects, we first set to analyse quantitatively the dynamics of neural tissue convergence. To that end, control and Shh-GOF mutant embryos were injected with nuclear (H2B-RFP) and membrane-GFP fluorescence proteins and embryos were imaged *in toto* by time-lapse confocal microscopy over a ~9 hour time period (~12-21hpf) (Figure 4.6B-D). Using the dorsal view, we measured the width of the neural plate /neural keel, at the level of the forming otic vesicle (Figure 6B-D). We find that, compared to control embryos, the Shh-GOF neural plate appeared to be wider from the earliest time-point analysed (13hpf, Figure 4.6E). Shh-GOF tissue converges for a longer period (until 18hpf) as compared to the same region in wild type (WT) embryos (average±SEM speed 21,39±5,70µm/h in Shh-GOF vs 2,56±2,45µm/h in WT, Figure 6E,F). Moreover, once convergence movements are completed (>18hpf), the Shh-GOF neural tube remains wider than the WT (Figure 4.6E), suggesting that the NT defects that we observed in Shh-GOF mutant embryos might be driven by abnormalities at the cell and/or tissue levels during convergence movements.

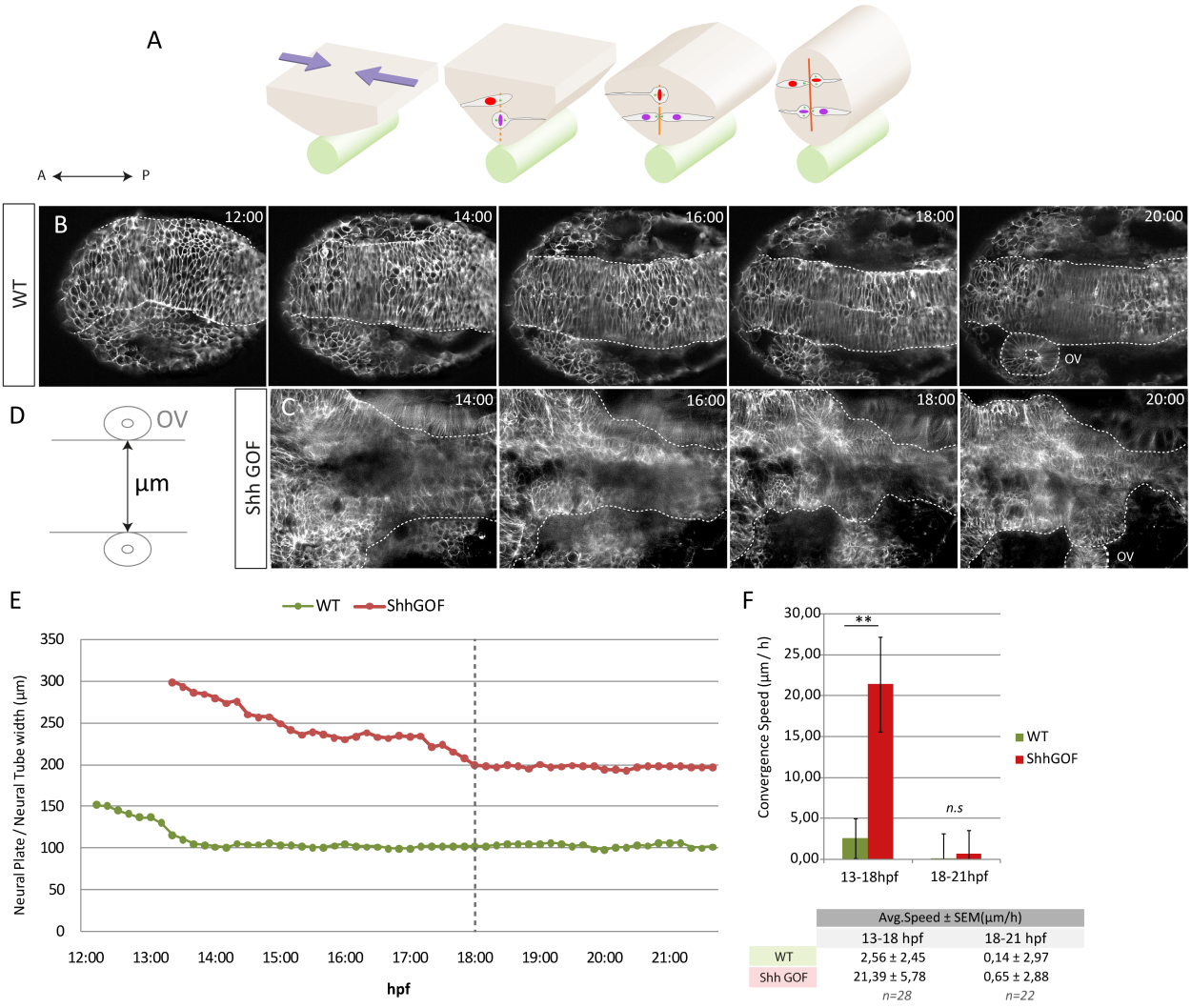

Figure 4.6 - Convergence is delayed in Shh-GOF embryos
(A) Schematic representation of neurulation in teleosts; cartoon of a transverse sections from the neural plate to the neural tube stages. Convergence movements narrow the distance between the neural plate borders in order to shape a neural rod. Notochord is represented in green. (B,C) Wild type and Shh-GOF embryos injected with membrane-GFP were live-imaged from 12 to 21 hours-post-fertilization (hpf). (B) Selected representative snapshots (at indicated hpf) of a time-lapse imaged wt embryo, from a dorsal point of view showing membrane-GFP (white). Basal borders of the neural plate are outlined (dotted line). (C) Selected representative snapshots (at indicated hpf) of a Shh-GOF time-lapse imaged embryo. (D) Schematic representation of the measures distance between neural plate borders, at the level of the otic vesicles (OV). (E) Quantification of neural plate width (µm) from 12hpf to 21hpf (WT, green line) or 13hpf to 21hpf (Shh-GOF, red line). Plot shows that Shh-GOF embryos exhibit a wider neural plate at all stages. WT neural plate convergence, interpreted from a decrease in neural plate width, proceeds until 14hpf in WT embryos and until 18hpf in Shh-GOF embryos. (F) Quantification of the convergence speed (µm/h) at two time points. Convergence speed was calculated measuring width differences between 10min time intervals. At 13-18hpf convergence speed is significantly higher in Shh-GOF embryos (red bar, 21.39±5.78µm/h) compared to WT (green, 2.56±2.45µm/h) (**p ≤ 0.01). A-P indicates embryo axis

4.4 -Primary cilia are longer in Shh-GOF mutant embryos

In NE cells, a single primary cilium pointing to the lumen coordinates Shh signalling responses. Activation of Shh responses requires Smo accumulation to the cilia membrane that mediates the stabilization of Gli transcription factors to activate target gene expression (Figure 4.7A). Thus we next set to test whether the convergence and

NT defects that we observed in Shh-GOF mutant embryos might be driven by defects associated to the primary cilia.

Embryos were injected at one cell stage with activators of the Shh pathway (SmoM2 or dnPKA). Transverse sections through the anterior spinal cord confirmed the existence of duplicated continuous lumens lined by progenitor cells exhibiting primary cilia immunostained with Acetylated Tubulin (Figure 4.7B). Interestingly, primary cilia are longer in Shh-GOF mutants compared to WT embryos (Figure 4.7C), as previously reported (Yu *et al.*, 2008). It has been shown that longer cilia attenuate intracellular Shh signalling by decreasing the activity of Gli proteins, the transcriptional mediators of Shh activity. This mechanism has been proposed to modify the cellular response to Shh in the floor plate to distinguish these cells from the rest of the neuroepithelium (Cruz *et al.*, 2010)

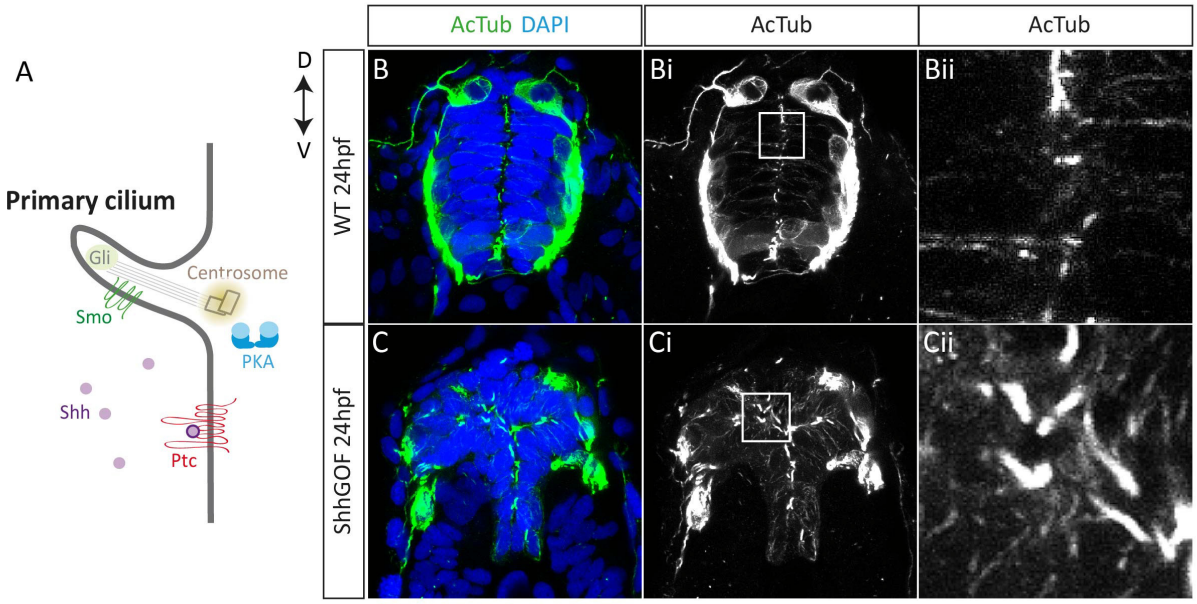

Figure 4.7 - Cilia are longer after Shh activation
(A) Schematic representation of the Shh signalling pathway associated to primary cilia. Selected transverse sections through the spinal cord of embryos 24 hours post fertilization (hpf) show longer apical cilia in Shh gain of function (Shh-GOF) embryos. (B,Bi) Section through the anterior spinal cord level show Acetylated Tubulin immunostaining (B-green, Bi-white) in luminal primary cilia and neurons at the basal side of the neuroepithelium. (Bii) High magnification detail of Acetylated Tubulin staining (white) in a dorsal WT spinal cord region. (C,Ci) Section through a comparable spinal cord section Shh-GOF embryos show Acetylated Tubulin staining (C-green, Ci-white) in primary cilia arranged along the ectopic luminal surface. Shh-GOF embryos display longer cilia. (Cii) High magnification detail of Acetylated Tubulin staining (white) in a dorsal Shh-GOF spinal cord region. Cilia length increases after activation of the Shh pathway.
D-V indicates embryo axis.

In early developing zebrafish embryos, primary cilia are reliably labelled *in vivo* by the expression of a GFP-tagged small GTPase ADP-ribosylation factor-like 13b (Tg(Arl13b-GFP); Borovina *et al.*, 2010). Arl13b-GFP embryos were injected at one cell stage with activators of the Shh pathway. WT Arl13b-GFP embryos were imaged *in vivo* by time-lapse confocal microscopy over a ~4 hour time period (12-16hpf) and compared to Shh-GOF (injected with SmoM2) embryos (Figure 4.8A). To assess the extent of convergence movements, primary cilia were tracked using the Particle Tracker ImageJ Plugin (see Materials and Methods), within a dorsal view at the level of the forming otic vesicle (Figure 4.8B,C). We find that cilia of the control and the Shh-GOF mutant embryos both converge towards the forming midline with comparable trajectories (Figure 4.8Bi, Ci). The speed of the movement towards the midline was maintained constant along the imaged period (Figure 4.8Bii, Cii). Moreover, compared to control embryos, Shh-GOF cilia move with similar speed (Average speed±SEM control cilia 0,89±0,11µm/min, Shh-GOF 0,90±0,14µm/min, Figure 4.8E), and similar persistency (Average persistency±SEM control cilia 0,42±0,00, Shh-GOF 0,36±0,01, Figure 4.8Ei), towards the midline. Together these analyses indicate that, although activation of the Shh-pathway was sufficient to increase the length of the primary cilia, the impact of these changes in either apical positioning of the cilia, or in the motion properties of progenitor cells during convergence were minimal.

4.5 Cell motion properties during neurulation are resistant to Shh-signalling

Because of the drastic 3D morphogenetic movements that cells undergo during ZF neurulation, direct imaging of these 3D morphogenetic process with cellular resolution is challenging. To overcome this difficulty, here we have taken advantage of Selective plane Illumination fluorescence Microscopy (SPIM), that uses a focused light-sheet to illuminate the specimen from the side, to achieve excellent resolution at high penetration depths in whole ZF embryos (Figure 4.9A). This allowed uninterrupted imaging sessions on single embryos from early neural plate (~10hpf) to neural tube formation (~20hpf).

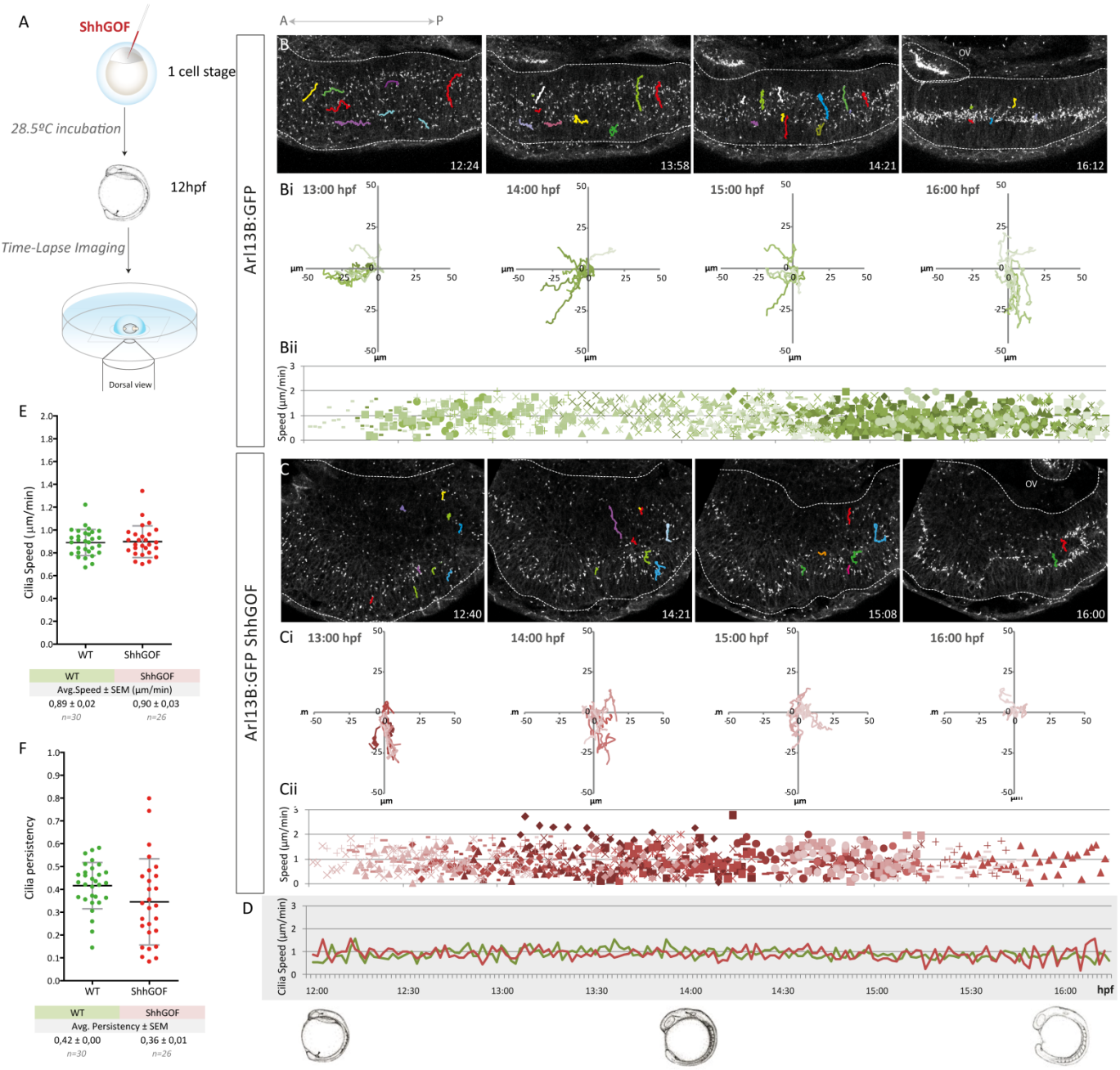

Figure 4.8 -Cilia motion is unaffected in Shh-GOF embryos

(A) Schematic representation of the experimental procedure for *in vivo* cilia tracking. Tg-Arl13B:GFP embryos were injected at 1 cell stage with Shh pathway activators (SmoM2 or dnPKA) and incubated at 28.5ºC until reaching 12hours post fertilization (hpf). At that stage, embryos were embedded in an agarose matrix and mounted in a glass-bottom dish in order to proceed to live imaging. (B, C) Snapshots of control injected Tg-Arl13B:GFP (B) or Shh-GOF injected Tg-Arl13B:GFP (C) embryos imaged from a dorsal view at the level of the otic vesicles (OV). Individual cilia (white) trajectories are shown (random color lines) at indicated time-points. Dotted white lines delimit the neural plate borders. (Bi, Ci) Individual cilia trajectories in control (green lines) and Shh-GOF (red lines) embryos are plotted in 1hour-interval graphs, considering zero the last tracked time point for each cilium. Left to right in the x graph axis represents anterior to posterior embryo axis, up to down in the y graph axis represents lateral to medial embryo axis. (Bi) WT cilia trajectories move from posterior to anterior (13:00hpf) and then progressively change the directionality of their trajectories (14:00-15:00 hpf) until reaching a lateral to medial movement (16:00hpf). (Ci) Shh-GOF cilia trajectories display predominantly lateral to medial movement (13:00-15:00 hpf) and end with random movements (16:00 hpf) when reaching their final location. (Bii, Cii) Speed of each tracked cilium in WT (green) and Shh-GOF (red) was calculated between 1.5min time-intervals and plotted in a graph representing the entire imaging period. (D) An average total cilia speed was obtained at each time point between 12hpf and 16hpf. Average cilia speed remains constant along this time window in WT and Shh-GOF conditions. (E) An average speed was obtained for each WT (green dots) and Shh-GOF (red dots) cilia path. Resulting average cilia speed was comparable in both conditions (Average±SEM speed: WT 0,89±0,02µm/min, Shh-GOF 0,90±0,03µm/min). (F) An average persistency was obtained for each WT (green dots) and Shh-GOF (red dots) cilia path. Resulting average cilia persistency (black line) was slightly lower and displayed higher variability in Shh-GOF embryos, with no significant differences. (Average±SEM speed: WT 0,89±0,02µm/min, Shh-GOF 0,90±0,03µm/min).Average values represented by a black line, Standard deviations by grey lines.

Dorsal and transversal views of the same embryo were acquired every 2 minutes of healthy embryos labelled with nuclear (H2B-RFP) and membrane-GFP fluorescence proteins (Figure 4.9A,B). In order to minimize antero-posterior variation, we analysed the phenotype at the hindbrain and anterior spinal cord levels, taking the otic vesicle as a landmark (Figure 4.9B). These data provided tractable 3D movies that cover the period of neural keel and neural rod formation and lumen opening, allowing us to directly assess the cell motion properties of NE cells during neurulation.

Because NT lumen formation in the ZF embryo involves detachment of dividing cells from each other at the midline (Papan and Campos-Ortega, 1994), we first tracked the nuclei of progenitors committed to these midline crossing divisions (C-divisions) during convergence. Migrating nuclei were tracked using the semi-automatized TrackMate Process Manual ImageJ macro (see materials and methods). We observed that nuclei move towards the NT midline, where cells round up and divide apically, while daughter cells become incorporated into opposite sides of the NT (Figure 4.9C,D).

To assess the extent of cell movements, we first calculated individual nuclei speeds at different times along neurulation (between 10 and 20hpf). Analyses from the dorsal view show that nuclei movements towards the midline maintained a constant average speed along development (Average speed±SEM 1,02±0,02µm/min, Figure 4.9E,F). Because of the extensive 3D cell movements, we also calculated individual nuclei speeds at different times from the transversal view, which showed a comparable average speed with little variation (Average speed±SEM 1,08±0,02µm/min, Figure 4.9E). Next we calculated the persistency of individual nuclei movement towards the NT midline, to show that either from the dorsal (Average persistency 0,39±0,03, Figure 4.9G) and the transversal views (Average persistency 0,42±0,02, Figure 4.9G), persistency of cell movements was highly comparable. Together these analyses showed that, although extensive 3D cell rearrangements occur during cell convergence and NT formation, the dorsal-view analysis reliably assessed cell motion properties.

We further checked whether the NT defects that we observed in Shh-GOF mutant embryos are driven by defects in the motion properties of individual cells. However

results show that in Shh-GOF mutant embryos nuclei move towards the NT midline before committing a midline crossing division, with directionality comparable to those of the WT embryos (data not shown). Moreover Shh-mutant cells move towards the NT midline with a speed (Average speed±SEM 1,17±0,04μm/min, Figure 4.9H) and persistency (Average persistency 0,40±0,04, Figure 4.9I) that are both comparable to that of the WT cells.

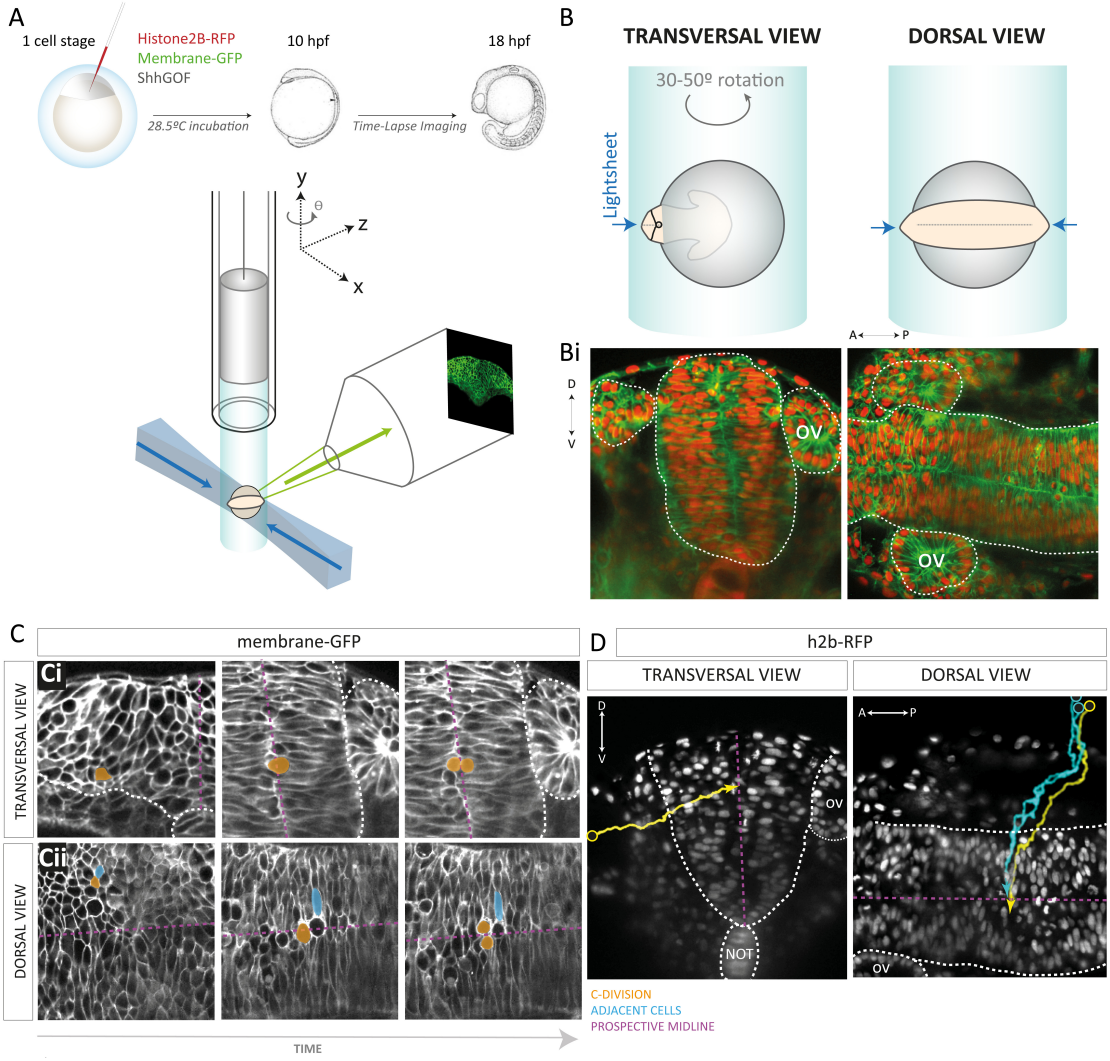

Figure 4.9 -Cell motility is unaffected by Shh signalling

(A) Schematic representation of the experimental procedure for selective plane illumination (SPIM) based *in vivo* microscopy. Embryos were injected at 1 cell stage with cellular markers and Shh pathway activators SmoM2 or dnPKA. Embryos were incubated at 28.5ºC until reaching 10hours post fertilization (hpf). At that stage, embryos were mounted in an agarose matrix held by a glass capillary and introduced in the SPIM device. (B) A transversal embryonic view is obtained by placing the anterior-posterior embryo axis perpendicular towards one of the light sheets. Dorsal embryo view is obtained when the anterior to posterior axis is placed in parallel to the double light sheet coming from either side. By rotation of the sample (θ) both views were sequentially obtained between 2 minutes time intervals. (Bi) Representative images of transversal (left) and dorsal (right) time-lapse movie views of the same embryo. Cells are tagged with membrane-GFP (green) and histone2B-RFP (red). A white dotted line demarcates the neural tube borders and the otic vesicle (OV). (C) Left to Right: C-Divisions (yellow) were tracked in the transversal (upper row) and dorsal (lower row) neural plate views since the earliest recorded time point to the mitosis at the prospective midline. (Ci) Three selected representative snapshots of a cell committed to C-Division (yellow) are shown in a transversal view: the first shows the earliest time point at which the cell is identified; second and third snapshots correspond to the initial cell rounding and final cytokinesis of the C-Division. (Cii) Three selected representative snapshots of a cell committed to C-Division (yellow) and an initially adjacent cell (blue) are shown in a dorsal view: the first shows the earliest time point at which the cell committed to C-Division is identified (yellow) and one neighboring cell (blue); second and third snapshots correspond to the initial cell rounding and final cytokinesis of the C-Division, and show the final relative position of the adjacent cell. White shows membrane-GFP. A magenta line represents the prospective lumen, the white dotted line demarcates the neural tube borders. A-P and D-V represent indicate the embryo axis. (D) Left to right: Transversal snapshot with one overlaid C-Division trajectory (yellow), and dorsal snapshot with one C-Division (yellow) and two adjacent cells trajectories (blue). A circle is placed at the trajectory start and an arrow placed at the end. White shows nuclear-RFP. A magenta line represents the prospective lumen, the white dotted line demarcates the neural tube borders. A-P and D-V represent indicate the embryo axis.

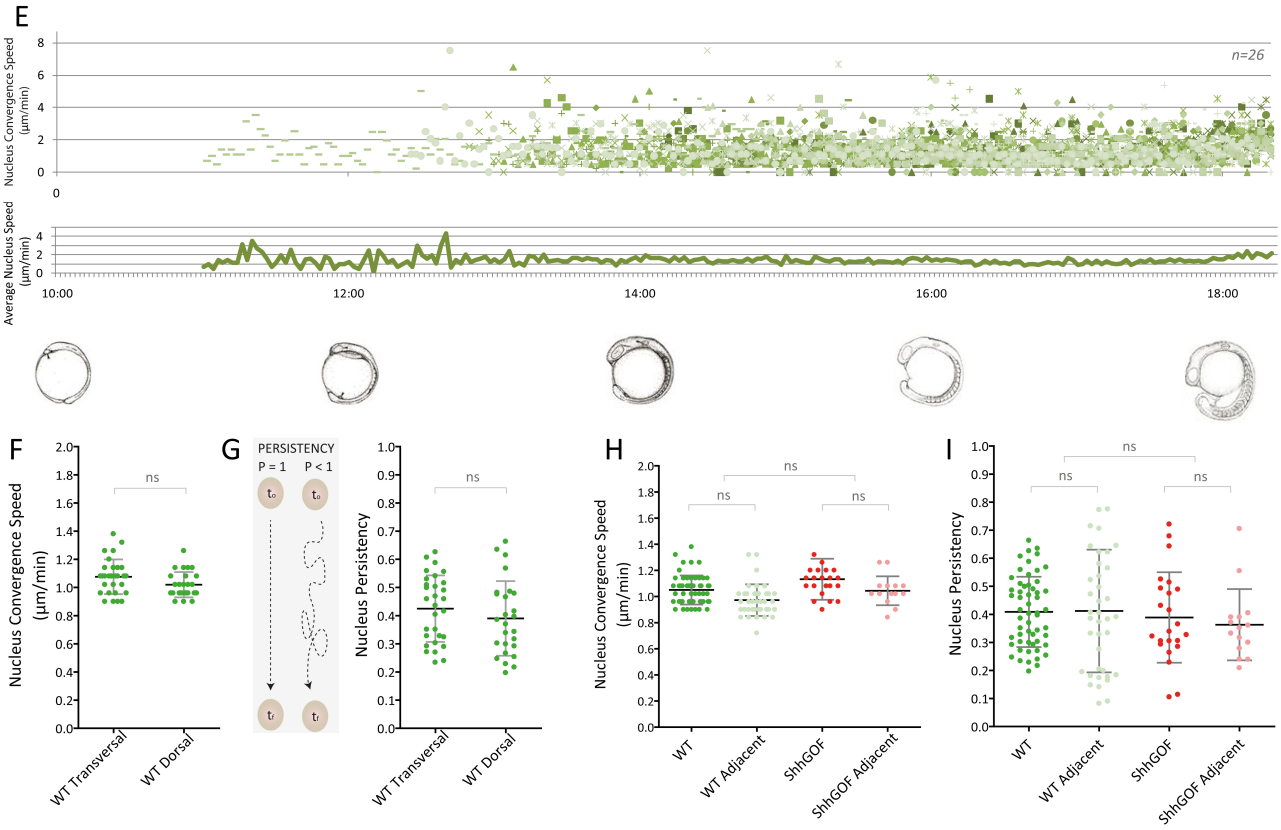

(E) Speed of each dorsal WT tracked C-Division (green) was calculated between 2 min time-intervals and plotted in a graph representing the entire imaging period. An average total nucleus speed was obtained at each time point between 11hpf and 19hpf. Nuclear speed remains constant along this time window in WT C-Division performing cells. (F-G) Average speed and persistency values were obtained for tracked WT nucleus undergoing C-Division (green dots) in both Transversal and Dorsal views. (F) Resulting average nucleus speed is comparable in both views (Avg±SEM speed: Dorsal 1.02±0.018 µm/min, Transversal 1.08±0.022 µm/min). (G) Schematic representation of the meaning of persistency: the ratio between the wandered distance between two points and the shortest distance between the two points in a straight line. Therefore a persistency of 1 represents a straight line trajectory. The closer to zero in the persistency, the less straight is the trajectory. Analysis shows that the average nucleus persistency is similar in both views (Avg±SEM persistency: Dorsal 0.39±0.026, Transversal 0.42±0.021). (H-I) Average speed and persistency values were obtained for tracks of WT nucleus undergoing C-Division (green dots) and their adjacent cells (light green dots) and Shh-GOF undergoing C-division (red dots) and their adjacent cells (light red dots). Data of the dorsal and transversal views are pooled. (H) Speed values are comparable between WT C-Division tracks and their adjacent cells, as they are between Shh-GOF C-Division tracks and their respective adjacent cells. (Avg±SEM speed: WT C-Divisions 1.05±0.015 µm/min, WT AdjacentCells 0.97±0.019 µm/min Shh-GOF C-Divisions 1.13±0.032 µm/min, Shh-GOF AdjacentCells 1.04±0.029 µm/min) There are no significant differences between WT and Shh-GOF conditions. (I) Persistency values are similar between WT C-Division tracks and their adjacent cells, as they are between Shh-GOF C-Division tracks and their respective adjacent cells. Shh-GOF persistency shows slightly lower non-significant values compared to the WT condition. (Avg±SEM persistency: WT C-Divisions 0.41±0.016, WT AdjacentCells 0.41±0.035, Shh-GOF C-Divisions 0.39±0.034, Shh-GOF AdjacentCells 0.36±0.033). Average values represented by a black line, standard deviations by grey lines

These results indicated that the motion properties of progenitor cells committed to complete a midline crossing C-division are resistant to over-activation of the Shh pathway, and suggested that it might be the interaction of these cells with their neighboring cells which might be affected by the Shh-activation, resulting in the neural tube defects observed. Thus, we next set to analyse the motion properties of progenitor cells accompanying those committed to C-divisions. To that end, we tracked 3-4 nuclei that converge adjacent to those committed to C-divisions, but divide to generate daughter cells that remained within the same half of the forming NT (non C-divisions; see blue trajectories in Figure 4.9C,D). In WT embryos, adjacent progenitor cells converge to the midline with trajectories closely accompanying those of the c-dividing progenitors (Figure 4.9D), at a similar speed (Average speed±SEM 0,97±0,02□μm/min, Figure 4.9H), and with a similar persistency (Average persistency 0,41±0,04, Figure 4.9I), indicating that at convergence, neural progenitors committed to a midline crossing division exhibit similar motion properties to those of progenitor not performing C-divisions. Additionally, these observations suggested that commitment to perform a C-division is not predetermined before convergence movements. Moreover, in Shh-GOF mutant embryos, progenitor cells adjacent to those committed to crossing divisions also converge to the midline with similar trajectories (not shown), speed (Average speed±SEM 1,04±0,03 μm/min; Figure 4.9H) and persistency (Average persistency 0,36±0,03 Figure 4.9I) to neural progenitor cells performing C-divisions. Together these analyses indicated that during convergence, the motion properties of NE cells are resistant to over-activation of the Shh pathway.

4.6.-Shh regulates the rate of cell division during ZF neurulation

Neurulation in the Zebrafish embryo requires the coupling of cell movements to specific cell cycles, therefore since our analyses indicate cell movements to be resistant to Shh-signalling, we next set to analyse cell divisions during neurulation. Cell lineage analysis showed that during convergence and extension movements, cells in single clones all tend to divide very synchronously, maintaining synchrony until cycle 16 (majority of crossing divisions occurring at cycle 16; Kimmel *et al.*, 1994). Moreover, dividing progenitor significantly lengthen the duration of the cell cycles along early development.

Taking advantage of our imaging sessions on single embryos from early neural plate (~10hpf) to neural tube formation and lumen opening (~20hpf), we first calculated the time that progenitor cells require to transit from chromosomal condensation to the separation of the sister cells. Analyses have been performed in transversal views of SPIM movies acquired every 2 minutes of WT healthy embryos, in which chromosomes labelling with H2B-RFP allowed the unequivocal identification and tracking of dividing progenitors (Figure 4.10A). Results show the lengthening of mitosis, concomitant to the previously reported lengthening of the whole cell cycle during NT development (Kimmel *et al.*, 1994), from an average length (±SEM) of 11,75±0,2 minutes (at 10-12hpf), to an average of 15,75±0,32 minutes (at >16hpf) after NT formation and lumen opening (Figure 4.10B,E).

When we analysed neurulating ZF embryos in which Shh signalling was over-activated, we first observed that the lengthening of mitosis only occurs after lumen opening, at the NT stage (Figure 4.10B,E). Moreover, compared to control embryos, mitoses are significantly shorter in Shh-GOF mutant embryos all along NT development (Figure 10B). These Shh-dependent shortening of mitosis might be mediated by the over-expression of cell cycle regulators (Alvarez-Medina *et al.*, 2009) and may be responsible for the significant increase in pH3 staining observed in Shh-GOF mutant embryos (Average ratio of pH3+/DAPI±SEM cells/section 4,28±0,46 in WT, vs 6,54±0,43 in Shh-GOF mutant embryos, Figure 4.10C), and the resulting overgrowth of the neural tissue (Figure 4.10C,D).

In order to search for the mitosis phase responsible for this total average lengthening, we next subdivided the mitosis in three visually identifiable periods; an initial period encompassing chromosomal condensation to anaphase, the metaphase; and a late period encompassing anaphase to sister cell separation, cytokinesis (Figure 4.10D). Although the three phases lengthened during NT development (Figure 4.10D,E), the time required for completion of the early phase (condensation to anaphase) showed the most significant increase along development of WT zebrafish embryo (from average length±SEM of 6,18±0,15mins at 10-12hpf to 9,25±0,31mins at >16hpf Figure 4.10D,E). Interestingly though, when compared the first part of the mitosis (condensation to anaphase), it was significantly shorter in Shh-GOF mutant embryos, all along NT development (Figure 4.10D,E). Moreover, the duration of the late mitotic phases (both metaphase and anaphase to sister cell separation) also lengthened during NT development, both in WT and in Shh-GOF mutant embryos (Figure 4.10D,E), although these changes were not statistically significant. Interestingly, the metaphase duration in Shh-GOF mutant embryos was slightly longer compare to that of WT embryos (although not significant) (Figure 4.10D,E). Altogether these analyses showed that activation of the Shh-pathway caused a significant shortening in the length of cell divisions, importantly though this shortening was not accompanied by a shortening in the metaphase duration.

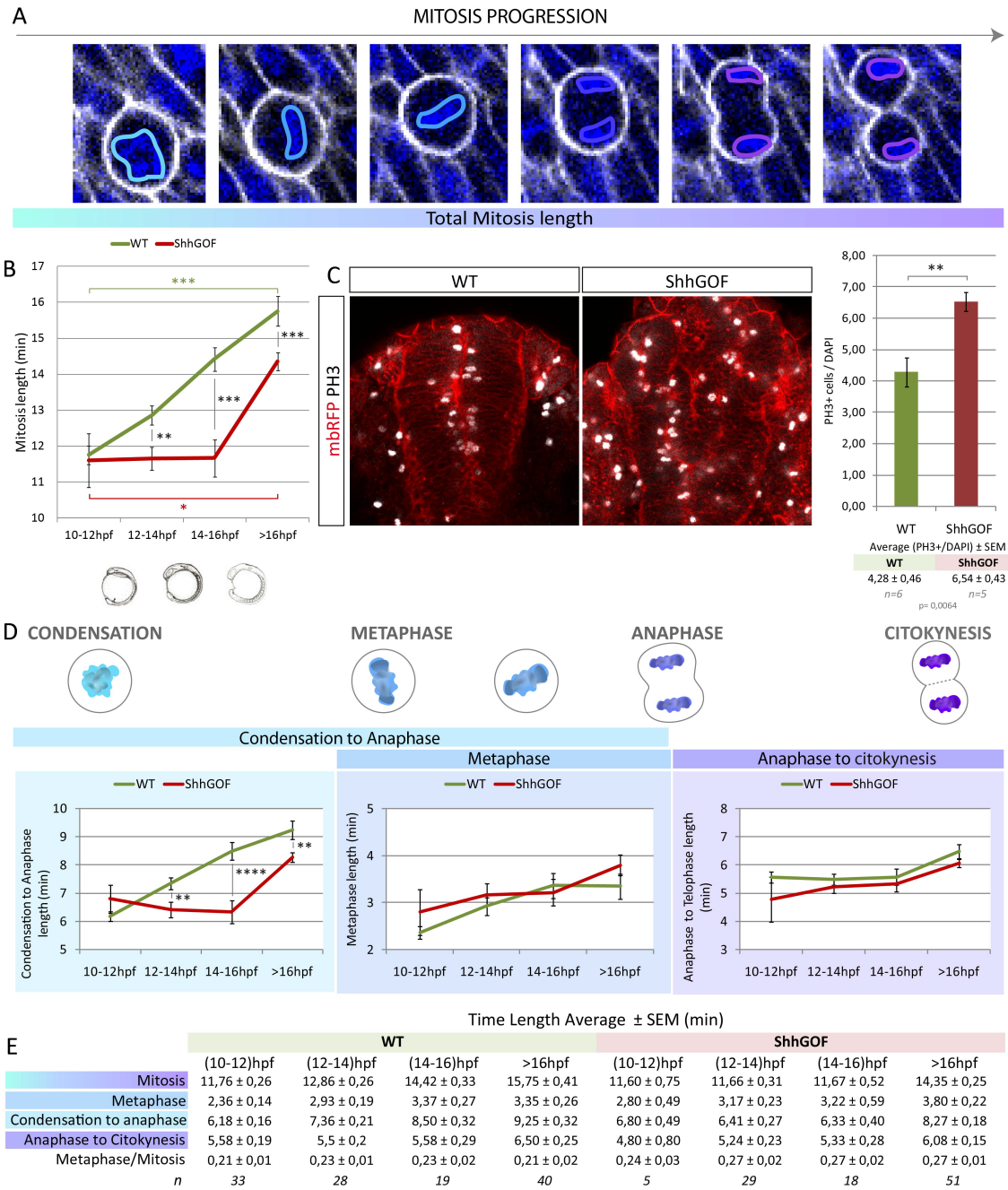

E

Time Length Average ± SEM (min)

	WT				ShhGOF			
	(10-12)hpf	(12-14)hpf	(14-16)hpf	>16hpf	(10-12)hpf	(12-14)hpf	(14-16)hpf	>16hpf
Mitosis	11,76 ± 0,26	12,86 ± 0,26	14,42 ± 0,33	15,75 ± 0,41	11,60 ± 0,75	11,66 ± 0,31	11,67 ± 0,52	14,35 ± 0,25
Metaphase	2,36 ± 0,14	2,93 ± 0,19	3,37 ± 0,27	3,35 ± 0,26	2,80 ± 0,49	3,17 ± 0,23	3,22 ± 0,59	3,80 ± 0,22
Condensation to anaphase	6,18 ± 0,16	7,36 ± 0,21	8,50 ± 0,32	9,25 ± 0,32	6,80 ± 0,49	6,41 ± 0,27	6,33 ± 0,40	8,27 ± 0,18
Anaphase to Citokynesis	5,58 ± 0,19	5,5 ± 0,2	5,58 ± 0,29	6,50 ± 0,25	4,80 ± 0,80	5,24 ± 0,23	5,33 ± 0,28	6,08 ± 0,15
Metaphase/Mitosis	0,21 ± 0,01	0,23 ± 0,01	0,23 ± 0,02	0,21 ± 0,02	0,24 ± 0,03	0,27 ± 0,02	0,27 ± 0,02	0,27 ± 0,01
n	*33*	*28*	*19*	*40*	*5*	*29*	*18*	*51*

Figure 4.10 - Shh increases cell division rate and decreases mitosis length
(A) Selected snapshot of a time-lapse movie showing the sequence of mitosis events: DNA condensation (light blue outline), metaphase plate formation and metaphase plate rotation (medium blue outline), anaphase (dark blue outline), telophase and cytokinesis (purple outline in both). Blue shows H2B-RFP expression, white shows membrane-GFP expression. (B) Mitotic length was measured from DNA condensation to cytokinesis in WT (green line) and Shh-GOF (red line) embryos. Mitosis length values were classified into intervals of 2h of development (10-12hpf, 12-14hpf, 14-16hpf, >16hpf). Mitosis gradually increase their length along development in WT embryos (***p<0.001, values in Table E),. Shh-GOF mitosis only significantly lengthen after 16hpf (*p<0.05). Mitosis length is significantly shorter in Shh-GOF embryos from 12hpf to >16hpf. (C) Representative transversal views of WT and Shh-GOF embryos at the otic vesicle (OV) level. Red shows membrane-RFP expression, white shows mitotic PH3+ cells. Graph plots quantification of mitotic PH3+ cells in whole mount preparations at the OV level of WT (green) and Shh-GOF (red) embryos show a significant increase in the mitotic index (Average(PH3+/DAPI)±SEM:WT 4,28±046, Shh-GOF 6,54±0,43; **p<0.01). (D) The average duration of mitosis phases was measured in WT (green) and Shh-GOF (red). The time from condensation to anaphase shows a significant decrease in Shh-GOF mitotic cells from 12hpf to >16hpf (12-16hpf **p<0.01, >16hpf***p<0.001). Metaphase was slightly but not significantly lengthened in Shh-GOF mitotic cells between 10-14hpf and after 16hpf, unlike anaphase to cytokinesis phase that was non-significantly shortened from 10hpf to >16hpf. Average±SEM values are represented in Table E.

4.7 -Shh signalling diminish metaphase plane rotations in crossing C-divisions during ZF neurulation

Because lumen formation involves detachment of the cells from each other at the midline and their lateral displacement, crossing C-divisions are supposed to play an instructive role in lumen opening during neural tube formation of zebrafish embryos. Thus we next analysed the timing at which progenitor cells divide generating two sister cells across the NT midline.

Next to analyse the length of these particular divisions, we calculated the time that progenitor cells, committed to a crossing C-division, require to transit from chromosomal condensation to the separation of the sister cells across the NT midline. Results showed that the duration of the entire mitosis was comparable in WT and Shh-GOF mutant embryos (average length±SEM 13,60±0,25mins in WT vs 13,39±0,32mins in Shh-GOF mutant embryos, Figure 4.11A,B). However, when compare the length of the three visually identifiable periods of the mitosis; the period encompassing chromosomal condensation to anaphase appear to be significantly shorter in Shh-GOF mutant embryos (Average±SEM 8,10±0,23mins in WT embryos 7,48±0,31mins in Shh-GOF mutant embryo), while both the metaphase (Average±SEM 3,20±0,17mins vs 3,48±0,29mins) and the late anaphase to sister cell separation (Average±SEM 5,50±0,19mins vs 5,91±0,15mins) appear slightly longer in Shh-GOF mutant embryos (Figure 4.11C,D).

The final allocation of daughter cells to both sides of the neural tube in crossing C-divisions is determined by the orientation of the mitotic spindle perpendicular to the forming midline, this final orientation is achieved by active spindle rotations at metaphase (Kaltschmidt *et al.*, 2000; Geldmacher-Voss *et al.*, 2003). Thus taking advantage of our imaging sessions in which dividing progenitors have chromosomes labelled with H2B-RFP, we next calculated the total changes in angle degrees that metaphase plates achieve during rotations (see experimental procedures) until the

beginning of anaphase. Results show that in Shh-GOF mutant embryos, the metaphase plate of C-divisions rotate significantly less compared to those of the WT embryos (Average±SEM, 54,12±12,57 degrees in WT vs 22,97±10,00 degrees in Shh-GOF mutant embryos; Figure 4.11 E,F). Moreover, metaphase rotations are significantly slower in the Shh-GOF mutant embryos compared to WT embryos (Average±SEM, 16,33±3,30 degrees/min in WT, 6,21±1,91 degrees/min in Shh-GOF mutant embryos) (Figure 4.11E,G). These analyses indicate that enhanced Shh-signalling compromises the capacity of metaphase plate to undergo rotations, even though metaphases of Shh-GOF mutant cells are slightly longer than those of the WT cells, and suggested a compromise in the final orientation of cell divisions.

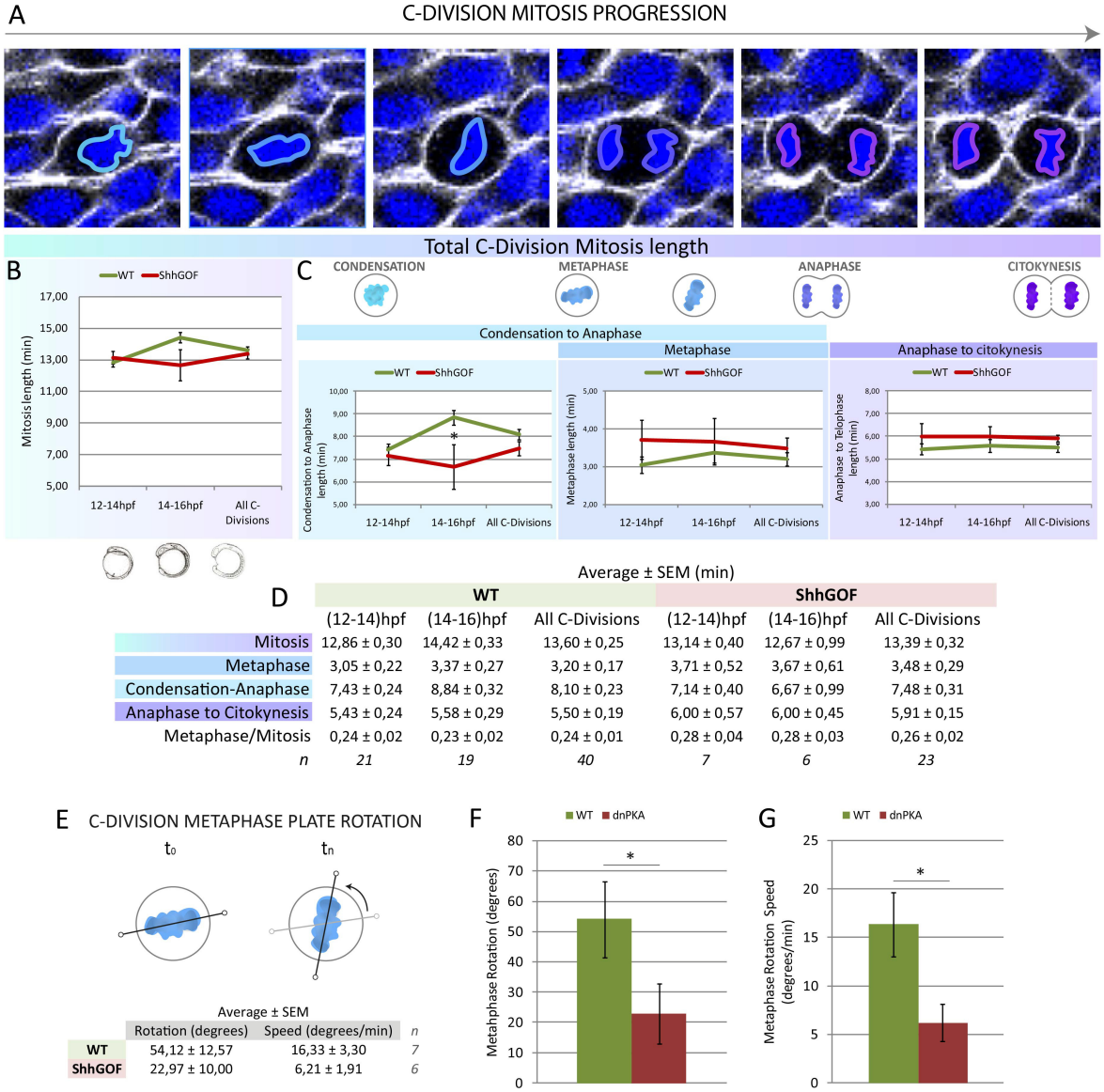

D

Average ± SEM (min)

	WT			ShhGOF		
	(12-14)hpf	(14-16)hpf	All C-Divisions	(12-14)hpf	(14-16)hpf	All C-Divisions
Mitosis	12,86 ± 0,30	14,42 ± 0,33	13,60 ± 0,25	13,14 ± 0,40	12,67 ± 0,99	13,39 ± 0,32
Metaphase	3,05 ± 0,22	3,37 ± 0,27	3,20 ± 0,17	3,71 ± 0,52	3,67 ± 0,61	3,48 ± 0,29
Condensation-Anaphase	7,43 ± 0,24	8,84 ± 0,32	8,10 ± 0,23	7,14 ± 0,40	6,67 ± 0,99	7,48 ± 0,31
Anaphase to Citokynesis	5,43 ± 0,24	5,58 ± 0,29	5,50 ± 0,19	6,00 ± 0,57	6,00 ± 0,45	5,91 ± 0,15
Metaphase/Mitosis	0,24 ± 0,02	0,23 ± 0,02	0,24 ± 0,01	0,28 ± 0,04	0,28 ± 0,03	0,26 ± 0,02
n	*21*	*19*	*40*	*7*	*6*	*23*

Average ± SEM

	Rotation (degrees)	Speed (degrees/min)	*n*
WT	54,12 ± 12,57	16,33 ± 3,30	*7*
ShhGOF	22,97 ± 10,00	6,21 ± 1,91	*6*

Figure 4.11 - Metaphase plate rotations of C-divisions diminish in Shh-GOF mutant embryos
(A) Selected snapshot of a time-lapse movie showing the sequence of events in a c-division: DNA condensation (light blue outline), metaphase plate formation and metaphase plate rotation (medium blue outline), anaphase (dark blue outline), telophase and cytokinesis (purple outline in both). Blue shows H2B-RFP expression, white shows membrane-GFP expression. (B) C-division mitotic length was measured from DNA condensation to cytokinesis in WT (green line) and Sonic hedgehog gain of function (Shh-GOF, red line) embryos. Mitoses lengths were measured at two time-points (12-14hpf and 14-16hpf) or a pooled (All C-Divisions). During the early time window C-Division mitosis length is similar between WT and Shh-GOF embryos. A significant mitosis shortening occurs in Shh-GOF at 14-16hpf. Average pooled C-Division mitosis length is similar between WT and Shh-GOF, *p<0.05). (C) The length of C-Divisions different mitosis parts was measured in WT (green) and Shh-GOF (red). The time required from condensation to anaphase was shorter in Shh-GOF, only at the 14- 16hpf time point. C-Divisions taking place between 12-14hpf and all the pooled C-Divisions show comparable lengths between WT and Shh-GOF. Metaphase was slightly but not significantly longer in Shh-GOF mitotic cells. Anaphase to cytokinesis phases were also slightly but not significantly longer in Shh-GOF embryos. Average±SEM values are represented in Table E. (E) Schematic representation of mitotic metaphase plate rotation. Once metaphase plate is established To (blue) it rotates before reaching the final division plane Tn. Angle rotation was measured between To-Tn. (F) Metaphase plate rotations were measured in WT (green) and Shh-GOF (red) C-Divisions comprised between 14-16hpf. Total metaphase plate rotation is significantly lower in Shh-GOF C-Divisions than in WT C-Divisions (Average±SEM degrees: WT 54,12±12,57º, Shh-GOF 22,97±10,00º, *p<0.05). (G) Speed of metaphase (rotation degrees/minute) was measured in WT (green) and Shh-GOF (red) C-Divisions. Average metaphase rotation speed is significantly lowered in Shh-GOF C-Divisions (Average±SEM speed: WT (16,33±3,30 deg/min, Shh-GOF 6,21±1,91 deg/min, *p<0.05)

4.8-Shh signalling randomizes mitotic spindle orientation during ZF neurulation

Because the orientation of cell division has a strong impact in lumen opening in the ZF neural tube, we next sought to study whether the reduction in metaphase plane rotations that we observed in Shh-GOF mutant embryos might have an impact in the final orientation of mitosis during neurulation.

Taking advantage of our imaging sessions on single embryos from early neural plate (~10hpf) to neural tube formation and lumen opening (~20hpf), we analysed the spindle orientation of mitosis that occur during these periods. Time-lapse SPIM movies of embryos labelled with nuclear H2B-RFP and membrane-GFP fluorescence proteins, allowed us to directly determine the orientation of mitosis of NE cells (Figure 4.12A). We assessed mitotic orientation with respect to the midline, in transversal views of movies acquired every 2 minutes of WT healthy embryos. Most of the metaphase plates observed underwent striking planar rotations, which ceased when cells entered anaphase, as previously reported (Geldmacher-Voss *et al.*, 2003). Because chromosomal plates separate at anaphase without major additional changes in spindle orientation, we used the ImageJ angle measurement command (see experimental procedures) to measure the orientation of the mitotic spindle, with respect to the midline in two hour time periods (Figure 4.12B).

Results show that mitosis occurring at the neural keel/neural rod periods (10-12hpf) show a preferential oblique orientation (Average degrees±SEM 56±27°, Figure 4.12C,Ci). At these stages sister cells remained on the same side of the neurocoel and are frequently separated in the antero-posterior axis, contributing the axial elongation of the neural rod (Kimmel *et al.*, 1994). However, soon after (12-14hpf), mitoses show a clear preferential orientation perpendicular to the midline, with little variations (Average degrees±SEM 89±16°; Figure 4.12C,Ci). After cytokinesis, these divisions frequently separate sister cells across the forming midline producing a bilaterally symmetrical progeny (Kimmel *et al.*, 1994; Geldmacher-Voss *et al.*, 2003). At neural tube stage (after lumen opening, >16hpf), the mitotic spindle is formed always parallel

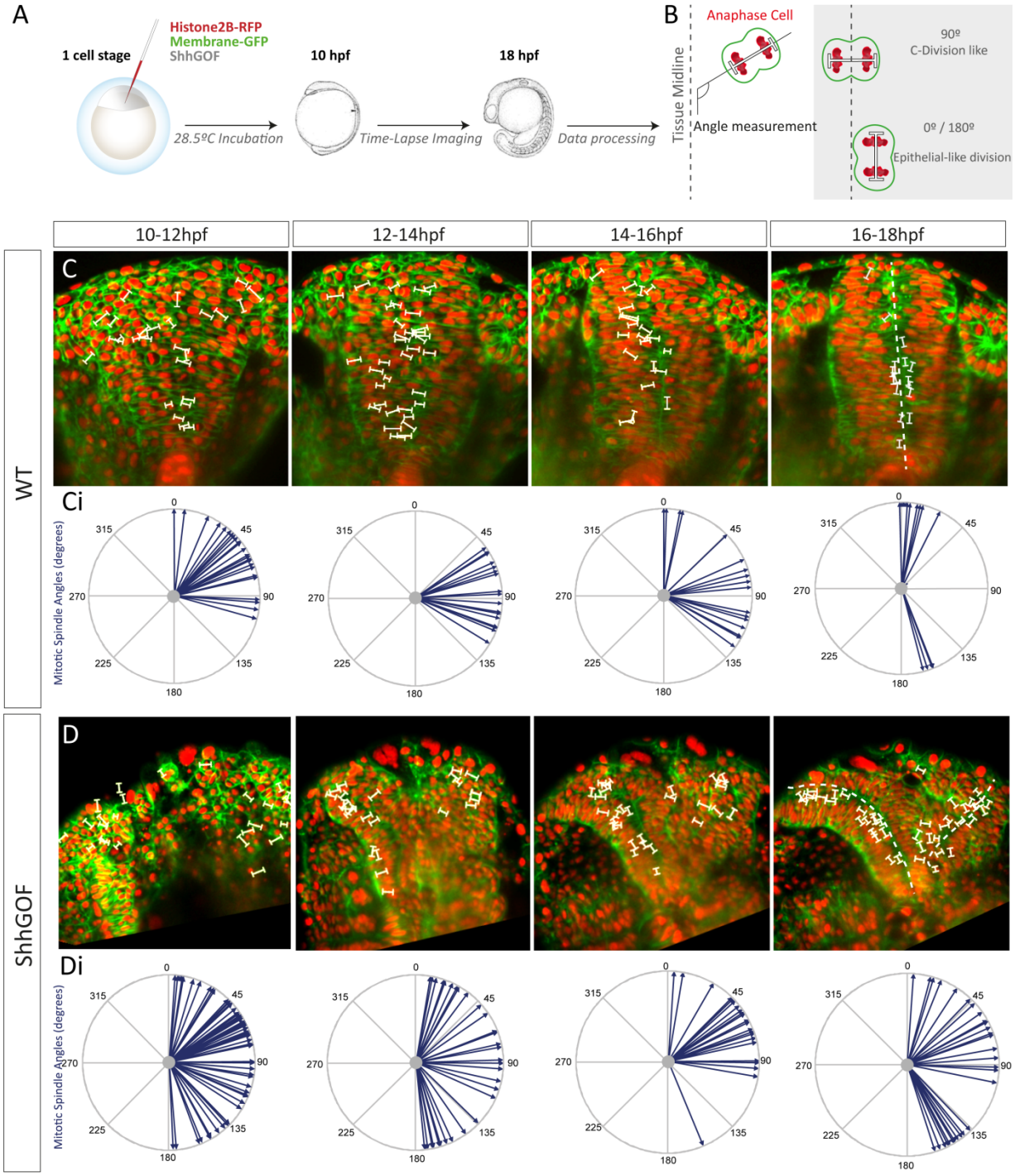
A
1 cell stage
Histone2B-RFP
Membrane-GFP
ShhGOF
10 hpf
18 hpf
28.5ºC Incubation
Time-Lapse Imaging
Data processing
B
Anaphase Cell
Tissue Midline
Angle measurement
90º
C-Division like
0º / 180º
Epithelial-like division
10-12hpf
12-14hpf
14-16hpf
16-18hpf
WT
C
Ci
Mitotic Spindle Angles (degrees)
ShhGOF
D
Di
E
n=25
58±27º
n=35
84±16º
n=21
76±40º
n=11
7±8º
n=4
162±3º
n=36
89±50º
n=33
93±58º
n=24
67±31º
n=15
50±26º
n=14
140±24º

Figure 4.12 - Mitosis orientation is randomized during lumen opening in Shh-GOF embryos
(A) Schematic representation of the experimental design for mitotic spindle orientation analysis. Embryos were injected at 1 cell stage with membrane-GFP (green), Histone2b-RFP (red) and Shh pathway activators. Embryos were incubated at 28.5ºC until reaching 10 hours post fertilization (hpf) and imaged *in vivo* by time-lapse microscopy. (B) Illustration of the angle measurement method. A line was drawn in the prospective tissue midline at each analysed time point. A capped white bar representing the mitotic spindle was drawn in perpendicular to chromosome plates separating at anaphase or telophase. The angle was defined by the prospective midline and the spindle orientation was measured. This method produces measured angle values ranging from 0 to 180º (degrees), being 90º a spindle orientation perpendicular to the midline and 0º or 180º spindle orientations parallel to the midline. A white bar lines the mitotic spindle orientation of all spotted mitosis in the selected z-plane. (C, D) Selected representative snapshots (at the indicated hpf) of a time-lapse imaged WT (C) or Shh-GOF (D) embryo, tagged with membrane-GFP (green) and Histone2B-RFP (red). All the mitotic spindle (white bars) visualized in the 2h interval were projected at the respective snapshot for each category. (Ci, Di) Individual mitotic spindle orientations (blue arrows) were represented in polar graphs for each indicated time window. Numbers indicate the degrees towards the tissue midline. (E) Polar graphs summarizing the predominant mitotic spindle angles in WT (green) and Shh-GOF (red) during the indicated time point. Average mitotic spindle orientation degrees for each time period are represented by a line (WT green, Shh-GOF red), and standard deviations are represented by a faded shade (light green for WT, light red for Shh-GOF). Numbers below each graph represent Average±Standard Deviation.

to the midline (Average degrees±SEM 162±3°, Figure 4.12C,Ci) producing sister cells that always remained on the same side of the neurocoel.

In Shh-GOF mutant embryos we first observed a strikingly high variability in the orientation of mitosis all along NT development, as compared to WT embryos (Figure 4.12). Mitosis occurring at the neural keel/neural rod periods (10-12hpf) showed a preferential oblique orientation, although with a high variability (Average degrees±SEM 89±50°, Figure 12D,Di). This observation was maintained later (12-14hpf), when WT embryos exhibited a clear preferential orientation of mitosis plane perpendicular to the forming midline, Shh-GOF mutant embryos still showed a high variability in the spindle orientation with no preferentially final mitosis orientation (Average degrees±SEM 93±58°, Figure 4.12D,Di). Moreover, at neural tube stage (after lumen opening, >16hpf), the orientation of mitotic spindle in Shh-GOF mutant embryos is still highly variable (Average degrees±SEM 140±24°, Figure 4.12D,Di).

Altogether these analyses indicate that, although the duration of the metaphase in Shh-GOF mutant embryos is similar to that of the WT embryos, the metaphase plate is less active both in total rotated angle and in rotations per minute. We propose that this prevents the organization of a spindle perpendicular to the midline and

randomizes mitotic spindle orientation. However sister cells are still separated towards the two sides of the forming NT, ectopic lumens open in Shh-GOF mutant embryos.

5. DISCUSSION

5. DISCUSSION

In this work we show that Sonic Hedgehog (Shh) activity is required for the formation of a single central lumen in the developing zebrafish spinal cord. Cyclopamine-dependent decrease of Shh activity leads to lumen disruption, producing multiple small lumens with proper apical polarization. On the other hand, excess of Sonic Hedgehog activity leads to neural tube duplication associated to delayed convergence to the midline and disturbed mitotic spindle orientation. The phenotype produced by Shh activity is not correlated with changes in cell motion properties (speed or persistency) during neurulation or to disruption of apicobasal polarity, but rather on delayed convergence, regulation of the mitotic process and the subsequent mitotic spindle orientation.

5.1 MOTION PROPERTIES OF NEUROEPITHELIAL CELLS ARE INDEPENDENT OF SHH-SIGNALLING

The process of convergence comprises the set of cellular movements that narrow the embryonic germ layers along the antero-posterior axis during gastrulation and formation of the spinal cord. Our results show that convergence movements are not abolished after increase of Shh activity, however at the neurulation onset the neural plate/keel is wider. Diverse mechanisms could drive this initial defect - such as increased cell density or delayed convergence movements, among others- however since our experimental time window missed the earlier time points, we cannot conclude defects in the preceding convergence movements.

The notochord has been previously described as a regulator of neural plate convergence cell movements through the polarization of protrusive activity and cell oriented movement in *Xenopus* embryos (Ezin *et al.*, 2003). However, most efforts in the last decade have focused on characterizing convergent defective Planar Cell Polarity (PCP) pathway mutants, that show affected cell migration velocities (Roszko *et*

al., 2015). In our analysis of individual cell movements we observed that Shh-GOF cells do not show different motile properties such as velocity or persistency, compared to WT behaviour. Our results show that during the period of neurulation, regulation of cell motility was not the major cause of morphogenetic defects derived from Shh activity.

Because primary cilia recruit all components of the Shh-signalling pathway serving as a Shh "antenna", we also followed cilia trajectories in Shh-GOF mutants. In these analyses of cilia trajectories we glimpsed a differential movement: at the time when WT embryos are still undergoing anteriorward movements (13hpf), Shh-GOF are already trending towards the medial midline.

A feature of convergent defective PCP mutants is that they fail to position their motile floor plate cilia and MTOCs at the posterior end of the cell, once cells have elongated mediolaterally (Borovina *et al.*, 2010; Sepich *et al.*, 2011). It is interesting to point the shared localization of Shh and PCP pathway components at the cilia, and regulation of common mechanisms controlling convergence could be possible.

5.2 ESTABLISHMENT OF APICO-BASAL POLARITY IS INDEPENDENT ON SHH-SIGNALLING

A continuous basal lamina underlies the neuroectoderm by the end of gastrulation (Latimer and Jessen, 2010), while apical polarity only becomes evident at later neurulation stages (Hong and Brewster, 2006; Tawk *et al.*, 2007).

In the neural keel and rod, it has been shown that apical cell polarization starts with the centrosome localisation at the tissue midline (Buckley *et al.*, 2013), suggesting a role for the centrosome and/or the cilium in the organization of the apical junctional complex. We cannot discard a possible influence of Shh ciliary reception as a cue for centrosomal (cilium base) localization prior to cell division, given that the tissue apical polarity midline is misplaced in both Shh-GOF and Shh-LOF conditions.

However, our analysis showed that changes in Shh activity levels do not affect the

intrinsic capability of cells to polarize; both Shh-GOF and Shh-LOF conditions show cells polarized apico-basally; We observe a Laminin1-stained basal lamina lining the perimeter of the neural tube, and the apical marker ZO-1 at the duplicated lumens in Shh-GOF and the disrupted lumens in Shh-LOF. This might reflect that albeit polarization takes place at the wrong place, the mechanisms for cells to establish apico-basal polarization are robust and cell autonomous. This has been shown in small groups of cells such as MDCK cysts (Martin-Belmonte *et al.*, 2008) or zebrafish neural explants in a yolk (Girdler *et al.*, 2013): in both cases cells are able to polarize in absence of surrounding environmental signals.

5. 3 SHH DECREASES METAPHASE ROTATIONS IN C-DIVISIONS AND ALTER THEIR MITOTIC SPINDLE ORIENTATION

C-Divisions localize apical polarity components at their cytokinetic furrow and originate a bilateral progeny across the neural tube, at each side of the midline (Ciruna *et al.*, 2006; Tawk *et al.*, 2007). Therefore, the formation of the tissue midline (and prospective lumen) strongly relies on the orientation of C-Divisions (Tawk *et al.*, 2007; Quesada-Hernandez *et al.*, 2010; Zigman *et al.*, 2011).

In this study we analysed the mitotic behaviour in terms of length of the different phases, rotations of the metaphase plate, final orientation of the mitotic spindle and localization of the daughter cells.

We first observed that mitoses are gradually longer in WT embryos as development proceeds. This is coherent with the lengthening of the whole cell cycle along development (Kimmel *et al.*, 1994). However, mitoses in Shh-GOF embryos are shorter than in the WT condition, resulting in the observed increase in mitotic index and tissue overgrowth in Shh-GOF mutant embryos. Remarkably, divisions do not appear to lengthen gradually in Shh-GOF embryos, instead we observe a sudden increase in mitosis duration after 16hpf, coinciding with the time at which majority of crossing divisions are occurring.

In order to position the tissue midline C-Divisions need to properly orient their

metaphase plate, and a set of movements precedes the metaphase final orientation. Despite of the shortening of the time from condensation to anaphase, the duration of the metaphase is not decreased in Shh-GOF cells.

In the zebrafish neurula it is essential that C-Divisions follow stereotyped orthogonal orientations in order to position a central midline, and this orientation relies on various signals, including ciliary proteins such as ift88, and proteins implied in cell-cell adhesion, such as N-Cadherin and Scribble (Zigman *et al.*, 2011). Shh-GOF cells are able to undergo C-Divisions, however their metaphase plate rotates fewer degrees, indicating that Shh signalling could influence cell intrinsic cues controlling C-Division orientation and mislead the final plane of division. The morphogenetic consequence of a wrong plane of division would be an ectopic midline formation.

After midline establishment, however, planar divisions tend to align around the duplicated apical surfaces in Shh-GOF embryos, suggesting that intrinsic mechanisms of mitotic spindle alignment function properly once apicobasal polarity is well structured. This could be due to the cooperation between intrinsic mechanisms of spindle orientation (LGN-NuMA) and apical polarity(Par3)(Lechler and Fuchs, 2005).

The fact that early divisions show randomised mitotic orientation while later divisions align to the midline suggests Shh-dependent control of spindle orientation mechanisms independent on apical polarity. These could be, for example, by driving cell shape changes (explained in section 5.5), cell adhesion components or centrosomal proteins directly controlling the mitotic spindle. Another option would be that mitoses align towards the underlying basal lamina instead of the tissue midline, given that non-polarized cells can orient their mitotic spindles through integrin-mediated cell adhesion and actin remodelling (Toyoshima and Nishida, 2007).

What could then underlie differential mitosis features in Shh-GOF?

In Shh-GOF embryos we have observed that apical cilia change their features by increasing their length. It has been previously described that dnPKA-mediated

activation of Shh pathway induces long motile cilia along the entire dorso-ventral axis (Yu *et al.*, 2008). However whether this could be associated to defective mitotic spindle orientation is not known.

Could ciliary and basal body Shh components be inherited by the centrosome and exert effects on mitosis orientation? It has long been assumed that the primary cilia were completely disassembled prior to mitosis. However a recent report showed that, in the developing mouse neocortex, a portion of the ciliary membrane remains attached to the mother centriole nucleating the mitotic spindle pole (Paridaen *et al.*, 2013). Intriguingly, in the chick developing neural tube PKA localizes to the centrosomes throughout the entire mitosis, appearing particularly accumulated at the spindle poles during metaphase (unpublished observations by Dr. Murielle Saade). This suggests a likely role of Shh in control of the metaphase plate orientation. Other ciliary proteins, such as Ift88, have been implied in control of cell division orientation at gastrulation and neurulation (Borovina and Ciruna, 2013). Additionally, a complex vesicle trafficking network is located between the cilia and the spindle poles. Rab11 is a GTPase that mediates cilia formation through the transport of other Rab molecules towards the centrosomes (Westlake *et al.*, 2011). Decrease of Rab11 activity produces defects in primary cilium and Shh signalling impairment (Franco *et al.*, 2014). During mitosis, Rab11 localizes to the mitotic spindle poles regulating dynein dependent endosome localization, and impairment of Rab11 function disrupts astral microtubules and delays mitosis, resulting in misorientation of the plane of division (Hehnly and Doxsey, 2014).

We propose that localization of ciliary proteins to the centrosome, such as Shh pathway components (PKA) or molecules involved in vesicle trafficking (Rab11), could underlie Shh-dependent control of metaphase rotations and mitotic spindle orientation

5.4 UNCOVERING THE MOLECULAR MECHANISMS UNDERLYING SINGLE LUMEN FORMATION

The coordination of cell polarization and cell division leads to the formation of a

midline that precedes lumen formation. Abnormal formation of the midline will subsequently give rise to ectopic lumens (Tawk *et al.*, 2007). The particular mechanisms by which the neural tube lumen is opened are not yet well known, however Rab11 GTPase has been shown to be essential for zebrafish lumen opening (Buckley *et al.*, 2013)

Which are the Shh-dependent affected processes that interfere with single lumen formation in Shh-LOF embryos? The developing zebrafish gut is formed by hollowing -i.e. implying trafficking of polarity components-. In this case multiple lumens are initially formed, and after opening and enlarging result in two lumens that do not share a continuous apical surface and are separated by basolateral contacts. The fusion of the two lumens into a single requires remodelling of contacts between adjacent lumens, a process that is impaired in *smoothened (smo)* mutants due to the perturbations in the Rab11 trafficking pathway (Alvers *et al.*, 2014). Interestingly, in the zebrafish neural tube Rab11 is not required for apical polarity localization but it is essential for lumen opening (Buckley *et al.*, 2013), which opens above the floorplate and extends dorsally as small lumens coalesce along the midline in the zebrafish brain (Lowery and Sive, 2005). A functional interaction between Rab11 and the Shh pathway has been also described in the developing zebrafish retina, in which Rab11 family interacting protein 4 (Rab11-FIP4) interacts with Shh signalling to regulate cell cycle exit (Muto *et al.*, 2006).

Interestingly, multiple lumens in Shh-LOF embryos are reminiscent to those happening in the secondary neurulation of the chick embryo. At the time when secondary neurulation lumen formation occurs Shh expression is mild or absent, however at the time of lumen coalescence Shh is highly expressed in the forming notochord (unpublished observations from Elena González-Gobartt). This highlights the possibility of Shh-mediated lumen coalescence that would entail the formation of a single continuous lumen.

Function of Rab11 in lumen opening, in addition to its roles in cilia formation and

mitosis orientation make it an interesting candidate to be analysed. It will be therefore interesting to analyse the localization and function of Rab11 in both Shh-GOF and Shh-LOF.The possibility of Shh-dependent regulation of Rab11 trafficking is an exciting option that could explain a link between defective spindle orientation and a continuous luminal surface formation. We conclude that a possible mechanism for lumen formation is the regulation of Rab11 by the Shh pathway, and disturbing Shh signalling would therefore lead to the formation of disrupted multiple lumens.

5.5 HOW COULD SHH INFLUENCE THE MECHANICAL PROPERTIES OF THE TISSUE?

The formation of a single central lumen is affected when we modulate Shh activity levels. Lumen formation encompasses the coordination of many interrelated processes: localization of apical polarity components in the midline, interdigitation, C-divisions and lumen opening.

At the cellular level, we propose that Shh influences metaphase rotation and mitotic spindle orientation, both mechanisms that strongly influence on the formation midline. An additional perspective would be to approach the analysis of the characteristics of the whole tissue, instead of single cells. As novel views provided by tissue biomechanics emerge, it seems more likely to embed all these processes under common physical regulators.

Mechanical cues have been shown to regulate mitotic spindle orientation; therefore altered mechanical properties of the tissue could be causative of the Shh-GOF phenotype.

How could Shh influence the mechanical properties of the tissue? A precise link has been demonstrated between Shh-secreting notochord closeness and extracellular matrix (ECM) deposition in the zebrafish Kuppfer's Vesicle, the zebrafish laterality organ composed by motile cilia -alike the neural tube floorplate- and structured around a lumen. ECM deposition is localized in the regions adjacent to the notochord,

leading to restriction in apical expansion and cell shape changes (Compagnon *et al.*, 2014). Cell geometry is possibly affected in our model and could underlie the deviated mitotic spindle orientation that precedes morphogenetic neural tube defects (Minc *et al.*, 2011; Campinho *et al.*, 2013; Lancaster and Baum, 2014; Xiong *et al.*, 2014).

Mitosis location, timing and spindle orientation are strongly correlated with tissue structure along neural tube development. The broader Shh-GOF neural tissue might have altered mechanical properties, such as cell confinement in the central region. Cell confinement has been shown to decrease actin contractility and drive the apical centrosome positioning in MDCK cysts (Rodriguez-Fraticelli *et al.*, 2012). Regulation of the cortical actin network through external forces has been shown to modulate spindle orientation (Fink *et al.*, 2011).

There are then two main possibilities on how Shh activation influences mitotic spindle orientation:

- Cell autonomous mechanisms: such as changes in the intrinsic mitotic machinery driven by centrosome of trafficking proteins. Mosaic analysis of Shh-GOF cells in a WT surrounding tissue would elucidate this option.
- Context dependent mechanisms: such as biomechanical constraints that affect cell geometry.

Analysing the behaviour during mitosis with mechanosensing reporters or actin/myosin fluorescent-tagged proteins could help to resolve these questions.
An approach to define the biomechanical properties of the tissue would the Particle Image Velocimetry analysis (PIV), a method that enables the measurements of a velocity field in one plane, and can highlight regions in the tissue with differential mechanical properties. Analysis of the cellular geometry and PIV analysis combined with functional experiments of laser ablation, will help to understand the biophysical network embedding neural tube formation in WT embryos and when Shh activity is experimentally disturbed.

5. 6 FUTURE DIRECTIONS

Shh-GOF mutations underlie a range of caudal NTDs, including spina bifida in humans. We have seen that activation of Shh pathway leads to lumen duplication, while loss of Shh activity leads to a discontinuous lumen, remarking the importance of this signalling pathway in formation of a single central lumen. The effects of Shh are associated to changes in mitosis behaviour.

I propose the analysis of possible molecular effectors that can link the affected processes in both Shh-GOF and Shh-LOF with mitosis orientation and lumen formation, these are:

-Analysis of Rab11 location during mitosis and lumen opening

-Analysis of cell shape, microtubules and acto-myosin cytoskeleton during neural tube formation, and particularly on how it affects mitosis orientation.

- Analysis of tissue biomechanics analysis by applying Particle Image Velocimetry (PIV), in combination with laser ablation.

6. CONCLUSIONS

-CONCLUSIONS-

1- Sonic Hedgehog (Shh) is expressed during zebrafish neurulation in midline signalling centres

2.- Shh signalling is required for lumen positioning and complete lumen fusion.

3.- Shh signalling is sufficient to alter lumen positioning and to duplicate NT lumen.

4.- Shh signalling is dispensable for the apico-basal polarization of neural progenitors.

5.- Shh signalling is sufficient to generate wider neural plates and to delay tissue convergence.

6.- Individual cell movements are independent on Shh activity as analysed by a) tracking primary cilia, b) tracking cells committed to C-divisions, c) tracking cells accompanying those committed to C-divisions.

7.- Increase of Shh activity results in the expected tissue overgrowth mediated by shorter cell cycle and mitosis.

8- Increase of Shh activity shortens the time required to transit from condensation to anaphase while slightly lengthened metaphase duration.

9.- Increase of Shh activity compromises the capacity of metaphase plate to rotate prior to the final orientation of the division plane.

10- Cells with increased Shh activity are capable to perform midline-crossing divisions but with different preferential division planes, a feature that might result in ectopic lumen opening.

7. BIBLIOGRAPHY

Selected references

Alvarez-Medina, R., G. Le Dreau, M. Ros and E. Marti (2009). "Hedgehog activation is required upstream of Wnt signalling to control neural progenitor proliferation." Development**136**(19): 3301-3309.

Alvers, A. L., S. Ryan, P. J. Scherz, J. Huisken and M. Bagnat (2014). "Single continuous lumen formation in the zebrafish gut is mediated by smoothened-dependent tissue remodeling." Development**141**(5): 1110-1119.

Amorim, M. R., M. A. Lima, E. E. Castilla and I. M. Orioli (2007). "Non-Latin European descent could be a requirement for association of NTDs and MTHFR variant 677C > T: a meta-analysis." Am J Med Genet A**143A**(15): 1726-1732.

Andrew, D. J. and A. J. Ewald (2010). "Morphogenesis of epithelial tubes: Insights into tube formation, elongation, and elaboration." Dev Biol**341**(1): 34-55.

Ang, S. L. and J. Rossant (1994). "HNF-3 beta is essential for node and notochord formation in mouse development." Cell**78**(4): 561-574.

Araya, C., M. Tawk, G. C. Girdler, M. Costa, C. Carmona-Fontaine and J. D. Clarke (2014). "Mesoderm is required for coordinated cell movements within zebrafish neural plate in vivo." Neural Dev**9**: 9.

Avaron, F., L. Hoffman, D. Guay and M. A. Akimenko (2006). "Characterization of two new zebrafish members of the hedgehog family: atypical expression of a zebrafish indian hedgehog gene in skeletal elements of both endochondral and dermal origins." Dev Dyn**235**(2): 478-489.

Bagnat, M., I. D. Cheung, K. E. Mostov and D. Y. Stainier (2007). "Genetic control of single lumen formation in the zebrafish gut." Nat Cell Biol**9**(8): 954-960.

Bale, A. E. and K. P. Yu (2001). "The hedgehog pathway and basal cell carcinomas." Hum Mol Genet**10**(7): 757-762.

Barth, K. A. and S. W. Wilson (1995). "Expression of zebrafish nk2.2 is influenced by sonic hedgehog/vertebrate hedgehog-1 and demarcates a zone of neuronal differentiation in the embryonic forebrain." Development**121**(6): 1755-1768.

Barzi, M., J. Berenguer, A. Menendez, R. Alvarez-Rodriguez and S. Pons (2010). "Sonic-hedgehog-mediated proliferation requires the localization of PKA to the cilium base." J Cell Sci**123**(Pt 1): 62-69.

Berbari, N. F., A. K. O'Connor, C. J. Haycraft and B. K. Yoder (2009). "The primary cilium as a complex signaling center." Curr Biol**19**(13): R526-535.

Bonnafe, E., M. Touka, A. AitLounis, D. Baas, E. Barras, C. Ucla, A. Moreau, F. Flamant, R. Dubruille, P. Couble, J. Collignon, B. Durand and W. Reith (2004). "The transcription factor RFX3 directs nodal cilium development and left-right asymmetry specification." Mol Cell Biol**24**(10): 4417-4427.

Bornens, M. (2012). "The centrosome in cells and organisms." Science**335**(6067): 422-426.

Borovina, A. and B. Ciruna (2013). "IFT88 plays a cilia- and PCP-independent role in controlling oriented cell divisions during vertebrate embryonic development." Cell Rep**5**(1): 37-43.

Borovina, A., S. Superina, D. Voskas and B. Ciruna (2010). "Vangl2 directs the posterior tilting and asymmetric localization of motile primary cilia." Nat Cell Biol**12**(4): 407-412.

Buckley, C. E., X. Ren, L. C. Ward, G. C. Girdler, C. Araya, M. J. Green, B. S. Clark, B. A. Link and J. D. Clarke (2013). "Mirror-symmetric microtubule assembly and cell interactions drive lumen formation in the zebrafish neural rod." EMBO J**32**(1): 30-44.

Burren, K. A., D. Savery, V. Massa, R. M. Kok, J. M. Scott, H. J. Blom, A. J. Copp and N. D. Greene (2008). "Gene-environment interactions in the causation of neural tube defects: folate deficiency increases susceptibility conferred by loss of Pax3 function." Hum Mol Genet**17**(23): 3675-3685.

Campinho, P., M. Behrndt, J. Ranft, T. Risler, N. Minc and C. P. Heisenberg (2013). "Tension-oriented cell divisions limit anisotropic tissue tension in epithelial spreading during zebrafish epiboly." Nat Cell Biol**15**(12): 1405-1414.

Cao, Y., A. Park and Z. Sun (2010). "Intraflagellar transport proteins are essential for cilia formation and for planar cell polarity." J Am Soc Nephrol**21**(8): 1326-1333.

Carroll, E. A., D. Gerrelli, S. Gasca, E. Berg, D. R. Beier, A. J. Copp and J. Klingensmith (2003). "Cordon-bleu is a conserved gene involved in neural tube formation." Dev Biol**262**(1): 16-31.

Caspary, T., C. E. Larkins and K. V. Anderson (2007). "The graded response to Sonic Hedgehog depends on cilia architecture." Dev Cell**12**(5): 767-778.

Catala, M., M. A. Teillet, E. M. De Robertis and M. L. Le Douarin (1996). "A spinal cord fate map in the avian embryo: while regressing, Hensen's node lays down the notochord and floor plate thus joining the spinal cord lateral walls." Development**122**(9): 2599-2610.

Catala, M., M. A. Teillet and N. M. Le Douarin (1995). "Organization and development of the tail bud analyzed with the quail-chick chimaera system." Mech Dev**51**(1): 51-65.

Cayuso, J., F. Ulloa, B. Cox, J. Briscoe and E. Marti (2006). "The Sonic hedgehog pathway independently controls the patterning, proliferation and survival of neuroepithelial cells by regulating Gli activity." Development**133**(3): 517-528.

Chen, M. H., C. W. Wilson, Y. J. Li, K. K. Law, C. S. Lu, R. Gacayan, X. Zhang, C. C. Hui and P. T. Chuang (2009). "Cilium-independent regulation of Gli protein function by Sufu in Hedgehog signaling is evolutionarily conserved." Genes Dev**23**(16): 1910-1928.

Chiang, C., Y. Litingtung, E. Lee, K. E. Young, J. L. Corden, H. Westphal and P. A. Beachy (1996). "Cyclopia and defective axial patterning in mice lacking Sonic hedgehog gene function." Nature**383**(6599): 407-413.

Ciruna, B., A. Jenny, D. Lee, M. Mlodzik and A. F. Schier (2006). "Planar cell polarity signalling couples cell division and morphogenesis during neurulation." Nature**439**(7073): 220-224.

Clarke, J. (2009). "Role of polarized cell divisions in zebrafish neural tube formation." Curr Opin Neurobiol**19**(2): 134-138.

Colas, J.-F. and G. C. Schoenwolf (2001). "Towards a cellular and molecular understanding of neurulation." Developmental Dynamics**221**(2): 117-145.

Compagnon, J., V. Barone, S. Rajshekar, R. Kottmeier, K. Pranjic-Ferscha, M. Behrndt and C. P. Heisenberg (2014). "The notochord breaks bilateral symmetry by controlling cell shapes in the zebrafish laterality organ." Dev Cell**31**(6): 774-783.

Compagnon, J. and C. P. Heisenberg (2013). "Neurulation: coordinating cell polarisation and lumen formation." EMBO J**32**(1): 1-3.

Concha, M. L. and R. J. Adams (1998). "Oriented cell divisions and cellular morphogenesis in the zebrafish gastrula and neurula: a time-lapse analysis." Development**125**(6): 983-994.

Copp, A. J. (2005). "Neurulation in the cranial region--normal and abnormal." J Anat**207**(5): 623-635.

Copp, A. J., I. Checiu and J. N. Henson (1994). "Developmental basis of severe neural tube defects in the loop-tail (Lp) mutant mouse: use of microsatellite DNA markers to identify embryonic genotype." Dev Biol**165**(1): 20-29.

Copp, A. J. and N. D. Greene (2010). "Genetics and development of neural tube defects." J Pathol**220**(2): 217-230.

Copp, A. J. and N. D. Greene (2013a). "Neural tube defects--disorders of neurulation and related embryonic processes." Wiley Interdiscip Rev Dev Biol**2**(2): 213-227.

Copp, A. J. and N. D. E. Greene (2013b). "Neural tube defects—disorders of neurulation and related embryonic processes." Wiley Interdisciplinary Reviews: Developmental Biology**2**(2): 213-227.

Corbit, K. C., P. Aanstad, V. Singla, A. R. Norman, D. Y. Stainier and J. F. Reiter (2005). "Vertebrate Smoothened functions at the primary cilium." Nature**437**(7061): 1018-1021.

Cortellino, S., C. Wang, B. Wang, M. R. Bassi, E. Caretti, D. Champeval, A. Calmont, M. Jarnik, J. Burch, K. S. Zaret, L. Larue and A. Bellacosa (2009). "Defective ciliogenesis, embryonic lethality and severe impairment of the Sonic Hedgehog pathway caused by inactivation of the mouse complex A intraflagellar transport gene Ift122/Wdr10, partially overlapping with the DNA repair gene Med1/Mbd4." Dev Biol**325**(1): 225-237.

Creasy, M. R. and E. D. Alberman (1976). "Congenital malformations of the central nervous system in spontaneous abortions." J Med Genet**13**(1): 9-16.

Criley, B. B. (1969). "Analysis of embryonic sources and mechanims of development of posterior levels of chick neural tubes." J Morphol**128**(4): 465-501.

Cruz, C., V. Ribes, E. Kutejova, J. Cayuso, V. Lawson, D. Norris, J. Stevens, M. Davey, K. Blight, F. Bangs, A. Mynett, E. Hirst, R. Chung, N. Balaskas, S. L. Brody, E. Marti and J. Briscoe (2010). "Foxj1 regulates floor plate cilia architecture and modifies the response of cells to sonic hedgehog signalling." Development**137**(24): 4271-4282.

Currie, P. D. and P. W. Ingham (1996). "Induction of a specific muscle cell type by a hedgehog-like protein in zebrafish." Nature**382**(6590): 452-455.

Curtin, J. A., E. Quint, V. Tsipouri, R. M. Arkell, B. Cattanach, A. J. Copp, D. J. Henderson, N. Spurr, P. Stanier, E. M. Fisher, P. M. Nolan, K. P. Steel, S. D. Brown, I. C. Gray and J. N. Murdoch (2003). "Mutation of Celsr1 disrupts planar polarity of inner ear hair cells and causes severe neural tube defects in the mouse." Curr Biol**13**(13): 1129-1133.

Davidson, L. A. and R. E. Keller (1999). "Neural tube closure in Xenopus laevis involves medial migration, directed protrusive activity, cell intercalation and convergent extension." Development**126**(20): 4547-4556.

Dohn, M. R., N. A. Mundell, L. M. Sawyer, J. A. Dunlap and J. R. Jessen (2013). "Planar cell polarity proteins differentially regulate extracellular matrix organization and assembly during zebrafish gastrulation." Dev Biol**383**(1): 39-51.

Dolk, H., M. Loane and E. Garne (2010). "The prevalence of congenital anomalies in Europe." Adv Exp Med Biol**686**: 349-364.

Downs, K. M. (2009). "The enigmatic primitive streak: prevailing notions and challenges concerning the body axis of mammals." Bioessays**31**(8): 892-902.

Duband, J. L. (2010). "Diversity in the molecular and cellular strategies of epithelium-to-mesenchyme transitions: Insights from the neural crest." Cell Adh Migr**4**(3): 458-482.

Dzamba, B. J., K. R. Jakab, M. Marsden, M. A. Schwartz and D. W. DeSimone (2009). "Cadherin adhesion, tissue tension, and noncanonical Wnt signaling regulate fibronectin matrix organization." Dev Cell**16**(3): 421-432.

Echelard, Y., D. J. Epstein, B. St-Jacques, L. Shen, J. Mohler, J. A. McMahon and A. P. McMahon (1993). "Sonic hedgehog, a member of a family of putative signaling molecules, is implicated in the regulation of CNS polarity." Cell**75**(7): 1417-1430.

Ekker, S. C., A. R. Ungar, P. Greenstein, D. P. von Kessler, J. A. Porter, R. T. Moon and P. A. Beachy (1995). "Patterning activities of vertebrate hedgehog proteins in the developing eye and brain." Curr Biol**5**(8): 944-955.

Epstein, D. J., E. Marti, M. P. Scott and A. P. McMahon (1996). "Antagonizing cAMP-dependent protein kinase A in the dorsal CNS activates a conserved Sonic hedgehog signaling pathway." Development**122**(9): 2885-2894.

Ericson, J., P. Rashbass, A. Schedl, S. Brenner-Morton, A. Kawakami, V. van Heyningen, T. M. Jessell and J. Briscoe (1997). "Pax6 controls progenitor cell identity and neuronal fate in response to graded Shh signaling." Cell**90**(1): 169-180.

Ezin, A. M., P. Skoglund and R. Keller (2003). "The midline (notochord and notoplate) patterns the cell motility underlying convergence and extension of the Xenopus neural plate." Dev Biol**256**(1): 100-114.

Fink, J., N. Carpi, T. Betz, A. Betard, M. Chebah, A. Azioune, M. Bornens, C. Sykes, L. Fetler, D. Cuvelier and M. Piel (2011). "External forces control mitotic spindle positioning." Nat Cell Biol**13**(7): 771-778.

Franco, I., F. Gulluni, C. C. Campa, C. Costa, J. P. Margaria, E. Ciraolo, M. Martini, D. Monteyne, E. De Luca, G. Germena, Y. Posor, T. Maffucci, S. Marengo, V. Haucke, M. Falasca, D. Perez-Morga, A. Boletta, G. R. Merlo and E. Hirsch (2014). "PI3K class II alpha controls spatially restricted endosomal PtdIns3P and Rab11 activation to promote primary cilium function." Dev Cell**28**(6): 647-658.

Garcia-Gonzalo, F. R. and J. F. Reiter (2012). "Scoring a backstage pass: mechanisms of ciliogenesis and ciliary access." J Cell Biol**197**(6): 697-709.

Geldmacher-Voss, B., A. M. Reugels, S. Pauls and J. A. Campos-Ortega (2003). "A 90-degree rotation of the mitotic spindle changes the orientation of mitoses of zebrafish neuroepithelial cells." Development**130**(16): 3767-3780.

Girdler, G. C., C. Araya, X. Ren and J. D. Clarke (2013). "Developmental time rather than local environment regulates the schedule of epithelial polarization in the zebrafish neural rod." Neural Dev**8**: 5.

Gong, Y., C. Mo and S. E. Fraser (2004). "Planar cell polarity signalling controls cell division orientation during zebrafish gastrulation." Nature**430**(7000): 689-693.

Gray, R. S., I. Roszko and L. Solnica-Krezel (2011). "Planar cell polarity: coordinating morphogenetic cell behaviors with embryonic polarity." Dev Cell**21**(1): 120-133.

Greene, N. D. and A. J. Copp (2014). "Neural tube defects." Annu Rev Neurosci**37**: 221-242.

Greene, N. D., D. Gerrelli, H. W. Van Straaten and A. J. Copp (1998). "Abnormalities of floor plate, notochord and somite differentiation in the loop-tail (Lp) mouse: a model of severe neural tube defects." Mech Dev**73**(1): 59-72.

Greene, N. D., P. Stanier and A. J. Copp (2009). "Genetics of human neural tube defects." Hum Mol Genet**18**(R2): R113-129.

Griffith, C. M., M. J. Wiley and E. J. Sanders (1992). "The vertebrate tail bud: three germ layers from one tissue." Anat Embryol (Berl)**185**(2): 101-113.

Haigo, S. L., J. D. Hildebrand, R. M. Harland and J. B. Wallingford (2003). "Shroom induces apical constriction and is required for hingepoint formation during neural tube closure." Curr Biol**13**(24): 2125-2137.

Hammerschmidt, M., M. J. Bitgood and A. P. McMahon (1996). "Protein kinase A is a common negative regulator of Hedgehog signaling in the vertebrate embryo." Genes Dev**10**(6): 647-658.

Harrington, M. J., K. Chalasani and R. Brewster (2010). "Cellular mechanisms of posterior neural tube morphogenesis in the zebrafish." Dev Dyn**239**(3): 747-762.

Harris, M. J. and D. M. Juriloff (2010). "An update to the list of mouse mutants with neural tube closure defects and advances toward a complete genetic perspective of neural tube closure." Birth Defects Res A Clin Mol Teratol**88**(8): 653-669.

Haycraft, C. J., B. Banizs, Y. Aydin-Son, Q. Zhang, E. J. Michaud and B. K. Yoder (2005). "Gli2 and Gli3 localize to cilia and require the intraflagellar transport protein polaris for processing and function." PLoS Genet**1**(4): e53.

Hehnly, H. and S. Doxsey (2014). "Rab11 endosomes contribute to mitotic spindle organization and orientation." Dev Cell**28**(5): 497-507.

Heisenberg, C. P., M. Tada, G. J. Rauch, L. Saude, M. L. Concha, R. Geisler, D. L. Stemple, J. C. Smith and S. W. Wilson (2000). "Silberblick/Wnt11 mediates convergent extension movements during zebrafish gastrulation." Nature**405**(6782): 76-81.

Hong, E. and R. Brewster (2006). "N-cadherin is required for the polarized cell behaviors that drive neurulation in the zebrafish." Development**133**(19): 3895-3905.

Hong, E., P. Jayachandran and R. Brewster (2010). "The polarity protein Pard3 is required for centrosome positioning during neurulation." Dev Biol**341**(2): 335-345.

Horne-Badovinac, S. and E. Munro (2011). "Developmental biology. Tubular transformations." Science**333**(6040): 294-295.

Houde, C., R. J. Dickinson, V. M. Houtzager, R. Cullum, R. Montpetit, M. Metzler, E. M. Simpson, S. Roy, M. R. Hayden, P. A. Hoodless and D. W. Nicholson (2006). "Hippi is essential for node cilia assembly and Sonic hedgehog signaling." Dev Biol**300**(2): 523-533.

Huang, P. and A. F. Schier (2009). "Dampened Hedgehog signaling but normal Wnt signaling in zebrafish without cilia." Development**136**(18): 3089-3098.

Huangfu, D. and K. V. Anderson (2005). "Cilia and Hedgehog responsiveness in the mouse." Proc Natl Acad Sci U S A**102**(32): 11325-11330.

Huangfu, D., A. Liu, A. S. Rakeman, N. S. Murcia, L. Niswander and K. V. Anderson (2003). "Hedgehog signalling in the mouse requires intraflagellar transport proteins." Nature**426**(6962): 83-87.

Humke, E. W., K. V. Dorn, L. Milenkovic, M. P. Scott and R. Rohatgi (2010). "The output of Hedgehog signaling is controlled by the dynamic association between Suppressor of Fused and the Gli proteins." Genes Dev**24**(7): 670-682.

Ingham, P. W. (1998). "The patched gene in development and cancer." Curr Opin Genet Dev**8**(1): 88-94.

Ingham, P. W. and A. P. McMahon (2001). "Hedgehog signaling in animal development: paradigms and principles." Genes Dev**15**(23): 3059-3087.

Iruela-Arispe, M. L. and G. J. Beitel (2013). "Tubulogenesis." Development**140**(14): 2851-2855.

Jaffe, A. B., N. Kaji, J. Durgan and A. Hall (2008). "Cdc42 controls spindle orientation to position the apical surface during epithelial morphogenesis." J Cell Biol**183**(4): 625-633.

Jessell, T. M. (2000). "Neuronal specification in the spinal cord: inductive signals and transcriptional codes." Nat Rev Genet**1**(1): 20-29.

Jessell, T. M. and J. R. Sanes (2000). "Development. The decade of the developing brain." Curr Opin Neurobiol**10**(5): 599-611.

Jessen, J. R., J. Topczewski, S. Bingham, D. S. Sepich, F. Marlow, A. Chandrasekhar and L. Solnica-Krezel (2002). "Zebrafish trilobite identifies new roles for Strabismus in gastrulation and neuronal movements." Nat Cell Biol**4**(8): 610-615.

Jia, J., A. Kolterud, H. Zeng, A. Hoover, S. Teglund, R. Toftgard and A. Liu (2009). "Suppressor of Fused inhibits mammalian Hedgehog signaling in the absence of cilia." Dev Biol**330**(2): 452-460.

Johnson, R. L., E. Laufer, R. D. Riddle and C. Tabin (1994). "Ectopic expression of Sonic hedgehog alters dorsal-ventral patterning of somites." Cell**79**(7): 1165-1173.

Jones, C., V. C. Roper, I. Foucher, D. Qian, B. Banizs, C. Petit, B. K. Yoder and P. Chen (2008). "Ciliary proteins link basal body polarization to planar cell polarity regulation." Nat Genet**40**(1): 69-77.

Kaltschmidt, J. A., C. M. Davidson, N. H. Brown and A. H. Brand (2000). "Rotation and asymmetry of the mitotic spindle direct asymmetric cell division in the developing central nervous system." Nat Cell Biol**2**(1): 7-12.

Kamei, M., W. B. Saunders, K. J. Bayless, L. Dye, G. E. Davis and B. M. Weinstein (2006). "Endothelial tubes assemble from intracellular vacuoles in vivo." Nature**442**(7101): 453-456.

Keller, R., D. Shook and P. Skoglund (2008). "The forces that shape embryos: physical aspects of convergent extension by cell intercalation." Phys Biol**5**(1): 015007.

Kieserman, E. K. and J. B. Wallingford (2009). "In vivo imaging reveals a role for Cdc42 in spindle positioning and planar orientation of cell divisions during vertebrate neural tube closure." J Cell Sci**122**(Pt 14): 2481-2490.

Kilian, B., H. Mansukoski, F. C. Barbosa, F. Ulrich, M. Tada and C. P. Heisenberg (2003). "The role of Ppt/Wnt5 in regulating cell shape and movement during zebrafish gastrulation." Mech Dev**120**(4): 467-476.

Kim, S. and B. D. Dynlacht (2013). "Assembling a primary cilium." Curr Opin Cell Biol**25**(4): 506-511.

Kimmel, C. B., W. W. Ballard, S. R. Kimmel, B. Ullmann and T. F. Schilling (1995). "Stages of embryonic development of the zebrafish." Dev Dyn**203**(3): 253-310.

Kimmel, C. B., R. M. Warga and D. A. Kane (1994). "Cell cycles and clonal strings during formation of the zebrafish central nervous system." Development**120**(2): 265-276.

Krauss, S., J. P. Concordet and P. W. Ingham (1993). "A functionally conserved homolog of the Drosophila segment polarity gene hh is expressed in tissues with polarizing activity in zebrafish embryos." Cell**75**(7): 1431-1444.

Lammer, E. J., L. E. Sever and G. P. Oakley, Jr. (1987). "Teratogen update: valproic acid." Teratology**35**(3): 465-473.

Lancaster, O. M. and B. Baum (2014). "Shaping up to divide: coordinating actin and microtubule cytoskeletal remodelling during mitosis." Semin Cell Dev Biol**34**: 109-115.

Latimer, A. and J. R. Jessen (2010). "Extracellular matrix assembly and organization during zebrafish gastrulation." Matrix Biol**29**(2): 89-96.

Le Douarin, N. M., M. A. Teillet and M. Catala (1998). "Neurulation in amniote vertebrates: a novel view deduced from the use of quail-chick chimeras." Int J Dev Biol**42**(7): 909-916.

Lechler, T. and E. Fuchs (2005). "Asymmetric cell divisions promote stratification and differentiation of mammalian skin." Nature**437**(7056): 275-280.

Leck, I. (1974). "Causation of neural tube defects: clues from epidemiology." Br Med Bull**30**(2): 158-163.

Lemire, R. J. (1969). "Variations in development of the caudal neural tube in human embryos (Horizons XIV-XXI)." Teratology**2**(4): 361-369.

Liu, A., B. Wang and L. A. Niswander (2005). "Mouse intraflagellar transport proteins regulate both the activator and repressor functions of Gli transcription factors." Development**132**(13): 3103-3111.

Liu, K. D., A. Datta, W. Yu, P. R. Brakeman, T. S. Jou, M. A. Matthay and K. E. Mostov (2007). "Rac1 is required for reorientation of polarity and lumen formation through a PI 3-kinase-dependent pathway." Am J Physiol Renal Physiol**293**(5): F1633-1640.

Lowery, L. A. and H. Sive (2004). "Strategies of vertebrate neurulation and a re-evaluation of teleost neural tube formation." Mechanisms of Development**121**(10): 1189-1197.

Lowery, L. A. and H. Sive (2005). "Initial formation of zebrafish brain ventricles occurs independently of circulation and requires the nagie oko and snakehead/atp1a1a.1 gene products." Development**132**(9): 2057-2067.

Lu, X., A. G. Borchers, C. Jolicoeur, H. Rayburn, J. C. Baker and M. Tessier-Lavigne (2004). "PTK7/CCK-4 is a novel regulator of planar cell polarity in vertebrates." Nature**430**(6995): 93-98.

Lubarsky, B. and M. A. Krasnow (2003). "Tube morphogenesis: making and shaping biological tubes." Cell**112**(1): 19-28.

Mailleux, A. A., M. Overholtzer and J. S. Brugge (2008). "Lumen formation during mammary epithelial morphogenesis: insights from in vitro and in vivo models." Cell Cycle**7**(1): 57-62.

Malcoe, L. H., G. M. Shaw, E. J. Lammer and A. A. Herman (1999). "The effect of congenital anomalies on mortality risk in white and black infants." Am J Public Health**89**(6): 887-892.

Marino, S. (2005). "Medulloblastoma: developmental mechanisms out of control." Trends Mol Med**11**(1): 17-22.

Marti, E., D. A. Bumcrot, R. Takada and A. P. McMahon (1995a). "Requirement of 19K form of Sonic hedgehog for induction of distinct ventral cell types in CNS explants." Nature**375**(6529): 322-325.

Marti, E., R. Takada, D. A. Bumcrot, H. Sasaki and A. P. McMahon (1995b). "Distribution of Sonic hedgehog peptides in the developing chick and mouse embryo." Development**121**(8): 2537-2547.

Martin-Belmonte, F., W. Yu, A. E. Rodriguez-Fraticelli, A. J. Ewald, Z. Werb, M. A. Alonso and K. Mostov (2008). "Cell-polarity dynamics controls the mechanism of lumen formation in epithelial morphogenesis." Curr Biol**18**(7): 507-513.

May, S. R., A. M. Ashique, M. Karlen, B. Wang, Y. Shen, K. Zarbalis, J. Reiter, J. Ericson and A. S. Peterson (2005). "Loss of the retrograde motor for IFT disrupts localization of Smo to cilia and prevents the expression of both activator and repressor functions of Gli." Dev Biol**287**(2): 378-389.

McMahon, A. P., P. W. Ingham and C. J. Tabin (2003). "Developmental roles and clinical significance of hedgehog signaling." Curr Top Dev Biol**53**: 1-114.

Mikawa, T., A. M. Poh, K. A. Kelly, Y. Ishii and D. E. Reese (2004). "Induction and patterning of the primitive streak, an organizing center of gastrulation in the amniote." Dev Dyn**229**(3): 422-432.

Miller, K. A., C. J. Ah-Cann, M. F. Welfare, T. Y. Tan, K. Pope, G. Caruana, M. L. Freckmann, R. Savarirayan, J. F. Bertram, M. S. Dobbie, J. F. Bateman and P. G. Farlie (2013). "Cauli: a mouse strain with an Ift140 mutation that results in a skeletal ciliopathy modelling Jeune syndrome." PLoS Genet**9**(8): e1003746.

Minc, N., D. Burgess and F. Chang (2011). "Influence of cell geometry on division-plane positioning." Cell**144**(3): 414-426.

Mitchell, L. E. (2005). "Epidemiology of neural tube defects." Am J Med Genet C Semin Med Genet**135C**(1): 88-94.

Morin, X., F. Jaouen and P. Durbec (2007). "Control of planar divisions by the G-protein regulator LGN maintains progenitors in the chick neuroepithelium." Nat Neurosci**10**(11): 1440-1448.

Murdoch, J. N. and A. J. Copp (2010). "The relationship between sonic Hedgehog signaling, cilia, and neural tube defects." Birth Defects Res A Clin Mol Teratol**88**(8): 633-652.

Murdoch, J. N., K. Doudney, C. Paternotte, A. J. Copp and P. Stanier (2001). "Severe neural tube defects in the loop-tail mouse result from mutation of Lpp1, a novel gene involved in floor plate specification." Hum Mol Genet**10**(22): 2593-2601.

Muto, A., K. Arai and S. Watanabe (2006). "Rab11-FIP4 is predominantly expressed in neural tissues and involved in proliferation as well as in differentiation during zebrafish retinal development." Dev Biol**292**(1): 90-102.

Nachury, M. V., E. S. Seeley and H. Jin (2010). "Trafficking to the ciliary membrane: how to get across the periciliary diffusion barrier?" Annu Rev Cell Dev Biol**26**: 59-87.

Nievelstein, R. A., N. G. Hartwig, C. Vermeij-Keers and J. Valk (1994). "Embryonic development of the mammalian caudal neural tube." Teratology**49**(6): 445.

Nigg, E. A. and T. Stearns (2011). "The centrosome cycle: Centriole biogenesis, duplication and inherent asymmetries." Nat Cell Biol**13**(10): 1154-1160.

Nishimura, T., H. Honda and M. Takeichi (2012). "Planar cell polarity links axes of spatial dynamics in neural-tube closure." Cell**149**(5): 1084-1097.

O'Rahilly, R. and F. Muller (1994). "Neurulation in the normal human embryo." Ciba Found Symp**181**: 70-82; discussion 82-79.

Ocbina, P. J. and K. V. Anderson (2008). "Intraflagellar transport, cilia, and mammalian Hedgehog signaling: analysis in mouse embryonic fibroblasts." Dev Dyn**237**(8): 2030-2038.

Ossipova, O., I. Chuykin, C. W. Chu and S. Y. Sokol (2015). "Vangl2 cooperates with Rab11 and Myosin V to regulate apical constriction during vertebrate gastrulation." Development**142**(1): 99-107.

Pai, Y. J., N. L. Abdullah, S. W. Mohd-Zin, R. S. Mohammed, A. Rolo, N. D. Greene, N. M. Abdul-Aziz and A. J. Copp (2012). "Epithelial fusion during neural tube morphogenesis." Birth Defects Res A Clin Mol Teratol**94**(10): 817-823.

Papan, C. and J. A. Campos-Ortega (1994). "On the formation of the neural keel and neural tube in the zebrafish Danio (Brachydanio) rerio." Roux's archives of developmental biology **204**(4): 178-186.

Paridaen, J. T., M. Wilsch-Brauninger and W. B. Huttner (2013). "Asymmetric inheritance of centrosome-associated primary cilium membrane directs ciliogenesis after cell division." Cell**155**(2): 333-344.

Park, T. J., B. J. Mitchell, P. B. Abitua, C. Kintner and J. B. Wallingford (2008). "Dishevelled controls apical docking and planar polarization of basal bodies in ciliated epithelial cells." Nat Genet**40**(7): 871-879.

Pedersen, L. B., I. R. Veland, J. M. Schroder and S. T. Christensen (2008). "Assembly of primary cilia." Dev Dyn**237**(8): 1993-2006.

Peyre, E., F. Jaouen, M. Saadaoui, L. Haren, A. Merdes, P. Durbec and X. Morin (2011). "A lateral belt of cortical LGN and NuMA guides mitotic spindle movements and planar division in neuroepithelial cells." J Cell Biol**193**(1): 141-154.

Placzek, M. and J. Briscoe (2005). "The floor plate: multiple cells, multiple signals." Nat Rev Neurosci**6**(3): 230-240.

Quesada-Hernandez, E., L. Caneparo, S. Schneider, S. Winkler, M. Liebling, S. E. Fraser and C. P. Heisenberg (2010). "Stereotypical cell division orientation controls neural rod midline formation in zebrafish." Curr Biol**20**(21): 1966-1972.

Reichenbach, A., P. Schaaf and H. Schneider (1990). "Primary neurulation in teleosts--evidence for epithelial genesis of central nervous tissue as in other vertebrates." J Hirnforsch**31**(2): 153-158.

Reiter, J. F., O. E. Blacque and M. R. Leroux (2012). "The base of the cilium: roles for transition fibres and the transition zone in ciliary formation, maintenance and compartmentalization." EMBO Rep**13**(7): 608-618.

Riddle, R. D., R. L. Johnson, E. Laufer and C. Tabin (1993). "Sonic hedgehog mediates the polarizing activity of the ZPA." Cell**75**(7): 1401-1416.

Rodriguez-Fraticelli, A. E., M. Auzan, M. A. Alonso, M. Bornens and F. Martin-Belmonte (2012). "Cell confinement controls centrosome positioning and lumen initiation during epithelial morphogenesis." J Cell Biol**198**(6): 1011-1023.

Roelink, H., A. Augsburger, J. Heemskerk, V. Korzh, S. Norlin, A. Ruiz i Altaba, Y. Tanabe, M. Placzek, T. Edlund, T. M. Jessell and et al. (1994). "Floor plate and motor neuron induction by vhh-1, a vertebrate homolog of hedgehog expressed by the notochord." Cell**76**(4): 761-775.

Roelink, H., J. A. Porter, C. Chiang, Y. Tanabe, D. T. Chang, P. A. Beachy and T. M. Jessell (1995). "Floor plate and motor neuron induction by different concentrations of the amino-terminal cleavage product of sonic hedgehog autoproteolysis." Cell**81**(3): 445-455.

Rohatgi, R., L. Milenkovic and M. P. Scott (2007). "Patched1 regulates hedgehog signaling at the primary cilium." Science**317**(5836): 372-376.

Rosenbaum, J. L. and G. B. Witman (2002). "Intraflagellar transport." Nat Rev Mol Cell Biol**3**(11): 813-825.

Ross, A. J., H. May-Simera, E. R. Eichers, M. Kai, J. Hill, D. J. Jagger, C. C. Leitch, J. P. Chapple, P. M. Munro, S. Fisher, P. L. Tan, H. M. Phillips, M. R. Leroux, D. J. Henderson, J. N. Murdoch, A. J. Copp, M. M. Eliot, J. R. Lupski, D. T. Kemp, H. Dollfus, M. Tada, N. Katsanis, A. Forge and P. L. Beales (2005). "Disruption of Bardet-Biedl syndrome ciliary proteins perturbs planar cell polarity in vertebrates." Nat Genet**37**(10): 1135-1140.

Roszko, I., S. S. D, J. R. Jessen, A. Chandrasekhar and L. Solnica-Krezel (2015). "A dynamic intracellular distribution of Vangl2 accompanies cell polarization during zebrafish gastrulation." Development**142**(14): 2508-2520.

Saitsu, H. and K. Shiota (2008). "Involvement of the axially condensed tail bud mesenchyme in normal and abnormal human posterior neural tube development." Congenit Anom (Kyoto)**48**(1): 1-6.

Saraga-Babic, M., D. Sapunar and J. Wartiovaara (1995). "Variations in the formation of the human caudal spinal cord." J Hirnforsch**36**(3): 341-347.

Saraga-Babic, M., V. Stefanovic, J. Wartiovaara and E. Lehtonen (1993). "Spinal cord-notochord relationship in normal human embryos and in a human embryo with double spinal cord." Acta Neuropathol**86**(5): 509-514.

Sawyer, J. M., J. R. Harrell, G. Shemer, J. Sullivan-Brown, M. Roh-Johnson and B. Goldstein (2010). "Apical constriction: a cell shape change that can drive morphogenesis." Dev Biol**341**(1): 5-19.

Schauerte, H. E., F. J. van Eeden, C. Fricke, J. Odenthal, U. Strahle and P. Haffter (1998). "Sonic hedgehog is not required for the induction of medial floor plate cells in the zebrafish." Development**125**(15): 2983-2993.

Schoenwolf, G. C. (1984). "Histological and ultrastructural studies of secondary neurulation in mouse embryos." Am J Anat**169**(4): 361-376.

Schoenwolf, G. C. and J. Delongo (1980). "Ultrastructure of secondary neurulation in the chick embryo."

Schoenwolf, G. C. and J. L. Smith (1990). "Mechanisms of neurulation: traditional viewpoint and recent advances." Development**109**(2): 243-270.

Scholpp, S., O. Wolf, M. Brand and A. Lumsden (2006). "Hedgehog signalling from the zona limitans intrathalamica orchestrates patterning of the zebrafish diencephalon." Development**133**(5): 855-864.

Seeley, E. S. and M. V. Nachury (2010). "The perennial organelle: assembly and disassembly of the primary cilium." J Cell Sci**123**(Pt 4): 511-518.

Sepich, D. S., C. Calmelet, M. Kiskowski and L. Solnica-Krezel (2005). "Initiation of convergence and extension movements of lateral mesoderm during zebrafish gastrulation." Dev Dyn**234**(2): 279-292.

Sepich, D. S., D. C. Myers, R. Short, J. Topczewski, F. Marlow and L. Solnica-Krezel (2000). "Role of the zebrafish trilobite locus in gastrulation movements of convergence and extension." Genesis**27**(4): 159-173.

Sepich, D. S., M. Usmani, S. Pawlicki and L. Solnica-Krezel (2011). "Wnt/PCP signaling controls intracellular position of MTOCs during gastrulation convergence and extension movements." Development**138**(3): 543-552.

Shimokita, E. and Y. Takahashi (2011). "Secondary neurulation: Fate-mapping and gene manipulation of the neural tube in tail bud." Dev Growth Differ**53**(3): 401-410.

Shkumatava, A., S. Fischer, F. Muller, U. Strahle and C. J. Neumann (2004). "Sonic hedgehog, secreted by amacrine cells, acts as a short-range signal to direct differentiation and lamination in the zebrafish retina." Development**131**(16): 3849-3858.

Shum, A. S. and A. J. Copp (1996). "Regional differences in morphogenesis of the neuroepithelium suggest multiple mechanisms of spinal neurulation in the mouse." Anat Embryol (Berl)**194**(1): 65-73.

Shum, A. S., L. S. Tang, A. J. Copp and H. Roelink (2010). "Lack of motor neuron differentiation is an intrinsic property of the mouse secondary neural tube." Dev Dyn**239**(12): 3192-3203.

Simons, M., J. Gloy, A. Ganner, A. Bullerkotte, M. Bashkurov, C. Kronig, B. Schermer, T. Benzing, O. A. Cabello, A. Jenny, M. Mlodzik, B. Polok, W. Driever, T. Obara and G. Walz (2005). "Inversin, the gene product mutated in nephronophthisis type II, functions as a molecular switch between Wnt signaling pathways." Nat Genet**37**(5): 537-543.

Smith, J. L. and G. C. Schoenwolf (1989). "Notochordal induction of cell wedging in the chick neural plate and its role in neural tube formation." J Exp Zool**250**(1): 49-62.

Smith, J. L. and G. C. Schoenwolf (1991). "Further evidence of extrinsic forces in bending of the neural plate." J Comp Neurol**307**(2): 225-236.

Solnica-Krezel, L. and D. S. Sepich (2012). "Gastrulation: making and shaping germ layers." Annu Rev Cell Dev Biol**28**: 687-717.

Strahle, U., P. Blader and P. W. Ingham (1996). "Expression of axial and sonic hedgehog in wildtype and midline defective zebrafish embryos." Int J Dev Biol**40**(5): 929-940.

Strahle, U., S. Jesuthasan, P. Blader, P. Garcia-Villalba, K. Hatta and P. W. Ingham (1997). "one-eyed pinhead is required for development of the ventral midline of the zebrafish (Danio rerio) neural tube." Genes Funct**1**(2): 131-148.

Tada, M. and C. P. Heisenberg (2012). "Convergent extension: using collective cell migration and cell intercalation to shape embryos." Development**139**(21): 3897-3904.

Taverna, E. and W. B. Huttner (2010). "Neural progenitor nuclei IN motion." Neuron**67**(6): 906-914.

Tawk, M., C. Araya, D. A. Lyons, A. M. Reugels, G. C. Girdler, P. R. Bayley, D. R. Hyde, M. Tada and J. D. Clarke (2007). "A mirror-symmetric cell division that orchestrates neuroepithelial morphogenesis." Nature**446**(7137): 797-800.

Tempe, D., M. Casas, S. Karaz, M. F. Blanchet-Tournier and J. P. Concordet (2006). "Multisite protein kinase A and glycogen synthase kinase 3beta phosphorylation leads to Gli3 ubiquitination by SCFbetaTrCP." Mol Cell Biol**26**(11): 4316-4326.

Toyoshima, F. and E. Nishida (2007). "Integrin-mediated adhesion orients the spindle parallel to the substratum in an EB1- and myosin X-dependent manner." EMBO J**26**(6): 1487-1498.

Tran, P. V., C. J. Haycraft, T. Y. Besschetnova, A. Turbe-Doan, R. W. Stottmann, B. J. Herron, A. L. Chesebro, H. Qiu, P. J. Scherz, J. V. Shah, B. K. Yoder and D. R. Beier (2008). "THM1 negatively modulates mouse sonic hedgehog signal transduction and affects retrograde intraflagellar transport in cilia." Nat Genet**40**(4): 403-410.

Tukachinsky, H., L. V. Lopez and A. Salic (2010). "A mechanism for vertebrate Hedgehog signaling: recruitment to cilia and dissociation of SuFu-Gli protein complexes." J Cell Biol**191**(2): 415-428.

Ueno, N. and N. D. Greene (2003). "Planar cell polarity genes and neural tube closure." Birth Defects Res C Embryo Today**69**(4): 318-324.

van Straaten, H. W. and A. J. Copp (2001). "Curly tail: a 50-year history of the mouse spina bifida model." Anat Embryol (Berl)**203**(4): 225-237.

Wang, B., J. F. Fallon and P. A. Beachy (2000). "Hedgehog-regulated processing of Gli3 produces an anterior/posterior repressor gradient in the developing vertebrate limb." Cell**100**(4): 423-434.

Wang, J., N. S. Hamblet, S. Mark, M. E. Dickinson, B. C. Brinkman, N. Segil, S. E. Fraser, P. Chen, J. B. Wallingford and A. Wynshaw-Boris (2006). "Dishevelled genes mediate a conserved mammalian PCP pathway to regulate convergent extension during neurulation." Development**133**(9): 1767-1778.

Warga, R. M. and C. B. Kimmel (1990). "Cell movements during epiboly and gastrulation in zebrafish." Development**108**(4): 569-580.

Wen, X., C. K. Lai, M. Evangelista, J. A. Hongo, F. J. de Sauvage and S. J. Scales (2010). "Kinetics of hedgehog-dependent full-length Gli3 accumulation in primary cilia and subsequent degradation." Mol Cell Biol**30**(8): 1910-1922.

Westlake, C. J., L. M. Baye, M. V. Nachury, K. J. Wright, K. E. Ervin, L. Phu, C. Chalouni, J. S. Beck, D. S. Kirkpatrick, D. C. Slusarski, V. C. Sheffield, R. H. Scheller and P. K. Jackson (2011). "Primary cilia membrane assembly is initiated by Rab11 and transport protein particle II (TRAPPII) complex-dependent trafficking of Rabin8 to the centrosome." Proc Natl Acad Sci U S A**108**(7): 2759-2764.

Xie, J., M. Murone, S. M. Luoh, A. Ryan, Q. Gu, C. Zhang, J. M. Bonifas, C. W. Lam, M. Hynes, A. Goddard, A. Rosenthal, E. H. Epstein, Jr. and F. J. de Sauvage (1998). "Activating Smoothened mutations in sporadic basal-cell carcinoma." Nature**391**(6662): 90-92.

Xiong, F., W. Ma, T. W. Hiscock, K. R. Mosaliganti, A. R. Tentner, K. A. Brakke, N. Rannou, A. Gelas, L. Souhait, I. A. Swinburne, N. D. Obholzer and S. G. Megason (2014). "Interplay of cell shape and division orientation promotes robust morphogenesis of developing epithelia." Cell**159**(2): 415-427.

Xiong, F., A. R. Tentner, P. Huang, A. Gelas, K. R. Mosaliganti, L. Souhait, N. Rannou, I. A. Swinburne, N. D. Obholzer, P. D. Cowgill, A. F. Schier and S. G. Megason (2013). "Specified neural progenitors sort to form sharp domains after noisy Shh signaling." Cell**153**(3): 550-561.

Yang, H.-J., K.-C. Wang, J. G. Chi, M.-S. Lee, Y.-J. Lee, S.-K. Kim and B.-K. Cho (2003). "Neural differentiation of caudal cell mass (secondary neurulation) in chick embryos: Hamburger and Hamilton Stages 16–45." Developmental Brain Research**142**(1): 31-36.

Yang, X., J. Zou, D. R. Hyde, L. A. Davidson and X. Wei (2009). "Stepwise maturation of apicobasal polarity of the neuroepithelium is essential for vertebrate neurulation." J Neurosci**29**(37): 11426-11440.

Ybot-Gonzalez, P., P. Cogram, D. Gerrelli and A. J. Copp (2002). "Sonic hedgehog and the molecular regulation of mouse neural tube closure." Development**129**(10): 2507-2517.

Ybot-Gonzalez, P., C. Gaston-Massuet, G. Girdler, J. Klingensmith, R. Arkell, N. D. Greene and A. J. Copp (2007a). "Neural plate morphogenesis during mouse neurulation is regulated by antagonism of Bmp signalling." Development**134**(17): 3203-3211.

Ybot-Gonzalez, P., D. Savery, D. Gerrelli, M. Signore, C. E. Mitchell, C. H. Faux, N. D. Greene and A. J. Copp (2007b). "Convergent extension, planar-cell-polarity signalling and initiation of mouse neural tube closure." Development**134**(4): 789-799.

Yin, C., B. Ciruna and L. Solnica-Krezel (2009). "Convergence and extension movements during vertebrate gastrulation." Curr Top Dev Biol**89**: 163-192.

Yin, C., M. Kiskowski, P. A. Pouille, E. Farge and L. Solnica-Krezel (2008). "Cooperation of polarized cell intercalations drives convergence and extension of presomitic mesoderm during zebrafish gastrulation." J Cell Biol**180**(1): 221-232.

Yu, X., C. P. Ng, H. Habacher and S. Roy (2008). "Foxj1 transcription factors are master regulators of the motile ciliogenic program." Nat Genet**40**(12): 1445-1453.

Zhang, X. M., M. Ramalho-Santos and A. P. McMahon (2001). "Smoothened mutants reveal redundant roles for Shh and Ihh signaling including regulation of L/R asymmetry by the mouse node." Cell**105**(6): 781-792.

Zheng, Y. (2010). "A membranous spindle matrix orchestrates cell division." Nat Rev Mol Cell Biol**11**(7): 529-535.

Zhou, J., S. Pal, S. Maiti and L. A. Davidson (2015). "Force production and mechanical accommodation during convergent extension." Development**142**(4): 692-701.

Zigman, M., A. Trinh le, S. E. Fraser and C. B. Moens (2011). "Zebrafish neural tube morphogenesis requires Scribble-dependent oriented cell divisions." Curr Biol**21**(1): 79-86.

8. APPENDICES

APPENDICES

TO STUDY THE IN VIVO CONTROL OF PRIMARY NEUROGENESIS IN VERTEBRATE EMBRYOS

INTRODUCTION

The vertebrate nervous system is an extraordinarily complex assembly of diverse cell types, all of which arise from the pluripotent neuroepithelial cells. Neuroepithelial cells form a single cell thick pseudostratified epithelium, with cell division occurring at the apical face (Sauer, 1935). The production of appropriate numbers of cells requires a finely tuned balance between the three different modes of divisions that neuroepithelial cells undergo (Franco and Muller, 2013; Taverna et al., 2014): self-expanding (symmetric proliferative, PP) divisions that ensure the expansion of the progenitor pool by generating two daughter cells with identical progenitor potential; self-renewing (asymmetric, PN) divisions that generate one daughter cell with a developmental potential indistinguishable from the parental cell and another with a more restricted potential; and self-consuming (terminal symmetric neurogenic, NN) divisions that generate two cells committed to differentiation, thereby depleting the progenitor pool. Premature transition to neuron-generating mode of division quickly exhausts the reservoir and restricts the number of neurons that can be produced later, and is considered a major cause of microcephaly, thus the relevance in understanding the mechanisms regulating such events. Although not fully understood, the picture emerging suggests that some intrinsic mechanisms controlling the mode of division in the developing vertebrate nervous system reflect the contributions of centrosome asymmetry, spindle orientation and the inheritance of apical membrane domains However, while these decisions are likely to be primarily dictated by extrinsic signals, the nature of these factors are only beginning to be revealed. To begin these analysis we set for two strategies; on the one and to search for extrinsic signals that might control the mode of cell division, on the other hand to study the possible role for

intrinsic mechanisms in this process, taking the chick embryo spinal cord as a model system.

We first developed the molecular markers that provide the single cell resolution necessary to in vivo identify and quantify the three modes of division (PP/PN/NN) . Using these reporters and a mathematical model that predicts their dynamics, we revealed a new role for Shh in the maintenance of stem-cell identity in the developing ventral spinal cord. We defined a phase of progenitor expansion followed by a phase of reduction in which motor neuron progenitors are consumed. By in vivo gain-of and loss-of-function experiments, we demonstrated that active Shh signaling favors the self-expansion mode of division and that a reduction in Shh activity is required to switch the mode of division to that which generates motor neurons (Saade et al., 2013, SEE APPENDIX 1).

Motor neurons are generated early in spinal cord development, and at a high speed (terminating at ~100hpf), however, we and others have demonstrated that the generation of interneurons, although it is initiated at approximately the same developmental time (~50hpf), is maintained for longer periods, after the termination of Shh-activity. Thus we next searched for alternative morphogen-activities regulating the mode of cell division during the generation of interneurons. We found that variations in the level of endogenous SMAD1/5 activity are associated with the different modes of division. By in vivo experiments we showed that high levels of SMAD1/5 signalling maintain self-expanding (PP) divisions, and that a reduction in SMAD1/5 activity is required for progenitors to switch to neuron-generating divisions. These results led us to conclude that an endogenous gradient of SMAD1/5 activity at the mitotic phase, dictates the resulting mode of division, that control neurogenesis of spinal interneurons (Le Dreau et al., 2014, SEE APPENDIX 2).

Primary microcephaly in which growth is significantly reduced without an effect on brain structure associates to several human loci. Unexpectedly, all primary microcephaly proteins are ubiquitous and localise to centrosomes for at least part of the cell cycle, suggesting the centrosome as a final integration point for many

regulatory pathways affecting prenatal neurogenesis (Thornton and Woods, 2009). Thus we also sought to study centrosome behavior and the possible role in the regulation of the mode of division in vertebrate neural stem cell progenitors. A collaboration was launched with the group of Dr. Cayetano González, which focuses on the study of centrosomes in the Drosophila embryo. The hypothesis leading this study was the identification of a role for centrosomes in the regulation of the mode of division in vertebrate neural progenitor cells. While we were performing these experiments another study was published with very similar conclusions (Wang et al 2009). Since our results were at that point highly preliminary, we decided to discontinue these experiments. The following sections describe the experimental approaches and the results obtained at that point.

As a result of this project we contributed in a review (Lesage et al., 2010, SEE APPENDIX 3) describing the parallelisms and striking differences between the self-renewing asymmetric divisions of neural stem cells in Drosophila (neuroblasts) and those in the mouse (radial glial cells). We focused on the case of centrosome asymmetry and the contribution of spindle orientation and non-spindle-related centrosome functions.

MATERIALS AND METHODS

(See also material and methods in the two published papers)

DNA constructs

In vivo live imaging experiments were performed with a RFP fused Histone to label the nucleus (pCS2 H2B-RFP), *Homo sapiens* CEP152-EGFP (provided by Dr C.González) and a pDendra2N vector (Clontech, Cat#632545)

In vivo loss-of-function (LOF) experiments were performed by the generation of short hairpin RNAs (shRNA) cloned into to pSHIN vector (Kojima et al., 2004). DNA sequences for chick SasS6 shRNA were designed in Dharmacon DesignCenter (www.dharmacon.com). As a control shRNA we used human HDAC in pSHIN. SasS6 shRNA target sequence, 5'-GGAGGAGAATACAGAGAAA-3'

For rescue experiment a short hairpin insensitive version of *Gallus gallus* version of Sas6 (GgSas6) was cloned into pCIG vector.

Chick embryo *in ovo* electroporation

Fertilized eggs from White-Leghorn chickens were incubated at 38.5ºC in an atmosphere of 70% humidity. Embryos were staged according to Hamburger and Hamilton (HH, 1951) and electroporated with Clontech purified plasmid DNA diluted in H_2O with 50ng/ml Fast Green (Sigma) at a concentration of 1µg/µl unless otherwise indicated. Plasmid DNA was injected into the lumen of HH12 neural tubes under a Leica MZ6 scope. Electrodes were placed either side of the neural tube and electroporation carried out in ovo using a Intracel Dual Pulse TSS-100 electroporator delivering five 50 ms square pulses of 20-25 V. Transfected embryos were allowed to develop and harvested at the indicated time points, then dissected out in PBS, fixed and processed for analysis.

Immunohistochemistry

Embryos were fixed 2-4 hours in 4% paraformaldehyde at 4ºC or, for centriolar or cytoskeleton labelling, they were alternatively fixed overnight in MetOH 20mM EGTA at 4ºC and rinsed 20 seconds in acetone. Embryos were embdedded for vibratome sectioning in 10% sucrose-5% agarose. 40µm transverse sections were obtained using a Leica vibratome VT 1000S and processed for immunochemistry. Free-floating sections were placed in blocking solution (2% Sheep Serum in PBT with 0.1% Triton X-100) for 30 min at room temperature before overnight incubation with the appropriated primary antibodies in blocking solution at 4ºC. The following day sections were washed with PBT and incubated with conjugated secondary antibodies for 2-3 h in the dark at room temperature. Floating sections were washed with PBT and mounted into slides with coverslips using Mowiol (polyvinyl alcohol 4-88, Sigma) with 0.2 ng/µl DAPI (Sigma).

Antibodies against the following proteins were used; γTubulin, αTubulin, Acetylated Tubulin (Sigma), Sas6 (Santa Cruz), ZO-1 (DSHB).

Alexa488- and Alexa555-conjugated secondary antibodies (Molecular Probes) were used. After single or double staining, sections were mounted, analysed and

photographed using a Leica Confocal SP5 microscope using the Leica Application Suite AF software. An average of 20 images were acquired at 0.5µm optical slices and subsequently processed with Adobe Photoshop CS4 software (Adobe).

Image acquisition was performed of at least 4 different embryos from each experimental condition (n>4).

Fluorescent associated cell sorting (FACS), mRNA extraction and quantitative PCR

Electroporated embryos were dissected out and trypsinized for 5-10 minutes in Trypsin-EDTA 0.5% (Sigma). Trypsinization was stopped with 20% horse serum in PBS/0.1% glucose solution. GFP+ cells from cell suspension were sorted by flow cytometry using a MoFlo flow cytometer (DakoCytomation, Fort Collins, CO, USA).

The same number of FACS-separated cells was used in each condition of each experiment (25.000).

mRNA from FACS-separated cells was extracted by TRIZOL (Invitrogen) protocol with 2 µl of pellet paint co-precipitant (Novagene). Reverse transcription was performed with Transcriptor Kit (Roche), following the manufacturer's procedure. qPCR was carried out in triplicate with SYBRgreen (Roche) in LC480 Lightcycler (Roche). A standard curve was obtained for each amplicon by plotting the number of cycles at which the fluorescence crossed the threshold (crossing values) against increasing amounts of DNA template. All experimental values were normalized to those obtained for GAPDH. PCR amplifications were assessed from 4 independent cell pools per experimental condition. Data are expressed in arbitrary units and represent mean standardised values ± s.d(Figure2). Primer sequences: SasS6A FW, ’5 -AGTACCAACAACAGCACG-3’; SasS6A RV, 5 -TTCTCCCGACGCAGTGA-3’; SasS6B FW, 5’-TCTCGGAACTTGAGGTCAT-3’, SasS6B RV, 5’-TCAGCATCCAGAGTGGT-3’

Spinal cord slice culture and time-lapse imaging

Electroporated embryos were dissected out and cleaned in Gibco DMEM F12 medium (Invitrogen), the healthiest and best transfected were selected and cut in 300µm slices using a Vibratome 800 McIlwain Tissue Chopper. Slices were selected and embedded in a 2µl unpolymerized matrix drop containing 10mg/ml Fibrinogen in DMEM F12 on an optical glass-bottom culture dish (MatTek). Next, a 0.5µl drop of Thrombin

(Amersham) was added over the fibrinogen matrix to induce its polymerization. Finally the embedded sample was kept in 300µl of warm DMEM F12 medium with 1:100 Penicillin/Streptomicin and 1:1000 Mito-plus serum (Becton Dickinson) at 38'5ºC with 5% CO_2 and humidity in a cell culture chamber during at least 30min until the start of imaging. Spinning disc time-lapse confocal microscopy was performed on a a PerkinElmer UltraView ERS confocal spinning disk or on an Andor Technology confocal spinning disk, both adapted with a environmental chamber with adjustable temperature and CO_2.

Images were acquired using a 40X lens(0.60NA KORR Ph2 LD ACHROMPLAN) or 63X lens (1.40NA OIL DIC PLAN-APOCHROMAT), from 20-40 optical sections spaced 0.5-1µm apart at 0,5-1min intervals Images were subsequently processed with Volocity (Improvision) or IQ 1.10.2 (Andor Technology).

RESULTS

Sas6 is expressed in centrosomes of neural progenitor cells

Spindle assembly abnormal protein 6 homolog (Sas6) is an essential protein in centriole biogenesis localized into the central part of the cartwheel structure (Nakazawa Y, 2007) and needs to be tightly regulated during the cell cycle; this control is achieved though the oscillation of the levels of Sas6 which is degraded in mitosis and starts to accumulate again at the end of the following G1 (Strnad P, 2007). Sas6 phenotype when disrupted consists in the absence of centriole duplication, while when overexpressed it produces extra centrioles (Bettencourt-Dias M, 2009).

To begin to study centrosome behaviour we first determined the relative localization of Sas6 to other centrosomal components. Pericentriolar matrix material (PMC) lining the neural tube (NT) lumen and at the mitotic cell spindle poles (white arrow) was identified with an antibody against γ-Tubulin (Figure 1A). Mitotic spindles flanked by centrosomes were labelled with anti-α-Tubulin (Figure 1B) and Sas6 expression was detected lining the lumen, and co-localized with PCM in interphase cells (Figure 1C) indicating the reliable labelling of centrosomal proteins.

Next, we introduced a plasmid encoding the core centrosomal protein CEP152 fused with enhanced green fluorescent protein (CEP152-GFP) into the developing NT by in

ovo electroporation. As expected, CEP152-GFP formed pairs of dots located at the ventricular zone (VZ) surface (Fig1D), that appear as the cilia centrosomal basal body (Figure1E) and co-localize with γTubulin stained centrosomes (Figure 1F), indicating that transient expression of CEP152-GFP reliably labels the two centrosomes in the developing chick NT.

Moreover, staining against endogenous Sas6 protein revealed an unexpected location at the tips of the mitotic spindle (possibly the kinetochores) during metaphase plate formation (Figure1C,G,H) leading to hypothetize a possible unknown novel role for Sas-6 independent on its centrosomal function when located in the kinetochores during certain phases of mitosis.

Sas6 activity is required for neuroepithelial integrity

To test the impact of the removal or impairment of centrosomes on neural progenitors, we next targeted Sas6). To that end, embryos were electroporated with a short hairpin against Sas6 (shSas6) construct to knockdown the endogenous protein expression or control shHDAC, and GFP+ cells were sorted for mRNA extraction (Figure2A). RTqPCR results show that electroporation of shSas6 was sufficient to reduce 60% of endogenous Sas6 expression (relative mRNA levels (Mean ± s.d) (0.343 ± 0.132) p=0.01) (Figure2B).

In each cell cycle centrosomes are replicating in a semi-conservative manner, thereby to get rid of centrosomes after shRNA electroporation we need to wait at least two cell cycles. Taking into consideration that an average cell cycle takes 16h (ref), we waited 48hpe to allow shRNA to be effective and two rounds of cell division to occur (Figure2C). Results show that staining for γTubulin was diminished 48hpe in shSas6 condition and tissue had lost its architecture (Fig2D).

We proceeded to do a time course analysis with apical polarity markers to capture the sequence of events leading to loss of tissue structure. To that end embryos were electroporated at HH12 and harvested at 24, 30 or 48hpe. Control electroporation condition shHDAC shows that ZO1, an apical polarity marker, is unaffected after 48hpe (Fig3A,Ai). shSas6 expressing embryos show undisturbed ZO1 localization at 24hpe (Fig3B,Bi). However at 30hpe, tissue seems to start losing its apical structure (Fig3,C,Ci)

and at 48hpe tissue architecture is severely affected and apical ZO1 staining diminished (Fig3D,Di).

Converse gain-of-function experiments were performed *in vivo* by the electroporation of a short hairpin insensitive version of *Gallus gallus* Sas6, which efficiency was tested by RTqPCR. Sas6 mRNA levels sifnificantly increase even when co-electroporated with shSas6 (Mean ± s.d) (25.1 ± 6.52) p=0.003) (Figure4A). Transversal sections show higher amount of electroporated mitotic cells appeared in the luminal region (Figure4B,C, yellow arrows) when compared to the control side. Often mitotic cells would appear ectopically interspersed in the tissue (Figure4B,C, red arrows). We guessed that this could be due either to centrosome amplification of centrosome inactivation, leading to a mitosis blocking defect.

In vivo analysis of centrosome behaviour in dividing neural progenitors

From the literature it is known that one centrosome is apically localized, where it forms the basal body of the cilium. Nonetheless, details of the centrosome behaviour during the whole cell cycle remain unknown. Despite of the unequal centrosome inheritance between proliferating and differentiating sibling cells in asymmetric cell division both centrosomes in the vertebrate neural progenitors stay apical until the onset of mitosis. We were able to monitor the neural progenitors live, using a RFP-tagged histone H2B and EGFP-Cep152, and check centrosome behaviour prior to division in these cells by using a spinning disk confocal microscope.

We could observe several centrosome behaviours, in which both centrosomes detach both from the apical pole at the same time point, or centrosomes detach separately. We wanted to find whether different centrosome behaviours could be coupled with different types of divisions, therefore two approaches were considered:

1) Developing reporters for the different type of divisions (See Appendix 1)
2) I*n vivo* single cell photoconversion once the centrosome behaviour is captured.

In order to link centrosomal behavior to cell fate of the descendance further developed the single cell photoconversion approach in neural tube slice cultures co-

electroporated with EGFP-Cep152 and a cytoplasmic photoconvertible chromophore: Dendra2. The fluorescent protein Dendra2 switches its maximum emission wavelength from 507nm to 573nm after a pulse of UV laser light. After visualizing a mitotic cell and the behaviour of its centrosomes, prior to anaphase, we photoconverted the dividing cell in order to trace the fate of the descending sibling cells. First trials in this direction were performed (Fig5)

CONCLUSIONS

While we were performing these experiments another study was published with very similar conclusions (Wang et al 2009). Since our results were at that point highly preliminary, we decided to discontinue these experiments.

FIGURE 1

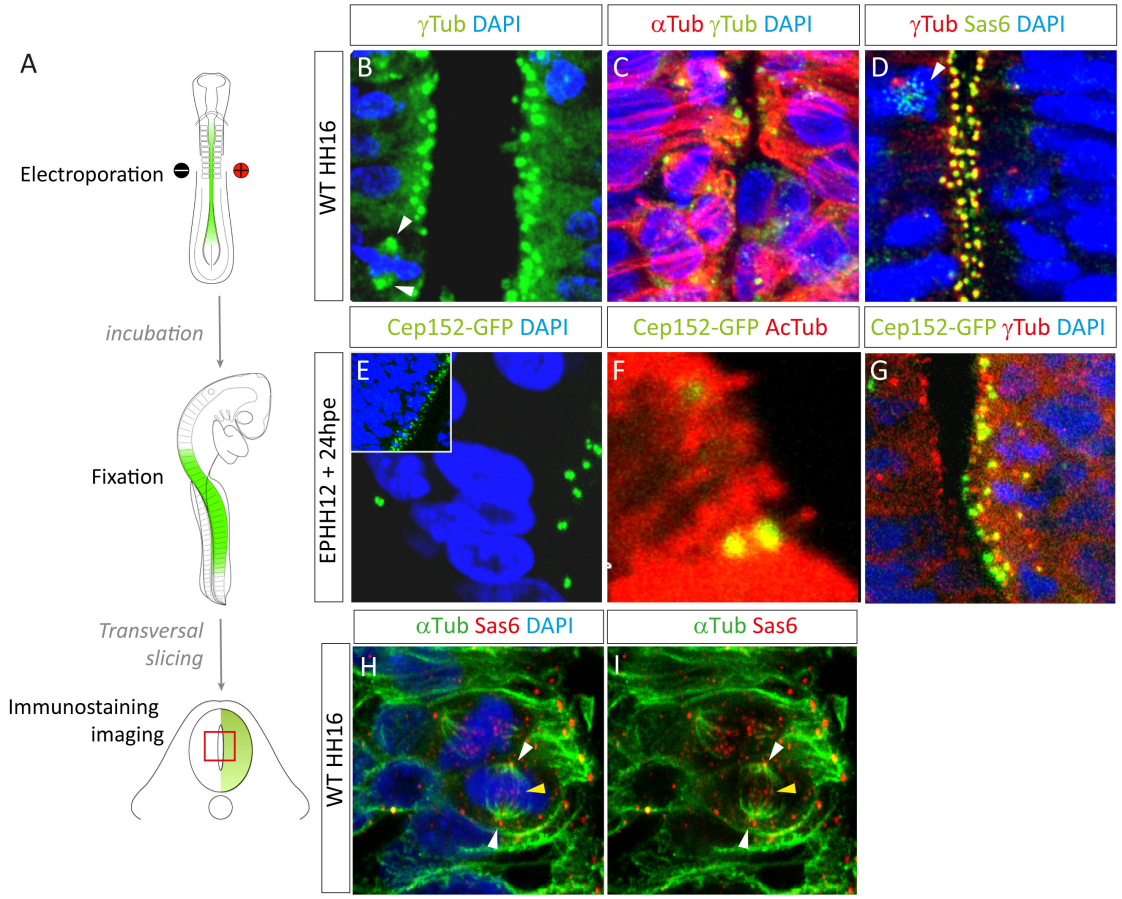

Figure 1: Sas6 localization in neural progenitor cells

(A) Schematic representation of experimental procedure. *In ovo* HH12 stage chick embryo electroporation is followed by 24h of incubation, embryo fixation, transversal sectioning, immunohistochemistry procedure and microscopy imaging analysis. (B-D) Antibodies for centrosome characterization. Images show magnifications at the apical neural tube region (red square). (B) γTubulin (green) labels the pericentriolar material (PCM), aligned in the apical region or at the mitotic spindle poles (white arrow). (C) αTubulin (red) labels mitotic spindles and other microtubular structures. γTubulin (green) localizes at the poles of the mitotic spindles. (D) Sas6 (green) colocalizes with γTubulin (red) at the centrosomes in interphase cells. (E) Electroporation of Cep152-GFP (green) labels centrioles at the apical cell tip in interphase cells. (F) Cep152-GFP has a basal location to cilia immunostained by Acetylated Tubulin (red). (E) Cep152-GFP centriole labeling (green) colocalizes with γTubulin (red) PCM staining. (H,I) Manification of mitotic cells stained with anti αTubulin (green) and antiSas6 (red) show Sas6 location plus end tips of the microtubules (yellow arrow) close to the nucleus, in addition to the spindle pole centrioles (white arrows). Nuclei stained with DAPI appear in blue.

FIGURE 2

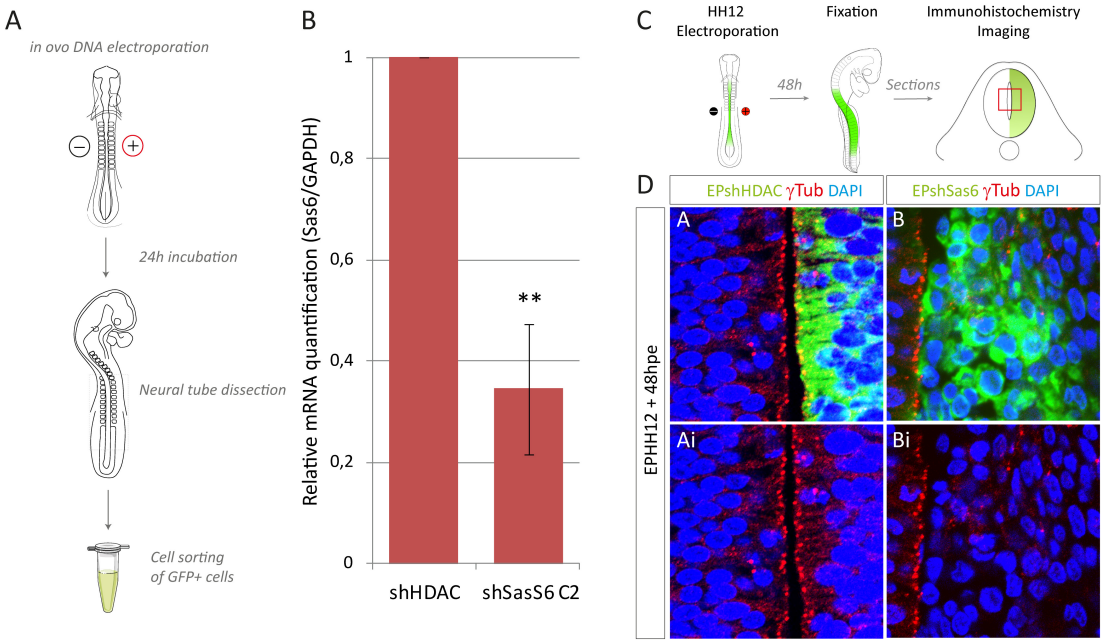

Figure 2: Sas6 is required for neuroepithelial integrity

(A) Schematic representation of RT-qPCE experimental procedure. Embryos were electroporated at HH12. After 24h of incubation, dissected neural tubes were trypsinized and GFP+ cells sorted. (B) RTqPCR show a significant decrease of Sas6mRNA levels in embryos electroporated with shSas6 in comparison to control shHDAC electroporation (normalized mRNA levels, arbitraty units (Mean ± s.d) (0.343 ± 0.132) $p \leq 0.01$). (C) Schematic representation of experimental procedure. *In ovo* HH12 stage chick embryo electroporation is followed by 48h of incubation, embryo fixation, transversal sectioning, immunohistochemistry procedure and microscopy imaging analysis. Images show magnifications at the apical neural tube region (red square) (D) Representative images showing γTubulin PCM staining (red) lining the apical region and spindle poles of mitotic cells in embryos electroporated with contro shHDAC-GFP (green) (A,Ai). After electroporation of shSas6-GFP (green), neuroepithelial architecture is lost and γTubulin staining diminished (red).
Nuclei stained with DAPI appear in blue.

FIGURE 3

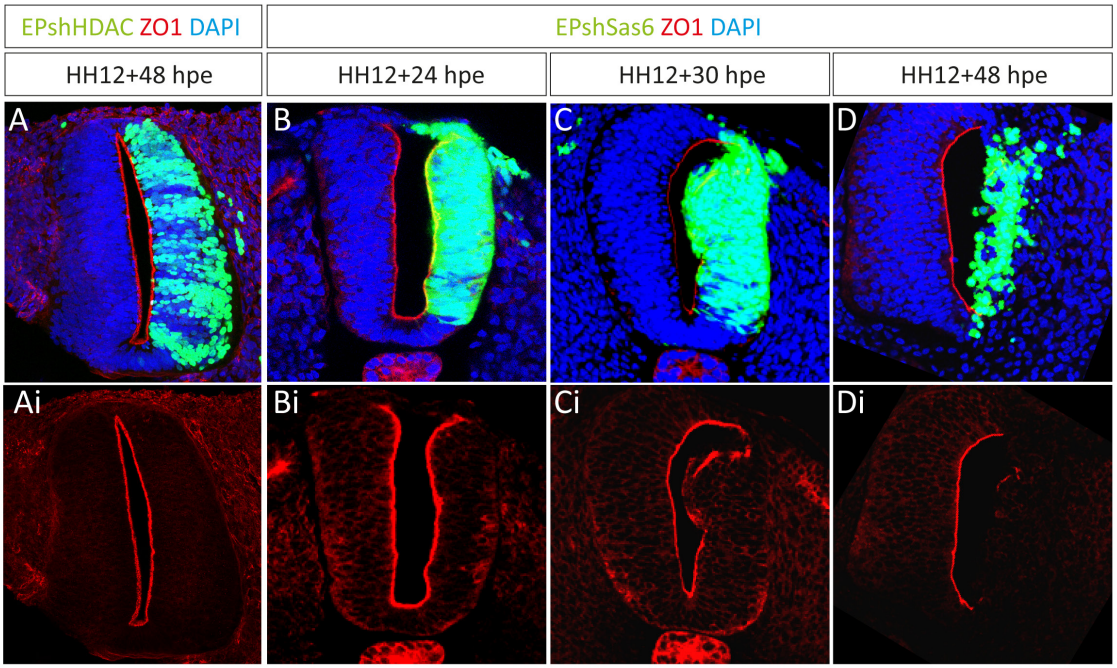

Figure 3: Time-course of shSas6 effects on neuroepithelial apical polarity

Representative transversal sections of HH12 electroporated embryos harvested at different times post electroporation show a loss of the apical polarity marker ZO1 after shSas6 expression. (A,Ai) HH12 control shHDAC-GFP electroporation (green) and immunostaining against the apical polarity marker ZO1 (red) show that tissue structure and polarity are not affected 48 hours post electroporation (hpe). (B,Bi) After 24h, HH12 shSas6-GFP electroporation (green) show no effects on ZO1 staining (red). (C,Ci) 30hpe, ZO1 is disturbed in the dorsal apical region. (D) 48hpe ZO1 marker is decreased and neuroepithelial structure lost.
Nuclei stained with DAPI appear in blue.

FIGURE 4

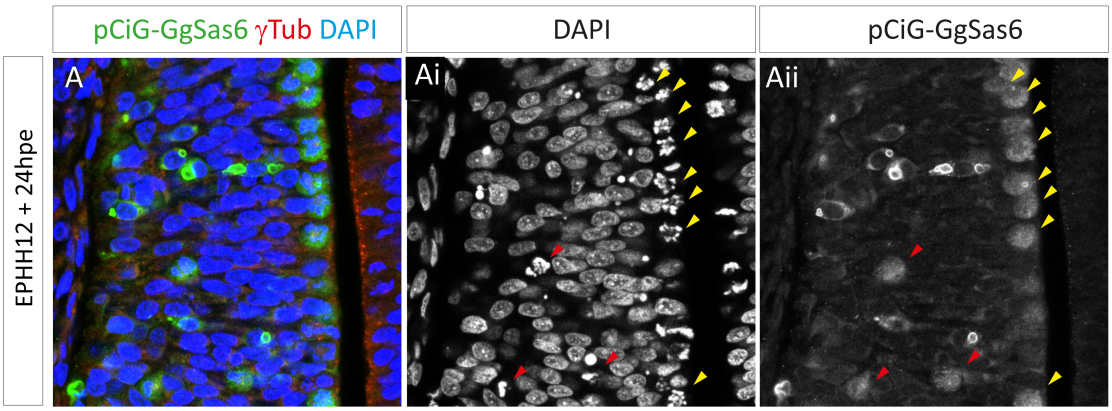

Figure 4: Sas6 gain of function

(A) Representative image of HH12 electroporation of pCIG GgSas6-GFP (green), stained against PCM marker γTubulin (red) and DAPI for nuclei (blue). 24 hours post electroporation (hpe) there is an increase in apical mitotic cells. (Ai) DAPI nuclei staining (white) shows the frequent apical mitosis (yellow arrows). Cells showing DNA condensation also appear in non-apical regions (red arrows). (Aii) Most of the pCIG GgSas6-GFP (white) electroporated cells appear as mitotic figures (Ai).

FIGURE 5

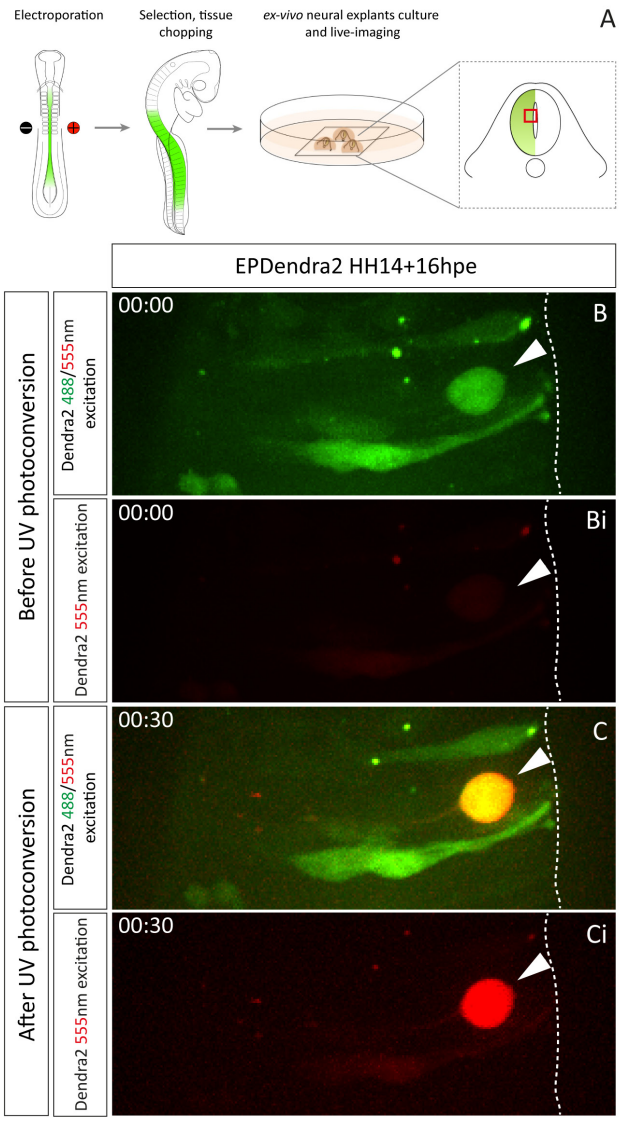

Figure 5: Dendra2 live photoconversion of mitotic cells

(A) Schematic representation of experimental procedure. *In ovo* HH12 stage chick embryo electroporation is followed by 24h of incubation, embryo harvesting and obtention of neural transverse sections that are cultured in glass-bottom dishes for subsequent live imaging. Red square represents the imaged region. (B,C) Representative snapshots of *ex vivo* cultured cells electroporated with the photoswitchable chromophore Dendra 2. (B) A mitotic cell (white arrow) shows rounding at the apical surface (white dotted line). Before UV-induced photoconversion, Dendra2 emission appears after 488nm wavelength laser excitation (green), but is not excited by 555nm wavelength laser light (Bi, red). (C) After a directed UV-laser light pulse, A fraction of Dendra2 protein irreversibly switches (red) and can be excited by 555nm wavelength laser light (C,Ci).

APPENDIX I

Cell Reports
Article

Sonic Hedgehog Signaling Switches the Mode of Division in the Developing Nervous System

Murielle Saade,[1] Irene Gutiérrez-Vallejo,[1] Gwenvael Le Dréau,[1] M. Angeles Rabadán,[1] David G. Miguez,[1] Javier Buceta,[2,*] and Elisa Martí[1,*]
[1]Instituto de Biología Molecular de Barcelona, CSIC, Parc Científic de Barcelona, Baldiri Reixac 20, Barcelona 08028, Spain
[2]Computer Simulation and Modeling Laboratory, Parc Científic de Barcelona, Baldiri Reixac 4-8, Barcelona 08028, Spain
*Correspondence: javier.buceta@pcb.ub.es (J.B.), emgbmb@ibmb.csic.es (E.M.)
http://dx.doi.org/10.1016/j.celrep.2013.06.038

SUMMARY

The different modes of stem cell division are tightly regulated to balance growth and differentiation during organ development and homeostasis, and these regulatory processes are subverted in tumor formation. Here, we developed markers that provided the single-cell resolution necessary to quantify the three modes of division taking place in the developing nervous system in vivo: self-expanding, PP; self-replacing, PN; and self-consuming, NN. Using these markers and a mathematical model that predicts the dynamics of motor neuron progenitor division, we identify a role for the morphogen Sonic hedgehog in the maintenance of stem cell identity in the developing spinal cord. Moreover, our study provides insight into the process linking lineage commitment to neurogenesis with changes in cell-cycle parameters. As a result, we propose a challenging model in which the external Sonic hedgehog signal dictates stem cell identity, reflected in the consequent readjustment of cell-cycle parameters.

INTRODUCTION

Stem cells are found in all multicellular organisms, and they are characterized by their capacity to self-renew. Such populations are maintained in two ways: through asymmetric divisions that generate one stem cell daughter with a developmental potential indistinguishable from that of the parental cell and a cell with a more restricted potential or through symmetric proliferative divisions that generate two stem cells and that serve to expand the stem cell pool. Alternatively, stem cells can undergo symmetric divisions that generate two cells that enter the differentiation pathway and exhaust the stem cell pool. The tight regulation of these different modes of division is crucial to balance growth and differentiation during organ development and homeostasis, and the subversion of these regulatory processes may lead to tumor formation. Nevertheless, the mechanisms controlling such events are far from being well understood.

The embryonic vertebrate nervous system represents an ideal model to study these processes, because these three modes of divisions occur early in the developing neuroepithelium. Neuroepithelial cells form a single-cell thick pseudostratified epithelium, with cell division occurring at the apical face (Sauer, 1935). The intense research over recent years has defined some of the intrinsic mechanisms that govern the mode of division in the developing nervous system. In *Drosophila* neuroblasts, particular attention has been paid to the contribution of centrosome asymmetry, spindle orientation, and the inheritance of apical membrane domains (Gonzalez, 2007; Rebollo et al., 2007; Yu et al., 2006). Although not fully understood, the picture emerging suggests that some of the intrinsic mechanisms controlling the mode of division in the developing vertebrate nervous system may reflect similar features (Das and Storey, 2012; Ghosh et al., 2008; Lesage et al., 2010; Marthiens and ffrench-Constant, 2009; Morin et al., 2007; Shitamukai et al., 2011; Wang et al., 2009). However, although these decisions are likely to be primarily dictated by extrinsic signals, the nature of these factors remains unknown.

Signaling through growth factors is associated with both development and cancer, and factors like Wnts and Hedgehog are believed to increase stem cell number by stimulating stem cell proliferation. However, the maintenance of stem cell identity is believed to depend on direct cell-to-cell communication and intrinsic cell behavior (Beachy et al., 2004; Pierfelice et al., 2011). Sonic Hedgehog (Shh) is a growth factor that augments proliferation in stem cell niches within the adult telencephalon (Lai et al., 2003; Machold et al., 2003). Moreover, Shh signaling promotes the proliferation and survival of neural progenitors in the developing nervous system (Cayuso et al., 2006), in addition to its main role in patterning (Briscoe, 2009).

In this study, we have analyzed the possibility that Shh signaling contributes to neural stem cell identity. We combined in vivo analysis with a mathematical model to quantify the dynamics of cell division in the motor neuron (MN) progenitor domain of the chick spinal cord. In this way, we unveil a switch in the mode of division, and, indeed, the model predicts this switch to occur in synchrony with the loss of Shh activity in the ventral spinal cord. Experimental data showed that maintaining Shh signaling artificially high is sufficient to prevent this developmental switch and to maintain self-expanding divisions. In

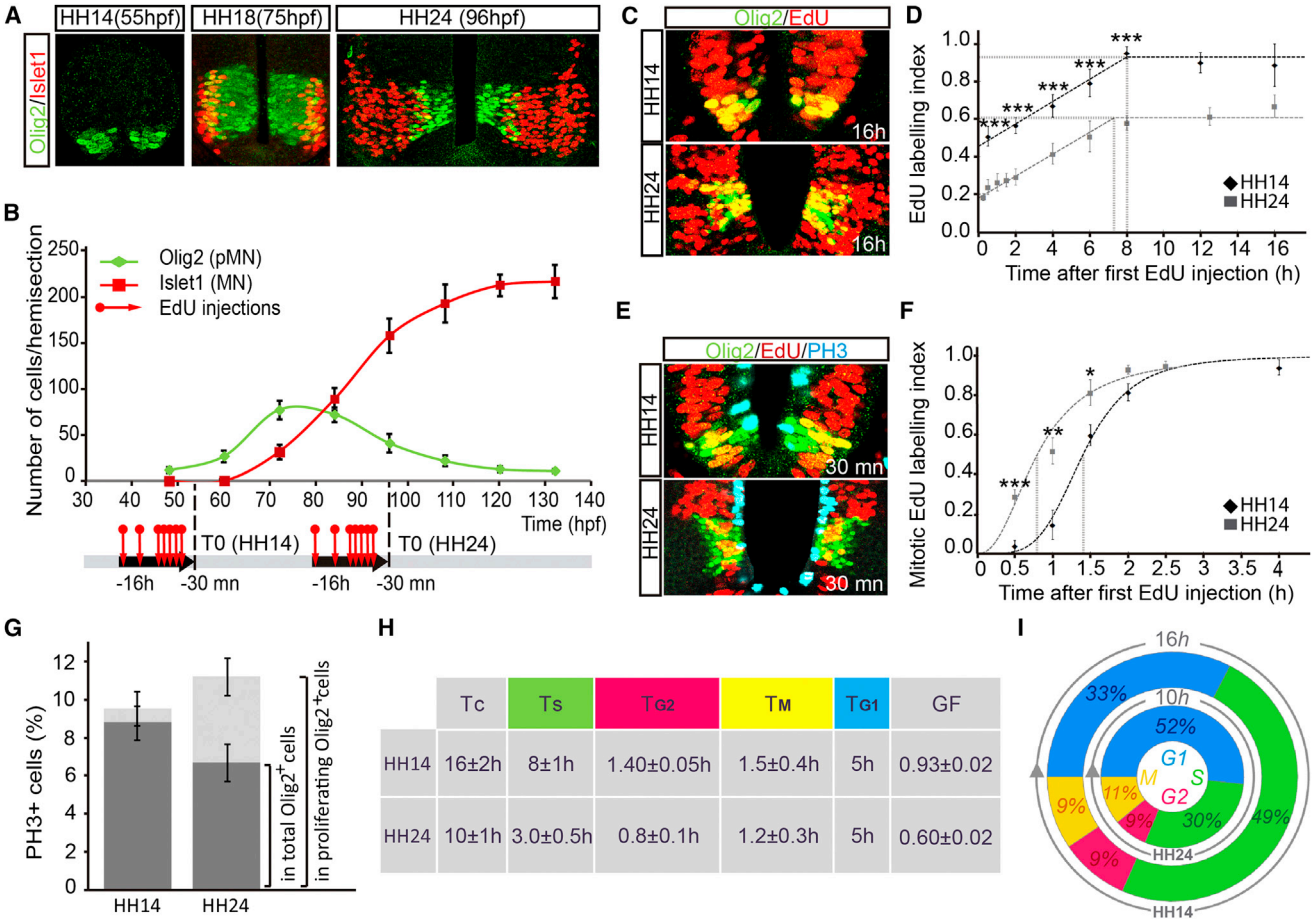

Figure 1. A Shorter Cell-Cycle Duration Is Concomitant with the Differentiation of Motor Neurons

(A and B) Quantification of the total number of pMN (green, Olig2$^+$ cells) and MN (red, Islet1$^+$ cells) emerging over 100 hr of development (hpf). In (A) representative immunostained sections are shown, whereas in (B) the number of cells expressing the marker at each time point is shown. EdU-injection times are indicated (red arrows), as is the timing of embryo harvesting, To (HH14 and HH24).

(C and D) Cumulative EdU labeling of Olig2$^+$ pMN. (C) Representative sections double stained for EdU-Olig2. (D) Quantification of EdU$^+$/Olig2$^+$ cells after cumulative EdU labeling for the times indicated. Dashes lines to the axes indicate GF and the time at which the labeling index reaches a plateau ($T_C - T_S$).

(E) Representative sections triple stained for EdU$^+$/Olig2$^+$/pH3$^+$.

(F) Quantification of double-labeled EdU$^+$/pH3$^+$ cells within the Olig2$^+$ domain. Dashes lines indicate T_{G2}.

(G) Percentage of pH3$^+$ cells in the total versus proliferating Olig2 domain according to T_C and GF.

(H) Cell-cycle parameters of Olig2$^+$ pMN progenitors at early (HH14) and late (HH24) phases, calculated from data in (C)–(G). The length of G1 (T_{G1}) was deduced from the lengths of the other phases ($T_C - T_S - T_{G2} - T_M$).

(I) Proportion of each phase in the whole cell cycle at HH14 and HH24, according to T_C.

Data represent mean ± SEM (*p < 0.05, **p < 0.01, ***p < 0.001).

addition, this study provides insight into the process linking lineage commitment to neurogenesis and changes in cell-cycle parameters, allowing us to propose a model in which Shh signaling dictates stem cell identity and the cell-cycle parameters rearrange as a consequence.

RESULTS

The Cell-Cycle Parameters Rearrange at the Time of Motor Neuron Differentiation

To study the dynamics of MN generation, we used specific markers that identify progenitors (Olig2) and newly differentiated MNs (Islet1: Figure 1A). We quantified the total number of Olig2$^+$ and Islet1$^+$ cells that emerge over a 100 hr period of development. Olig2$^+$ cells first appear at ~48 hr post fertilization (hpf; Hamburger-Hamilton [HH] stage 12, Hamburger and Hamilton, 1992), and there is a rapid expansion of these cells that peaks at ~70/80 hpf (HH stage 18) and thereafter becomes a small yet constant population after ~110/120 hpf (HH stage 25/26). Islet1$^+$ MNs first appear at ~60/70 hpf (HH stage 17/18), and their number increased before reaching a plateau at ~120 hpf (HH stage 26: Figure 1B). The rate at which Olig2$^+$ cells become incorporated into the system depends on the balance between self-expansion and the cell loss mediated by cell death.

However, experimental data reveal that apoptotic events can be disregarded during this developmental period (Cayuso et al., 2006). Thus, to study the rate of cell incorporation, we determined the cell-cycle parameters of Olig2$^+$ cells by assessing the accumulation of 5-ethynyl-2-deoxyuridine (EdU), both at the time of progenitor expansion (HH 14, 55 hpf) and at the time of progenitor consumption (HH24, 96 hpf, Figure 1B). The growth fraction decreased over the 100 hpf period analyzed (from 0.93 ± 0.02 during the expansion phase to 0.60 ± 0.02 in the reduction phase) (Figures 1C and 1D; Nowakowski et al., 1989). The length of G2+M+G1 was comparable in the early pMNs (8 hr) and in the late pMNs (7 hr). However, when the length of the S phase (T_S) and the total cell cycle (T_C) was calculated, these parameters were longer for early (8 ± 1 and 16 ± 2 hr) than for late (3.0 ± 0.5 and 10 ± 1 hr) pMNs, indicating that cells in the neurogenic phase have a shorter cell cycle.

To study the duration of the G2 and M phases, we combined EdU labeling with staining for phospho-Histone H3 (pH3). The appearance of EdU in mitotic figures revealed that there were fewer pH3/EdU-positive cells among the early pMNs than the late pMNs. Indeed, the average G2 length (T_{G2}) calculated from the curve was 1.40 ± 0.05 hr in the early phase, and it decreases to 0.8 ± 0.1 hr in late pMNs (Figures 1E and 1F). With regards to the M phase, we first determined the proportions of Olig2$^+$ cells that were in M phase in function of the pH3 immunolabeling, and we then calculated the length of the M phase (T_M) from the respective T_C and growth fractions (Figure 1G). Accordingly, the T_M appeared to be comparable in early (1.5 ± 0.4 hr) and in late pMNs (1.2 ± 0.3 hr; Figure 1H). These data revealed a global acceleration of division during the neurogenic phase due to the alteration of several cell-cycle parameters (Figure 1I), including the shortening of G2, as reported in the spinal cord (Peco et al., 2012), and a striking shortening of the S phase, as reported during the neurogenic phase in the cerebral cortex (Arai et al., 2011). Additionally, the proportion of the cycle occupied by the G1 phase was bigger in the late stages, as reported in the cerebral cortex (Arai et al., 2011; Lange et al., 2009; Pilaz et al., 2009).

Self-Expanding Proliferative Divisions Are Extinguished by the Time of Motor Neuron Generation

Although the rate of cell division accelerates, the number of MN progenitors decreases, suggesting that the mode of division might change over time. Each Olig2$^+$ cell can expand the pool of progenitor cells by generating two progenitors (PP). Alternatively, Olig2$^+$ cells can generate one (PN) or two Islet1$^+$ cells (NN: Figure 2A), although these events cannot be determined with the currently available molecular markers. Thus, to obtain the single-cell resolution necessary for such analysis, we generated molecular tools that unequivocally identify the three types of divisions in the chick NT and followed their behavior in vivo (Figure 2B).

We first took advantage of the Sox2p enhancer element that drives expression in the NT (Uchikawa et al., 2003) to track proliferative progenitors. The Sox2p-GFP construct proved to be a reliable reporter to selectively label divisions that will generate at least one progenitor (PP/PN: Figure S1; Movie S1). Next, we assessed the expression of the antiproliferative gene Tis21 (PC3, BTG2) (Iacopetti et al., 1999), whose expression in the mammalian neuroepithelium is restricted to neurogenic progenitors (Haubensak et al., 2004), and we demonstrated that the Tis21p-RFP construct identifies neurogenic divisions (PN/NN) after electroporation into the chick NT (Figure S1).

Coelectroporation of these two reporters revealed the coexistence of progenitors: (1) only expressing Sox2p-GFP (PP); (2) coexpressing Sox2p-GFP and Tis21p-RFP (PN); and (3) only expressing Tis21p-RFP (NN: Figures 2B and S2; Movie S2). Quantification of the three types of divisions in the pH3$^+$/Olig2$^+$ cell population showed that at the time of pMN pool expansion (60 hpf), 82% ± 4% of progenitors undergo PP divisions, whereas the remaining 18% ± 4% undergo PN divisions (Figures 2C–2E). By contrast, when Olig2$^+$ cell numbers reach the peak (~70 hpf) the PP mode of division is reduced to 37% ± 9% and replaced by 56% ± 6% PN and 7% ± 4% NN. Soon after the peak (~75 hpf) the PP mode of division accounts only for a 7% ± 6%, whereas 53% ± 7% PN and 40% ± 5% NN divisions are observed. At the time of pMN consumption (80–90 hpf), self-expanding progenitors are inexistent, whereas neurogenic progenitors are evenly distributed in this population (56% ± 3% PN and 44% ± 3% NN at 80 hpf, and 42% ± 6% PN and 58% ± 6% NN at 88 hpf: Figures 2C–2E). These data show that PP divisions are most abundant at the time of pMN growth, although this mode of division is rapidly replaced by PN and NN divisions in similar proportions. Accordingly, Olig2$^+$ progenitors are consumed by an accelerated rate of division and a change in the mode of division.

Mathematical Modeling Reveals a Developmental Switch for Motor Neuron Generation

To elucidate how the transition between the different modes of division is achieved as the cell cycle becomes shorter, we devised a mathematical model (Figures 3A and 3B). Our model is based on chemical kinetics formalism, and it assumes three irreversible reactions that account for the different modes of division observed: PP, PN, and NN. This set of reactions can be translated into a pair of ordinary differential equations that characterize the production of progenitor cells (P) and MNs (N) as a function of the rate of division (Supplemental Information). Thus, a change in the number of progenitors indicates a phase in which the rate of proliferative division is higher/lower than the rate of symmetric neurogenic divisions. Note that the rate of division is inversely proportional to the length of the cell cycle, which, according to our data, decreases as development progresses. We can reconcile these facts and reproduce the dynamics of progenitor and MN generation by invoking a sharp switch or transition in the mode of division (Figure 3A): before a given developmental time, t*, only PP divisions occur, whereas only PN/NN divisions occur after t*. This basic model already qualitatively reproduces the experimental observation in terms of the number of progenitors (P) and differentiated cells (N) and the proportion of divisions (Figure 3B). Moreover, it allows us to predict the number of MNs generated in the long-term N_{max} as a function of the maximum number of progenitors, P_{max}: $N_{max} = 3P_{max}$. Using this model, we can estimate the time of switching as ~80 hpf (HH stage 18). Importantly, we must stress that the fundamental mechanism driving this dynamic situation is

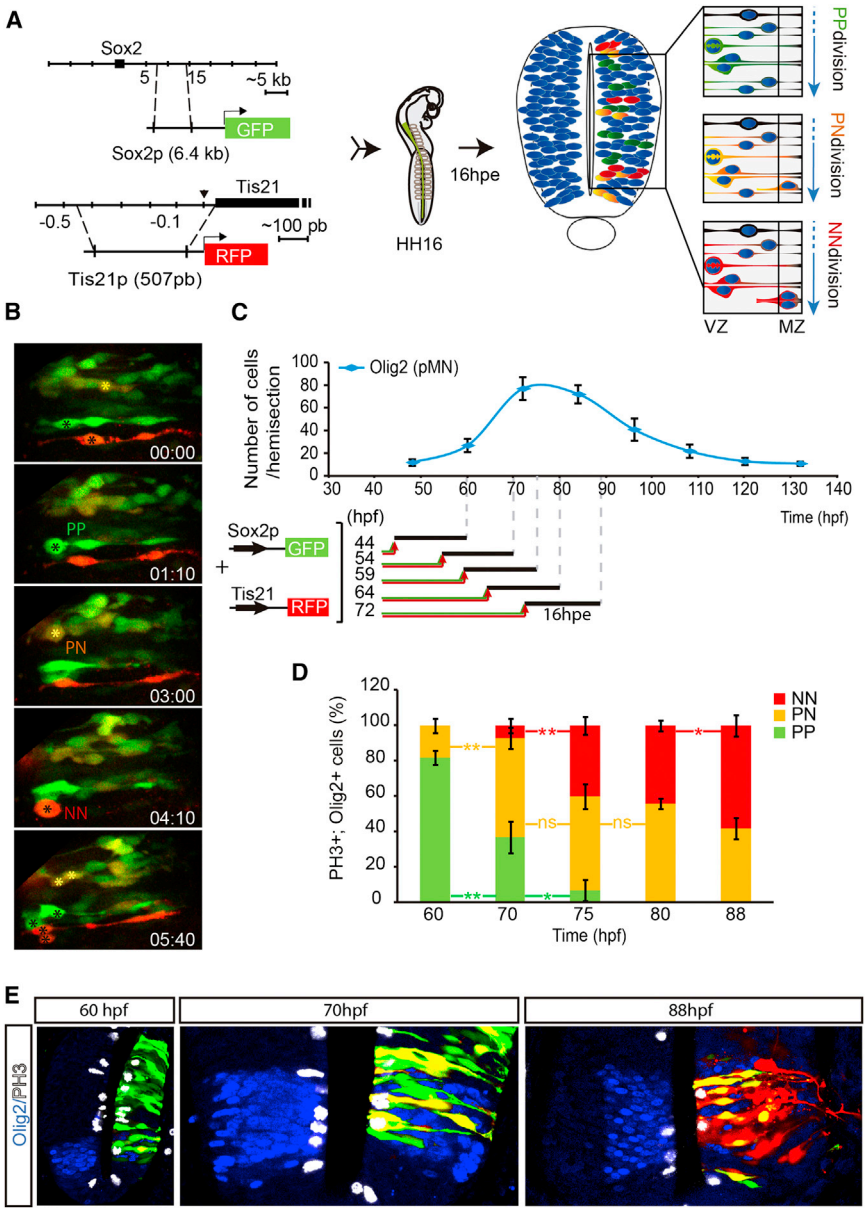

Figure 2. Self-Expanding Proliferative Divisions Are Extinguished at the Time of Motor Neuron Generation

(A) Representation of Sox2p-GFP and Tis21p-RFP reporter coelectroporation in chick NT to reveal PP divisions (green), PN divisions (yellow), and NN divisions (red).

(B) Snapshots of a time-lapse recording in vivo of the three color-coded divisions (see also Movie S1).

(C) Scheme representing the reporter coelectroporation experiments, harvested at 16 hpe.

(D) Quantification of pH3$^+$ cells expressing reporters within the Olig2$^+$ domain 16 hpe at the hpf indicated. Data represent the mean ± SEM (*ns*, nonsignificant, *p < 0.05, **p < 0.01). (For full characterization of the Sox2p-EGFP and Tis21p-RFP reporters, see Figures S1 and S2; Movie S2.)

(E) Representative sections quadruple stained for pH3 (white), Olig2 (blue), and Sox2p-GFP (green)/Tis21p-RFP (red) at the indicated stages.

not the difference in the cell-cycle duration (neither that between modes of cell division nor that at different developmental stages) but, rather, on the switch between the modes of division.

Further quantitative insight can be obtained by modifying the model in order to incorporate cell-cell/embryo-embryo variability, and a less restricted set of parameters in terms of the switch. Importantly, in this modified version of the model we included a fourth reaction (β) that accounts for the rate at which Olig2$^+$ cells are incorporated into the system de novo due to Shh-driven Olig2 expression (Balaskas et al., 2012), a number that cannot be resolved on the basis of experimental data. The model parameters were then estimated by minimizing the total error with respect to the experimental data (number of P and N cells) without any further constraints other than the cell-cycle duration at 55 hpf (16 ± 2 hr) and 96 hpf (10 ± 1 hr), and the initial cell number: $P_0 = 12$, $N_0 = 0$. In terms of the dynamics of the number of P and N cells (Figure 3C), and the proportion of the type of divisions (Figure 3D; Movie S3), our results are consistent with the experimental data. Indeed, as shown in Figure 3D, the results confirm the existence of a switch in the mode of division at 73 hpf (HH stage 18) driven by a sudden drop in self-expanding proliferative divisions (see Experimental Procedures). Importantly, our model also suggests a sharp decrease in the incorporation of new Olig2$^+$ cells (β reaction) at that time, as well as predicting an abrupt change in the length of the cell cycle at 83 hpf. The model shows that the maximum incorporation of Olig2$^+$ cells due to Shh-mediated gene expression is around one cell per hour and this contributes as much as 30% of the population of progenitor cells up to the switching time (see Experimental Procedures).

Altogether, our mathematical analysis indicates the existence of a developmental switch at HH stage 18. The fact that the sharp reduction in the number of PP divisions is synchronized with a sudden loss in the Shh-mediated incorporation of Olig2$^+$ cells suggests that Shh activity may act as an external signal controlling this process, a hypothesis that we tested experimentally.

Sonic Hedgehog Controls the Mode of Division in the Neural Tube

We first determined the temporal and spatial dynamics of intracellular Shh signaling in the chick NT, by electroporating either a 8×3′Gli-BS-RFP or a 8×3′Gli-BS-Luc reporter. Shh-responding

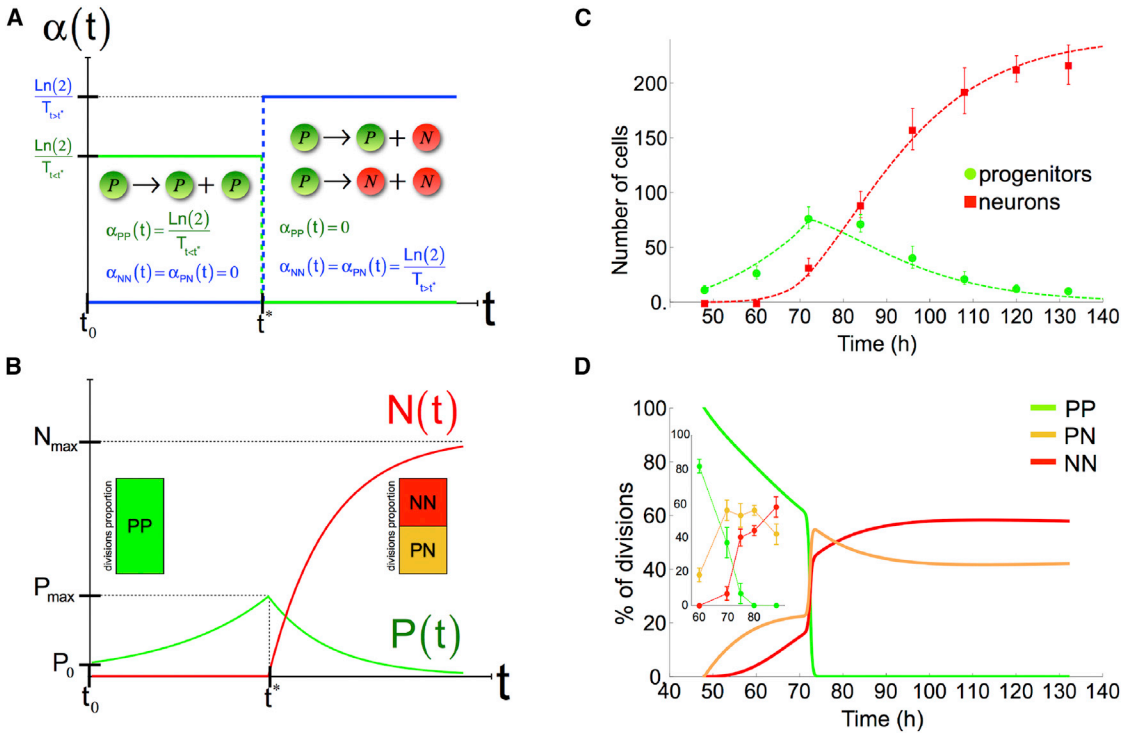

Figure 3. Mathematical Modeling Reveals a Developmental Switch

(A) α(t) stands for the division rate that is inversely proportional to the cell-cycle duration T. Before t*, only proliferative divisions (PP) take place, whereas after t* only neurogenic divisions occur (either PN or NN).

(B) This hypothesis can be translated into a set a differential equations that qualitatively reproduces the experimental data in terms of the P and N cell numbers and the division proportions (see Experimental Procedures). This basic model also allows to estimate the expected number of MNs in the long run (N_{max}) as a function of the maximum number of proliferative cells in the domain (P_{max}): $N_{max} = 3P_{max}$.

(C) A refinement of the model that incorporates variability and the de novo incorporation of Olig2$^+$ cells, due to Shh signaling, quantitatively reproduces the experimental data of cell numbers: symbols/lines correspond to the in vivo/in silico data.

(D) The modeling predicts a developmental switch in terms of the division modes around 73 hpf (HH18) characterized by a sudden drop of PP divisions and a smoother change in terms of the PN and NN divisions proportions. The inset stands for the experimental data in terms of the division proportions (see Figure 2D). As predicted by the modeling, before the switch the PN divisions proportion is larger than the NN one, around the switching time the PN divisions show a maximum, and finally, after the switch, the NN divisions proportion surpasses the PN ones.

See also Movie S3.

cells were restricted to the ventral NT, largely within the pMN domain (Olig2$^+$ cells; 26% ± 6% RFP$^+$ cells at ~45–50 hpf, Figures 4A and 4D). Endogenous Shh activity peaks at ~60–66 hpf (49% ± 4% RFP$^+$ cells), following this peak, the amplitude of Gli activity declines progressively (30% ± 1% RFP$^+$ cells at ~75–82 hpf; 14% ± 2% RFP$^+$ cells at ~90–98 hpf), similar to what was recently reported in a transgenic mouse (Balaskas et al., 2012). By luciferase assay, a similar profile representing Shh activity in the NT has been obtained (Figures 4C and 4D). Interestingly, the high activity of Shh signaling coincides with the expansion phase of the Olig2 domain followed by a progressive decrease (70/80 hpf) concomitant with appearance of the first neurogenic divisions. Later on, Gli activity is barely detectable in the ventral NT from ~90 hpf onward, when PP divisions are extinguished (Figures 4A–4D). All these observations suggest a role for Shh signaling in the expansion of progenitors in the system.

To test the potential role of Shh in controlling the mode of division, we artificially maintained Shh activity high by introducing a dominant active form of the Hh receptor Smoothened (SmoM2) (Hynes et al., 2000) (Figure 5A). HH12 embryos coelectroporated with SmoM2 together with the Sox2p /Tis21p reporters were analyzed at 24 hour post exposure (hpe; 75 hpf), in which the rate of PP divisions (in pH3$^+$ cells) increased significantly (from 29% ± 6% in controls to 58% ± 7% in SmoM2 embryos). The increase in PP divisions takes place at the expense of NN divisions (20% ± 5% in the control as opposed to 6% ± 1% in SmoM2 embryos), together with a reduction, although not statistically significant in the proportion of PN divisions (51% ± 7% in the control to 36% ± 7% in SmoM2 embryos (Figures 5B and 5C).

The same phenotype has been obtained by introducing another activator of Shh signaling, a dominant-negative form of PKA (dnPKA) (Figures S3).

These data indicate that active Shh signaling maintains PP divisions and prevents the switch to neurogenic divisions. These changes in the mode of division would not only result in the overgrowth reported previously (Cayuso et al., 2006) but, in addition,

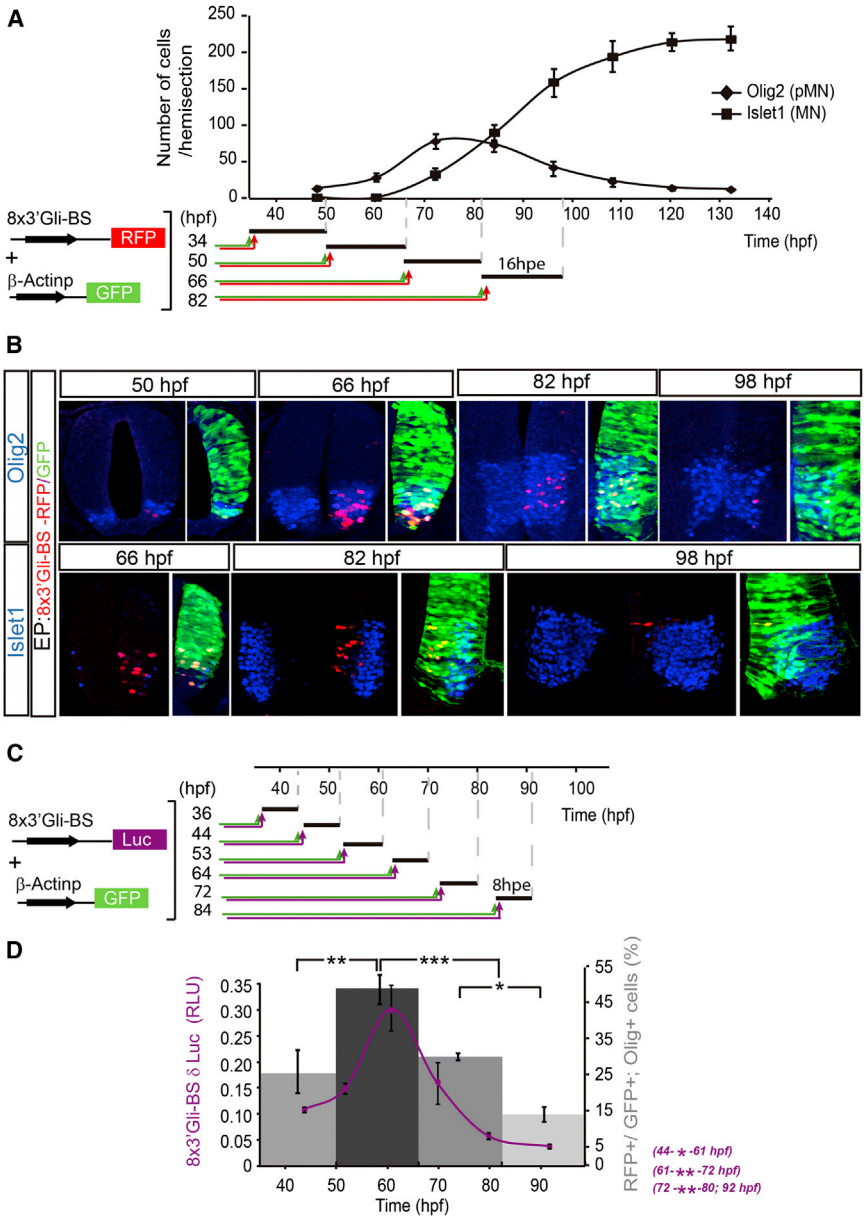

Figure 4. Analysis of Temporal and Spatial Dynamics of Intracellular Shh Signaling in the Ventral NT

(A) Scheme representing the 8×3′Gli-BS-RFP reporter coelectroporation experiments, harvested at 16 hpe.

(B) Representative sections triple stained for Olig2 or Islet1 (blue), GFP-electroporation control (green), and 8×3′Gli-BS-RFP (red) at the indicated hpf. Note that RFP$^+$ cells are excluded from the Islet1$^+$-differentiated MNs.

(C) Scheme representing the 8×3′Gli-BS-Luc reporter coelectroporation experiments, harvested at 8 hpe.

(D) Solid bars represent quantification of Olig2$^+$/GFP$^+$/RFP$^+$ cells 16 hpe at the hpf indicated. Purple line represents Luc/Renilla activity, 8 hpe, at the hpf indicated.

Data represent the mean ± SEM (*p < 0.05, **p < 0.01, ***p < 0.001).

in an unbalanced generation of neurons. As such, embryos analyzed 48 hpe of Shh signaling activation had more progenitors and fewer neurons (Figure S3). Moreover, when we interrogate our mathematical model for the mode of division, in response to a 24 hr delay in t^* (see Experimental Procedures), we observed a result that is in agreement with our experimental data (Figure 5C).

The complementary experiments were performed by prematurely reducing Shh activity through the expression of a dominant active form of the Hh receptor, Patched1 (mPtc1$^{\Delta loop2}$) (Briscoe et al., 2001). Dampening Shh activity reduced the rate of PP divisions from 25% ± 7% in the control embryos to 8% ± 1% in the mPtc1$^{\Delta loop2}$-EP embryos. This reduction in PP divisions took place at the expense of NN divisions, which increased from 18% ± 2% in the control to 42% ± 8% in mPtc1$^{\Delta loop2}$ embryos, whereas PN divisions remained largely unaffected (57% ± 8% in the control and 50% ± 7% in mPtc1$^{\Delta loop2}$ embryos: Figures 5D and 5E). Again, the in silico counterpart provides similar results when we anticipate t^* by 16 hr (Figure 5E). In summary, these data indicate that active Shh signaling favors the self-expansion mode of division and that a reduction in Shh activity is required to switch the mode of division to that which generates neurons.

Shh Signaling Instructs Stem Cell Commitment, which Is Reflected in the Readjustment of Cell-Cycle Parameters

Lineage commitment of stem cells and cell-cycle progression are two tightly linked events, although it is still unclear whether changes in cell-cycle parameters are the cause or the consequence of differentiation. Our experimental data revealed an accelerated rate of division in the neurogenic phase, although the mathematical model does not attribute particular relevance to the speeding up of the cell cycle when defining the parameters underlying differentiation. Thus, we tested whether stem cell maintenance mediated by Shh involves the regulation of cell-cycle parameters. We examined this by coelectroporating the two reporters (Sox2p/Tis21p) together with control or Shh activator (GOF), and, at 24 hpe, single-cell suspensions were sorted via fluorescence-activated cell sorting (FACS), and the proportions of PP, PN, and NN cells were assessed. The results confirmed the histological data obtained, because activation of Shh signaling increased the proportion of PP divisions from 37% ± 4% in the controls to 52% ± 2% in the Shh-GOF embryos. This increase occurred at the expense

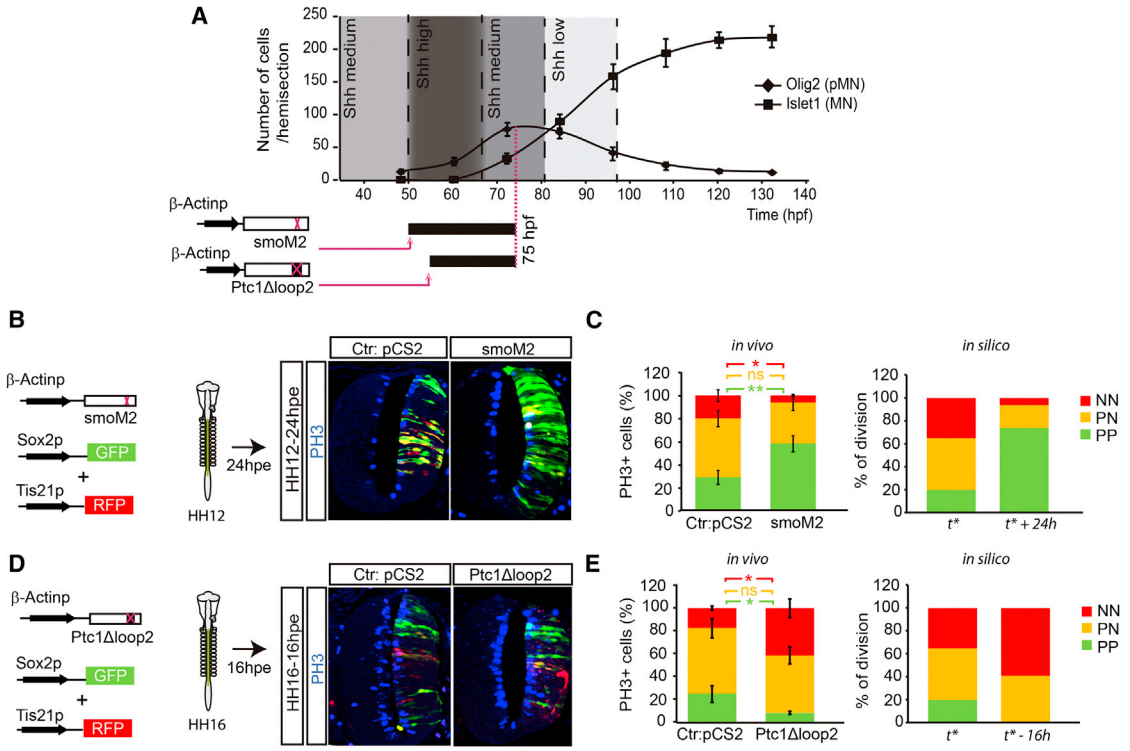

Figure 5. Shh Activity Promotes the Self-Expanding Mode of Division in the Neural Tube

(A) Levels of endogenous Shh activity (adapted from data on Figure 4) in the ventral NT is imposed onto the dynamics of MN generation over 100 hr of chick development (hpf). To experimentally manipulate Shh levels, gain of function was achieved by electroporation of SmoM2 and loss of function by electroporation of $Ptc^{\Delta loop2}$ (solid bars indicate the timing of manipulation).

(B and C) PP divisions persist when the Shh pathway is constitutively activated. (B) Representative sections immunostained for pH3 (blue) of control (pCS2) or Shh gain of function (GOF; SmoM2) embryos coelectroporated with Sox2p (green)/Tis21p (red) (C) in vivo quantification of reporter-expressing mitotic cells ($pH3^+$). Data represent mean ± SEM (ns, nonsignificant, *$p < 0.05$, **$p < 0.01$). In silico, the mathematical model reproduces the experimental data in terms of the proportion of divisions when Shh activity (*t**) is delayed 24 hr.

(D and E) Inhibition of Shh signaling drives the switch to NN divisions. (D) Representative sections of control (pCS2) and Shh loss of function (LOF) condition ($Ptc^{\Delta loop2}$) embryos coelectroporated with Sox2p/Tis21p and immunostained for pH3 (blue). (E) In vivo quantification of reporter-expressing mitotic cells ($pH3^+$).

Data represent the mean ± SEM (ns, nonsignificant, *$p < 0.05$). In silico, the mathematical model reproduces the experimental data in terms of the proportion of divisions when Shh activity (*t**) is anticipated 16 hr. See also Figure S3.

of NN divisions (23% ± 1% in the control as opposed to 11% ± 2% in Shh-GOF), with no significant changes in the proportion of PN divisions (41% ± 4% in the control to 37% ± 1% in Shh-GOF: Figure 6A). The DNA content was assessed in such samples by flow cytometry (following Hoechst staining). In a population of asynchronous cycling cells, the fraction of cells in a given phase of the cell cycle (G1/G0 identified by 2n content and G2/M identified by 4n) is proportional to the length of that phase, and this is relative to the total length of the cell cycle.

The DNA content profiles obtained for PP and PN cells were very similar in control and Shh-overexpressing embryos (PP, 60% ± 2% of 2n and 11% ± 2% of 4n in controls as opposed to 62% ± 3% of 2n and 9% ± 2% of 4n in Shh-GOF; PN, 50% ± 2% of 2n and 17% ± 2% of 4n in controls as opposed to 47% ± 5% of 2n and 16% ± 4% of 4n in Shh-GOF: Figure 6B). Hence, whereas activation of the Shh pathway increased the proportion of PP divisions, cell-cycle parameters were not affected. By contrast, assessing the DNA content of the NN cell population revealed a very different profile, with numerous aneuploid cells and a nonnegligible proportion of hypoploid cells (<2n: Figure 6B). Interestingly, this particular DNA-content profile was comparable in NN divisions from control and Shh-GOF electroporated embryos: 26% ± 2% of 2n, 15% ± 3% of 4n in controls as opposed to 22% ± 3% of 2n, 16% ± 6% of 4n in Shh-GOF embryos (Figure 6B). Accordingly, this feature would appear to be associated with neurogenesis and not with morphogen activity.

DISCUSSION

Using newly developed markers that identify the three modes of division in vivo (self-expanding, PP; self-renewing, PN; and self-consuming, NN) and a mathematical model that predicts their dynamics, our study reveals a role for the morphogen Sonic hedgehog in the maintenance of stem cell identity in the developing ventral spinal cord.

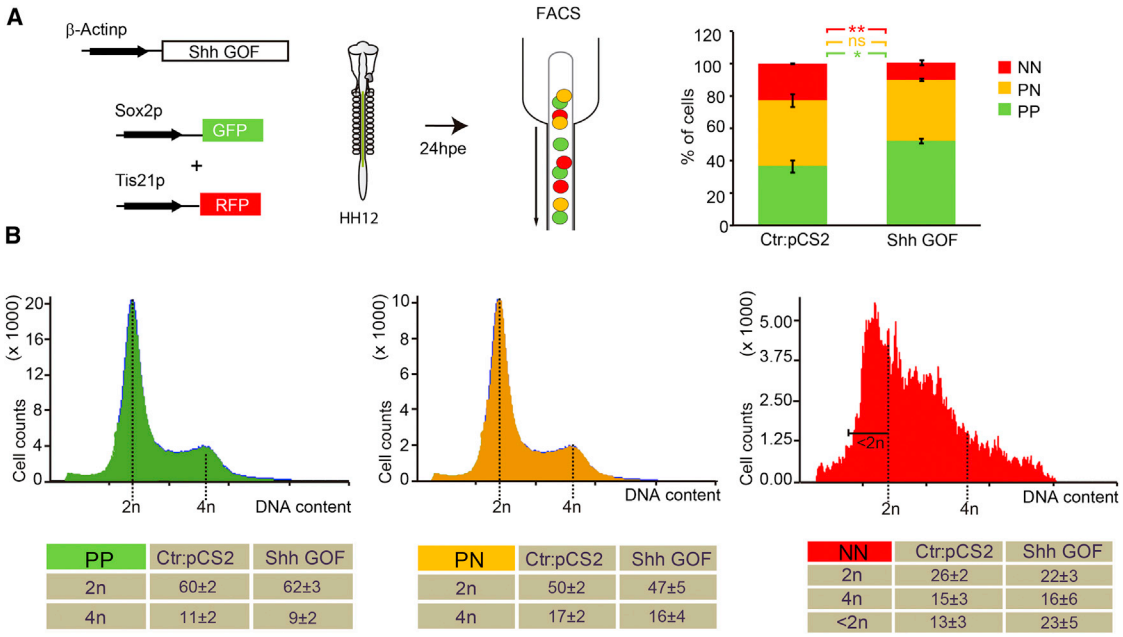

PP	Ctr:pCS2	Shh GOF
2n	60±2	62±3
4n	11±2	9±2

PN	Ctr:pCS2	Shh GOF
2n	50±2	47±5
4n	17±2	16±4

NN	Ctr:pCS2	Shh GOF
2n	26±2	22±3
4n	15±3	16±6
<2n	13±3	23±5

Figure 6. *Shh* Activity Promotes the Self-Expanding Mode of Division and the Cell-Cycle Parameters Are Rearranged as a Consequence

(A) Constitutive activation of the Shh pathway augments the proportion of Sox2p$^+$ cells at the expense of Tis21p$^+$ cells. Electroporated NTs were dissociated at the time indicated and sorted by flow cytometry for GFP, GFP/RFP, RFP expression in control (Ctr: pCS2), and Shh-GOF embryos. Quantification shows reporter-expressing cells in each condition. Data represent the mean ± SEM (ns, nonsignificant, *$p < 0.05$, **$p < 0.01$).

(B) Flow cytometry analysis of samples to assess the DNA content (Hoechst incorporation) in each of the three cell populations sorted by GFP, GFP/RFP, and RFP. The fraction of cells in a given phase of the cell cycle is shown for each condition (G1/G0 = 2n, G2/M = 4n and <2n in case of hypoploidy).

Cell-Cycle Parameters and Stem Cell Identity

This study takes advantage of the unequivocal identification of MN progenitors by Olig2 expression and newly differentiated MNs by Islet1 expression. We define a phase of progenitor expansion followed by a phase of reduction in which MN progenitors are consumed. We used cumulative EdU labeling to provide a breakdown of the cell-cycle parameters in these two phases, defining the T_C in the expansion phase to be very similar in length to that determined by live imaging of the chick spinal cord in organotypic slice culture at an equivalent stage (Wilcock et al., 2007). However, the first striking observation is the significant shortening of the T_C in the neurogenic phase; the length of the early G1 phase is maintained constant, even though it now represents ~50% of the whole cycle.

Previous analyses of cell-cycle kinetics during neurogenesis considered neural progenitors as a uniform population. However, a recent study in the developing mammalian telencephalon discriminated four subpopulations of progenitors considering proliferative versus neurogenic divisions in both apical and basal progenitor populations (Arai et al., 2011). These analyses demonstrate that the variations of two cell-cycle phases, G1 and S, are correlated to distinct behaviors. A G1 lengthening is associated with the transition from apical to basal progenitors and thereby represents a direct relation with a restriction in lineage potential. However, S phase shortening is correlated to terminal division and commitment to neuronal differentiation, both in apical and basal progenitors. Because the duration gained by G1 lengthening is longer than the duration lost due to S phase shortening, the transition from apical to basal progenitors is accompanied by a global increase in cell-cycle duration. Thus, this study confirms the recent evidence that neuron production is associated with short cell cycle (due to S phase shortening) and provides additional observations by dissecting the relationships between cell-cycle parameters and lineage restriction and commitment.

Our results show that the T_C is shortened by curtailing the late S and G2 phases of the cycle. The striking shortening of the S phase is reminiscent of the data obtained in terminal committed progenitors in the developing mammalian cerebral cortex (Arai et al., 2011), and it raises the intriguing possibility that the duration of the S phase is a key factor in the maintenance of the proliferative capacity of neural stem cells. Indeed, self-expanding progenitors should be more dependent on DNA replication fidelity and repair, as errors would be inherited by their progeny. Moreover, progenitors committed to differentiation in the mammalian cerebral cortex upregulate genes implicated in shortening the S phase (Arai et al., 2011).

We sorted the three populations and analyzed their DNA content by flow cytometry using the newly developed reporters to identify the three progenitor identities (PP, PN, and NN). The profiles of DNA content obtained for PP and PN populations were comparable, with a similar proportion of 2n-containing cells (~50%/60%) representing cells within the G1 phase, and a similar proportion of 4n-containing cells (~10%/16%) representing cells in the G2/M phases. In this study, cell-cycle parameters have been analyzed separately in each type of progenitor,

indicating that the switch from divisions driving cell expansion to that of self-renewal takes place without significant rearrangement of cell-cycle parameters.

The second striking observation is that the DNA content of progenitors committed to a terminal NN neurogenic division displays a very unusual profile, with numerous aneuploidies and a nonnegligible proportion of hypoploid cells (<2n). Somatic aneuploidies are at least partially generated by chromosome missegregation during mitosis, and they might account for the origins of neuronal diversity in the normal nervous system (Muotri and Gage, 2006). Aneuploidies in the embryonic cerebral cortex account for ~30% of the total pool of neural progenitor cells (Rehen et al., 2001), and they are also present in the developing retina (Morillo et al., 2010). This report of aneuploidies in the spinal cord provides evidence that this phenomenon may be a general mechanism operating throughout the developing CNS, whereby shortening of the S phase in terminal neurogenic divisions would expose cells to more chromosome missegregation, and the resulting aneuploid cells may contribute to neuronal diversity. However, these data indicate that the rearrangements in cell-cycle parameters are the consequence and not the cause of cell-fate choices in neurogenesis.

The Contribution of Quantitative Biology

Here, we present a mathematical model that highlights a straightforward mechanism, a division mode switch, that couples extrinsic Shh signaling to the maintenance of stemness and consequently, with the dynamics of proliferation and the generation of appropriate numbers of MNs. Our proposal transcends the customary definition of "model" in biology because it provides a quantitative mathematical description of the mechanism that not only explains the observed phenomenology, but also allows predictions to be made. Indeed, our approach can produce a long-term prediction of the number of MNs as a function of the maximum number of stem cells, which was consistent with the experimental observations. Moreover, we benefited from this model to elucidate the relative contribution of a regulatory process during proliferative expansion, namely, the Olig2 expression driven by Shh, which would have been impossible to resolve on the basis of molecular markers. In this regard, we estimated that delayed Shh-driven Olig2 expression contributes as much as 30% to the final number of stem cells, that symmetric NN neurogenic divisions do not consume proliferative cells between stages HH14-HH18, and that most of the increase in the stem cell pool during that period is due to self-expanding proliferative divisions. As a matter of discussion, we note that the developmental switch, although sharp and validating our proposal, is somehow smoother in experiments than in the modeling prediction. In this regard, we point out that the timing of the experimental events (embryonic stage in hours) cannot possibly be assessed with total precision and the modeling cannot capture this fact. The latter leads to a source of unpredictability that we interpret as the origin of this quantitative, but not qualitative, disagreement. In any case, the modeling correctly captures and predicts the mechanism underlying the cellular kinetics and has been shown to be a valid and predictive framework for tissue homeostasis due to proliferation and differentiation in the developing neural tube.

The Contribution of Sonic Hedgehog to Stem Cell Fate

During normal growth of the nervous system, Shh signaling plays an important role in maintaining neural progenitor proliferation by directly controlling the expression of cell-cycle regulators (Alvarez-Medina et al., 2009; Bénazéraf et al., 2006; Cayuso et al., 2006; Kenney and Rowitch, 2000; Lobjois et al., 2004; Peco et al., 2012). However, we propose here a challenging model in which Shh signaling drives cell-fate choices upstream of the rearrangement of cell-cycle parameters. Thus, the oncogenic capacity of Hh signaling (Beachy et al., 2004) might depend not only on the expression of cell-cycle regulators, but also on the maintenance of stem cell identity. The responses to Shh are mediated by two transmembrane proteins, Smoothened (Smo) and Patched (Ptc), as well as by downstream transcription factors of the Gli family (Ingham et al., 2011; Jiang and Hui, 2008). Moreover, Hedgehog signaling in vertebrates is strongly connected to the primary cilium (Huangfu and Anderson, 2005). The cilia of neuroepithelial cells are located apically, the membrane domain in which the proteins required for Shh activity localize, including the Shh ligand (Chamberlain et al., 2008) and components of the signal transduction machinery (Ingham et al., 2011; Jiang and Hui, 2008). The ciliary basal body, formed from the mother centriole, serves as a docking area for a large number of pericentriolar proteins, including a pool of PKA that participates in the transduction of Shh signals (Barzi et al., 2010). Because a functional link between centriole maturation and the maintenance of stem cell identity was recently demonstrated in the developing mammalian neocortex (Wang et al., 2009), it is tempting to speculate that the daughter cell that inherits the mother centriole projects a cilium before its sister cell, and thus it continues to receive Shh signals. Additional intrinsic mechanisms related to maintenance of stem cell identity in the developing vertebrate nervous system, such as the control of spindle orientation and the inheritance of apical membrane domains (Lesage et al., 2010), might also be directly regulated by the reception and or activation of Shh, possibilities that open an attractive field for future research.

EXPERIMENTAL PROCEDURES

DNA Constructs

The Sox2p-GFP reporter corresponds to the chicken genomic fragments that cover the 7.6–14 kb Sox2 locus (Uchikawa et al., 2003), and it was cloned into the ptk:EGFP plasmid. The Tis21 promoter (nucleotides −442 to +65) was amplified by PCR from the mouse genome using the following primers:

5′-GGGATGAGTGGCAGAGATGT-3′
5′-GGTGGCTGAGGAAGTAGCTG-3′,

and then cloned into the ptk:RFP plasmid (Uchikawa et al., 2003). The DNAs inserted into the pCIG or pCS2 expression plasmid (with or without –H2B:GFP or –H2B:RFP) were a mutant form of Patched1 (mPtc1$^{\Delta loop2}$) (Briscoe et al., 2001), a mutant version of Smoothened (SmoM2) (Hynes et al., 2000), and a mutant version of PKA-R1 (dnPKA) (Epstein et al., 1996).

Endogenous Shh activity was tested by electroporation of a Gli-BS-RFP reporter construct containing synthetic 8×3′Gli binding sites (Sasaki et al., 1997).

Chick Embryo In Ovo Electroporation

White-Leghorn chick embryos were staged according to Hamburger and Hamilton (HH) (Hamburger and Hamilton, 1992) and electroporated with

Clontech Laboratories purified plasmid DNA (1–2 μg/ml) in H2O with Fast Green (50 ng/ml). Transfected embryos were allowed to develop to the specific stages and then dissected out and processed as indicated.

In Situ Hybridization, Immunohistochemistry, and Cumulative EdU Incorporation

For in situ hybridization, embryos were fixed overnight at 4°C in 4% paraformaldehyde diluted in PBS, rinsed, and processed for whole-mount RNA in situ hybridization using probe to chickTis21 from the chicken EST project following standard procedures.

Immunofluorescence and EdU staining were performed on transverse sections (40 μm), after fixation in 4% paraformaldehyde for 2–4 hr at 4°C. EdU (1 mM) was injected into the lumen of the chick NT at ~2 hr intervals up to 8 hr and ~4 hr up to 16 hr before harvesting. EdU was detected in sections using the Click-iT EdU imaging kit (Invitrogen). The antibodies used were anti-Olig2 (Millipore), anti-islet1 (DSHB), anti-PH3 (Upstate), anti-Sox2 (Invitrogen), and anti-Tuj1 (Covance), and anti-RFP (kindly provided by Dr. S. Pons, IIBB-CSIC). The cells were counted in five sections from each of the six embryos in each experimental condition (n > 3).

Fluorescence-Activated Cell Sorting

Embryos were electroporated with dnPKA or pCIG in combination with Sox2p-GFP and Tis21p-RFP at the stages indicated, and 24 hpe a single-cell suspension was obtained after a 10–15 min digestion in Trypsin-EDTA (Sigma). At least three independent experiments (six embryos in each experimental condition) were analyzed by FACS. Hoechst and GFP/RFP fluorescence were determined by flow cytometry using a MoFlo flow cytometer (DakoCytomation), and the cellular DNA content was analyzed (Ploidy analysis) in single fluorescence histograms using Multicycle software (Phoenix Flow Systems).

In Vivo Luciferase Reporter Assay

Embryos were electroporated with the DNAs indicated together with a Sox2p-luciferase reporter, a NeuroDp-Luciferase reporter (Huang et al., 2000), or with a 8 × 3′Gli-BS luciferase reporter construct containing synthetic Gli binding sites (Sasaki et al., 1997), and with a renilla-construct (Promega) for normalization. GFP-positive NTs were dissected out at 48 hpe and homogenized in passive lysis buffer. Firefly- and renilla-luciferase activity was measured by the Dual Luciferase Reporter Assay System (Promega), and the data are represented as the mean ± SEM from 12 embryos per experimental condition (n > 3).

RT-Quantitative Real-Time PCR

Embryos were electroporated with the plasmids indicated and the NT was dissected out at 48 hpe. Single-cell suspensions were obtained after a 10–15 min digestion with Trypsin-EDTA (Sigma) and GFP^+ cells were sorted by flow cytometry using a MoFlo flow cytometer (DakoCytomation). Total RNA was extracted following the Trizol protocol (Invitrogen), and reverse transcription and real-time PCR were performed according to manufacturer's instructions (Roche) on a LC480 Lightcycler (Roche). Specific primers for qPCR amplification of the Statmin2 gene were purchased (QuantiTec Primer Assays, QIAGEN), whereas specific primers for the Sox2 gene were designed (5-GGGCACCAATACCATGACGA-3′ and 5′-GCGTAACTGTCCATCCTCTG-3′, Sigma). Primers specific for chick Gapdh were used for normalization. PCR amplifications were assessed from pools of electroporated NTs (15 embryos/pool), using three independent pools per experimental condition. The data represent standardized mean values ± SEM.

Spinal Cord Slice Culture and Time-Lapse Analysis

Embryos were coelectroporated at HH14 or HH18 with the Tis21-RFP and Sox2-GFP reporters, and embryo slices (200 μm) were obtained 10–14 hpe with a Vibratome 800 series McIlwain Tissue Chopper. The tissue was embedded in rat tail collagen type I in glass bottom culture dishes (MatTek, coated with poly-L-lysine; Sigma) and cultured in 5% CO2 air at 37°C for 2 hr in DMEM-F12 (D6421; Sigma-Aldrich) supplemented with B27, GlutaMAX (both from Gibco) and penicillin-streptomycin (Invitrogen). Slice cultures were imaged in an environmental chamber kept at 37.5°C and buffered with a 5% CO2/95% air mix using either a 25× (Plan Apochromat NA 0.75 water immersion) or a 40× lens (C-Apochromat NA 1.2 water immersion) on an inverted microscope (inverted Zeiss Axio Observer Z1) equipped with an Argon multiline gas laser at 488 nm and a DPSS laser at 561 nm. Images were acquired from 20–40 optical sections spaced 2 μm apart at 10 min intervals for up to 30 hr using ZEN software (Zeiss). The data were analyzed with Volocity (Improvision) or ImageJ software.

Mitotic EdU Labeling Index: Fitting Function

By means of an error minimization algorithm, we fit the mitotic labeling index data (see Figure 1F) to the following function:

$$f(t) = \frac{(t/T_{G2})^n}{1 + (t/T_{G2})^n}.$$

In this function, there are two fitting parameters, T_{G2} and n, that corresponds to the duration of the G2 phase and the sharpness of the mitotic response, respectively. Note that $f(T_{G2}) = 1/2$ regardless the value of n.

Calculation of the Duration of the M Phase

At a given developmental stage, all cells of the ventral domain, N, are identified by means of Olig2 labeling. Only a subset of these cells is cycling, γN, γ being the growth fraction calculated by the Edu labeling index (Figure 1D). In addition, only a percentage, π, of the cells of the ventral domain are in the mitotic phase M as identified by the PH3 labeling (see Figures 1E and 1G). We estimate the duration of the M phase as follows. If the cell-cycle duration at a given developmental stage is T_C, and assuming that the cycle progressions of cells are uncorrelated, then the probability density of finding a cell in a particular stage of its cell cycle is $1/T_C$. Thus, the probability of finding a cell in the M phase reads T_M/T_C, where T_M is the duration of the M phase. Moreover, the number of cells in the M phase, N_M, are $N_M = \gamma N T_M/T_C$. Consequently, the duration of the mitotic phase is $T_M = T_C\pi/\gamma$.

Statistical Analysis of Experimental Data

Quantitative data are expressed as mean ± SEM. Statistical analysis was performed using the Statview software. Significance was assessed by performing ANOVA followed by the Student-Newman-Keuls test, except for experiments with Figures 1D, 1F, 5C, 5E, 6A, and S3 whose effects were examined using the Student's t test (*$p < 0.05$, **$p < 0.01$, and ***$p < 0.001$). The errors of the cell-cycle phases are estimated using the SE propagation technique using the corresponding formulas.

In Silico Shh Activity Maintenance/Reduction Experiments

In order to implement in silico Shh activity maintenance/reduction experiments that mimic their in vivo counterparts, we proceed as follows. In vivo maintenance of Shh activity is done by using a dominant active form of Smo (SmoM2). This sustains Shh activity levels at least for 24 hr (HH12 embryos electroporated with SmoM2 were analyzed at 24 hpe) (Figure 5A). Because Shh is responsible of the switch at a developmental time t^*, we delay all t^*s (see above) by 24 hr but keeping the rest of the parameters unchanged. As for the reduction of Shh activity, HH12 embryos electroporated with a dominant-negative regulator ($mPtc1^{\Delta loop2}$) were analyzed at 16 hpe (Figure 5A). Thus, we anticipate all t^*s by 16 hr but, again, keeping the rest of the parameters unchanged. Importantly, note that the analyzed proportion of divisions, Equation 3, does not depend on either β, the rate of incorporation of proliferative cells due to Shh activity that more likely changes due to these perturbation experiments, or the number of P and N cells in the primordium (the whole tube is analyzed in vivo and not only the ventral domain).

For additional materials and methods (Mathematical Modeling), see the Extended Experimental Procedures.

SUPPLEMENTAL INFORMATION

Supplemental Information includes Extended Experimental Procedures, three figures, and three movies and can be found with this article online at http://dx.doi.org/10.1016/j.celrep.2013.06.038.

ACKNOWLEDGMENTS

The authors wish to thank Susana Usieto for her invaluable technical assistance, and Drs. Fabienne Pituello and Saul Ares for comments on the manuscript. For providing DNAs, we thank Dr. Masanori Uchikawa, Osaka University, Japan and Dr. Roger Tsien, UCSD, USA. The work in E.M.'s laboratory was supported by grants BFU2010-18959 and CSD2007-00008, and the work in the J.B. laboratory was supported by grants BFU2010-21847-C02-01 and 2009-SGR/01055.

Received: February 5, 2013
Revised: May 28, 2013
Accepted: June 25, 2013
Published: July 25, 2013

REFERENCES

Alvarez-Medina, R., Le Dreau, G., Ros, M., and Martí, E. (2009). Hedgehog activation is required upstream of Wnt signalling to control neural progenitor proliferation. Development *136*, 3301–3309.

Arai, Y., Pulvers, J.N., Haffner, C., Schilling, B., Nüsslein, I., Calegari, F., and Huttner, W.B. (2011). Neural stem and progenitor cells shorten S-phase on commitment to neuron production. Nat. Commun. *2*, 154.

Balaskas, N., Ribeiro, A., Panovska, J., Dessaud, E., Sasai, N., Page, K.M., Briscoe, J., and Ribes, V. (2012). Gene regulatory logic for reading the Sonic Hedgehog signaling gradient in the vertebrate neural tube. Cell *148*, 273–284.

Barzi, M., Berenguer, J., Menendez, A., Alvarez-Rodriguez, R., and Pons, S. (2010). Sonic-hedgehog-mediated proliferation requires the localization of PKA to the cilium base. J. Cell Sci. *123*, 62–69.

Beachy, P.A., Karhadkar, S.S., and Berman, D.M. (2004). Tissue repair and stem cell renewal in carcinogenesis. Nature *432*, 324–331.

Bénazéraf, B., Chen, Q., Peco, E., Lobjois, V., Médevielle, F., Ducommun, B., and Pituello, F. (2006). Identification of an unexpected link between the Shh pathway and a G2/M regulator, the phosphatase CDC25B. Dev. Biol. *294*, 133–147.

Briscoe, J. (2009). Making a grade: Sonic Hedgehog signalling and the control of neural cell fate. EMBO J. *28*, 457–465.

Briscoe, J., Chen, Y., Jessell, T.M., and Struhl, G. (2001). A hedgehog-insensitive form of patched provides evidence for direct long-range morphogen activity of sonic hedgehog in the neural tube. Mol. Cell *7*, 1279–1291.

Cayuso, J., Ulloa, F., Cox, B., Briscoe, J., and Martí, E. (2006). The Sonic hedgehog pathway independently controls the patterning, proliferation and survival of neuroepithelial cells by regulating Gli activity. Development *133*, 517–528.

Chamberlain, C.E., Jeong, J., Guo, C., Allen, B.L., and McMahon, A.P. (2008). Notochord-derived Shh concentrates in close association with the apically positioned basal body in neural target cells and forms a dynamic gradient during neural patterning. Development *135*, 1097–1106.

Das, R.M., and Storey, K.G. (2012). Mitotic spindle orientation can direct cell fate and bias Notch activity in chick neural tube. EMBO Rep. *13*, 1030.

Epstein, D.J., Marti, E., Scott, M.P., and McMahon, A.P. (1996). Antagonizing cAMP-dependent protein kinase A in the dorsal CNS activates a conserved Sonic hedgehog signaling pathway. Development *122*, 2885–2894.

Ghosh, S., Marquardt, T., Thaler, J.P., Carter, N., Andrews, S.E., Pfaff, S.L., and Hunter, T. (2008). Instructive role of aPKCzeta subcellular localization in the assembly of adherens junctions in neural progenitors. Proc. Natl. Acad. Sci. USA *105*, 335–340.

Gonzalez, C. (2007). Spindle orientation, asymmetric division and tumour suppression in Drosophila stem cells. Nat. Rev. Genet. *8*, 462–472.

Hamburger, V., and Hamilton, H.L. (1992). A series of normal stages in the development of the chick embryo. 1951. Dev. Dyn. *195*, 231–272.

Haubensak, W., Attardo, A., Denk, W., and Huttner, W.B. (2004). Neurons arise in the basal neuroepithelium of the early mammalian telencephalon: a major site of neurogenesis. Proc. Natl. Acad. Sci. USA *101*, 3196–3201.

Huang, H.P., Liu, M., El-Hodiri, H.M., Chu, K., Jamrich, M., and Tsai, M.J. (2000). Regulation of the pancreatic islet-specific gene BETA2 (neuroD) by neurogenin 3. Mol. Cell. Biol. *20*, 3292–3307.

Huangfu, D., and Anderson, K.V. (2005). Cilia and Hedgehog responsiveness in the mouse. Proc. Natl. Acad. Sci. USA *102*, 11325–11330.

Hynes, M., Ye, W., Wang, K., Stone, D., Murone, M., Sauvage, Fd., and Rosenthal, A. (2000). The seven-transmembrane receptor smoothened cell-autonomously induces multiple ventral cell types. Nat. Neurosci. *3*, 41–46.

Iacopetti, P., Michelini, M., Stuckmann, I., Oback, B., Aaku-Saraste, E., and Huttner, W.B. (1999). Expression of the antiproliferative gene TIS21 at the onset of neurogenesis identifies single neuroepithelial cells that switch from proliferative to neuron-generating division. Proc. Natl. Acad. Sci. USA *96*, 4639–4644.

Ingham, P.W., Nakano, Y., and Seger, C. (2011). Mechanisms and functions of Hedgehog signalling across the metazoa. Nat. Rev. Genet. *12*, 393–406.

Jiang, J., and Hui, C.C. (2008). Hedgehog signaling in development and cancer. Dev. Cell *15*, 801–812.

Kenney, A.M., and Rowitch, D.H. (2000). Sonic hedgehog promotes G(1) cyclin expression and sustained cell cycle progression in mammalian neuronal precursors. Mol. Cell. Biol. *20*, 9055–9067.

Lai, K., Kaspar, B.K., Gage, F.H., and Schaffer, D.V. (2003). Sonic hedgehog regulates adult neural progenitor proliferation in vitro and in vivo. Nat. Neurosci. *6*, 21–27.

Lange, C., Huttner, W.B., and Calegari, F. (2009). Cdk4/cyclinD1 overexpression in neural stem cells shortens G1, delays neurogenesis, and promotes the generation and expansion of basal progenitors. Cell Stem Cell *5*, 320–331.

Lesage, B., Gutierrez, I., Martí, E., and Gonzalez, C. (2010). Neural stem cells: the need for a proper orientation. Curr. Opin. Genet. Dev. *20*, 438–442.

Lobjois, V., Benazeraf, B., Bertrand, N., Medevielle, F., and Pituello, F. (2004). Specific regulation of cyclins D1 and D2 by FGF and Shh signaling coordinates cell cycle progression, patterning, and differentiation during early steps of spinal cord development. Dev. Biol. *273*, 195–209.

Machold, R., Hayashi, S., Rutlin, M., Muzumdar, M.D., Nery, S., Corbin, J.G., Gritli-Linde, A., Dellovade, T., Porter, J.A., Rubin, L.L., et al. (2003). Sonic hedgehog is required for progenitor cell maintenance in telencephalic stem cell niches. Neuron *39*, 937–950.

Marthiens, V., and ffrench-Constant, C. (2009). Adherens junction domains are split by asymmetric division of embryonic neural stem cells. EMBO Rep. *10*, 515–520.

Morillo, S.M., Escoll, P., de la Hera, A., and Frade, J.M. (2010). Somatic tetraploidy in specific chick retinal ganglion cells induced by nerve growth factor. Proc. Natl. Acad. Sci. USA *107*, 109–114.

Morin, X., Jaouen, F., and Durbec, P. (2007). Control of planar divisions by the G-protein regulator LGN maintains progenitors in the chick neuroepithelium. Nat. Neurosci. *10*, 1440–1448.

Muotri, A.R., and Gage, F.H. (2006). Generation of neuronal variability and complexity. Nature *441*, 1087–1093.

Nowakowski, R.S., Lewin, S.B., and Miller, M.W. (1989). Bromodeoxyuridine immunohistochemical determination of the lengths of the cell cycle and the DNA-synthetic phase for an anatomically defined population. J. Neurocytol. *18*, 311–318.

Peco, E., Escude, T., Agius, E., Sabado, V., Medevielle, F., Ducommun, B., and Pituello, F. (2012). The CDC25B phosphatase shortens the G2 phase of neural progenitors and promotes efficient neuron production. Development *139*, 1095–1104.

Pierfelice, T., Alberi, L., and Gaiano, N. (2011). Notch in the vertebrate nervous system: an old dog with new tricks. Neuron *69*, 840–855.

Pilaz, L.J., Patti, D., Marcy, G., Ollier, E., Pfister, S., Douglas, R.J., Betizeau, M., Gautier, E., Cortay, V., Doerflinger, N., et al. (2009). Forced G1-phase reduction alters mode of division, neuron number, and laminar phenotype in the cerebral cortex. Proc. Natl. Acad. Sci. USA *106*, 21924–21929.

Rebollo, E., Sampaio, P., Januschke, J., Llamazares, S., Varmark, H., and González, C. (2007). Functionally unequal centrosomes drive spindle orientation in asymmetrically dividing Drosophila neural stem cells. Dev. Cell *12*, 467–474.

Rehen, S.K., McConnell, M.J., Kaushal, D., Kingsbury, M.A., Yang, A.H., and Chun, J. (2001). Chromosomal variation in neurons of the developing and adult mammalian nervous system. Proc. Natl. Acad. Sci. USA *98*, 13361–13366.

Sasaki, H., Hui, C., Nakafuku, M., and Kondoh, H. (1997). A binding site for Gli proteins is essential for HNF-3beta floor plate enhancer activity in transgenics and can respond to Shh in vitro. Development *124*, 1313–1322.

Sauer, F.C. (1935). Mitosis in the neural tube. J. Comp. Neurol. *62*, 377–405.

Shitamukai, A., Konno, D., and Matsuzaki, F. (2011). Oblique radial glial divisions in the developing mouse neocortex induce self-renewing progenitors outside the germinal zone that resemble primate outer subventricular zone progenitors. J. Neurosci. *31*, 3683–3695.

Uchikawa, M., Ishida, Y., Takemoto, T., Kamachi, Y., and Kondoh, H. (2003). Functional analysis of chicken Sox2 enhancers highlights an array of diverse regulatory elements that are conserved in mammals. Dev. Cell *4*, 509–519.

Wang, X., Tsai, J.W., Imai, J.H., Lian, W.N., Vallee, R.B., and Shi, S.H. (2009). Asymmetric centrosome inheritance maintains neural progenitors in the neocortex. Nature *461*, 947–955.

Wilcock, A.C., Swedlow, J.R., and Storey, K.G. (2007). Mitotic spindle orientation distinguishes stem cell and terminal modes of neuron production in the early spinal cord. Development *134*, 1943–1954.

Yu, F., Kuo, C.T., and Jan, Y.N. (2006). Drosophila neuroblast asymmetric cell division: recent advances and implications for stem cell biology. Neuron *51*, 13–20.

Cell PRESS
Open ACCESS

EXTENDED EXPERIMENTAL PROCEDURES

Mathematical Modeling

Basic Model. In terms of the chemical kinetics formalism, the reactions that account for the divisions of progenitor, P, and motor neuron, N, cells read (see Figure 3):

$$P \xrightarrow{\alpha_{PP}} P+P$$
$$P \xrightarrow{\alpha_{PN}} P+N$$
$$P \xrightarrow{\alpha_{NN}} N+N$$

Where α_{ZZ} stands for the division rate such that $\alpha_{ZZ}=ln(2)/T_t$ is the division rate leading to ZZ cells (i.e., $ZZ\in\{PP,PN,NN\}$); T_t being the cell cycle duration at time t. The above reactions lead to the following set of differential equations,

$$\dot{P}=(\alpha_{PP}-\alpha_{NN})P$$
$$\dot{N}=(\alpha_{PN}+2\alpha_{NN})P$$

Cell quantification reveals two distinct phases: first, for $t<t^*$, P cells increase from $P_0=P(t_0)$ as N cells almost show no increase from $N_0=N(t_0)=0$; second, for $t>t^*$, P cells decrease from a maximum $P_{\max}$ as N cells increase and reach a "stationary" value $N_{\max}$. In addition, these phases show a reduction of the cell cycle duration from $T_{t<t^*}=(16\pm2)h$ to $T_{t>t^*}=(10\pm1)h$. Importantly, the fundamental mechanism does not rely on cell cycle differences but on a developmental switch in terms of the division modes. Thus, the division dynamics indicates that before a given time, t^*, $\alpha_{PP}>\alpha_{NN}$ ($\dot{P}>0$) and afterward $\alpha_{PP}<\alpha_{NN}$ ($\dot{P}<0$). Note that the latter cannot be explained in terms of the cell cycle duration reduction. We can reconcile all these facts by hypothesizing a developmental switch such that before t^* only proliferative divisions take place and after t^* the divisions that lead to motor neuron cells, either NN or PN, are the only ones that occur. This hypothesis implies the following functional form for the division rates:

$$\alpha_{PP}(t)=\frac{ln(2)}{T_{t<t^*}}\cdot\theta(t^*-t)$$
$$\alpha_{PN}(t)=\alpha_{NN}(t)=\frac{ln(2)}{T_{t>t^*}}\cdot\theta(t-t^*)$$

where $\theta(z)$ is the Heaviside step function:

$$\theta(z)=\begin{cases}1 & if\ \ z>0\\ 0 & if\ \ z<0\end{cases}$$

Under these conditions, the differential equations can be solved:

$$P(t)=P_0 2^{\frac{\tau}{T_{t<t^*}}}\left[\theta(t^*-\tau)+\theta(\tau-t^*)2^{\frac{(t^*-\tau)(T_{t<t^*}+T_{t>t^*})}{T_{t<t^*}T_{t>t^*}}}\right]$$
$$N(t)=3P_0 2^{\frac{\tau}{T_{t<t^*}}}\theta(\tau-t^*)\left[2^{\frac{(t^*-\tau)}{T_{t<t^*}}}-2^{\frac{(t^*-\tau)(T_{t<t^*}+T_{t>t^*})}{T_{t<t^*}T_{t>t^*}}}\right]$$

Where $\tau=t-t_0$. The maximum values of P and N read,

$$P_{max}=P_0 2^{t^*/T_{t<t^*}}$$

$$N_{max}=3P_0 2^{t^*/T_{t<t^*}}$$

such that $N_{max}=3P_{max}$. These values allow also to provide estimates of t^* as a function of P_0 and $T_{t<t^*}$: $t^*\simeq80$ hpf.

Modified Model. Cell-to-cell and embryo-to-embryo variability (e.g., cell asynchronous divisions, embryo asynchronous development) can be effectively included in the basic modeling approach imposing less restrictive conditions for the sharpness and the temporal location of the switching dynamics. We model that behavior by means of Hill functions,

$$\alpha_{ZZ}(t)=\frac{ln(2)\left[1+\left(\tau/t_T^*\right)^{n_T}\right]}{\left(T_{t<t^*}+\left(\tau/t_T^*\right)^{n_T}T_{t>t^*}\right)}\frac{\left[\left(\tau/t_{ZZ}^*\right)^{n_{ZZ}}+\delta_{PP,ZZ}\left(1-\left(\tau/t_{ZZ}^*\right)^{n_{ZZ}}\right)\right]}{1+\left(\tau/t_{ZZ}^*\right)^{n_{ZZ}}}$$

Where $\delta_{i,j}$ stands for the Kronecker delta. At a given time, τ, the contribution of ZZ divisions to the total number of divisions, i.e., the division proportion, $f_{ZZ}(t)$, reads,

$$f_{ZZ}(t) = \frac{\alpha_{ZZ}(t)}{\sum_{YY} \alpha_{YY}(t)}$$

Importantly, note that in the modified model we do not assume sharp transitions in any of the division modes, $n_{ZZ} \neq \infty$, or in the cell cycle duration transition, $n_T \neq \infty$. Moreover, the developmental times at which the transitions occur, t^*_{ZZ}, can be different in this modified version depending on the division type, and these times can be also different that the time at which the cell cycle duration differences become evident, t^*_T. In addition, in the modified model we also consider the effect of the incorporation of cell to the Olig2+ progenitor pool due to Shh induction by means of an extra reaction,

$$\varnothing \xrightarrow{\beta} P$$

β being a constant that represents the maximum rate of induction due to Shh. Since experimental data indicates that Shh induction decreases as time progresses,

$$\beta(t) = \frac{\beta}{1 + \left(\tau / t^*_\beta\right)^{n_\beta}}$$

We point out that the division proportion, $f_{ZZ}(t)$, is independent of this additional reaction. Altogether, the ordinary differential equations describing the process now read,

$$\dot{P} = (\alpha_{PP}(t) - \alpha_{NN}(t))P + \beta(t)$$
$$\dot{N} = (\alpha_{PN}(t) + 2\alpha_{NN}(t))P$$

We notice that in the limit $\beta \to 0$, $n_X \to \infty$, $t^*_X \to t^*$ $\forall X \in \{\beta, T, PP, NN, PN\}$, the basic model is recovered. Consequently, the modified model includes 13 free parameters: n_{PP}, n_{PN}, n_{NN}, n_T, n_β, t^*_{PP}, t^*_{PN}, t^*_{NN}, t^*_T, t^*_β, β, $T_{t<t^*}$, and $T_{t>t^*}$. In order to obtain their values, we develop and implement an error minimization algorithm with respect to the experimental data using Wolfram's Mathematica software suite. The only constraints we impose are: $P_0 = 12$, $N_0 = 0$, $T_{t<t^*} \in (14, 16)$ hours, and $T_{t>t^*} \in (9, 11)$ hours. Under these conditions the algorithm recursively converges to the following parameter set,

n_{PP}	n_{PN}	n_{NN}	n_T	n_β	β	$T_{t<t^*}$	$T_{t>t^*}$
78.6	1.0	2.6	78.2	99.9	0.9h^{-1}	14.0h	11.0h

t^*_{PP}	t^*_{PN}	t^*_{NN}	t^*_T	t^*_β
73.0hpf	82.9hpf	78.0hpf	82.9hpf	73.0hpf

We notice that exponents, n_X, with values larger than 10 can be effectively considered as ∞ (i.e., an abrupt transition). Consequently, the model predicts a sharp transition for *PP* divisions at time $t^*_{PP} = 73$ hpf. According to these results, the effect of Shh induction in terms of the incorporation of cells to the Olig2+ pool is, ~ 1 cell per hour. Thus, up to the transition point, the total increase of Olig2+ cells due to the Shh induction is around 25 cells, that is, $\sim 30\%$ of the total cell population. We also point out that the transition time regulating a change in the cell cycle duration and that controlling an increase in *PN* divisions are coincident at ~ 83 hpf. As a matter of discussion, we cannot neglect the possibility that this parameter data set correspond to a local, but not global, minima during the error minimization process. Still, we notice that different initial conditions for the parameter data set converge to the aforementioned values and suggest, at least, a well-defined and relevant minima in the parameter space.

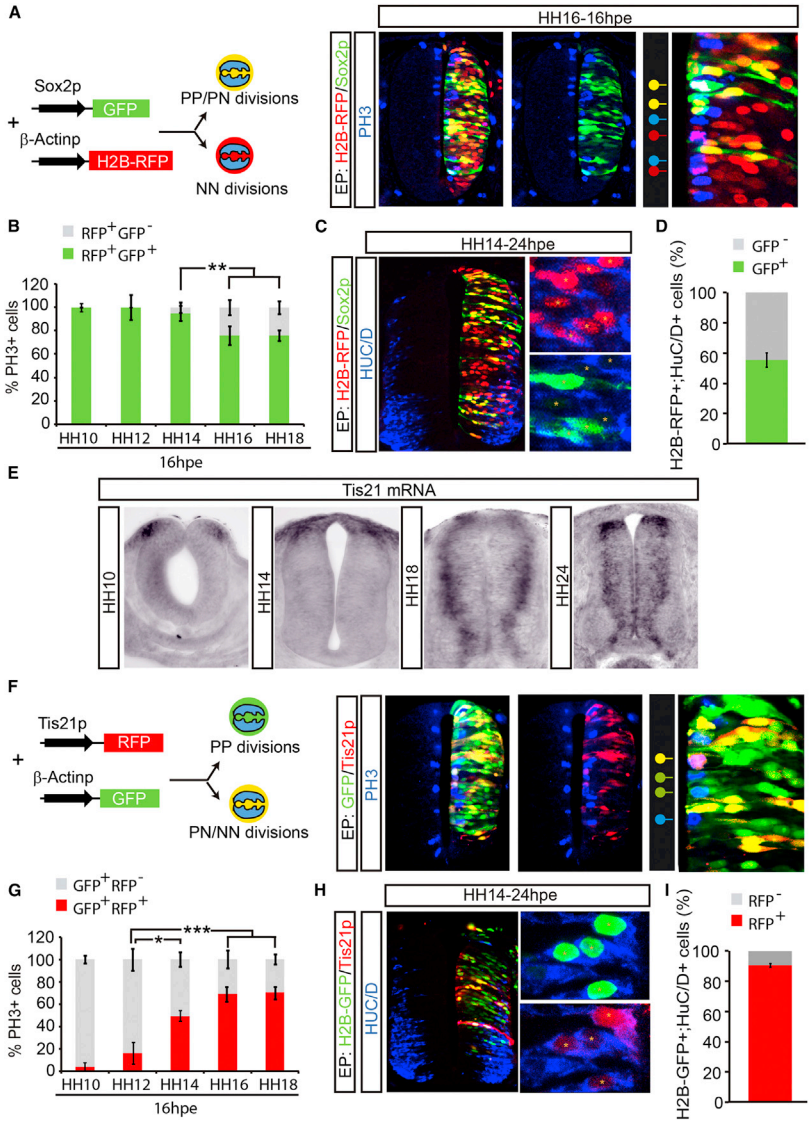

Figure S1. Characterization of the Two Reporters: Sox2p-GFP and Tis21p-RFP, Related to Figure 2

(A–D) To track proliferative progenitors, we co-electroporated the Sox2p fluorescent reporter (Sox2p-GFP) together with a control vector (pCAGGS-H2B-RFP) and analyzed the expression of GFP/RFP in pH3 immunostained mitoses 16 hpe (a period in which only one cell cycle could be completed according to our EdU data. (A) Representation of co-electroporation of Sox2p-GFP with control plasmid H2B-RFP. Selected sections immunostained for pH3 revealed: i) non-electroporated mitosis (blue); ii) mitosis expressing only the control vector (red), identified as NN; and iii) mitosis coexpressing the control and Sox2p (yellow) vectors, identified as PP/PN divisions. (B) Proportion of pH3-labeled mitosis expressing Sox2p (16 hpe) at the developmental HH stages indicated, showing a significant decrease in Sox2p expression to ~76 ± 4% at HH16-18. Data represents mean ± SEM (**$p < 0.01$). (C) Only a fraction of the electroporated cells that differentiate into neurons (H2B-RFP$^+$;HuC/D$^+$, asterisks) were GFP+, suggesting that these cells come from a PN division. (D) 55 ± 5% of differentiating electroporated (H2B-RFP$^+$;HuC/D$^+$) cells show pSox2 activity. Data represents mean ± SEM.

(E–I) To track neurogenic divisions, we took advantage of the Tis21 gene. (E) In situ hybridization shows the expression of cTis21 at the indicated stages. Prior to the onset of neurogenesis Tis21 expression is restricted to a dorsal domain. From the onset of neurogenesis cTis21 is expressed in the ventricular zone (were progenitors reside) and is excluded from newborn neurons. (F) Co-electroporation of the Tis21p-RFP-reporter with the H2B-GFP control plasmid. Selected sections immunostained for pH3 revealed: i) non-electroporated mitosis (blue); ii) mitosis expressing only the control vector (green), identified as PP; and iii) mitosis co-expressing the control and Tis21p (yellow) vectors, identified as PN/NN divisions. (G) Proportion of pH3-labeled mitosis expressing Tis21p (16 hpe) at the developmental HH stages indicated showing a significant increase in Tis21p expression to 49 ± 5% at HH14; 69 ± 7% at HH16; and 70 ± 5% at HH18, respectively. Data represents mean ± SEM (*$p < 0.05$, ***$p < 0.001$). In (H) the electroporated cells that differentiate into neurons (H2B-GFP$^+$;HuC/D$^+$, asterisks) expressing RFP are shown, suggesting that these cells come from a PN or a NN division. (I) 91 ± 1% of differentiating electroporated (H2B-GFP$^+$;HuC/D$^+$) cells show pTis21 activity. Data represent mean ± SEM.

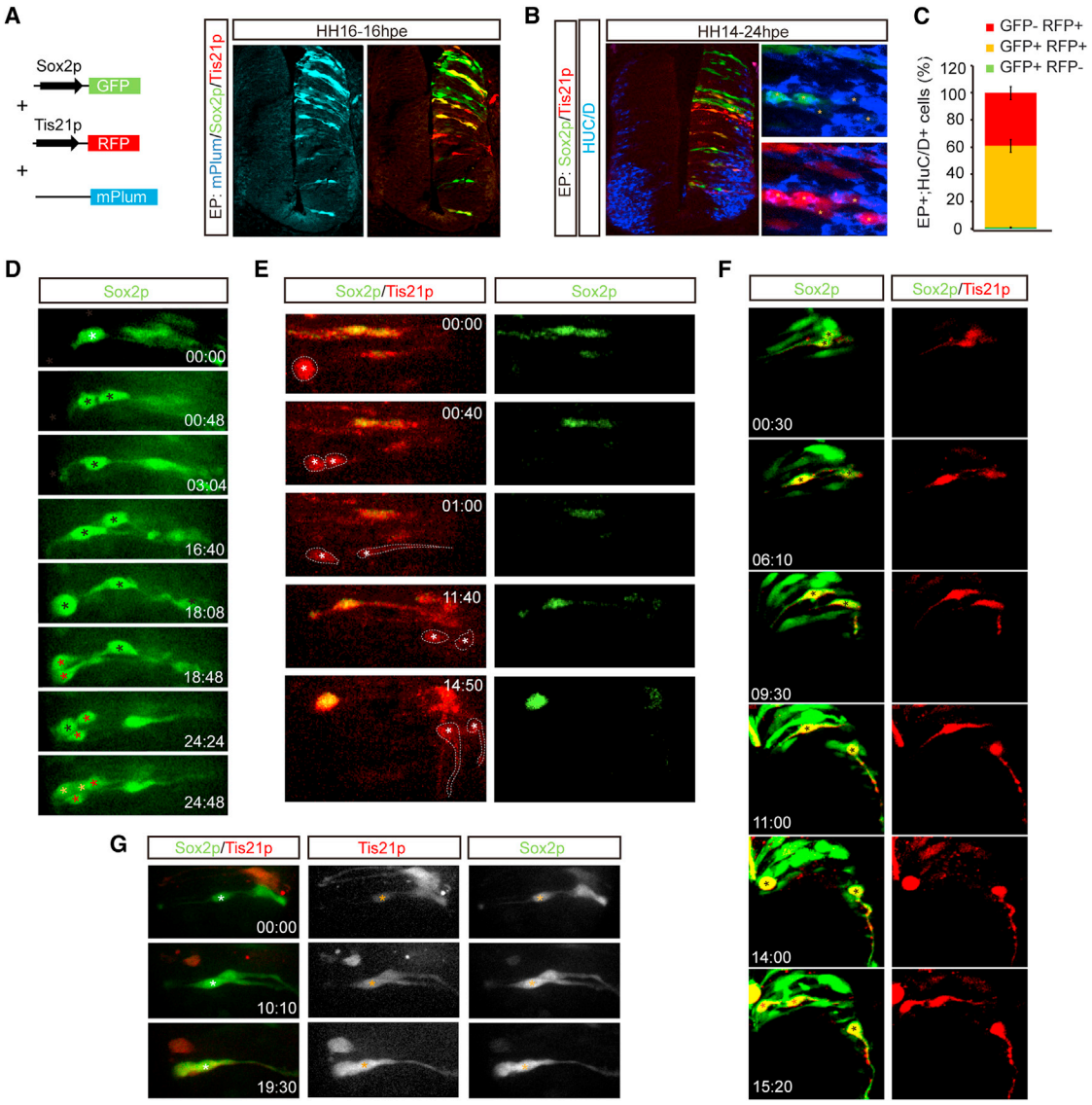

Figure S2. Sox2p-GFP and Tis21p-RFP Provide the Single Cell Resolution Necessary to Identify Each Type of Division, Related to Figure 2

(A) Control experiments show the co-electroporation Sox2p-GFP, Tis21p-RFP reporters, together with a control vector expressing mPlum, which serves as a co-electroporation control.

(B) Selected section from embryos co-electroporated with the Sox2p-GFP and the Tis21p-RFP-reporter, and immunostained with the pan-neural marker HuC/D. HH14 embryos show that 24hpe, 39 ± 5% of the differentiated (HuC/D$^+$ cells) electroporated cells were RFP$^+$;GFP$^-$, 60 ± 5% were RFP+;GFP+ while only 1.0 ± 0.4% of the cells were RFP-;GFP$^+$. Thus, nearly all the differentiating electroporated cells showing activity of the Sox2p-GFP reporter show concomitant pTis21:RFP activity.

(C) The proportion of differentiating electroporated cells showing activity of pTis21:RFP, pSox2:GFP or both. 39% of the differentiated electroporated cells were RFP+;GFP-, 60% were RFP+;GFP+ while only 1% of the cells were RFP-;GFP+.

(D) Snap-shots of a time-lapse (see Movie S1), in vivo recording two consecutive division of a Sox2p-GFP electroporated cell. Color coded asterisks mark each daughter pairs (asterisks).

(E) Snap-shots of a time-lapse, in vivo recording a Tis21p-RFP$^+$/GFP$^-$ mitosis from which the two resulting daughters cells enter the differentiation pathway, migrate laterally and growth an axon (asterisks).

(F) Snap-shots of a time-lapse in vivo recording of the two daughters cells resulting from the division of a GFP$^+$;RFP$^+$ cell, that have different fates (asterisk). One daughter cell migrates apically to re-enter mitosis, the other daughter cell migrates laterally, grow a cell process and initiate differentiation (asterisks cells).

(G) Snap-shots of a time-lapse in vivo recording of Sox2p-GFP/Tis21p-RFP co-electroporated cells. A neuroepithelial cells that is initially expressing only Sox2 (asterisk), gradually activates the expression of Tis21, before dividing to generate two GFP$^+$/RFP$^+$ daughter cells.

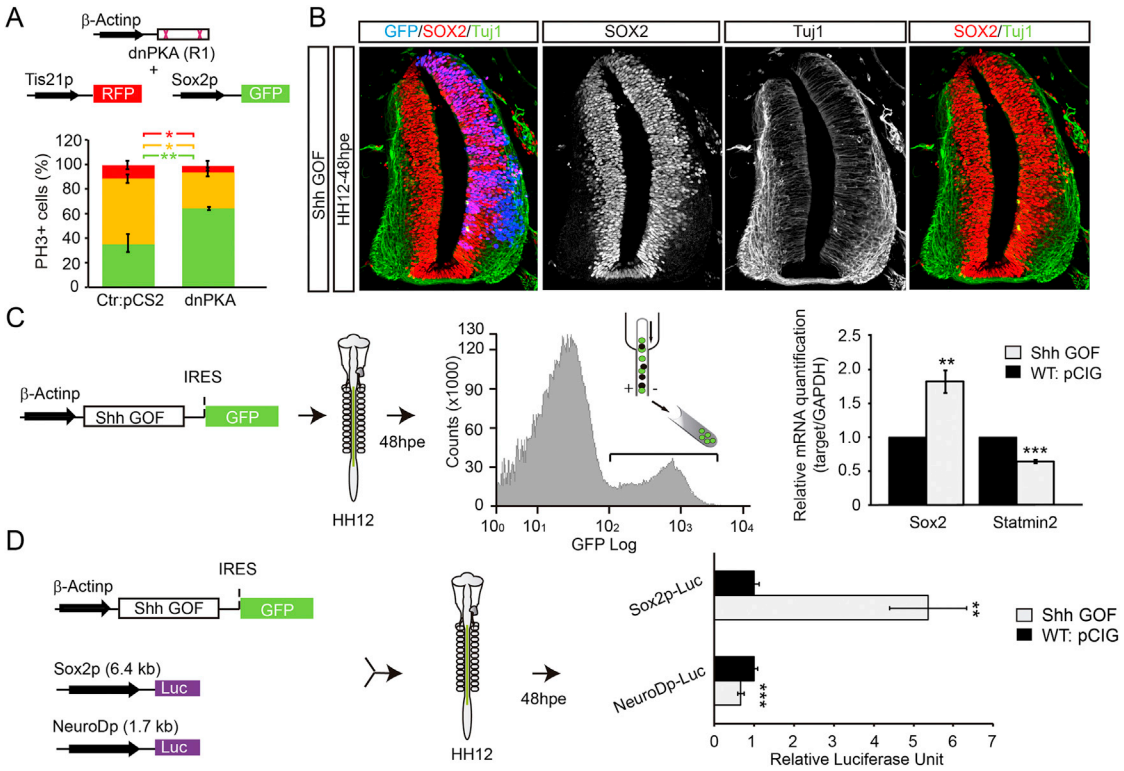

Figure S3. Sustained Activation of Shh Signaling during NT Development Increases the Proportion of Neural Progenitors, Related to Figure 4

(A) To experimentally manipulate Shh levels, gain-of-function was achieved by electroporation of dnPKA, and embryos were co-electroporated with Sox2p-GFP/Tis21p-RFP, quantification show reporter-expressing mitotic cells (pH3+) 24 hpe.

(B) Selected sections corresponding to Shh GOF (blue) were then immunostained 48 hpe for the progenitor marker Sox2 (red) and the pan-neural marker Tuj1 (green) to show the overgrowth of the electroporated side of the tube.

(C) Quantification of Sox2 (progenitor) and Statmin2 (neural) expression measured by RT–qPCR 48 hpe in control (standardized as 1) and Shh GOF-EP embryos (Sox2: 2.0 ± 0.2; Statmin2: 0.60 ± 0.02).

(D) The activity of progenitor and neural reporters was tested by quantifying luciferase activity at HH12-48 hpe (for Sox2p WT: 1.0 ± 0.1; Shh GOF: 5 ± 1 and for NeuroDp WT: 1.0 ± 0.1; Shh GOF: 0.6 ± 0.1). Data represents mean ± SEM (*P<0.05, **P<0.01, ***P<0.001).

APPENDIX II

Published February 10, 2014

The strength of SMAD1/5 activity determines the mode of stem cell division in the developing spinal cord

Gwenvael Le Dréau, Murielle Saade, Irene Gutiérrez-Vallejo, and Elisa Martí

Instituto de Biología Molecular de Barcelona, Consejo Superior de Investigaciones Científicas, Parc Científic de Barcelona, Barcelona 08028, Spain

The different modes of stem cell division are tightly regulated to balance growth and differentiation during organ development and homeostasis. However, the mechanisms controlling such events are not fully understood. We have developed markers that provide the single cell resolution necessary to identify the three modes of division occurring in a developing nervous system: self-expanding, self-renewing, and self-consuming. Characterizing these three modes of division during interneuron generation in the developing chick spinal cord, we demonstrated that they correlate to different levels of activity of the canonical bone morphogenetic protein effectors SMAD1/5. Functional in vivo experiments showed that the premature neuronal differentiation and changes in cell cycle parameters caused by SMAD1/5 inhibition were preceded by a reduction of self-expanding divisions in favor of self-consuming divisions. Conversely, SMAD1/5 gain of function promoted self-expanding divisions. Together, these results lead us to propose that the strength of SMAD1/5 activity dictates the mode of stem cell division during spinal interneuron generation.

Introduction

The production of appropriate numbers and types of cells to form a functional central nervous system (CNS) requires a finely tuned balance between the different modes of divisions that neural stem and progenitor cells undergo (Lui et al., 2011; Franco and Müller, 2013). Three distinct modes of divisions occur during vertebrate CNS development: self-expanding (symmetric proliferative [PP]) divisions ensure the expansion of the progenitor pool by generating two daughter cells with identical progenitor potential, self-renewing (asymmetric [PN]) divisions generate one daughter cell with a developmental potential indistinguishable from that of the parental cell and another with a more restricted potential, and self-consuming (symmetric terminal neurogenic [NN]) divisions generate two cells committed to differentiation, thereby depleting the progenitor pool (Götz and Huttner, 2005; Lui et al., 2011; Franco and Müller, 2013). The balance between these modes of stem cell division is also at play during adult neurogenesis in order not to disrupt tissue homeostasis (Suh et al., 2009; Göritz and Frisén, 2012). Given the therapeutic potential of stem cell manipulations in regenerative medicine, it is important to understand the mechanisms regulating these modes of stem cell division.

The intense research over recent years has defined some of the intrinsic mechanisms that govern the mode of division in the developing nervous system. In *Drosophila melanogaster* neuroblasts, particular attention has been paid to the contribution of centrosome asymmetry, spindle orientation, and the inheritance of apical membrane domains (Yu et al., 2006; Gonzalez, 2007; Rebollo et al., 2007). Although not fully understood, the picture emerging suggests that some of the intrinsic mechanisms controlling the mode of division in the developing vertebrate nervous system may reflect similar features (Morin et al., 2007; Ghosh et al., 2008; Marthiens and ffrench-Constant, 2009; Wang et al., 2009; Lesage et al., 2010; Shitamukai et al., 2011; Das and Storey, 2012). However, these decisions are likely to be primarily dictated by extrinsic signals.

Various extrinsic factors have been reported to affect neural stem cell behavior (Fuentealba et al., 2012; Tiberi et al., 2012; Franco and Müller, 2013). However, whether these factors affect

Correspondence to Elisa Martí: emgbmc@ibmb.csic.es; or Gwenvael Le Dréau: gldbmc@ibmb.csic.es

Abbreviations used in this paper: BMP, bone morphogenetic protein; BRE, BMP-responsive element; CNS, central nervous system; GBS, Gli binding site; hpe, hour postelectroporation; hpf, hour postfertilization; MZ, mantle zone; VZ, ventricular zone.

Supplemental Material can be found at:
http://jcb.rupress.org/content/suppl/2014/02/09/jcb.201307031.DC1.html

The Rockefeller University Press $30.00
J. Cell Biol. Vol. 204 No. 4 591–605
www.jcb.org/cgi/doi/10.1083/jcb.201307031

Published February 10, 2014

stem cell proliferation by regulating cell cycle entry, exit, or speed (Salomoni and Calegari, 2010) or whether they directly instruct the mode of stem cell division remains elusive. Additionally, the importance of a particular extrinsic factor appears to depend on the context and to be both stage and area specific (Falk and Sommer, 2009).

To search for the signals controlling the modes of stem cell division in the embryonic CNS, we have recently obtained the single cell resolution necessary for the in vivo identification of the three modes of stem cell division (PP, PN, and NN) within the developing chick spinal cord (Saade et al., 2013). This methodology, which is based on the pTis21:RFP and pSox2:GFP reporters, which are specifically activated during neuron- and progenitor-generating divisions, respectively, allowed us to establish that Sonic Hedgehog directly influences the mode of division of motor neuron progenitors by favoring PP divisions at the expense of PN and NN divisions (Saade et al., 2013). Interestingly, the spatial–temporal dynamics of Sonic Hedgehog signaling suggested that within the spinal cord, the requirement of this pathway in regulating the modes of division is restricted to motor neuron progenitors, leaving unresolved the nature of the extrinsic signal, which plays an equivalent role later during the generation of spinal interneurons.

Here, we characterized in vivo the modes of divisions used by interneuron progenitors within the developing chick spinal cord. We examined, based on its spatial–temporal activity, the putative involvement of the canonical bone morphogenetic protein (BMP) pathway in the control of those division modes. We found that at the mitotic phase, high, intermediate, and low levels of activity of the canonical BMP effectors SMAD1/5 correlate with PP, PN, and NN divisions, respectively. Furthermore, in vivo loss- and gain-of-function experiments showed that high levels of SMAD1/5 signaling promote PP divisions, whereas a reduction in SMAD1/5 activity forces spinal progenitors to prematurely switch to NN divisions. These results led us to conclude that an endogenous gradient of SMAD1/5 activity dictates the mode of division of spinal interneuron progenitors.

Results

PP, PN, and NN divisions co-occur during spinal cord neurogenesis

From the onset of neurogenesis within the developing vertebrate CNS, neural progenitors can use three distinct modes of divisions: self-expanding (symmetric proliferative [PP]), self-renewing (asymmetric [PN]), and self-consuming (NN; Götz and Huttner, 2005; Lui et al., 2011). We recently described a methodology based on the activity of the pTis21:RFP and pSox2:GFP reporters, which allows to unequivocally identify and distinguish these three modes of divisions in the chick spinal cord in vivo (Saade et al., 2013). Whereas the pTis21:RFP reporter distinguishes pTis21:RFP$^+$ neuron-generating divisions (PN and NN) from pTis21:RFP$^-$ ones (PP), the pSox2:GFP reporter discriminates pSox2:GFP$^+$ progenitor-generating (PP + PN) divisions from pSox2:GFP$^-$ (NN) ones (Saade et al., 2013).

Herein, we used this methodology to characterize the modes of divisions that neural progenitors undergo during the production of interneurons, which emerge along the whole dorsal–ventral axis, except the pMN domain, from stage HH18 (72 h postfertilization [hpf] and 30/36 somites; see Le Dréau et al., 2012). Coelectroporating in ovo these two reporters into HH14 chick embryos (54 hpf and 22 somites) revealed at 24 h postelectroporation (hpe; 24 hpe = ~HH18) that the three populations of electroporated cells (GFP$^+$/RFP$^-$, GFP$^+$/RFP$^+$, and GFP$^-$/RFP$^+$) are observed along the dorsal–ventral axis of the developing spinal cord (Fig. 1, A and B). To quantify the proportions of the three modes of divisions, we confined our analysis to 16 hpe on mitotic (pH3$^+$) electroporated cells to ensure that we only tracked cycling progenitor cells. Quantification at different time points demonstrated the progressive increase in the proportion of PN (GFP$^+$/RFP$^+$) divisions at the expense of PP (GFP$^+$/RFP$^-$) followed by the appearance of NN (GFP$^-$/RFP$^+$) divisions around 70 hpf (Fig. 1 C). Interestingly, we observed a sharp drop in the proportion of PP (GFP$^+$/RFP$^-$) divisions between 64 and 74 hpf (from 88 ± 11 to 32 ± 8; Fig. 1 C), as recently reported for the single pMN domain (Saade et al., 2013). Thus, the three different modes of neural progenitor division all occur along the dorsal–ventral axis during spinal interneuron generation (Fig. 1 D).

To pinpoint which extrinsic signal could be controlling the modes of progenitor divisions during spinal interneuron generation, we assessed the endogenous activity of the Sonic Hedgehog and canonical Wnt and BMP pathways, which are all known to play key roles in stem cell maintenance (Morrison and Spradling, 2008), and during early spinal cord development (Ulloa and Briscoe, 2007; Le Dréau and Martí, 2012). Electroporation of a Wnt-responsive reporter (TOP:H2B-RFP) together with a control H2B-GFP vector at HH14 showed at 24 hpe that the canonical Wnt activity was restricted to the most dorsal part of the neural tube (Fig. 1 E). Conversely, electroporation of a Gli binding site (GBS):H2B-GFP reporter serving as a readout of Sonic Hedgehog signaling showed its activity to be restricted to the ventral part of the neural tube (Fig. 1 F). In contrast, the canonical BMP pathway appeared to be active along the dorsal–ventral axis of the developing spinal cord, as demonstrated by the activity of the BMP-responsive element (BRE):EGFP reporter (Fig. 1 G). The BRE:EGFP reporter activity was high in the dorsal-most part of the neural tube, reflecting the early role of BMPs during neural patterning (Le Dréau et al., 2012; Tozer et al., 2013). In addition, scattered GFP$^+$ cells were detected along the whole dorsal–ventral axis, at the time of interneuron neurogenesis (Le Dréau et al., 2012). These results suggested that the canonical BMP pathway could be controlling the distinct modes of neural progenitor division during spinal interneuron generation.

The distinct modes of division are correlated to different levels of endogenous canonical BMP activity

Thus, we next examined whether the different modes of divisions were correlated in the developing spinal cord with distinct levels of endogenous activity of SMAD1/5/8, the effectors of the

Published February 10, 2014

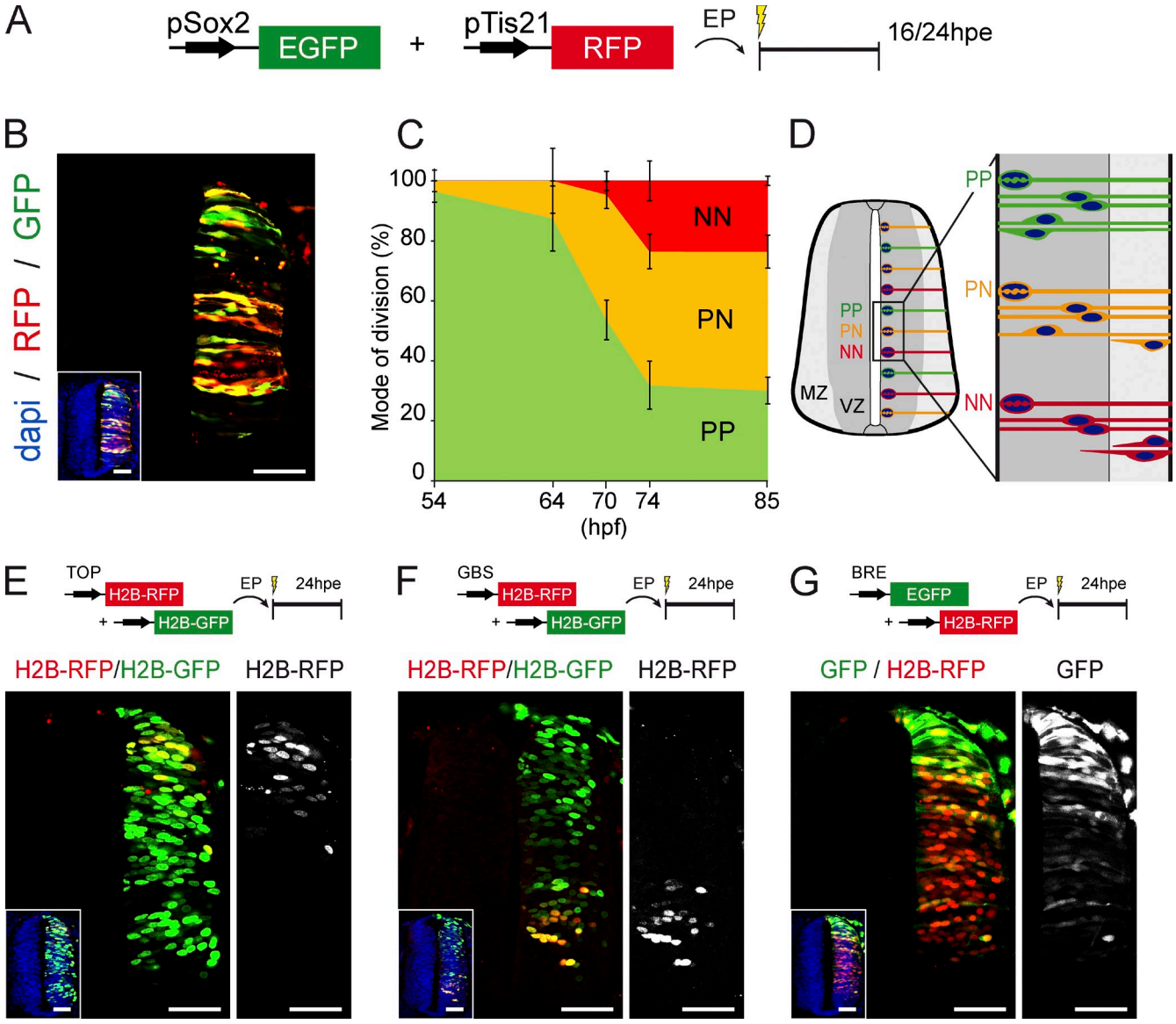

Figure 1. **PP, PN, and NN divisions co-occur during spinal cord neurogenesis.** (A) In ovo electroporation (EP) of the pTis21:RFP and pSox2:GFP reporters allows us to identify and discriminate the populations and divisions of PP, PN, and NN progenitors within the developing chick spinal cord. (B) Representative neural tube section obtained at 24 hpe of HH14 embryos, showing GFP$^+$;RFP$^-$ (PP), GFP$^+$;RFP$^+$ (PN), and GFP$^-$;RFP$^+$ (NN) cells in response to differential activities of the pTis21:RFP and pSox2:GFP reporters. The inset shows the neural tube morphology, with nuclei stained with DAPI. (C) The proportions of PP, PN, and NN divisions were assessed at 16 hpe at different developmental points, with a combination of the pSox2:EGFP and pTis21:RFP reporters and pH3 staining to reveal mitoses. Error bars show means ± SEM. (D) Illustration of the three modes of divisions occurring along the dorsal–ventral axis of a developing spinal cord during interneuron neurogenesis. (E–G) Representative neural tube sections obtained 24 h after coelectroporation of HH14 embryos with combinations of the TOP:H2B-RFP (E), GBS:H2B-RFP (F), or BRE:EGFP (G) with their respective controls. The insets show the neural tube morphology, with nuclei stained with DAPI. The right images show the signal observed in response to the specific activity of the corresponding reporter. Bars, 50 µM.

canonical BMP pathway (Massagué et al., 2005). To this end, we took advantage of an anti–phospho-SMAD1/5/8 (pS158) antibody to locate the active forms of SMAD1/5/8 in dividing neural progenitors. As previously reported in different areas of the developing vertebrate CNS (Müller et al., 2005; Alarcón et al., 2009), pS158 immunoreactivity was particularly strong in the mitotic nuclei lining the neural tube lumen (Fig. 2, A and B). This immunoreactivity was observed not only in all the nuclei stained with the mitotic marker pH3 (Fig. 2 A) but also in the nuclei displaying diffuse lamin B1 immunoreactivity, indicative of the lamin solubilization that occurs before chromosomal condensation and nuclear envelope breakdown (Fig. 2 B).

We quantified the pS158 immunoreactivity in mitotic nuclei 24 hpe and related this to the modes of division using the pSox2:GFP and pTis21:RFP reporters (Fig. 2, C–H). There was a 34% increase in nuclear pS158 intensity in pSox2$^+$ dividing cells as compared with pSox2$^-$ mitoses (mean nuclear pS158 intensity of 128 ± 3.5 in pSox2$^+$ vs. 95 ± 2.5 in pSox2$^-$; $P < 0.001$; Fig. 2, C and D), indicating that SMAD1/5/8 activity was weaker during NN divisions than during progenitor-generating (PP + PN) divisions. Conversely, the nuclear pS158 intensity in pTis21$^+$ divisions was significantly weaker than in pTis21$^-$ nuclei (mean nuclear pS158 intensity of 96 ± 4.1 in pTis21$^+$ vs. 115 ± 5.2 in pTis21$^-$; $P < 0.05$; Fig. 2, E and F), indicating

Published February 10, 2014

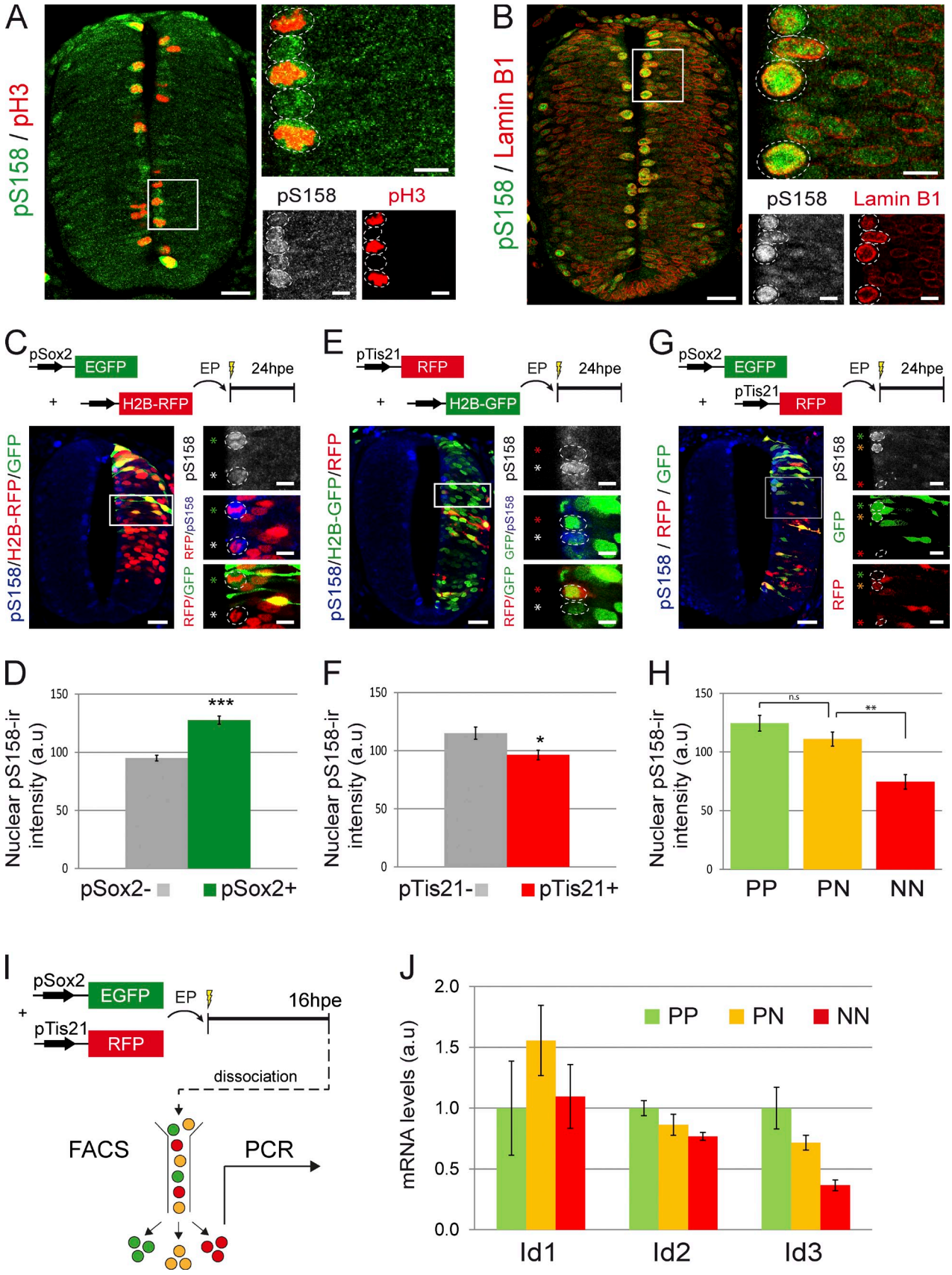

Figure 2. **Quantification of endogenous SMAD1/5 activity and *Id* gene expression in function of the mode of division.** (A and B) Representative sections of HH18 neural tubes stained for the active form of SMAD1/5/8 (pS158) and pH3 (A) or lamin B1 (B). (C–H) Analysis of the endogenous SMAD1/5/8 activity in the distinct modes of divisions. Neural tube sections were stained for pS158 24 hpe of HH14 embryos with a combination of the pSox2:EGFP

Published February 10, 2014

stronger SMAD1/5/8 activity during PP divisions than in neurogenic (PN + NN) divisions. Finally, quantification of the nuclear pS158 staining after coelectroporation with both reporters confirmed that SMAD1/5/8 activity was significantly weaker in neural progenitors undergoing NN divisions than in those undergoing progenitor-generating (PP + PN) divisions (mean nuclear pS158 intensity of 75 ± 6.2 for NN vs. 111 ± 6.0 for PN [$P < 0.01$] and 124 ± 6.7 for PP vs. 111 ± 6.0 for PN [$P > 0.05$]; Fig. 2, G and H). Therefore, the variations in the endogenous level of SMAD1/5/8 activity were directly correlated with neural progenitor divisions, with the highest levels associated with PP divisions and the lowest levels with NN divisions.

To support this idea, we investigated whether target genes of the canonical BMP pathway showed changes in expression levels in correlation with the distinct modes of divisions. Genes of the *Id* (*Inhibitor of DNA binding*) family are considered as prototypical direct targets of the canonical BMP pathway (Hollnagel et al., 1999; Korchynskyi and ten Dijke, 2002; Ying et al., 2003). Within the developing spinal cord, *Id1*, *Id2*, and *Id3* might indeed represent bona fide direct targets of the canonical BMP pathway, as their expression levels were, respectively, increased and decreased in response to BMP signaling gain and loss of function (Fig. S1). Therefore, we next analyzed by semiquantitative PCR their expression levels within PP, PN, and NN cell subpopulations that had been previously purified by FACS 16 h after coelectroporation of the pSox2:EGFP and pTis21:RFP reporters (Fig. 2 I). Both *Id2* and *Id3* transcripts presented expression levels higher in PP than in PN than in NN subpopulations (Fig. 2 J). Thus, the regulation of two out of three likely direct target genes of the canonical BMP pathway presented a pattern similar to the one obtained after pS158 quantification. Altogether, these results strongly support the idea that the distinct modes of progenitor division are correlated to different levels of endogenous canonical BMP activity during spinal interneuron neurogenesis.

SMAD1/5 activity is required to maintain self-expanding divisions and to restrain neurogenic divisions

Next, we determined whether SMAD activity influences the modes of division adopted by spinal progenitors. Because we previously demonstrated that SMAD8 is required only for the generation of the most dorsal population of interneurons (dI1; Le Dréau et al., 2012), we focused our attention on the activity of SMAD1 and SMAD5.

We analyzed the consequences of SMAD1/5 inhibition on the modes of division after electroporation of shRNA constructs targeting chick *Smad1* or *Smad5* (sh-S1 and sh-S5, respectively; see Materials and methods). We first performed coelectroporation experiments in which the pTis21:RFP reporter was combined with the sh-S1/5 or control vectors together with an H2B-GFP–expressing vector to follow electroporated cells (Fig. 3 A). 24 hpe, we observed a significant increase in the percentage of $pTis21^+$ dividing progenitors in the absence of SMAD1/5 activity compared with control (percentages of $H2B\text{-}GFP^+;pH3^+;pTis21^+$ cells were 66 ± 2 for control, 86 ± 3 for sh-S1, and 85 ± 3 for sh-S5; $P < 0.01$; Fig. 3 B), indicating that reduced SMAD1/5 activity increased the proportion of neuron-generating divisions (PN + NN).

Similar experiments performed with the pSox2:EGFP reporter revealed that the proportion of $pSox2^+$ dividing progenitors was significantly lower than in the controls when this reporter was coelectroporated with sh-S1/5 constructs (percentages of $H2B\text{-}RFP^+;pH3^+;pSox2^+$ cells were 81 ± 2 for control, 58 ± 5 for sh-S1, and 65 ± 3 for sh-S5; $P < 0.01$; Fig. 3, C and D). These results indicated that *Smad1/5* knockdown reduced the proportion of progenitor-generating divisions (PP + PN). Coelectroporation of a constitutively active SMAD5 mutant (SMAD5-SD) together with the sh-S5 construct reverted both the proportions of $pTis21^+$ divisions and $pSox2^+$ divisions at the levels obtained by control electroporation (Fig. S2, A and B), thereby ensuring of the specificity of the phenotype.

Considering that PP and NN divisions correspond to $pTis21^-$ and $pSox2^-$ divisions, respectively (see Materials and methods; Saade et al., 2013), we extracted the proportion of PN divisions as %PN = 100 − (%PP + %NN). This revealed that *Smad1/5* knockdown induced an increase in NN divisions of approximately twofold (percentages of NN were 19 ± 2 for control, 42 ± 5 for sh-S1, and 36 ± 3 for sh-S5; $P < 0.01$; Fig. 3 E) and an equivalent approximate twofold reduction in PP divisions (percentages of PP were 34 ± 2 for control, 14 ± 3 for sh-S1, and 15 ± 3 for sh-S5; $P < 0.01$: Fig. 3 E), without affecting PN divisions (percentages of PN were 47 ± 4 for control, 44 ± 8 for sh-S1, and 50 ± 6 for sh-S5: Fig. 3 E). Moreover, inhibiting SMAD1/5 activity by overexpressing Somitabun, a *Smad5* mutant acting as a dominant negative to SMAD1/5/8 (Hild et al., 1999), produced similar results (Figs. 3 F and S2, C and D). Interestingly, increasing concentrations of Somitabun resulted in a gradual increase in the proportion of NN divisions concomitant with a gradual decrease in the proportion of PP divisions (Fig. 3 F). Together, these results established that the mode of division adopted by spinal progenitors depends on the level of SMAD1/5 activity and that high SMAD1/5 activity is required to maintain PP divisions and restrain premature NN divisions (Fig. 3 G).

We next performed the converse experiment by analyzing the consequences of SMAD1/5 overactivation on the modes of divisions. Constitutively active forms of SMAD1 or SMAD5 (SMAD1-SD and SMAD5-SD, respectively; see Le Dréau et al.,

and the control H2B-RFP vector (C), the pTis21:RFP and the control H2B-GFP vector (E), or both pSox2:EGFP and pTis21:RFP reporters (G). The intensity of the mean nuclear pS158 staining was measured in $pSox2^-$ and $pSox2^+$ mitoses (D), in $pTis21^-$ and $pTis21^+$ mitoses (F), or in mitotic $GFP^+;RFP^-$ (PP), $GFP^+;RFP^+$ (PN), and $GFP^-;RFP^+$ (NN) progenitors (H). (I) Illustration of the methodology used to analyze the levels of Id1/2/3 transcripts expressed by the PP, PN, and NN subpopulations. (J) Semiquantitative PCR analysis of the mRNA levels of Id1, Id2, and Id3 transcripts expressed by $GFP^+;RFP^-$ (PP), $GFP^+;RFP^+$ (PN), and $GFP^-;RFP^+$ (NN) cells. a.u., arbitrary unit; EP, electroporation. Error bars show means ± SEM. *, $P < 0.05$; **, $P < 0.01$; ***, $P < 0.001$. Bars: (main images) 25 µM; (insets) 10 µM. The higher magnification pictures originate from the corresponding insets. The dotted lines delineate nuclei. The asterisks show the cells of interest.

Published February 10, 2014

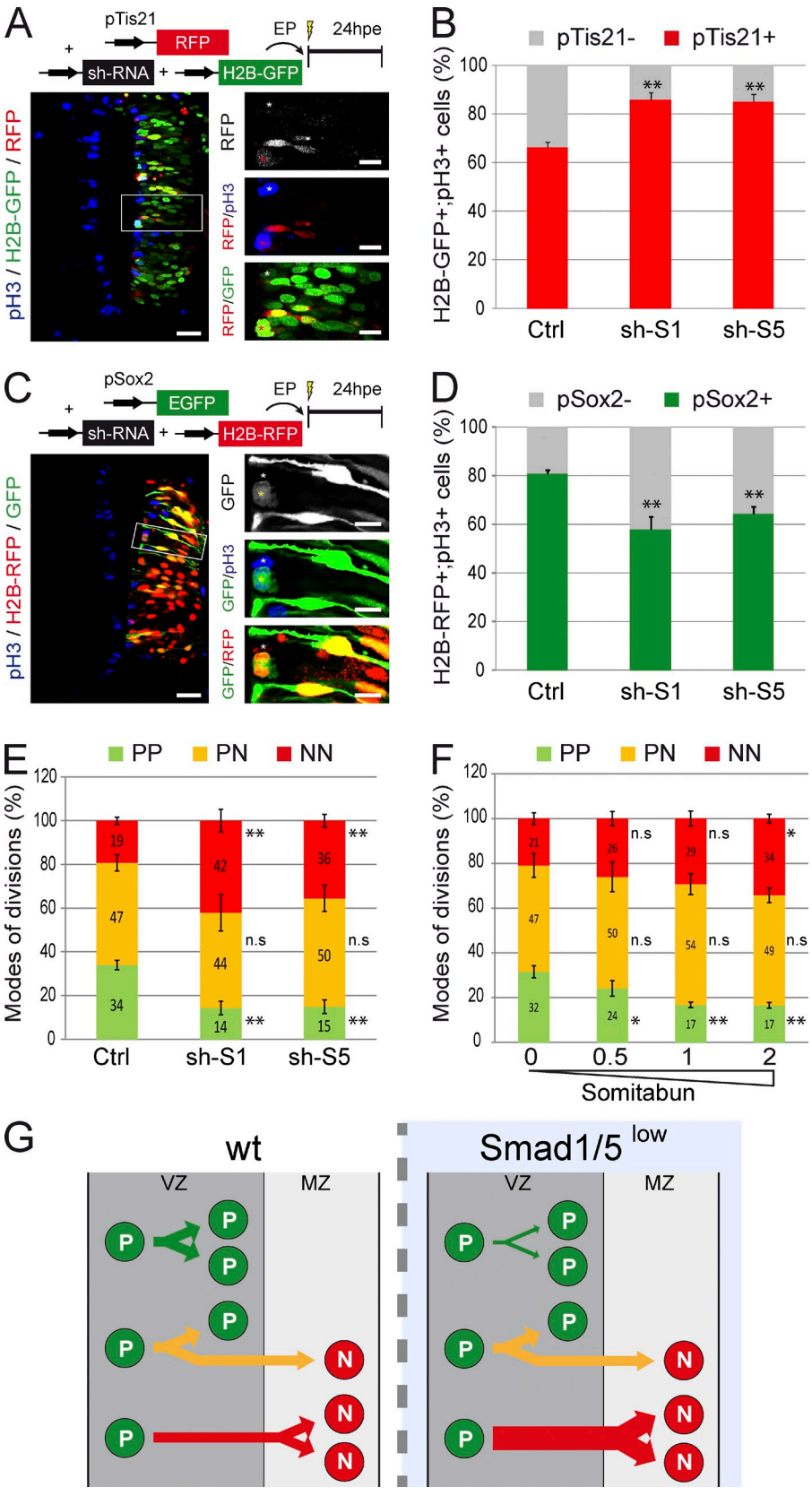

Figure 3. **SMAD1/5 activity is required to maintain self-expanding divisions.** (A–D) Analysis of neurogenic (PN + NN) and progenitor-generating (PP + PN) divisions in vivo. Transverse sections were stained for pH3 to identify mitotic progenitors at 24 hpe of HH14 embryos with control (Ctrl) or *Smad1/5* shRNA (sh-S1 and sh-S5) constructs, together with the pTis21:RFP reporter and a control H2B-GFP vector (A) or with the pSox2:GFP reporter and control H2B-RFP vector (C). The higher magnification pictures originate from the corresponding insets. Proportions of mitotic electroporated (H2B-GFP$^+$;pH3$^+$ [B] or H2B-RFP$^+$;pH3$^+$ [D]) progenitors based on the activity of the pTis21:RFP (B) or pSox2:EGFP (D) reporters. (E) Proportions of the three modes of divisions (PP, PN, and NN) obtained 24 hpe with control or *Smad1/5* shRNA vectors (sh-S1 or sh-S5). These percentages were deduced from the earlier results, considering that the %PP = %pTis21$^-$, %NN = %pSox2$^-$, and %PN = 100 − (%PP + %NN). (F) Proportions of the modes of divisions obtained 24 hpe with 0, 0.5, 1, or 2 µg/µl Somitabun. (G) Illustration of the increase in NN divisions obtained at the expense of PP divisions after SMAD1/5 inhibition in spinal neural progenitors. EP, electroporation; wt, wild type. Error bars show means ± SEM. *, P < 0.05; **, P < 0.01. Bars: (main images) 25 µM; (insets) 10 µM.

Published February 10, 2014

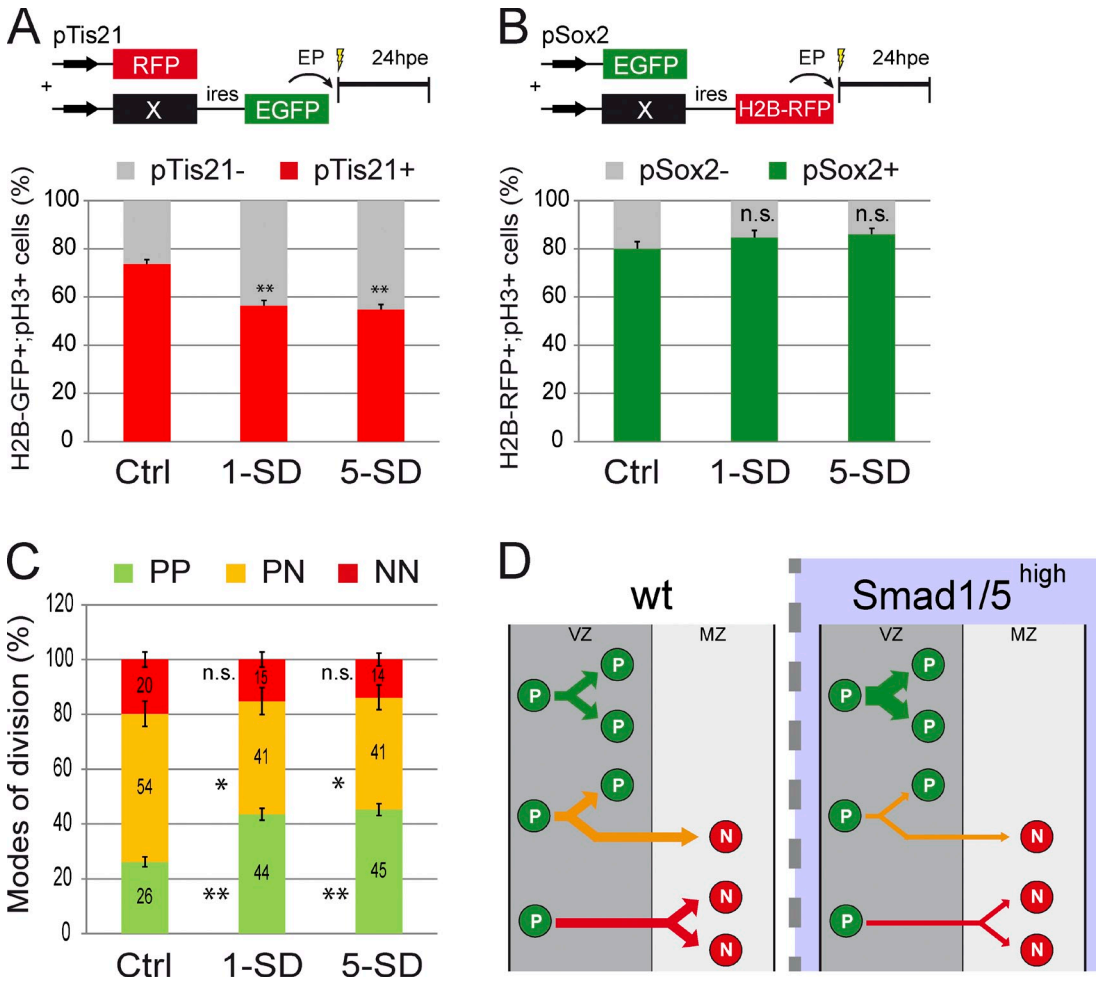

Figure 4. **Strong SMAD1/5 activity promotes PP divisions at the expense of PN and NN divisions.** (A and B) Proportions of mitotic electroporated progenitors (H2B-GFP$^+$;pH3$^+$ [A] or H2B-RFP$^+$;pH3$^+$ [B]) based on the activity of the pTis21:RFP (A) or pSox2:EGFP (B) reporters at 24 h after coelectroporation of HH14 embryos with control (Ctrl), SMAD1-SD (1-SD), or SMAD5-SD (5-SD). (C) Percentages of the three modes of divisions (PP, PN, and NN) obtained at 24 hpe with the constructs indicated and deduced from earlier results, considering that %PP = %pTis21$^-$, %NN = %pSox2$^-$, and %PN = 100 − (%PP + %NN). (D) Illustration of the increase in PP divisions obtained at the expense of PN and NN divisions after SMAD1/5 overactivation in spinal progenitors. EP, electroporation; wt, wild type. Error bars show means ± SEM. *, $P < 0.05$; **, $P < 0.01$.

2012) were electroporated in combination with the pTis21:RFP or pSox2:GFP reporters. SMAD1/5-SD significantly decreased the proportion of pTis21$^+$ divisions (percentages of H2B-GFP$^+$;pH3$^+$;pTis21$^+$ cells were 74 ± 2 for control, 57 ± 2 for SMAD1-SD, and 55 ± 2 for SMAD5-SD; $P < 0.01$; Fig. 4 A). The percentage of pSox2$^+$ dividing cells augmented only slightly after SMAD1/5 overactivation (percentages of H2B-RFP$^+$;pH3$^+$;pSox2$^+$ cells were 80 ± 3 for control, 85 ± 3 for SMAD1-SD, and 86 ± 2 for SMAD5-SD: Fig. 4 B). The percentages of the three modes of divisions deduced from these data suggested that SMAD1/5 overactivation increased PP divisions (percentages of PP were 26 ± 1 for control, 44 ± 2 for SMAD1-SD, and 45 ± 2 for SMAD5-SD; $P < 0.01$; Fig. 4 C) at the expense of PN (percentages of PN were 54 ± 5 for control, 41 ± 5 for SMAD1-SD, and 41 ± 4 for SMAD5-SD; $P < 0.05$; Fig. 4 C) and NN divisions (percentages of NN were 20 ± 3 for control, 15 ± 2 for SMAD1-SD, and 14 ± 2 for SMAD5-SD; Fig. 4 C). Thus, high levels of SMAD1/5 activity were sufficient to promote self-expanding divisions (Fig. 4 D).

SMAD1/5 activity is required to maintain spinal progenitor cells

We reasoned that the concomitant decrease in PP and increase in NN divisions, which are caused by SMAD1/5 inhibition should alter the pace of neuronal differentiation. We thus analyzed the time course of neuronal differentiation after interfering with SMAD1/5 activity. The proportion of electroporated cells (H2B-RFP$^+$) differentiated into neurons (HuC/D$^+$) was significantly higher from 24 h after *Smad1/5* knockdown onwards (percentages of H2B-RFP$^+$;HuC/D$^+$ cells at 38 hpe were 31 ± 3 for control, 55 ± 4 for sh-S1, and 54 ± 3 for sh-S5; $P < 0.01$; Figs. 5 A and S3 A), indicating that the loss of SMAD1/5 activity caused the premature differentiation of neural progenitors in a cell-autonomous manner. To confirm this result, we took advantage of the Tubb3enh:EGFP reporter (Bergsland et al., 2011), which contains an EGFP cassette driven by an enhancer of the *β3-tubulin* gene, the expression of which is activated during neuronal differentiation. More H2B-RFP$^+$;GFP$^+$ cells were observed in embryos electroporated

Published February 10, 2014

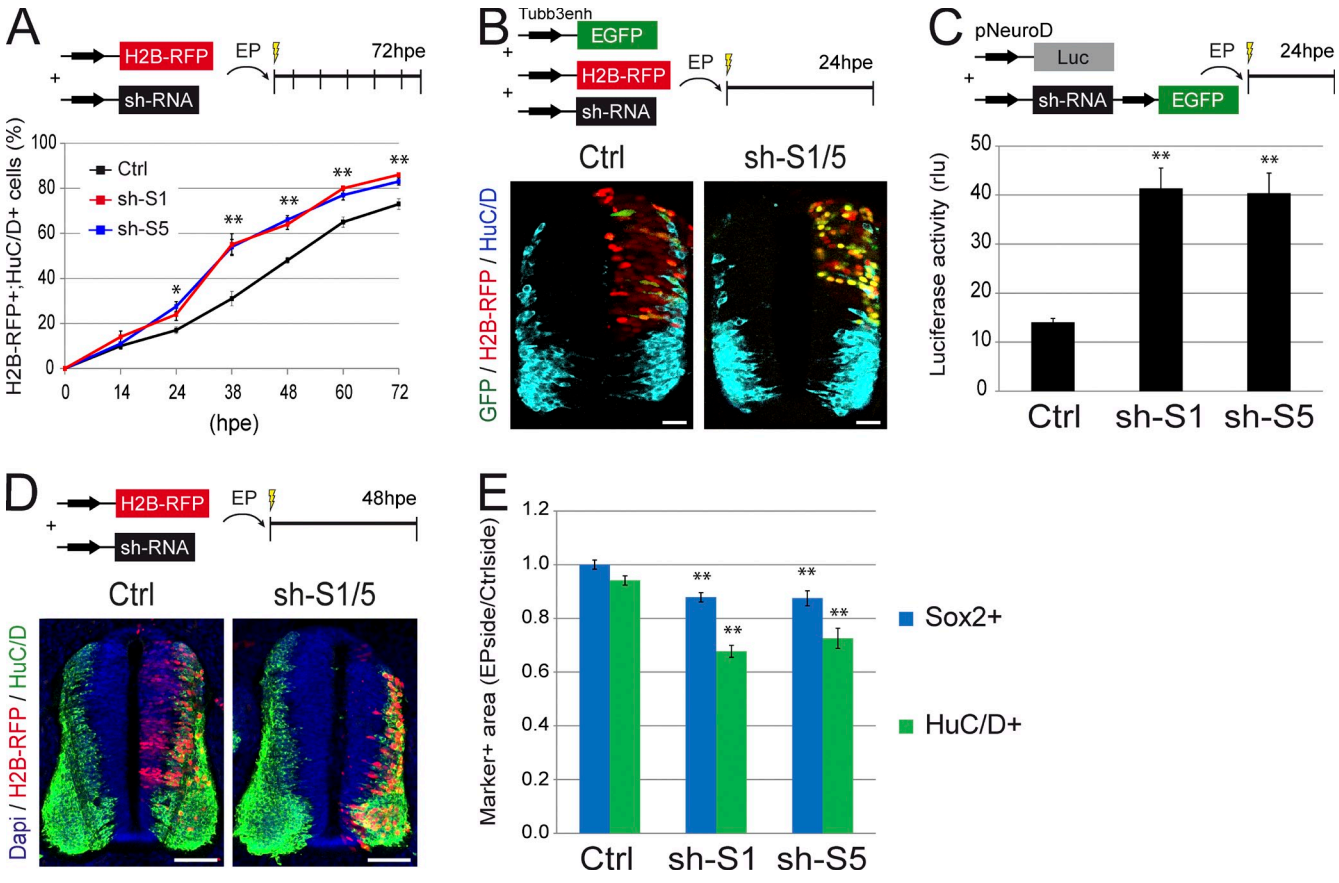

Figure 5. **SMAD1/5 inhibition triggers premature differentiation in a cell-autonomous manner.** (A) Proportions of electroporated cells differentiated into neurons (H2B-RFP$^+$;HuC/D$^+$) obtained after electroporation of HH14 embryos with control (Ctrl) and *Smad1/5* shRNA (sh-S1 and sh-S5) constructs, in sections of neural tubes recovered at the times indicated (hpe). (B) Representative sections stained for HuC/D expression 24 h after coelectroporation with the Tubb3enh: EGFP reporter, the control H2B-RFP vector, and control or *Smad1/5* shRNA (sh-S1/5). (C) Quantification of luciferase activity (expressed in relative luciferase units [rlu]) driven by the pNeuroD reporter at 24 hpe with the *Smad1/5* shRNA (sh-S1 or sh-S5) or control vectors. (D) Representative transverse sections of a chick neural tube at 48 hpe with control or *Smad1/5* shRNA (sh-S1/5). DAPI, HuC/D, and H2B-RFP stain nuclei, differentiating neurons and electroporated cells. (E) Analysis of the ratios of the areas occupied by the VZ (Sox2$^+$) and MZ (HuC/D$^+$) measured for the electroporated side and standardized to their contralateral controls. EP, electroporation. Error bars show means ± SEM. *, $P < 0.05$; **, $P < 0.01$. Bars: (B) 25 µM; (D) 50 µM.

with sh-S1 and sh-S5 than in the controls at 24 hpe (Fig. 5 B). At 24 hpe, *Smad1/5* knockdown had moreover triggered an approximately threefold increase in the activity of a luciferase (Luc) reporter driven by a fragment of the *NeuroD* promoter, a basic helix–loop–helix factor known to activate the panneurogenic differentiation program (pNeuroD:Luc; 14.0 ± 0.8 for control, 41.3 ± 4.2 for sh-S1, and 40.4 ± 4.1 for sh-S5; $P < 0.01$; Fig. 5 C).

At 48 hpe, the proportion of H2B-RFP$^+$;HuC/D$^+$ cells was still higher in sh-S1 and sh-S5 embryos than in control ones (Fig. 5, A and D). We also noticed that fewer HuC/D$^+$ cells were evident in the mantle zone (MZ; the lateral region of the neural tube formed by neurons) after *Smad1/5* knockdown than in the controls (Figs. 5 D and S3 A). This observation was confirmed by measuring the area occupied by the MZ, which showed an ~30% reduction in response to SMAD1/5 knockdown (Figs. 5 E and S3 B). Interestingly, this was associated with an ~15% decrease in the area occupied by the ventricular zone (VZ) containing the Sox2$^+$ progenitors (Figs. 5 E and S3 B).

Loss of SMAD1/5 activity causes a specific shortening of the S phase

Distinct stem cell fates and modes of division have been correlated with variations in the cell cycle kinetics of neural progenitors in the developing cerebral cortex (Dehay and Kennedy, 2007; Salomoni and Calegari, 2010). To test how SMAD1/5 activity influences the cell cycle, we measured the duration of the different cell cycle phases by performing cumulative BrdU experiments (see Materials and methods; Nowakowski et al., 1989). When we assessed the index of BrdU labeling in electroporated cells (H2B-RFP$^+$) located in the VZ at 48 hpe (Fig. 6 A), the fraction of cells in the S phase (indicated by the intercept of the BrdU labeling curve with the *y* axis) was significantly smaller for sh-S1 (0.24) and sh-S5 (0.21) cells than for the controls (0.35: Fig. 6 B). In contrast, the time needed for the BrdU labeling index to reach the plateau (representing the Tc − Ts length) was comparable for control (7.0 h), sh-S1 (7.6 h), and sh-S5 (7.7 h) cells. Similarly, the fraction of cycling cells was nearly identical in control (0.77 ± 0.01) and in sh-S1 (0.74 ± 0.01) and sh-S5 (0.76 ± 0.02) electroporated embryos. These data

Published February 10, 2014

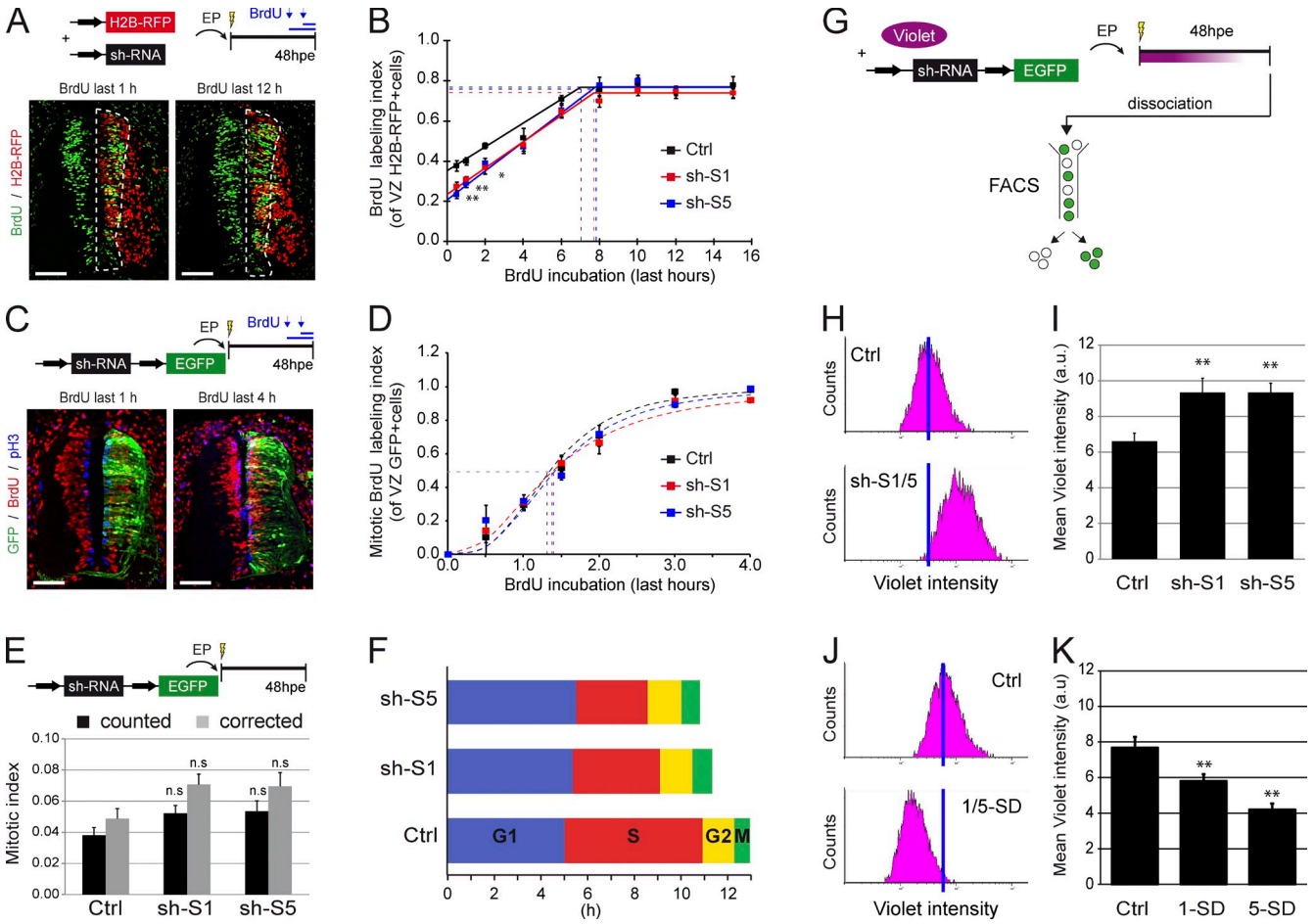

Figure 6. **Loss of SMAD1/5 activity causes a specific shortening of the S phase.** (A) Representative sections of neural tubes at 48 hpe, after incorporation of BrdU in the last 1 and 12 h. BrdU staining was observed in a fraction of the electroporated H2B-RFP$^+$ neural progenitors that were still present in the VZ (dashed lines). (B) BrdU labeling index calculated for neural progenitors electroporated (H2B-RFP$^+$) with control (Ctrl), *Smad1* (sh-S1), or *Smad5* (sh-S5) shRNA vectors. Dashed lines show the growth fraction (y axis) and the duration of BrdU incorporation needed to reach the plateau, which represents the ($T_c - T_S$) value (*x* axis). (C) Representative sections showing BrdU staining in a fraction of the mitotic (pH3$^+$) electroporated (GFP$^+$) neural progenitors. (D) Mitotic BrdU labeling index calculated for cells electroporated (GFP$^+$) with control, *Smad1*, or *Smad5* (sh-S5) shRNA vectors. Dashed lines show the duration of the BrdU incorporation needed to label 50% of the cell population (*y* axis), which represents the mean T_{G2} value (*x* axis). (E) Mitotic index calculated for cells electroporated (GFP$^+$) with control, *Smad1* (sh-S1), or *Smad5* (sh-S5) shRNA vectors. Both the mean values obtained from counting and those corrected with respect to differential growth fraction values are given. (F) Graphical representation of the duration of the cell cycle (Tc) and its distinct phases measured for control, *Smad1* (sh-S1), or *Smad5* shRNA (sh-S5) electroporated cells. (G–K) Illustration of the method used to assess neural progenitor divisions in vivo (G), after loss (H and I) or gain of function (J and K) of SMAD1/5 activity. (H and J) Representative pictures of the CellTrace violet intensity measured by flow cytometry in dissociated cells at 48 hpe with the indicated constructs. The blue bars highlight the mean intensity obtained in the control condition. (I and K) Quantification of the mean CellTrace violet intensity measured at 48 hpe with the indicated constructs. a.u., arbitrary unit; EP, electroporation. Error bars show means ± SEM. **, $P < 0.01$. Bars, 50 µM.

enabled us to calculate the total length of the cell cycle (Tc), which appeared to be significantly shorter after SMAD1/5 inhibition (mean Tc of 12.9 ± 0.9 h for control, 11.3 ± 0.7 h for sh-S1, and 10.8 ± 1.1 h for sh-S5: Fig. 6 F). Calculating the S-phase length (Ts) revealed a marked shortening after *Smad1/5* knockdown (mean Ts of 5.9 ± 0.6 h for control, 3.7 ± 0.4 h for sh-S1, and 3.1 ± 0.5 h for sh-S5; Fig. 6 F).

The length of the G2 phase (TG2) was derived from the BrdU labeling index of the mitotic electroporated cells (GFP$^+$;pH3$^+$) in the VZ at 48 hpe (Fig. 6 C). We observed no obvious changes in the labeling index curves of sh-S1, sh-S5, or control cells (Fig. 6 D), and the mean G2 duration calculated by the paradigm of labeled mitoses method (see Materials and methods; Quastler and Sherman, 1959) was comparable for control (1.3 ± 0.1 h), sh-S1 (1.4 ± 0.1 h), and sh-S5 (1.4 ± 0.1 h) cells (Fig. 6 F).

The duration of the M phase (TM) was derived from the mitotic index of the electroporated cells, and there were no changes in the mitotic indices after electroporation with control or sh-S1/5 vectors (mitotic index 0.04 ± 0.01 for control, 0.05 ± 0.01 for sh-S1, and 0.05 ± 0.01 for sh-S5; Fig. 6 E) or after applying a correction for the slight differences in growth fraction values (corrected mitotic index of 0.05 ± 0.01 for control, 0.07 ± 0.01 for sh-S1, and 0.07 ± 0.01 for sh-S5; Fig. 6 E). The TM was then calculated from the Tc and yielded comparable values for control (0.64 ± 0.1 h), sh-S1 (0.80 ± 0.1 h), and sh-S5 (0.76 ± 0.2 h) cells (Fig. 6 F). Finally, determination of the Tc, Ts, TG2, and TM allowed us to deduce the length of the G1 phase (TG1), which was similar in control (5.0 ± 1.7 h), sh-S1 (5.4 ± 1.3 h), and sh-S5 (5.5 ± 1.9 h) cells (Fig. 6 F). Together, these analyses indicated that interfering

Published February 10, 2014

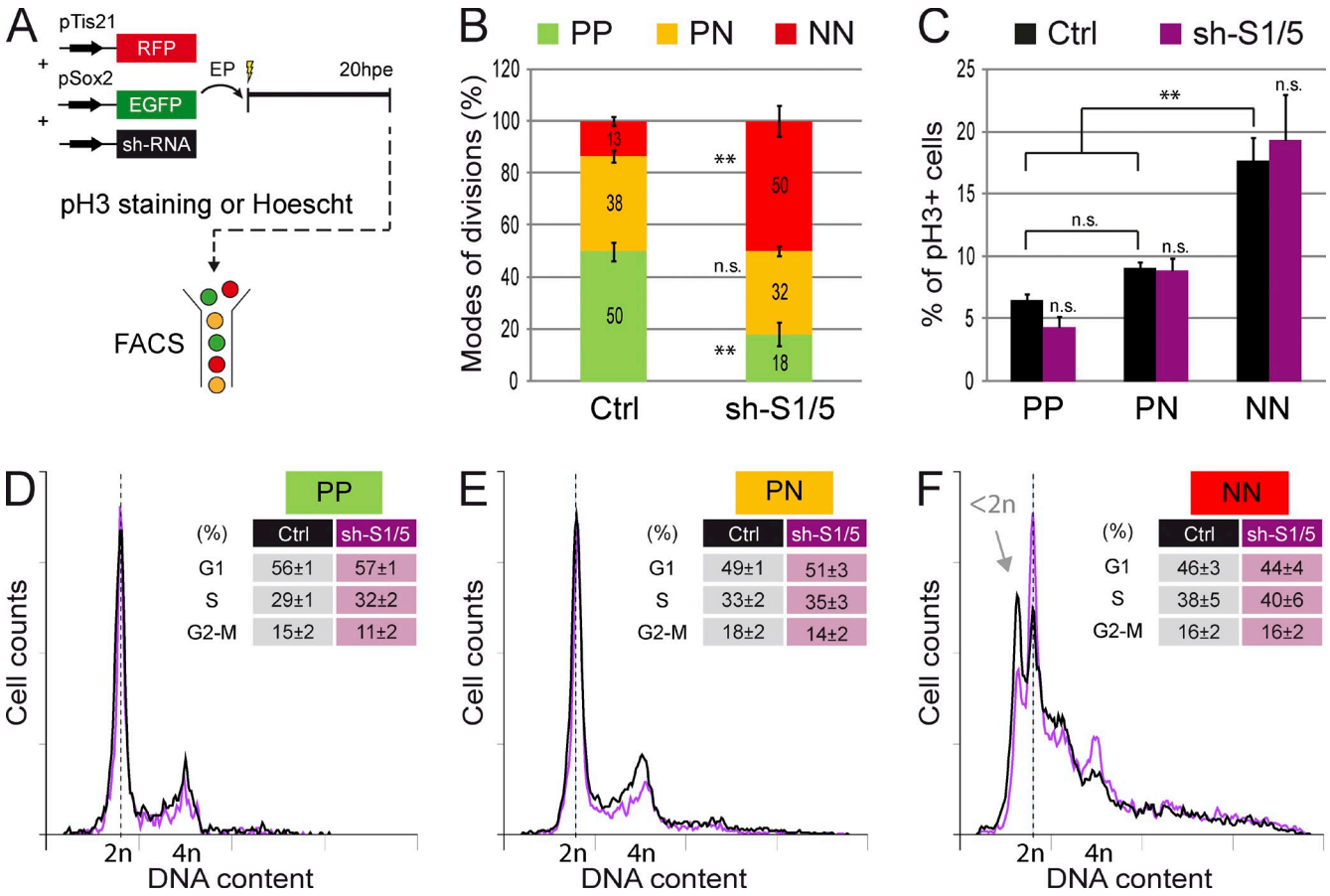

Figure 7. **Analysis of the cell cycle distribution of PP, PN, and NN progenitors.** (A) Illustration of the methodology used to analyze the cell cycle distribution of PP, PN, and NN divisions by flow cytometry in dissociated cells processed for pH3 staining or Hoechst incorporation 20 hpe with pTis21:RFP, pSox2:EGFP, and control or *Smad1/5* shRNA vectors. (B) Percentages of mitotic ($pH3^+$) $GFP^+;RFP^-$ (PP), $GFP^+;RFP^+$ (PN), and $GFP^-;RFP^+$ (NN) cells electroporated with control (Ctrl) or *Smad1/5* shRNA (sh-S1/5). (C) Mitotic indices of $GFP^+;RFP^-$ (PP), $GFP^+;RFP^+$ (PN), and $GFP^-;RFP^+$ (NN) cells electroporated with control or *Smad1/5* shRNA (sh-S1/5). (D–F) Overlays of representative DNA content profiles obtained after Hoechst incorporation for $GFP^+;RFP^-$ (D, PP), $GFP^+;RFP^+$ (E, PN), and $GFP^-;RFP^+$ (F, NN) cells electroporated with control or sh-S1/5 constructs. Mean values of the percentages of cells in G1, S, and G2–M phases are presented. EP, electroporation. Error bars show means ± SEM. **, $P < 0.01$.

with SMAD1/5 activity in spinal progenitors additionally causes a reduction of their mean cell cycle length as a result of a shortening of the S phase.

We also evaluated the mean number of divisions that electroporated cells performed in vivo using the CellTrace violet, a cytoplasmic retention dye, which is specifically subject to dilution upon cell division. The CellTrace violet was injected into the neural tube lumen at the time of electroporation, and its fluorescence intensity was measured in dissociated GFP^+ cells at 48 hpe by flow cytometry (Fig. 6 G). Compared with control embryos, electroporation with sh-S1 or sh-S5 increased the mean CellTrace violet intensity by 41% (mean violet intensity of 6.6 ± 0.5 for control, 9.3 ± 0.8 for sh-S1, and 9.3 ± 0.5 for sh-S5; $P < 0.01$; Fig. 6, H and I), indicating that on average, spinal progenitors with impaired SMAD1/5 activity underwent fewer divisions. Conversely, hyperactivation of SMAD1/5 activity through electroporation of SMAD1-SD and SMAD5-SD caused a reduction in the mean CellTrace violet intensity (mean violet intensity of 7.7 ± 0.6 for control, 5.8 ± 0.4 for SMAD1-SD, and 4.2 ± 0.4 for SMAD5-SD; $P < 0.01$; Fig. 6, J and K), implying that more neural progenitors divided in response to SMAD1/5 overactivation.

The regulation of the modes of division by SMAD1/5 precedes cell cycle alterations

It appears that modulating SMAD1/5 activity within spinal progenitors alters both their mode of division and their cell cycle kinetics. We next established an experimental design to discriminate which of these two events is directly controlled by SMAD1/5. Accordingly, we coelectroporated the two reporters (pTis21:RFP and pSox2:GFP) with the sh-S1/5 or control vectors, and we then dissociated the neural tube cells at 20 hpe, stained them for pH3, and analyzed them by flow cytometry (Fig. 7 A). The assessment of the proportions of PP, PN, and NN divisions among the mitotic ($pH3^+$) electroporated cells confirmed that *Smad1/5* knockdown increased the percentage of NN divisions at the expense of PP ones, without significantly altering PN divisions (Fig. 7 B). In the same set of experiments, we calculated the mitotic index for each of the three progenitor subpopulations. After control electroporation, although the percentages of mitotic PP and PN cells were comparable, that of mitotic NN progenitors was significantly higher (percentages of $pH3^+$ cells were 6.5 ± 0.5 for PP, 9.1 ± 0.4 for PN, and 17.6 ± 1.9 for NN in control conditions; $P < 0.01$; Fig. 7 C), suggesting that NN divisions were faster. Importantly, interfering with

Published February 10, 2014

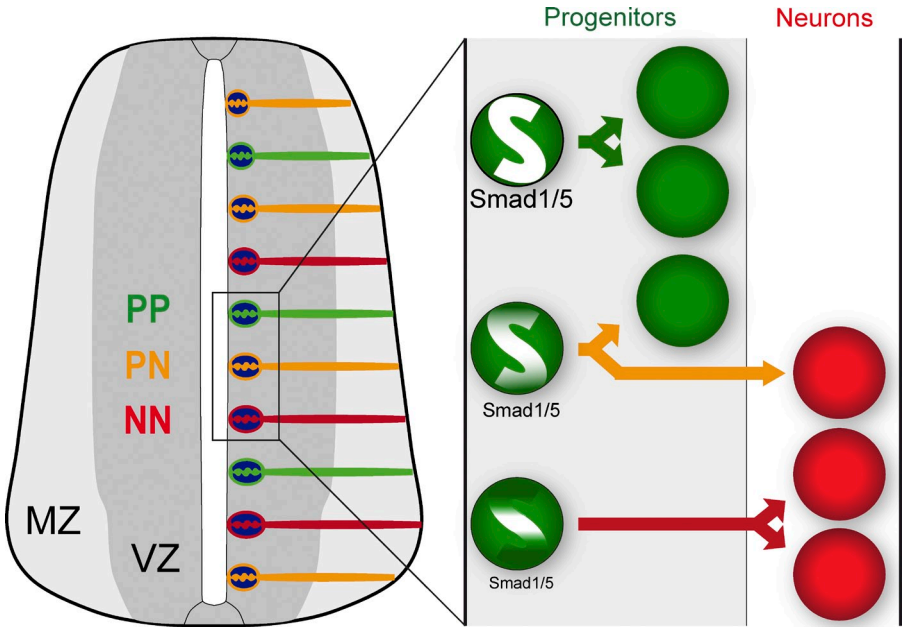

Figure 8. **Model of the control imposed by SMAD1/5 on the mode of divisions of neural progenitors during spinal interneuron generation.** From the onset of spinal interneuron generation, neural progenitors undergo along the dorsal–ventral axis three distinct modes of division: the symmetric proliferative mode (PP, green arrow), which results in the generation of two daughter progenitor cells; the asymmetric mode (PN, yellow arrow), leading to the generation of one daughter progenitor cell while the other daughter cell is committed to differentiate into a neuron; or the symmetric neurogenic (NN, red arrow) mode through which the two daughter cells are committed to differentiation. The decision of a neural progenitor to undergo one division mode or another is under the control of SMAD1/5, so that high, intermediate, and low levels of SMAD1/5 activity dictate neural progenitors to undergo PP, PN, and NN divisions, respectively.

SMAD1/5 activity did not affect the mitotic indices of any of the three progenitor populations compared with their respective controls (percentages of $pH3^+$ cells were 4.3 ± 0.9 for PP, 8.9 ± 1.0 for PN, and 19.3 ± 3.7 for NN after sh-S1/5 electroporation; Fig. 7 C).

Alternatively, the DNA content was assessed by flow cytometry after Hoechst staining, and its profile was similar for PP and PN cells (Figs. 7, D and E; and S4 C). In contrast, the NN cell population presented a surprising DNA content profile, showing numerous peaks and including a nonnegligible proportion of hypoploidy (Figs. 7 F and S4 D). Studying the distribution of the different cell cycle phases of the diploid populations revealed a significantly higher proportion of PP cells in G1 than PN and NN (mean percentages of G1 were 56 ± 1 for PP, 49 ± 1 for PN, and 46 ± 3 for NN; $P < 0.05$; Figs. 7, D–F; and S4 E), whereas the percentages of these diploid cells in S and G2–M were not significantly affected (Fig. 7, D–F). The aneuploid NN subpopulation presented significant alterations in the proportions of cells in the G1, S, and G2–M phases compared with the diploid populations (Fig. S4 E). SMAD1/5 inhibition affected the proportions of total PP, PN, and NN cells in a way similar to that previously observed in the mitotic electroporated cells (compare Fig. S4 B with Fig. 7 B), although it did not significantly alter either the DNA content profile or the cell cycle distribution in any of the cell populations (Figs. 7, D–F; and S4 E).

Therefore, these results confirmed that SMAD1/5 activity regulated the balance between the modes of divisions of spinal progenitors and further suggested that these changes in cell fate preceded the changes in cell cycle kinetics. Altogether, these data imply that SMAD1/5 directly control the mode of division of neural progenitors during spinal interneuron generation.

Discussion

Combining newly developed markers that identify the three modes of progenitor division in the developing spinal cord (self-expanding [PP], self-renewing [PN], and self-consuming [NN]) with in vivo manipulations of SMAD1/5 activity, we identified a new role for the canonical BMP effectors SMAD1/5 in dictating the mode of division of neural progenitors during spinal interneuron generation (Fig. 8). Inhibiting SMAD1/5 activity in spinal progenitors at the onset of interneuron generation provoked a premature increase in NN divisions at the expense of PP ones, leading neural progenitors to prematurely exit the cell cycle and undergo differentiation. A consequence of these cell-autonomous effects would be the depletion of the neural progenitor pool, as reflected by the reduction in the size of the VZ containing $Sox2^+$ neural progenitors. This would explain why we ultimately observed a reduction in neuron number after SMAD1/5 inhibition in the developing spinal cord (this study; Le Dréau et al., 2012). A similar mechanism could account for the impaired neurogenesis reported after BMP signaling inhibition during both corticogenesis and dentate development (Segklia et al., 2012; Choe et al., 2013). Accordingly, the canonical BMP signaling thus appears to be crucial for stem cell maintenance both during neural development and adult neurogenesis (Lim et al., 2000; Mira et al., 2010).

Variations in cell cycle kinetics are correlated with distinct stem cell fates in the developing cerebral cortex (Dehay and Kennedy, 2007; Salomoni and Calegari, 2010). By taking advantage of the pSox2:EGFP and pTis21:RFP reporters, we distinguished between spinal progenitors based on their mode of division and found that the cell cycle parameters differed in these three populations. In particular, there was an approximately twofold increase in the mitotic index of the NN progenitors over that of the PP and PN populations, suggesting that progenitors committed to NN divisions have a shorter cell cycle. This was consistent with the fact that the premature differentiation provoked by SMAD1/5 inhibition was accompanied by a reduction of the mean cell cycle length, the latter was caused by a shortening of the S phase. Thus, S-phase shortening was associated with neuronal commitment in the developing spinal cord,

Published February 10, 2014

as reported recently for neural progenitors in the developing mouse cerebral cortex (Arai et al., 2011). Yet our analyses demonstrated that SMAD1/5 inhibition altered the balance between these three division modes without provoking any significant changes in the cell cycle parameters. This leads us to propose that cell fate determination precedes any changes in the cell cycle and that the reduction of the mean cell cycle length is a consequence of the alteration in the balance of the modes of divisions, rather than a cause. Accordingly, differential regulation of cyclin D2 in response to asymmetric divisions was recently demonstrated in the developing murine cerebral cortex, its expression only persisting in the daughter cell that inherited the basal process and that maintained its progenitor identity (Tsunekawa et al., 2012). Importantly, the BMP-induced maintenance of adult stem cells is associated with quiescence (Lim et al., 2000; Mira et al., 2010; Ono et al., 2011; Oshimori and Fuchs, 2012), arguing against the idea that BMP activity determines stem cell fate by stimulating cell cycle progression.

Another significant observation was the identification of aneuploid progenitors in the developing spinal cord. There is a growing body of evidence that aneuploid neurons are generated during cerebral cortex development (Rehen et al., 2001; Peterson et al., 2012) and adult neurogenesis (Rehen et al., 2001; Muotri and Gage, 2006) and that these neurons are functional (Kingsbury et al., 2005). Aneuploidy is thought to represent one of the numerous mechanisms causing the variations in DNA content that occur in the CNS, and it is thought to contribute to neuronal diversity and potentially enhance an organism's adaptability (Kingsbury et al., 2006; Muotri and Gage, 2006). Interestingly, we only detected aneuploidy in the NN progenitors committed to terminal neurogenic divisions. Thus, the generation of aneuploid cells might be facilitated by the shortening of the S phase. In fact, changes in the expression of factors key to cell cycle regulation, DNA replication, DNA repair, and chromatin remodeling have already been observed in a genome-wide expression analysis that compared expanding (pTis21:GFP$^-$) and committed (pTis21:GFP$^+$) neural progenitors in the developing murine cerebral cortex (Arai et al., 2011). Restricting the occurrence of aneuploidy to terminally differentiating neural progenitors might therefore prevent the risk of transmitting potentially deleterious DNA alterations to the whole lineage.

Both the quantification of endogenous pS158 intensity and the comparison of *Id* gene expression levels in the three different progenitor subpopulations supported the notion that the mode of division was dictated by an endogenous gradient of SMAD1/5 activity during spinal interneuron generation, with the weakest activity forcing neural progenitors to enter NN divisions (Fig. 8). The idea of a gradient of BMP activity acting as a fate determinant was proposed recently in *Drosophila* germline stem cells (Xia et al., 2012), leading to the intriguing hypothesis that dramatic cellular decisions such as stem cell fate originate from subtle variations in the levels of SMAD activity. We quantified levels of SMAD1/5 activity during mitosis; however, we do not exclude the possibility that regulating cell fate decision through modifications of SMAD1/5 activity could occur earlier in the cell cycle. Another interesting question will be to determine whether *Id2* and *Id3* are effectively involved in instructing the mode of spinal progenitor division, as suggested by their expression gradually decreasing in PP, PN, and NN progenitors.

The canonical BMP activity is highly dynamic both spatially and temporally during spinal cord development (Le Dréau et al., 2012; Le Dréau and Martí, 2013; Tozer et al., 2013). The activity of the canonical BMP pathway is restricted to the most dorsal part of the neural tube at early stages (Le Dréau et al., 2012; Tozer et al., 2013) but deploys along the whole dorsal–ventral axis at the onset of interneuron generation (Le Dréau et al., 2012). Thus, the canonical BMP activity is likely to be required for the maintenance of self-expanding divisions only from that stage. Accordingly, Sonic Hedgehog signaling is crucial for the maintenance of self-expanding divisions earlier during development, within the context of motor neuron generation (Saade et al., 2013). Together, these results support the notion that the influence of a particular extrinsic factor on neural stem and progenitor cells is both stage and area specific (Falk and Sommer, 2009). Considering the diversity of extrinsic signals reported to affect neural stem cell maintenance (Fuentealba et al., 2012; Tiberi et al., 2012; Franco and Müller, 2013), one of the future challenges in the field of stem cell biology will be to identify the molecular mechanisms underlining these context-specific effects and to uncover the common key intrinsic factors acting downstream of these extrinsic cues to command the mode of stem cell division.

Materials and methods

Chick embryos

Eggs from white Leghorn chickens were staged according to the method of Hamburger and Hamilton (1951). In ovo electroporation was performed at stage HH14 (54 h of incubation with 22 somites) unless otherwise notified, and the embryos were recovered at the times indicated (12–72 hpe). Electroporation was performed as described previously (Le Dréau et al., 2012).

DNA constructs

The pCAGGS_ires_H2B-RFP and pCS2:H2B-GFP vectors were used at a concentration of 0.5 µg/µl as controls for electroporation. Inhibition of endogenous SMAD1/5 activity was induced by electroporation of pSuper or pSHIN vectors (3–4 µg/µl), which produce shRNAs that specifically target chick *Smad1* and *Smad5* and reduce to ~50% of their endogenous mRNA levels (Le Dréau et al., 2012). Alternatively, inhibition of SMAD activity was achieved by overexpressing the dominant-negative *Smad5* mutant Somitabun (Le Dréau et al., 2012) at various concentrations (combinations of 0:2, 0.5:1.5, 1:1, and 2:0 µg/µl of pCS2/Somitabun and empty pCS2 constructs]. The SMAD1-SD and SMAD5-SD mutants were used to overactivate endogenous SMAD1/5 activity. As previously described (Le Dréau et al., 2012), these pseudophosphorylated mutant versions of SMAD1 and SMAD5 were generated by PCR-mediated site-directed mutagenesis, replacing the three serines at the C-terminal end by aspartic acid, and cloned into pCAGGS-ires-GFP or into pCAGGS-ires-H2B-RFP.

The pTis21:RFP reporter was created by inserting a fragment of the promoter of the mouse *Tis21* gene (−442 to 65) into the ptk:RFP plasmid (Uchikawa et al., 2003), amplified from the mouse genome by PCR using the primers 5′-GGGATGAGTGGCAGAGATGT-3′ and 5′-GGTGGCTGAGGAAGTAGCTG-3′. The pSox2:EGFP reporter consisted of an EGFP cassette from the ptk2:EGFP plasmid under the control of a fragment of the chicken *Sox2* promoter covering the 7.6–14 kb of the *Sox2* locus. This fragment (provided by M. Uchikawa, Osaka University, Osaka, Japan) has already been shown to specifically reproduce endogenous Sox2 promoter activity in the developing spinal cord (Uchikawa et al., 2003).

The endogenous activities of the Sonic Hedgehog and canonical Wnt pathways were assessed using reporter constructs producing H2B-RFP under the control of a promoter containing synthetic 8× 3′GBSs (Sasaki et al., 1997; Saade et al., 2013) or synthetic T cell factor binding sites

Published February 10, 2014

(Korinek et al., 1998), respectively. As previously described (Le Dréau et al., 2012), the BRE:GFP reporter consists of an artificial promoter containing two copies of two distinct, highly conserved BRE encompassing the genomic regions −1,032/−1,052 (SBE-3, SBE-2, and GC′-5) and −1,080/−1,105 (CAGC-2, CAGC-1, and GC′-3,4) of the natural human *Id1* promoter (Korchynskyi and ten Dijke, 2002), which has been cloned upstream of the herpes simplex virus thymidine kinase minimal promoter in a vector carrying EGFP.

The Tubb3enh:EGFP reporter (Bergsland et al., 2011), consisting of an enhancer of the mouse Tubb3 gene inserted into the multiple cloning site of the bGlobin-GFP-MCSIII vector, was provided by J. Muhr (Karolinska Institute, Stockholm, Sweden) . The mPlum construct, which was developed and provided by the R.Y. Tsien laboratory (Howard Hughes Medical Institute, University of California, San Diego, La Jolla, CA), produces from a pUC19 backbone a far-red–emitting fluorescent protein obtained by directed mutagenesis of a monomeric mutant of DsRed (Wang and Tsien, 2006).

Immunohistochemistry and microscopy

Embryos were fixed for 2 h at 4°C in 4% PFA, and immunostaining was performed on either vibratome (40 µm) or cryostat (16 µm) sections following standard procedures. For BrdU detection, sections were incubated in 2 N HCl for 30 min and then rinsed with 0.1 M $Na_2B_4O_7$, pH 8.5. After washing in PBS–0.1% Triton X-100, the sections were incubated with the appropriate primary antibodies: rabbit anti-GFP, rabbit anti-Sox2, mouse anti-HuC/D, and mouse anti–lamin B1 (Invitrogen), rat anti-BrdU (AbD Serotec), rabbit anti-pS158 (Cell Signaling Technology), or rabbit anti-pH3 (EMD Millipore). Alexa Fluor 488–, Alexa Fluor 555–, and Cy5-conjugated secondary antibodies were obtained from Invitrogen and Jackson ImmunoResearch Laboratories, Inc. Sections were stained with 1 µg/ml DAPI and mounted in Mowiol (Sigma-Aldrich). Images were acquired at room temperature with the LAS software (Leica) on a confocal microscope (SP5; Leica) using 20× (dry HC Plan Apochromat, NA 0.70), 40× (oil HCX Plan Apochromat, NA 1.25–0.75), or 63× (oil HCX Plan Apochromat, NA 1.40–0.60) objective lenses. Maximal projections obtained from 2-µm z-stack images were processed in Photoshop CS5 and Illustrator CS4 (Adobe) for image merging and resizing and cell counting. Cell counts were typically performed on three to five images per embryo. The data represent the means ± SEM obtained from the values of at least $n = 5$ different embryos, for each time point and experimental condition.

Measurement of the Sox2$^+$ (VZ) and HuC/D$^+$ (MZ) areas

The effects of SMAD1/5 inhibition on the total numbers of neural progenitors or neurons were assessed by measuring the area occupied, respectively, by the VZ (containing the Sox2$^+$ progenitors) or the MZ (formed by the HuC/D$^+$ neurons). These areas were obtained from pictures of chick neural tube transverse sections stained for Sox2 and HuC/D, 48 hpe. The Sox2 and HuC/D channels were then extracted and measured using the ImageJ software (National Institutes of Health) by adapting the methodology previously described by K. Straatman (Advanced Imaging Facilities, University of Leicester, Leicester, England, UK). In brief, after splitting the channels of 2-µm z-stack maximal projection images, the look-up table of the channel of interest was inverted, and its threshold was adjusted. The HuC/D$^+$ or Sox2$^+$ areas were then measured for both control and electroporated neural tube sides by a particle analysis using a pixel^2 size ranging from 1,000 to infinity. The data are presented as the ratios ± SEM obtained by standardizing the values of the electroporated side to the corresponding values of the respective nonelectroporated side. Three images were used to calculate a mean value per embryo. The data represent the means ± SEM obtained from the values of ≥10 different embryos per experimental condition.

Quantification of pS158 staining

The intensity of the pS158 staining was quantified within mitotic progenitors during the distinct modes of divisions. HH14 embryos electroporated with either pSox2:EGFP and a control H2B-RFP vector, pTis21:RFP and a control H2B-GFP vector, or pSox2:EGFP and pTis21:RFP were recovered at 24 hpe and processed for immunohistochemistry using the phospho-SMAD1/5/8 antibody (pS158; Cell Signaling Technology). Maximal projections obtained from 2-µm z-stack images taken with a confocal microscope (SP5) were then analyzed using the ImageJ software. The nuclear area of the electroporated mitotic progenitors was then delimitated by polygonal selection, and the mean intensity of the nuclear pS158 staining was quantified as the mean gray value. Quantifications were performed on five to nine different images to calculate a mean value per embryo. The data represent the means ± SEM obtained from the values of at least eight different embryos per experimental condition.

Flow cytometry

HH14 embryos were recovered 16 or 20 h after coelectroporation with the pSox2:EGFP and pTis21:RFP reporters, in the absence (for PCR analysis) or additional presence (for cell cycle analysis) of control or sh-S1/5 vectors. Cell suspensions were obtained from pools of six to eight dissected neural tubes after digestion with trypsin-EDTA (Sigma-Aldrich) for 10–15 min and further processed on a cell sorter (FACS Aria III; BD) for EGFP and RFP fluorescence. To analyze the DNA content, the samples were incubated with 10 µg/ml of Hoechst (Sigma-Aldrich) at 37°C for 30 min. The cellular DNA content was analyzed in single fluorescence histograms using the Multicycle software (Phoenix Flow Systems). The mean ± SEM represents the percentages of cells in G1, S, and G2–M from the analysis of 9–10 cell pools per experimental condition. At least 5,000 cells for each progenitor population (PP, PN, and NN) were analyzed per pool. Alternatively, dissociated cell pools were processed for pH3 immunocytochemistry and analyzed for EGFP, RFP, and Cy5 fluorescence. The data are presented as the means ± SEM obtained from four to five cell pools per experimental condition.

Real-time PCR

Total RNA extracts were obtained following the TRIZOL protocol (Invitrogen) from subpopulations of GFP$^+$;RFP$^-$ (PP), GFP$^+$;RFP$^+$ (PN), and GFP$^-$;RFP$^+$ (NN) cells segregated and purified by FACS (20,000 cells per pool). Reverse transcription and real-time PCR were performed according to manufacturer's instructions (Roche) using a lightcycler (LC 480; Roche). Specific primers used for quantitative PCR amplification of *Id* genes were purchased (QuantiTect Primer Assays; QIAGEN). Oligonucleotides specific for chick Gapdh were used for normalization. PCR amplifications were assessed from four independent cell pools per experimental condition. Data are expressed in arbitrary units and represent mean standardized values ± SEM.

Analysis of the mean number of divisions

We assessed the mean number of divisions of neural progenitors in vivo using the cell proliferation kit (CellTrace violet; Invitrogen). Here, the violet cell tracer (1 mM), a cytoplasmic retention dye that becomes diluted as cells divide, was injected into the neural tube lumen at the time of electroporation. HH14 embryos were recovered at 48 hpe, the neural tube was carefully removed, and the cells were dissociated after a 10–15-min digestion in trypsin-EDTA. The fluorescence intensity of the violet tracer was measured in viable dissociated electroporated GFP$^+$ cells in the 405/450-nm excitation/emission range on a flow cytometer (Gallios; Beckman Coulter). The data are presented as the mean CellTrace violet intensity (±SEM) obtained from 6–16 embryos per experimental condition.

In situ hybridization

HH14 embryos were recovered at 24 hpe, fixed overnight at 4°C in 4% PFA, rinsed in PBS, and processed for whole-mount RNA in situ hybridization following standard procedures using probes for chick *Id1*, *Id2*, *Id3*, and *Id4* (from the chicken EST project; UK Human Genome Mapping Project Resource Centre). Hybridized embryos were postfixed in 4% PFA and washed in PBT (PBS with Tween). 45-µM-thick sections were cut with a vibratome (VT1000S; Leica), mounted, and photographed using a microscope (DC300; Leica). The data show representative pictures obtained from three independent embryos per experimental condition.

Luciferase reporter assay

Transcriptional activity of the *NeuroD* promoter was assessed in vivo following electroporation of the pNeuroD:Luc vector and a renilla luciferase reporter construct carrying the cytomegalovirus immediate early enhancer promoter for normalization (Promega), together with the indicated DNAs. 24 hpe, the neural tubes were dissected and processed following the Dual Luciferase Reporter Assay System protocol (Promega), as described previously (Le Dréau et al., 2012). The data are presented as the means ± SEM from 11–12 embryos per experimental condition.

Calculation of the duration of the cell cycle phases

The lengths of the cell cycle (Tc) and S phase (Ts) were calculated from the BrdU labeling indices assessed for electroporated cells (H2B-RFP$^+$) located in the VZ at 48 hpe, which were obtained from cumulative BrdU experiments following the nonlinear regression method described by Nowakowski et al. (1989). In brief, the best nonlinear parameters fitting the experimental data allow the calculation of the duration needed for the BrdU labeling index to reach the plateau, which provides the length Tc − Ts; the fraction of maximum labeling index, which corresponds to the growth

Published February 10, 2014

fraction value (GF); and the intercept of the BrdU labeling curve with the *y* axis, representing the fraction of cycling cells in S phase [GF × (Ts/Tc)].

The TM was derived from the mitotic index (MI) and calculated from the respective Tc, so that TM = Tc × MI, as reported previously (Arai et al., 2011). A correction was applied to the values obtained from cell counts, to take into account the slight differences in the growth fraction (deduced from the cumulative BrdU experiments): corrected TM = Tc × MI/GF.

The TG2 was calculated using the mitotic labeling index data obtained from cumulative BrdU experiments, according to the percentage of labeled mitoses paradigm as previously described (Quastler and Sherman, 1959; Peco et al., 2012), so that the mean TG2 length corresponds to the duration of BrdU incorporation required to obtain the half-maximal appearance of GFP^+;$pH3^+$:$BrdU^+$ cells. By means of an error minimization algorithm, provided by J. Buceta (Parc Cientific de Barcelona, Barcelona, Spain), the mitotic labeling index data were fitted to the following function:

$$f(t) = \frac{(t / T_{G2})^n}{1 + (t / T_{G2})^n}.$$

In this function, there are two fitting parameters, T_{G2} and n, which correspond, respectively, to TG2 and to the sharpness of the mitotic response. Note that $f(T_{G2}) = 1/2$ regardless the value of n.

The errors of the mean Tc, Ts, TM, TG2, and TG1 were estimated using the standard error propagation technique using the corresponding formulas. In brief, given a set of points $(x_i, y_i \pm \sigma_i)$, in which i = 1, 2, . . ., *M*, and a nonlinear fitting function $Y(x; \{a\})$, in which $\{a\}$ stands for a set of *N* parameters $(a_1, a_2, \ldots, a_N)$, the error minimization algorithm implements a standard Newton scheme to find the set $\{a\}$ that minimizes the amount:

$$\sum_{i=1}^{M} \left(\frac{Y(x_i; \{a\}) - y_i}{\sigma_i} \right)^2.$$

Thus, we weight differently every experimental point depending on its error (the larger the error, the smaller its weight).

Statistical analysis

The quantitative data are expressed as means ± SEM. Statistical analysis was performed using the StatView software (SAS Institute Inc.), and significance was assessed by performing analysis of variance followed by the Student–Newman–Keuls test. Otherwise, the significance was assessed using the Student's *t* test (Figs. 2, D and F; and 7, B–F). Concerning the durations of the cell cycle phases (Fig. 6) and the extrapolation of the proportion of PN (Figs. 3, E and F; and 4 C), the errors were estimated using the standard error propagation technique using the corresponding formulas (*, P < 0.05; **, P < 0.01; and ***, P < 0.001).

Online supplemental material

Fig. S1 shows the analysis of the mRNA expression of *Id* genes in response to modulations of the canonical BMP activity. Fig. S2 presents the proportions of $pTis21^+$ and $pSox2^+$ divisions obtained in response to experiments of rescue and dose-dependent effects of SMAD1/5 inhibition. Fig. S3 shows representative pictures of the cell-autonomous and overall effects of SMAD1/5 inhibition on the neuronal differentiation of spinal progenitors. Fig. S4 gives further details on the flow cytometry analysis of the cell cycle distribution of the PP, PN, and NN progenitors. Online supplemental material is available at http://www.jcb.org/cgi/content/full/jcb.201307031/DC1.

The authors wish to thank Susana Usieto for her invaluable technical assistance and members of E. Martí's laboratory for their helpful comments. We thank Dr. Masanori Uchikawa, Dr. Jonas Muhr, and Dr. Roger Tsien for kindly providing DNAs as well as Dr. Javier Buceta (Computer Simulation and Modelling Laboratory) for thoughtful discussions and providing the error minimization algorithm.

The work in E. Martí's laboratory was supported by the grants BFU2010-18959 and CSD2007-00008.

The authors declare no competing financial interests.

Submitted: 4 July 2013
Accepted: 13 December 2013

References

Alarcón, C., A.I. Zaromytidou, Q. Xi, S. Gao, J. Yu, S. Fujisawa, A. Barlas, A.N. Miller, K. Manova-Todorova, M.J. Macias, et al. 2009. Nuclear CDKs drive Smad transcriptional activation and turnover in BMP and TGF-beta pathways. *Cell*. 139:757–769. http://dx.doi.org/10.1016/j.cell.2009.09.035

Arai, Y., J.N. Pulvers, C. Haffner, B. Schilling, I. Nüsslein, F. Calegari, and W.B. Huttner. 2011. Neural stem and progenitor cells shorten S-phase on commitment to neuron production. *Nat. Commun.* 2:154. http://dx.doi.org/10.1038/ncomms1155

Bergsland, M., D. Ramsköld, C. Zaouter, S. Klum, R. Sandberg, and J. Muhr. 2011. Sequentially acting Sox transcription factors in neural lineage development. *Genes Dev.* 25:2453–2464. http://dx.doi.org/10.1101/gad.176008.111

Choe, Y., A. Kozlova, D. Graf, and S.J. Pleasure. 2013. Bone morphogenic protein signaling is a major determinant of dentate development. *J. Neurosci.* 33:6766–6775. http://dx.doi.org/10.1523/JNEUROSCI.0128-13.2013

Das, R.M., and K.G. Storey. 2012. Mitotic spindle orientation can direct cell fate and bias Notch activity in chick neural tube. *EMBO Rep.* 13:448–454. http://dx.doi.org/10.1038/embor.2012.42

Dehay, C., and H. Kennedy. 2007. Cell-cycle control and cortical development. *Nat. Rev. Neurosci.* 8:438–450. http://dx.doi.org/10.1038/nrn2097

Falk, S., and L. Sommer. 2009. Stage- and area-specific control of stem cells in the developing nervous system. *Curr. Opin. Genet. Dev.* 19:454–460. http://dx.doi.org/10.1016/j.gde.2009.08.002

Franco, S.J., and U. Müller. 2013. Shaping our minds: stem and progenitor cell diversity in the mammalian neocortex. *Neuron*. 77:19–34. http://dx.doi.org/10.1016/j.neuron.2012.12.022

Fuentealba, L.C., K. Obernier, and A. Alvarez-Buylla. 2012. Adult neural stem cells bridge their niche. *Cell Stem Cell*. 10:698–708. http://dx.doi.org/10.1016/j.stem.2012.05.012

Ghosh, S., T. Marquardt, J.P. Thaler, N. Carter, S.E. Andrews, S.L. Pfaff, and T. Hunter. 2008. Instructive role of aPKCzeta subcellular localization in the assembly of adherens junctions in neural progenitors. *Proc. Natl. Acad. Sci. USA*. 105:335–340. http://dx.doi.org/10.1073/pnas.0705713105

Gonzalez, C. 2007. Spindle orientation, asymmetric division and tumour suppression in *Drosophila* stem cells. *Nat. Rev. Genet.* 8:462–472. http://dx.doi.org/10.1038/nrg2103

Göritz, C., and J. Frisén. 2012. Neural stem cells and neurogenesis in the adult. *Cell Stem Cell*. 10:657–659. http://dx.doi.org/10.1016/j.stem.2012.04.005

Götz, M., and W.B. Huttner. 2005. The cell biology of neurogenesis. *Nat. Rev. Mol. Cell Biol.* 6:777–788. http://dx.doi.org/10.1038/nrm1739

Hamburger, V., and H.L. Hamilton. 1951. A series of normal stages in the development of chick embryo. *J. Morphol.* 88:49–92. http://dx.doi.org/10.1002/jmor.1050880104

Hild, M., A. Dick, G.J. Rauch, A. Meier, T. Bouwmeester, P. Haffter, and M. Hammerschmidt. 1999. The smad5 mutation somitabun blocks Bmp2b signaling during early dorsoventral patterning of the zebrafish embryo. *Development*. 126:2149–2159.

Hollnagel, A., V. Oehlmann, J. Heymer, U. Rüther, and A. Nordheim. 1999. Id genes are direct targets of bone morphogenetic protein induction in embryonic stem cells. *J. Biol. Chem.* 274:19838–19845. http://dx.doi.org/10.1074/jbc.274.28.19838

Kingsbury, M.A., B. Friedman, M.J. McConnell, S.K. Rehen, A.H. Yang, D. Kaushal, and J. Chun. 2005. Aneuploid neurons are functionally active and integrated into brain circuitry. *Proc. Natl. Acad. Sci. USA*. 102:6143–6147. http://dx.doi.org/10.1073/pnas.0408171102

Kingsbury, M.A., Y.C. Yung, S.E. Peterson, J.W. Westra, and J. Chun. 2006. Aneuploidy in the normal and diseased brain. *Cell. Mol. Life Sci.* 63:2626–2641. http://dx.doi.org/10.1007/s00018-006-6169-5

Korchynskyi, O., and P. ten Dijke. 2002. Identification and functional characterization of distinct critically important bone morphogenetic protein-specific response elements in the Id1 promoter. *J. Biol. Chem.* 277:4883–4891. http://dx.doi.org/10.1074/jbc.M111023200

Korinek, V., N. Barker, K. Willert, M. Molenaar, J. Roose, G. Wagenaar, M. Markman, W. Lamers, O. Destree, and H. Clevers. 1998. Two members of the Tcf family implicated in Wnt/β-catenin signaling during embryogenesis in the mouse. *Mol. Cell. Biol.* 18:1248–1256.

Le Dréau, G., and E. Martí. 2012. Dorsal-ventral patterning of the neural tube: a tale of three signals. *Dev. Neurobiol.* 72:1471–1481. http://dx.doi.org/10.1002/dneu.22015

Le Dréau, G., and E. Martí. 2013. The multiple activities of BMPs during spinal cord development. *Cell. Mol. Life Sci.* 70:4293–4305. http://dx.doi.org/10.1007/s00018-013-1354-9

Le Dréau, G., L. Garcia-Campmany, M.A. Rabadán, T. Ferronha, S. Tozer, J. Briscoe, and E. Martí. 2012. Canonical BMP7 activity is required for

the generation of discrete neuronal populations in the dorsal spinal cord. *Development*. 139:259–268. http://dx.doi.org/10.1242/dev.074948

Lesage, B., I. Gutierrez, E. Martí, and C. Gonzalez. 2010. Neural stem cells: the need for a proper orientation. *Curr. Opin. Genet. Dev.* 20:438–442. http://dx.doi.org/10.1016/j.gde.2010.04.013

Lim, D.A., A.D. Tramontin, J.M. Trevejo, D.G. Herrera, J.M. García-Verdugo, and A. Alvarez-Buylla. 2000. Noggin antagonizes BMP signaling to create a niche for adult neurogenesis. *Neuron*. 28:713–726. http://dx.doi.org/10.1016/S0896-6273(00)00148-3

Lui, J.H., D.V. Hansen, and A.R. Kriegstein. 2011. Development and evolution of the human neocortex. *Cell*. 146:18–36. http://dx.doi.org/10.1016/j.cell.2011.06.030

Marthiens, V., and C. ffrench-Constant. 2009. Adherens junction domains are split by asymmetric division of embryonic neural stem cells. *EMBO Rep.* 10:515–520. http://dx.doi.org/10.1038/embor.2009.36

Massagué, J., J. Seoane, and D. Wotton. 2005. Smad transcription factors. *Genes Dev.* 19:2783–2810. http://dx.doi.org/10.1101/gad.1350705

Mira, H., Z. Andreu, H. Suh, D.C. Lie, S. Jessberger, A. Consiglio, J. San Emeterio, R. Hortigüela, M.A. Marqués-Torrejón, K. Nakashima, et al. 2010. Signaling through BMPR-IA regulates quiescence and long-term activity of neural stem cells in the adult hippocampus. *Cell Stem Cell*. 7:78–89. http://dx.doi.org/10.1016/j.stem.2010.04.016

Morin, X., F. Jaouen, and P. Durbec. 2007. Control of planar divisions by the G-protein regulator LGN maintains progenitors in the chick neuroepithelium. *Nat. Neurosci.* 10:1440–1448. http://dx.doi.org/10.1038/nn1984

Morrison, S.J., and A.C. Spradling. 2008. Stem cells and niches: mechanisms that promote stem cell maintenance throughout life. *Cell*. 132:598–611. http://dx.doi.org/10.1016/j.cell.2008.01.038

Müller, T., K. Anlag, H. Wildner, S. Britsch, M. Treier, and C. Birchmeier. 2005. The bHLH factor Olig3 coordinates the specification of dorsal neurons in the spinal cord. *Genes Dev.* 19:733–743. http://dx.doi.org/10.1101/gad.326105

Muotri, A.R., and F.H. Gage. 2006. Generation of neuronal variability and complexity. *Nature*. 441:1087–1093. http://dx.doi.org/10.1038/nature04959

Nowakowski, R.S., S.B. Lewin, and M.W. Miller. 1989. Bromodeoxyuridine immunohistochemical determination of the lengths of the cell cycle and the DNA-synthetic phase for an anatomically defined population. *J. Neurocytol.* 18:311–318. http://dx.doi.org/10.1007/BF01190834

Ono, Y., F. Calhabeu, J.E. Morgan, T. Katagiri, H. Amthor, and P.S. Zammit. 2011. BMP signalling permits population expansion by preventing premature myogenic differentiation in muscle satellite cells. *Cell Death Differ.* 18:222–234. http://dx.doi.org/10.1038/cdd.2010.95

Oshimori, N., and E. Fuchs. 2012. Paracrine TGF-β signaling counterbalances BMP-mediated repression in hair follicle stem cell activation. *Cell Stem Cell*. 10:63–75. http://dx.doi.org/10.1016/j.stem.2011.11.005

Peco, E., T. Escude, E. Agius, V. Sabado, F. Medevielle, B. Ducommun, and F. Pituello. 2012. The CDC25B phosphatase shortens the G2 phase of neural progenitors and promotes efficient neuron production. *Development*. 139:1095–1104. http://dx.doi.org/10.1242/dev.068569

Peterson, S.E., A.H. Yang, D.M. Bushman, J.W. Westra, Y.C. Yung, S. Barral, T. Mutoh, S.K. Rehen, and J. Chun. 2012. Aneuploid cells are differentially susceptible to caspase-mediated death during embryonic cerebral cortical development. *J. Neurosci.* 32:16213–16222. http://dx.doi.org/10.1523/JNEUROSCI.3706-12.2012

Quastler, H., and F.G. Sherman. 1959. Cell population kinetics in the intestinal epithelium of the mouse. *Exp. Cell Res.* 17:420–438. http://dx.doi.org/10.1016/0014-4827(59)90063-1

Rebollo, E., P. Sampaio, J. Januschke, S. Llamazares, H. Varmark, and C. González. 2007. Functionally unequal centrosomes drive spindle orientation in asymmetrically dividing *Drosophila* neural stem cells. *Dev. Cell*. 12:467–474. http://dx.doi.org/10.1016/j.devcel.2007.01.021

Rehen, S.K., M.J. McConnell, D. Kaushal, M.A. Kingsbury, A.H. Yang, and J. Chun. 2001. Chromosomal variation in neurons of the developing and adult mammalian nervous system. *Proc. Natl. Acad. Sci. USA*. 98:13361–13366. http://dx.doi.org/10.1073/pnas.231487398

Saade, M., I. Gutiérrez-Vallejo, G. Le Dréau, M.A. Rabadán, D.G. Miguez, J. Buceta, and E. Martí. 2013. Sonic hedgehog signaling switches the mode of division in the developing nervous system. *Cell Rep*. 4:492–503. http://dx.doi.org/10.1016/j.celrep.2013.06.038

Salomoni, P., and F. Calegari. 2010. Cell cycle control of mammalian neural stem cells: putting a speed limit on G1. *Trends Cell Biol.* 20:233–243. http://dx.doi.org/10.1016/j.tcb.2010.01.006

Sasaki, H., C. Hui, M. Nakafuku, and H. Kondoh. 1997. A binding site for Gli proteins is essential for HNF-3beta floor plate enhancer activity in transgenics and can respond to Shh in vitro. *Development*. 124:1313–1322.

Segklia, A., E. Seuntjens, M. Elkouris, S. Tsalavos, E. Stappers, T.A. Mitsiadis, D. Huylebroeck, E. Remboutsika, and D. Graf. 2012. Bmp7 regulates the survival, proliferation, and neurogenic properties of neural progenitor cells during corticogenesis in the mouse. *PLoS ONE*. 7:e34088. http://dx.doi.org/10.1371/journal.pone.0034088

Shitamukai, A., D. Konno, and F. Matsuzaki. 2011. Oblique radial glial divisions in the developing mouse neocortex induce self-renewing progenitors outside the germinal zone that resemble primate outer subventricular zone progenitors. *J. Neurosci.* 31:3683–3695. http://dx.doi.org/10.1523/JNEUROSCI.4773-10.2011

Suh, H., W. Deng, and F.H. Gage. 2009. Signaling in adult neurogenesis. *Annu. Rev. Cell Dev. Biol.* 25:253–275. http://dx.doi.org/10.1146/annurev.cellbio.042308.113256

Tiberi, L., P. Vanderhaeghen, and J. van den Ameele. 2012. Cortical neurogenesis and morphogens: diversity of cues, sources and functions. *Curr. Opin. Cell Biol.* 24:269–276. http://dx.doi.org/10.1016/j.ceb.2012.01.010

Tozer, S., G. Le Dréau, E. Marti, and J. Briscoe. 2013. Temporal control of BMP signalling determines neuronal subtype identity in the dorsal neural tube. *Development*. 140:1467–1474. http://dx.doi.org/10.1242/dev.090118

Tsunekawa, Y., J.M. Britto, M. Takahashi, F. Polleux, S.S. Tan, and N. Osumi. 2012. Cyclin D2 in the basal process of neural progenitors is linked to non-equivalent cell fates. *EMBO J.* 31:1879–1892. http://dx.doi.org/10.1038/emboj.2012.43

Uchikawa, M., Y. Ishida, T. Takemoto, Y. Kamachi, and H. Kondoh. 2003. Functional analysis of chicken Sox2 enhancers highlights an array of diverse regulatory elements that are conserved in mammals. *Dev. Cell*. 4:509–519. http://dx.doi.org/10.1016/S1534-5807(03)00088-1

Ulloa, F., and J. Briscoe. 2007. Morphogens and the control of cell proliferation and patterning in the spinal cord. *Cell Cycle*. 6:2640–2649. http://dx.doi.org/10.4161/cc.6.21.4822

Wang, L., and R.Y. Tsien. 2006. Evolving proteins in mammalian cells using somatic hypermutation. *Nat. Protoc.* 1:1346–1350. http://dx.doi.org/10.1038/nprot.2006.243

Wang, X., J.W. Tsai, J.H. Imai, W.N. Lian, R.B. Vallee, and S.H. Shi. 2009. Asymmetric centrosome inheritance maintains neural progenitors in the neocortex. *Nature*. 461:947–955. http://dx.doi.org/10.1038/nature08435

Xia, L., X. Zheng, W. Zheng, G. Zhang, H. Wang, Y. Tao, and D. Chen. 2012. The niche-dependent feedback loop generates a BMP activity gradient to determine the germline stem cell fate. *Curr. Biol.* 22:515–521. http://dx.doi.org/10.1016/j.cub.2012.01.056

Ying, Q.L., J. Nichols, I. Chambers, and A. Smith. 2003. BMP induction of Id proteins suppresses differentiation and sustains embryonic stem cell self-renewal in collaboration with STAT3. *Cell*. 115:281–292. http://dx.doi.org/10.1016/S0092-8674(03)00847-X

Yu, F., C.T. Kuo, and Y.N. Jan. 2006. *Drosophila* neuroblast asymmetric cell division: recent advances and implications for stem cell biology. *Neuron*. 51:13–20. http://dx.doi.org/10.1016/j.neuron.2006.06.016

Le Dréau et al., http://www.jcb.org/cgi/content/full/jcb.201307031/DC1

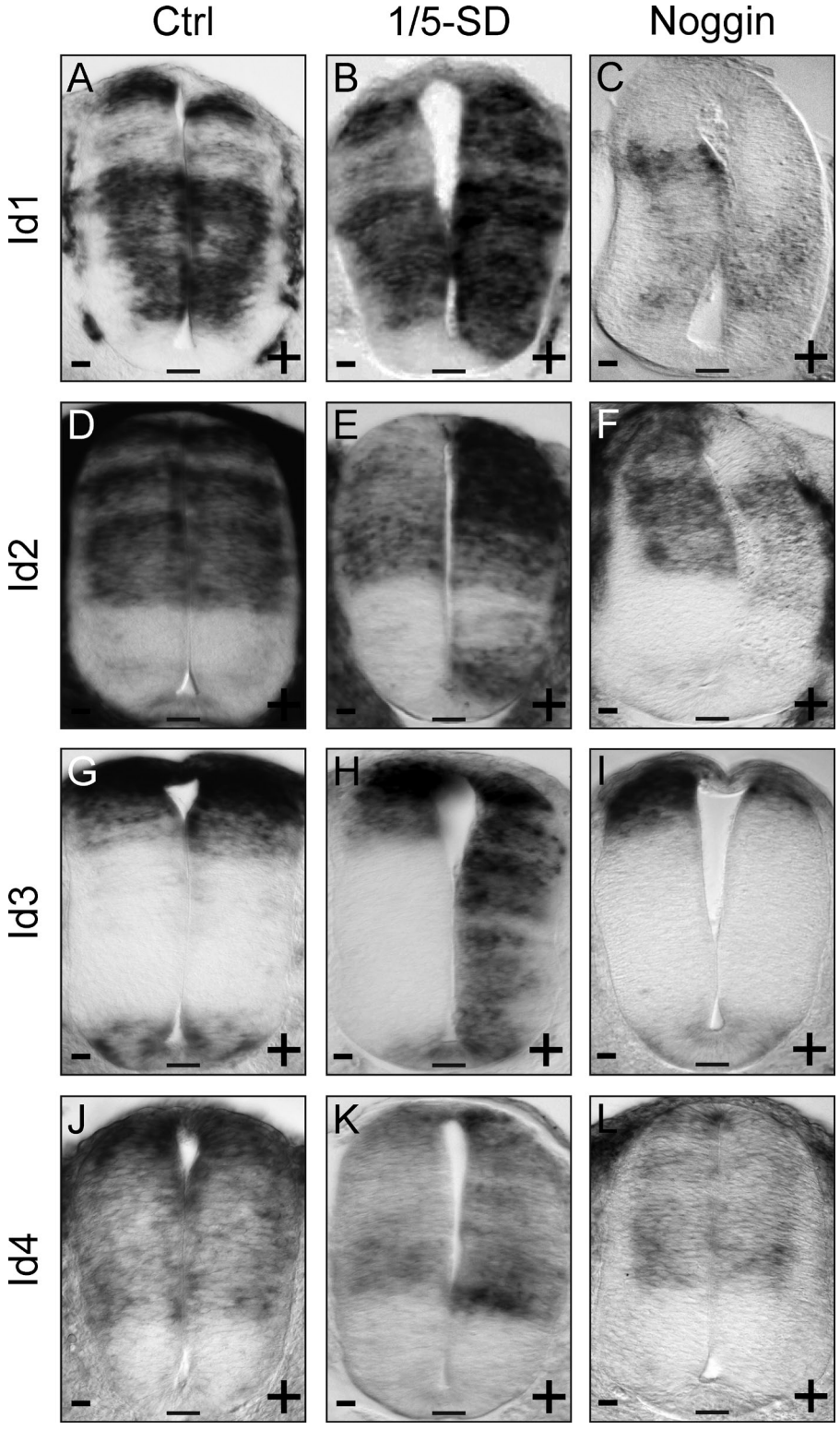

Figure S1. **Analysis of the expression of *Id* genes in response to modulations of the canonical BMP activity.** Relative to Fig. 2. (A–L) The expression of the chick *Id1* (A–C), *Id2* (D–F), *Id3* (G–I), and *Id4* (J–L) genes was assessed by in situ hybridization in sections of neural tubes recovered at 24 hpe of HH14 embryos with control constructs (A, D, G, and J) or constructs overexpressing the constitutively active mutants SMAD1/5-SD (B, E, H, and K) or the BMP antagonist Noggin (C, F, I, and L). Comparison of the signal intensities detected in the nonelectroporated (left, −) and electroporated (right, +) sides of representative neural tube sections revealed that *Id1*, *Id2*, and *Id3* mRNA levels are modulated in response to variations in canonical BMP activity. Ctrl, control. Bars, 25 µM.

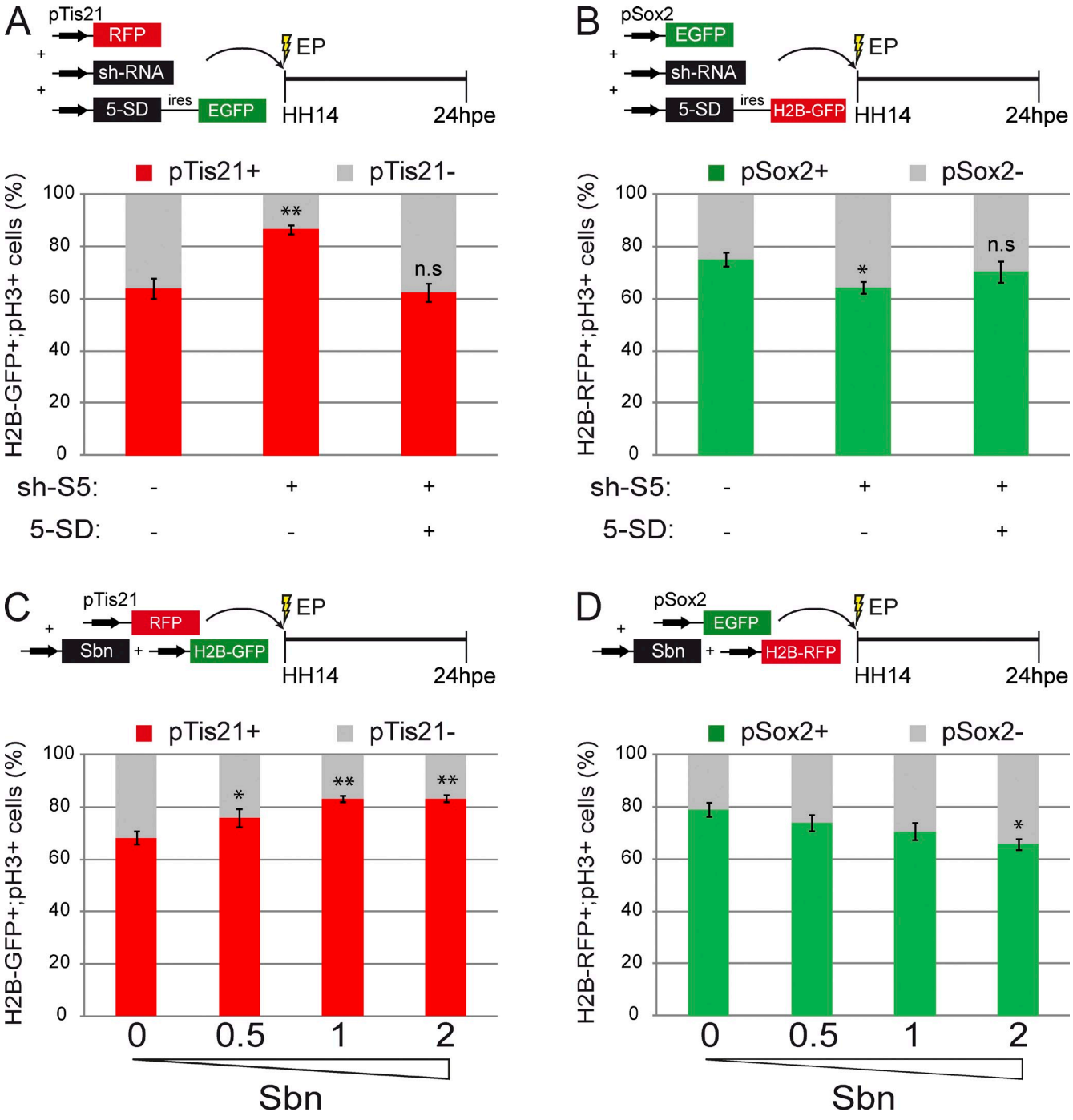

Figure S2. **Proportions of pTis21⁺ and pSox2⁺ divisions obtained in response to experiments of rescue and dose-dependent effects of SMAD1/5 inhibition.** Relative to Fig. 3. (A and B) The proportions of pTis21⁺ (A) and pSox2⁺ (B) divisions were assessed in mitotic electroporated (H2B-GFP⁺;pH3⁺ [A] or H2B-RFP⁺;pH3⁺ [B]) progenitors 24 h after coelectroporation with a control construct (Ctrl) or the Smad5 shRNA construct (sh-S5) alone or combined with the constitutively active SMAD5-SD mutant (5-SD). (C and D) The proportions of pTis21⁺ (C) and pSox2⁺ (D) divisions were assessed in mitotic electroporated (H2B-GFP⁺;pH3⁺ [C] or H2B-RFP⁺;pH3⁺ [D]) progenitors 24 h after coelectroporation with increasing concentrations of the dominant-negative Smad5 mutant Somitabun (Sbn), using combinations of 0:2, 0.5:1.5, 1:1, and 2:0 µg/µl pCS2/Somitabun and empty pCS2 constructs. EP, electroporation. Error bars show means ± SEM. *, $P < 0.05$; **, $P < 0.01$.

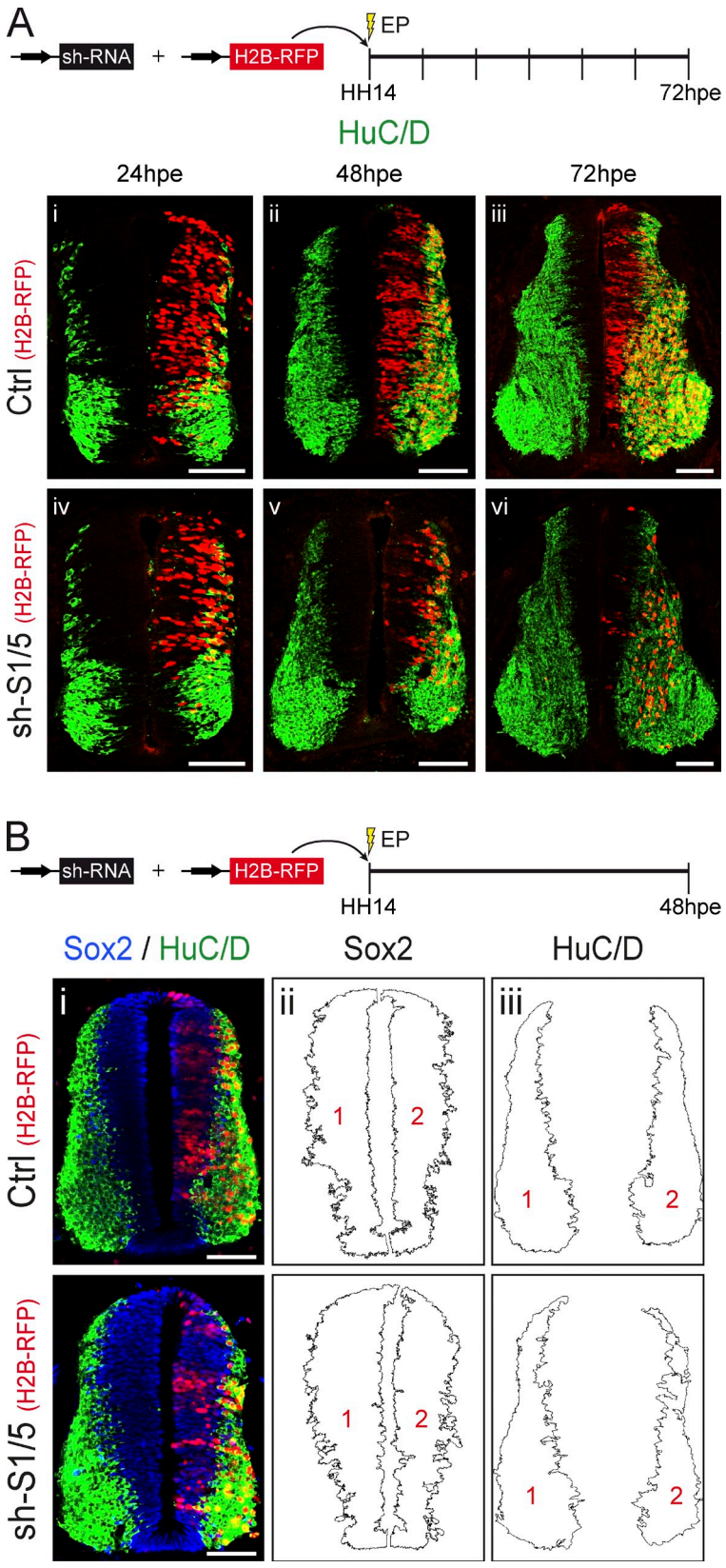

Figure S3. **Cell-autonomous and overall effects of SMAD1/5 inhibition on the neuronal differentiation of spinal progenitors.** Relative to Fig. 5. (A) Representative transverse sections obtained after electroporation of HH14 embryos with control (Ctrl, i–iii) or shRNA constructs against *cSmad1* or *cSmad5* (sh-S1/5, iv–vi) are shown 24 hpe (i and iv), 48 hpe (ii and v), and 72 hpe (iii and vi), demonstrating the premature differentiation of sh-S1/5 electroporated (H2B-RFP$^+$) cells into neurons (HuC/D$^+$). (B, i) Representative transverse sections of a chick neural tube at 48 hpe of HH14 embryos with control or sh-S1/5. Sox2, HuC/D, and H2B-RFP stain, respectively, the neural progenitors, differentiating neurons, and electroporated cells. The Sox2$^+$ (ii) and HuC/D$^+$ (iii) areas corresponding, respectively, to the VZ (containing the progenitors) and the MZ (formed by the differentiating neurons) were defined and measured using ImageJ processing. The areas measured for the electroporated side (2) were standardized to their contralateral controls (1) and are presented as ratios of the size of the VZ (Sox2$^+$) or MZ (HuC/D$^+$) areas (see Fig. 5 E). EP, electroporation. Bars, 50 µM.

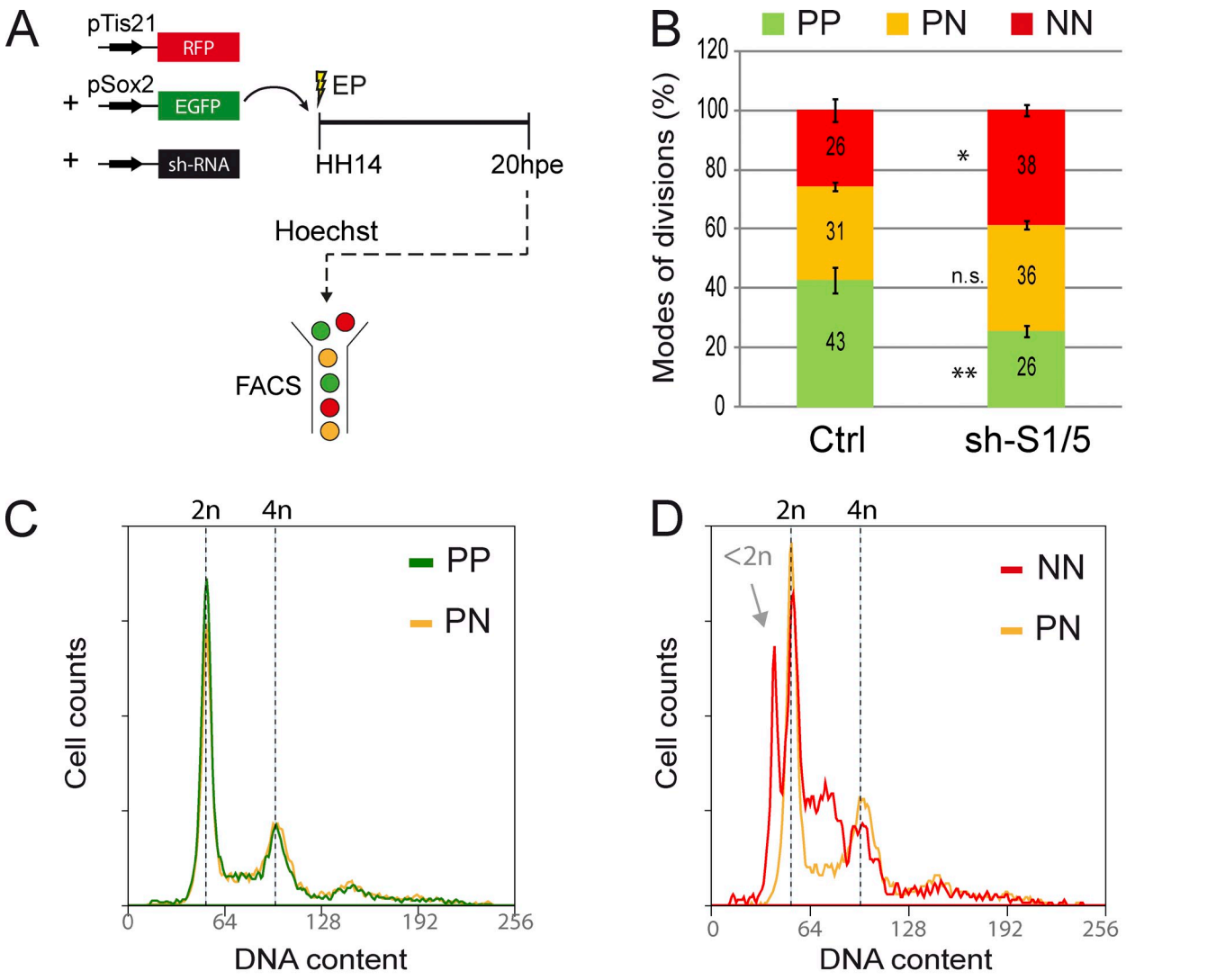

E

diploid cycle — aneuploid cycle

	PP		PN		NN			NN	
(%)	Ctrl	sh-S1/5	Ctrl	sh-S1/5	Ctrl	sh-S1/5	(%)	Ctrl	sh-S1/5
G1	56 ± 1	57 ± 1	49 ± 1	51 ± 3	46 ± 3	44 ± 4	G1	36 ± 2	32 ± 3
S	29 ± 1	32 ± 2	33 ± 2	35 ± 3	38 ± 5	40 ± 6	S	60 ± 2	64 ± 2
G2-M	15 ± 2	11 ± 2	18 ± 2	14 ± 2	16 ± 2	16 ± 2	G2-M	4 ± 1	4 ± 2

Figure S4. **Analysis of the cell cycle distribution of the PP, PN, and NN progenitors.** Relative to Fig. 7. (A) Methodology used to analyze by flow cytometry the cell cycle distribution of PP, PN, and NN divisions in dissociated cells processed for Hoechst incorporation at 20 h after coelectroporation of pTis21:RFP, pSox2:EGFP, and control or Smad1/5 shRNA vectors. (B) Proportions of total $GFP^+;RFP^-$ (PP), $GFP^+;RFP^+$ (PN), and $GFP^-;RFP^+$ (NN) cells obtained at 20 hpe with control (Ctrl) or Smad1/5 shRNA (sh-S1/5). (C and D) Overlays of representative DNA content profiles obtained for $GFP^+;RFP^-$ (PP) and $GFP^+;RFP^+$ (PN; C) or $GFP^+;RFP^+$ (PN) and $GFP^-;RFP^+$ (NN; D) cells electroporated with control constructs. (E) Cell cycle distribution obtained for $GFP^+;RFP^-$ (PP), $GFP^+;RFP^+$ (PN), and both diploid and aneuploid $GFP^-;RFP^+$ (NN) cells electroporated with control or Smad1/5 shRNA (sh-S1/5). EP, electroporation. Error bars show means ± SEM. *, $P < 0.05$; **, $P < 0.01$.

APPENDIX III

Available online at www.sciencedirect.com
ScienceDirect
Current Opinion in Genetics & Development

Neural stem cells: the need for a proper orientation

Bart Lesage[1], Irene Gutierrez[2], Elisa Martí[2] and Cayetano Gonzalez[1,3]

Drosophila neuroblasts and mouse radial glial cells can divide asymmetrically to self-renew while producing differentiating daughter cells that contribute to brain growth. Intense research activity in the past few years has started to unveil some of the processes that govern asymmetric division in these two cell types. Here we discuss the case of centrosome asymmetry and the contribution of spindle orientation and non-spindle-related centrosome functions. Although still fragmentary, the emerging picture suggests that both notable parallelisms and striking differences apply.

Addresses
[1] Cell Division Group, IRB Barcelona, PCB, c/Baldiri Reixac 10-12, 08028 Barcelona, Spain
[2] Instituto de Biología Molecular de Barcelona, CSIC, Parc Científic de Barcelona, c/Baldiri Reixac 21, 08028 Barcelona, Spain
[3] Institució Catalana de Recerca i Estudis Avançats, Passeig Lluís Companys 23, 08010 Barcelona, Spain

Corresponding authors: Gonzalez, Cayetano (gonzalez@irbbarcelona.org)

Current Opinion in Genetics & Development 2010, **20**:438–442

This review comes from a themed issue on
Developmental mechanisms, patterning and evolution
Edited by Claude Desplan and Margaret Buckingham

Available online 25th May 2010

0959-437X/$ – see front matter

DOI 10.1016/j.gde.2010.04.013

Introduction

Short-lived differentiated cells are continuously replenished by the mitotic activity of progenitor cells, which typically divide a few times before differentiating. Keeping a permanent supply of progenitors and, therefore, allowing for steady states that can last for decades relies on the activity of tissue stem cells (SCs) that are able to generate differentiating offspring and to self-renew. Theoretically, there are several strategies by which SCs can achieve such a dual goal of generating new tissue and maintaining the size of the SC compartment. One such mechanism is self-renewing asymmetric division (SRAD), a type of mitosis that results in two unequal daughter cells: one that enters the differentiation process and another that retains SC identity [1,2].

SRAD is best characterized in *Drosophila*, in the SCs of the germline and in neural SCs, usually referred to as neuroblasts in this organism. Neuroblasts in the central brain and the ventral ganglion of the *Drosophila* larval brain undergo numerous consecutive cycles of SRAD, each generating a ganglion mother cell and a self-renewed neuroblast (Figure 1). Ganglion mother cells can be considered as intermediate progenitors that divide once, producing two cells that terminally differentiate [3–5]. Unlike germline SCs, which are true adult SCs that maintain the steady state of gamete production throughout adulthood, neuroblasts contribute to tissue growth rather than to maintenance, are active only during development, and are programmed to disappear once neurogenesis is completed [6•,7].

SRAD is also at work in the developing cerebral cortex in mice embryos. Radial glial cells (RGCs; also known as apical progenitors or neural progenitors) originate between embryonic days E10 and E11 from neuroepithelial cells [8,9]. Between E13 and E18, when neurogenesis is at its peak, RGCs predominantly undergo SRAD, renewing themselves and giving rise to either a neuron or to a basal progenitor, which subsequently divides symmetrically to produce two basal progenitors or two neurons [10–12] (Figure 1). During this period, RGCs can still divide symmetrically and expand. Indeed, the fine balance between these symmetric and asymmetric cell divisions regulates the size of the adult brain [8,9].

Genetic and molecular analyses, combined with high-resolution live microscopy studies carried out in the past decades, have yielded a solid body of information on the mechanisms driving SRAD in *Drosophila* neuroblasts [3–5,13]. In the past few years, these results have inspired research into the much more complex process of SRAD in vertebrates, particularly in RGCs [3,8,14–16]. The data obtained so far reveal both tantalizing parallelisms and striking differences. Here we discuss the case of asymmetric centrosome behavior, originally observed in *Drosophila* neuroblasts and recently demonstrated in mouse RGCs, and discuss the contribution of spindle orientation as well as non-spindle-related centrosome functions to brain development.

Spindle orientation and the segregation of fate determinants

For years, it was generally assumed that alignment of the mitotic spindle along the apico-basal axis is an absolute requirement for proper SRAD in *Drosophila* neuroblasts [3–5,13]. This assumption was recently tested by live imaging of neuroblasts that expressed markers for cortical polarity and spindle and were mutated to disrupt spindle orientation without altering cortical polarity [17••]. These studies showed that in extreme cases of spindle misalignment (i.e. when the spindle is orthogonal rather than

Figure 1

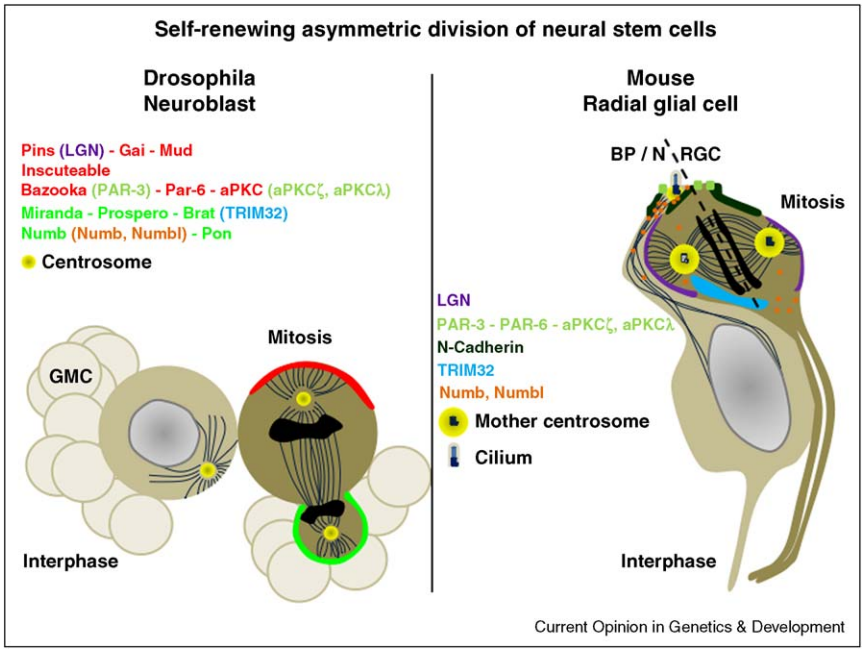

Self-renewing asymmetric division (SRAD) of neural stem cells. Diagrammatic view of SRAD in *Drosophila* larval neuroblasts (left) and mouse radial glial cells (RGCs; right). *Drosophila* neuroblasts are scattered, single cells, with polarity axes that are not in register. The most recent ganglion mother cell (GMC) remains near the basal side of the neuroblast. During interphase no molecular markers of cortical polarity are known, but the localization of the main microtubule-organizing center (centrosome; yellow) predicts where the apical complexes will assemble in the next mitosis. Mouse RGCs form a pseudostratified epithelium and remain polarized throughout the cell cycle, with their apical ends attached to the ventricular layer and the basal end feet extended toward the basal lamina. During interphase, a cilium protrudes at the apical end. SRAD of these cells generates a renewed RGC and either a basal progenitor (BP) or a neuron (n). At mitosis, bound to the apical cortex in *Drosophila* neuroblasts are, among others, the PAR and Pins complexes (red). Proteins bound to the basal cortex include the Mira and Pon complexes (green). Most of these proteins act as brain tumor suppressors in *Drosophila*. Although many of these proteins are conserved in mice, the behavior of most of them during SRAD of RGCs is still uncertain [41]. An exception might be E3 ubiquitin-protein ligase TRIM32 (light blue), which has been reported to be enriched in one of the two daughter cells and necessary and sufficient for suppressing RGC self-renewal and for inducing neuronal differentiation [42]. The mother (older) centrosome (dark blue) is retained by the self-renewed RGC [30••]. Both in *Drosophila* neuroblasts and in mouse RGCs, the Pins complex plays a key role in spindle orientation. In *Drosophila* neuroblasts, interaction of the apically localized Pins complex with astral microtubules from one of the spindle poles aligns the spindle along the axis of cortical polarity. Consequently, at cytokinesis, cleavage segregates the basal cortex (green) to the GMC and the apical cortex (red) to the renewed neuroblast. In mouse RGCs, the Pins complex (purple) is uniformly distributed on the lateral cortex that interacts with both asters to align the spindle orthogonally to the apico-basal axis [18••]. It is thought that the precise position of the cytokinesis furrow (dashed line) is such that apical cell fate determinants (light green) are segregated to only one of the two daughters, while adhesion molecules like N-cadherin (dark green) are partitioned between both cells [21••]. Abbreviations: Mud, Mushroom body defect; Brat, Brain tumor; Numbl, Numb-like; Pins, Partner of Inscutable; Pon, Partner of Numb.

parallel to the cortical axis), the molecules that are localized at the apical cortex (e.g. the PAR and Pins complexes; Figure 1) are partitioned between the two daughter cells rather than asymmetrically segregated to only one of them. Basal determinants, however, are still asymmetrically inherited by only one daughter cell. Remarkably, both daughters retain neuroblast identity and remain undifferentiated. These observations reveal that the distinct fates of the cells generated by normal SRAD of larval neuroblasts are governed by the ratio of apical to basal determinants, and that under normal expression levels the apical determinants dominate the basal determinants. Consistent with this interpretation, overexpression of the basal determinant Prospero shifts the balance toward ganglion mother cell fate and can deplete neuroblasts [17••].

The situation is not so clear in mouse RGCs, as different views exist regarding the link between cell fate decisions and mitotic spindle orientation in that species [12,15,18••]. In RGCs labeled by the expression of *Tis21* promoter-driven green fluorescent protein, immunofluorescence and live-imaging studies suggest that SRAD requires a slight tilt of the spindle axis to a nearly perpendicular orientation with respect to the apico-basal axis of the cell [12,19,20]. Such a tilt must be precise enough to position the cytokinesis furrow right between the apical compartment and the surrounding N-cadherin ring (dashed line in Figure 1). Consequently, putative apical cell fate determinants could be asymmetrically inherited, while adhesion molecules could be partitioned to both daughter cells, which can therefore remain anchored to the ventricular surface after mitosis [21••].

One possible apical determinant is partitioning defective 3 homolog (PAR-3), since compromising PAR-3 expression during the peak of neurogenesis results in a switch from SRAD to neurogenic symmetric divisions [22,23]. The lack of effect of inactivation of the PAR-3 partner, protein kinase C lambda (aPKC-lambda) on cell fate determination might be due to redundancy between this and other aPKC isoforms [24]. RGC polarity, however, is clearly disrupted after aPKC-lambda silencing [24].

Nevertheless, the relevance of controlled spindle orientation during SRAD in RGCs has been put in question by the phenotype of LGN (Mosaic protein LGN; homolog of *Drosophila* Pins) knockout mice ($Lgn^{-/-}$). Spindle orientation, and with it the plane of cytokinesis, is essentially randomized in RGCs from $Lgn^{-/-}$ mice. Yet cell fate determination and neurogenesis are not significantly affected, as strikingly substantiated by the viability and normal brain size of $Lgn^{-/-}$ mice [15,18••]. What is clearly affected in these mice is the attachment of RGCs to the ventricular zone, causing a significant number of these cells to lose contact with the neuroepithelium and to get scattered over the mantle zone [15,18••]. This observation demonstrates that controlled spindle orientation is required for both daughter cells to retain part of the cell adhesion domain, as proposed by Marthiens and ffrench-Constant [21••]. Interestingly, the RGCs that detach from the apical surface continue to proliferate at their new ectopic positions, maintaining a seemingly normal rate of neuronal production. This strongly suggests that the identity of RGCs and their ability to undergo SRAD do not necessarily require proximity to an apical niche and might be controlled by cell-intrinsic mechanisms [15,18••]. Identical results have been observed following *LGN* inactivation in the spinal cord neuroepithelium of the developing chick embryo [25••].

Centrosome asymmetry

A functional link between SRAD and centrosome asymmetry was first suggested by electron microscopy and immunofluorescence studies carried out in the germline SCs of male *Drosophila*, which revealed that through the cell cycle, the older (mother) centrosome maintains a robust aster proximal to the hub from which stemness signals originate [26•]. At mitosis, the mother centrosome is retained by the SC and the daughter centrosome is inherited by the differentiating cystoblast [26•]. A similar situation was observed in *Drosophila* neuroblasts, both larval [27•,28•] and embryonic [29], in which the dynamic nature of centrosome asymmetry was further demonstrated by time-lapse confocal microscopy. Centrosome asymmetry in *Drosophila* neuroblasts has a very early onset (i.e. the beginning of interphase), when two distinct centrosomes can be recognized. For most of the cell cycle, one centrosome remains bound to the apical cortex and organizes the cell's main microtubule network, while the other (essentially devoid of pericentriolar material and microtubule-organizing center activity) keeps moving through the cytoplasm. At mitosis, the apical centrosome is retained by the renewed neuroblast and the other is inherited by the resulting ganglion mother cell (Figure 1). Thus, despite the notable differences between germline SCs and neuroblasts in terms of cell cycle length, cytoarchitecture, and signaling pathways, both cell types display a stereotyped asymmetric behavior of the centrosomes, suggesting that centrosome asymmetry could be a common feature in cells that undergo SRAD.

Substantiating this suggestion, a recent report demonstrates that centrosome asymmetry also occurs and plays a crucial role in SRAD of rodent RGCs [30••]. Using a photoconvertible fluorescent tag fused to the centriolar protein Centrin-1, Wang *et al.* [30••] showed that the older (mother) centriole is preferentially inherited by the renewed RGC, while the newly made centrosome is inherited by the differentiating sister cell. More importantly, they also showed that depletion of Ninein, a component of the centriolar appendages required for centrioles to mature and acquire mother centrosome features, results in the exhaustion of the RGC pool. This observation demonstrates a functional link between centriole maturation and RGC fate [30••]. It remains unclear how the mother centrosome performs this function. In dividing NIH 3T3 mouse fibroblasts, the daughter cell that inherits the mother centriole usually projects a cilium before its sister cell does [31]. In RGCs, such a gap in timing, if it existed, could affect the receptiveness to different cell fate signals. Indeed, primary cilia have been shown to act as key transducers in a number of signal transduction pathways, including Sonic hedgehog protein (SHH) and platelet-derived growth factor (PDGF) pathways. Alternatively, or in addition to the above, cell fate specification may rely on the notably different centrosomal microtubule-organizing center activity of mother and daughter centrosomes [30••,32].

Centrosome functions

In *Drosophila* neuroblasts, all known cortical polarity cues are lost after cytokinesis, except for the position of the apical centrosome, which stays on the apical side of the renewed neuroblast where it organizes a microtubule aster that accurately predicts the future site of apical crescent assembly [27•,28•,29]. These data strongly suggested that the apical centrosome might serve as a polarity orientation cue that is passed on from one cell cycle to the next, a hypothesis that has been confirmed by a recent report showing that relocalizing the interphase aster results in concomitant repositioning of the apical cortex [33••]. An interesting corollary derived from this work is that neuroblast polarity can be reset at different angles without altering the position of the neuroblast with respect to the surrounding cells, highly suggestive of the possibility that neuroblast polarity orientation might be controlled in a cell-autonomous manner [33••]. In

addition, these studies showed that the orientation of neuroblasts polarity is set at each cell cycle to match the orientation in the last. Remarkably, after transient microtubules depolymerization, in some cells the centrosome that organized the apical aster ended up at the basal spindle pole while the centrosome originally destined for the GMC was retained by the neuroblast [33••]. These observations show that despite the centrosomes' conspicuous structural and functional differences, their maturation state does not appear to dictate the daughter cell's fate during SRAD of *Drosophila* neuroblasts [33••].

The apparently innocuous effect that uncontrolled spindle orientation appears to have on SRAD in RGCs is in sharp contrast with the severe consequences that loss of centrosomal proteins has for brain development. For instance, the five thus far cloned loci of which loss of function causes human microcephaly, a condition that results in severely smaller but anatomically normal brains, encode centrosome-related proteins [34]. The need for mature centrosome function to maintain the RGC pool is further substantiated by the shift toward neurogenesis at the expense of the RGC pool, caused by silencing of the genes encoding Hook homolog 3 (*Hook3*) or Pericentriolar material 1 (*Pcm1*), two proteins essential for the trafficking of pericentriolar satellites that sustain the assembly of pericentriolar material [35]. Interkinetic nuclear migration (i.e. the movement of the nucleus to the apical side of the RGC before mitosis) is also impaired following the silencing of genes encoding centrosomal proteins like Cep120 or its interacting transforming acidic coiled-coil-containing proteins, which also causes the reduction of the RGC pool [36].

The case of LIS-1 (mutated in lissencephaly) is also interesting in this regard. LIS-1 is a WD40-domain protein that regulates the Dynactin complex by directly binding Dynein and Dynactin subunit 1 (p150-glued). The Dynein–Dynactin complex has been shown to regulate organelle positioning, centrosome separation, and spindle orientation in different organisms [37]. In *Drosophila* neuroblasts Lis-1/Dynactin regulates metaphase spindle orientation [38]. In mouse RGCs, LIS-1 is also essential for the orientation of the mitotic spindle, by maintaining cortical Dynein and stabilizing cortical microtubules [39]. Loss of LIS-1 results in RGC depletion early in cortical development and a reduced number of cortical neurons [39]. Since similar phenotypes are caused by inactivation of *Cep120*, *Tacc* genes, *Ninein*, and *Hook3*, but not by *Lgn* deficiency, it is possible that the developmental consequences of LIS-1 loss of function might be due to centrosome dysfunction rather than, or in addition to, uncontrolled spindle orientation.

Conclusions

The current picture of SRAD in RGCs is still fuzzy. From what we know at the molecular level, it is clear that certain highly conserved modules, like the PAR and Pins complexes, are used in flies and rodents for similar purposes, but in different manners. It is also evident that other highly conserved components might be playing quite distinct roles. Something comparable applies at the microscopic level. Although centrosome behavior is distinctly asymmetric in both *Drosophila* neuroblasts and mouse RGCs, the actual role of such asymmetry appears to be quite different in the two species. Significant disparity also appears to exist between rodents and humans, where a very recent report reveals that RGCs in the outer region of the subventricular zone lack contact with the ventricular surface and are non-epithelial [40]. It can be anticipated that recent breakthrough developments in live imaging of molecular reporters will render a much more focused view on SRAD of RGCs in the near future.

Acknowledgements

We thank Dr Elke Van Ael for editing this manuscript. BL is a postdoctoral fellow of the Research Foundation Flanders (FWO). IG is a holder of a CSIC JAE-predoctoral Fellowship. Work in E.M.'s laboratory is supported by grants BFU2007-60487 and CONSOLIDER CSD2007-00008.Work in C.G.'s laboratory is supported by E.U. and Spanish grants: ONCASYM-037398 FP6, BFU2006-05813, SGR2005 Generalitat de Catalunya, and Consolider CENTROSOME_3D CSD2006-23.

References and recommended reading

Papers of particular interest, published within the annual period of review, have been highlighted as:

- • of special interest
- •• of outstanding interest

1. Morrison SJ, Kimble J: **Asymmetric and symmetric stem-cell divisions in development and cancer**. *Nature* 2006, **441**:1068-1074.

2. He S, Nakada D, Morrison SJ: **Mechanisms of stem cell self-renewal**. *Annu Rev Cell Dev Biol* 2009, **25**:377-406.

3. Zhong W, Chia W: **Neurogenesis and asymmetric cell division**. *Curr Opin Neurobiol* 2008, **18**:4-11.

4. Doe CQ: **Neural stem cells: balancing self-renewal with differentiation**. *Development* 2008, **135**:1575-1587.

5. Siller KH, Doe CQ: **Spindle orientation during asymmetric cell division**. *Nat Cell Biol* 2009, **11**:365-374.

6. • Truman JW, Bate M: **Spatial and temporal patterns of neurogenesis in the central nervous system of *Drosophila melanogaster***. *Dev Biol* 1988, **125**:145-157.
This seminal manuscript describes the timing and localization of SRAD in the larval brain of *Drosophila melanogaster*.

7. Maurange C, Cheng L, Gould AP: **Temporal transcription factors and their targets schedule the end of neural proliferation in *Drosophila***. *Cell* 2008, **133**:891-902.

8. Gotz M, Huttner WB: **The cell biology of neurogenesis**. *Nat Rev Mol Cell Biol* 2005, **6**:777-788.

9. Kriegstein A, Noctor S, Martinez-Cerdeno V: **Patterns of neural stem and progenitor cell division may underlie evolutionary cortical expansion**. *Nat Rev Neurosci* 2006, **7**:883-890.

10. Haubensak W, Attardo A, Denk W, Huttner WB: **Neurons arise in the basal neuroepithelium of the early mammalian telencephalon: a major site of neurogenesis**. *Proc Natl Acad Sci U S A* 2004, **101**:3196-3201.

11. Noctor SC, Martinez-Cerdeno V, Ivic L, Kriegstein AR: **Cortical neurons arise in symmetric and asymmetric division zones and migrate through specific phases**. *Nat Neurosci* 2004, **7**:136-144.

12. Attardo A, Calegari F, Haubensak W, Wilsch-Brauninger M, Huttner WB: **Live imaging at the onset of cortical neurogenesis reveals differential appearance of the neuronal phenotype in apical versus basal progenitor progeny**. *PLoS One* 2008, **3**:e2388.

13. Gonzalez C: **Spindle orientation, asymmetric division and tumour suppression in *Drosophila* stem cells**. *Nat Rev Genet* 2007, **8**:462-472.

14. Farkas LM, Huttner WB: **The cell biology of neural stem and progenitor cells and its significance for their proliferation versus differentiation during mammalian brain development**. *Curr Opin Cell Biol* 2008, **20**:707-715.

15. Shioi G, Konno D, Shitamukai A, Matsuzaki F: **Structural basis for self-renewal of neural progenitors in cortical neurogenesis**. *Cereb Cortex* 2009, **19(Suppl. 1)**:i55-i61.

16. Miyata T, Kawaguchi D, Kawaguchi A, Gotoh Y: **Mechanisms that regulate the number of neurons during mouse neocortical development**. *Curr Opin Neurobiol* 2010, **20**:22-28.

17. •• Cabernard C, Doe CQ: **Apical/basal spindle orientation is required for neuroblast homeostasis and neuronal differentiation in *Drosophila***. *Dev Cell* 2009, **17**:134-141.
This manuscript demonstrates that the ratio of apical/basal determinants specifies neuroblasts versus ganglion mother cell identity.

18. •• Konno D, Shioi G, Shitamukai A, Mori A, Kiyonari H, Miyata T, Matsuzaki F: **Neuroepithelial progenitors undergo LGN-dependent planar divisions to maintain self-renewability during mammalian neurogenesis**. *Nat Cell Biol* 2008, **10**:93-101.
Demonstration that loss of the PINS homolog LGN perturbs mitotic spindle orientation but does not affect neurogenesis in mice.

19. Fish JL, Kosodo Y, Enard W, Paabo S, Huttner WB: **Aspm specifically maintains symmetric proliferative divisions of neuroepithelial cells**. *Proc Natl Acad Sci U S A* 2006, **103**:10438-10443.

20. Kosodo Y, Roper K, Haubensak W, Marzesco AM, Corbeil D, Huttner WB: **Asymmetric distribution of the apical plasma membrane during neurogenic divisions of mammalian neuroepithelial cells**. *EMBO J* 2004, **23**:2314-2324.

21. •• Marthiens V, ffrench-Constant C: **Adherens junction domains are split by asymmetric division of embryonic neural stem cells**. *EMBO Rep* 2009, **10**:515-520.
This article suggests a mechanism by which after SRAD in RGCs, both daughters retain adherens while acquiring different fates.

22. Costa MR, Wen G, Lepier A, Schroeder T, Gotz M: **Par-complex proteins promote proliferative progenitor divisions in the developing mouse cerebral cortex**. *Development* 2008, **135**:11-22.

23. Bultje RS, Castaneda-Castellanos DR, Jan LY, Jan YN, Kriegstein AR, Shi SH: **Mammalian Par3 regulates progenitor cell asymmetric division via notch signaling in the developing neocortex**. *Neuron* 2009, **63**:189-202.

24. Imai F, Hirai S, Akimoto K, Koyama H, Miyata T, Ogawa M, Noguchi S, Sasaoka T, Noda T, Ohno S: **Inactivation of aPKClambda results in the loss of adherens junctions in neuroepithelial cells without affecting neurogenesis in mouse neocortex**. *Development* 2006, **133**:1735-1744.

25. •• Morin X, Jaouen F, Durbec P: **Control of planar divisions by the G-protein regulator LGN maintains progenitors in the chick neuroepithelium**. *Nat Neurosci* 2007, **10**:1440-1448.
Demonstration that loss of the PINS homolog LGN perturbs mitotic spindle orientation but does not affect neurogenesis in the chick neuroepithelium.

26. • Yamashita YM, Mahowald AP, Perlin JR, Fuller MT: **Asymmetric inheritance of mother versus daughter centrosome in stem cell division**. *Science* 2007, **315**:518-521.
Demonstration of unequal centrosomes in *Drosophila* male germline stem cells.

27. • Rebollo E, Sampaio P, Januschke J, Llamazares S, Varmark H, Gonzalez C: **Functionally unequal centrosomes drive spindle orientation in asymmetrically dividing *Drosophila* neural stem cells**. *Dev Cell* 2007, **12**:467-474.
Demonstration of unequal centrosomes in *Drosophila* larval neuroblasts.

28. • Rusan NM, Peifer M: **A role for a novel centrosome cycle in asymmetric cell division**. *J Cell Biol* 2007, **177**:13-20.
See annotation [27•].

29. Rebollo E, Roldan M, Gonzalez C: **Spindle alignment is achieved without rotation after the first cell cycle in *Drosophila* embryonic neuroblasts**. *Development* 2009, **136**:3393-3397.

30. •• Wang X, Tsai JW, Imai JH, Lian WN, Vallee RB, Shi SH: **Asymmetric centrosome inheritance maintains neural progenitors in the neocortex**. *Nature* 2009, **461**:947-955.
This study demonstrates a functional link between centrosome function and cell fate during neurogenesis in mice.

31. Anderson CT, Stearns T: **Centriole age underlies asynchronous primary cilium growth in mammalian cells**. *Curr Biol* 2009, **19**:1498-1502.

32. Stearns T: **Stem cells: a fateful age gap**. *Nature* 2009, **461**:891-892.

33. •• Januschke J, Gonzalez C: **The interphase microtubule aster is a determinant of asymmetric division orientation in *Drosophila* neuroblasts**. *J Cell Biol* 2010, **188**:693-706.
This article shows that the position of the interphase aster contributes to define polarity orientation in *Drosophila* neuroblasts.

34. Thornton GK, Woods CG: **Primary microcephaly: do all roads lead to Rome?** *Trends Genet* 2009, **25**:501-510.

35. Ge X, Frank CL, Calderon de Anda F, Tsai LH: **Hook3 interacts with PCM1 to regulate pericentriolar material assembly and the timing of neurogenesis**. *Neuron* 2010, **65**:191-203.

36. Xie Z, Moy LY, Sanada K, Zhou Y, Buchman JJ, Tsai LH: **Cep120 and TACCs control interkinetic nuclear migration and the neural progenitor pool**. *Neuron* 2007, **56**:79-93.

37. Kardon JR, Vale RD: **Regulators of the cytoplasmic dynein motor**. *Nat Rev Mol Cell Biol* 2009, **10**:854-865.

38. Siller KH, Doe CQ: **Lis1/dynactin regulates metaphase spindle orientation in *Drosophila* neuroblasts**. *Dev Biol* 2008, **319**:1-9.

39. Yingling J, Youn YH, Darling D, Toyo-Oka K, Pramparo T, Hirotsune S, Wynshaw-Boris A: **Neuroepithelial stem cell proliferation requires LIS1 for precise spindle orientation and symmetric division**. *Cell* 2008, **132**:474-486.

40. Hansen DV, Lui JH, Parker PR, Kriegstein AR: **Neurogenic radial glia in the outer subventricular zone of human neocortex**. *Nature* 2010, **464**:554-561.

41. Rasin MR, Gazula VR, Breunig JJ, Kwan KY, Johnson MB, Liu-Chen S, Li HS, Jan LY, Jan YN, Rakic P *et al.*: **Numb and Numbl are required for maintenance of cadherin-based adhesion and polarity of neural progenitors**. *Nat Neurosci* 2007, **10**:819-827.

42. Schwamborn JC, Berezikov E, Knoblich JA: **The TRIM-NHL protein TRIM32 activates microRNAs and prevents self-renewal in mouse neural progenitors**. *Cell* 2009, **136**:913-925.